UNIVERSITY OF SOUTHAMPTON

ANALYSIS AND INTERPRETATION OF SAR DATA FOR THE ENGLISH CHANNEL

BY

ALISON SCOON

Submitted in partial fulfilment for the degree of Doctor of Philosophy
Department of Oceanography, Faculty of Science,
University of Southampton

Submitted in April 1995

ABSTRACT

The launch of the ERS-1 SAR in 1991 has provided oceanographers with an opportunity to obtain repeatable direct measurements of small scale topography (roughness) of the sea surface. This thesis investigates the application of SAR for monitoring coastal oceanography in the English Channel. That a radar type instrument can detect small scale features, such as tidal fronts and nearshore shoals and banks, was demonstrated by a preliminary qualitative examination of Seasat SAR images. Further investigations of a small coastal front using an airborne altimeter, combined with results from an existing monitoring programme, verified that frontal features can be associated with variations in surface roughness. The quantitative analysis of ERS-1 SAR measures of backscatter in terms of the correspondence of the data to the modulation of short waves is the main subject of this work. The multi-temporal capabilities of ERS-1 SAR have enabled a rigorous analysis of these data, enabling both the performance of the calibration routine and the backscatter relationships with dynamic features to be examined for varied wind and tide conditions. A power loss caused by saturation of the analogue to digital converter (ADC) was found to result in underestimates of backscatter values by up to 3 dB, not previously accounted for. The significance and effectiveness of using the fullest possible correction was demonstrated by comparing SAR-derived estimates of backscatter across range with predictions from an empirical wind retrieval model (CMOD4), which describes the dependence of backscatter on incidence angle.

It was found that in the coastal zone the backscatter signal is dominated by transitional wind effects, which often confuse or obscure any dynamic sea surface signatures. Estimates of the wind speed contribution to surface roughness were successfully achieved using the CMOD4 to accuracies within the error bands of the model (±2 ms^{-1}). Comparisons of SAR-derived wind speeds between images demonstrated the importance of correcting for the effects of the SAR viewing geometry. It was empirically shown that a normalised SAR-derived apparent wind speed residual gave a proportional representation of surface roughness that could not be achieved using a direct measure of backscatter. It is shown that the non-linearities introduced into the data by these effects should be removed if comparisons of the backscatter signature of surface roughness variations are to be made between images, with physical variables, such as currents, or with model predictions.

CONTENTS

CHAPTER EIGHT USING SAR-DERIVED APPARENT WIND SPEED ESTIMATES TO EVALUATE SURFACE ROUGHNESS PATTERNS

CHAPTER NINE CONCLUSIONS AND FUTURE WORK

TABLES

FIGURES

PLATES

GLOSSARY

ABL	Atmospheric Boundary Layer
ADC	Analogue to Digital Converter
ATM	Airborne Thematic Mapper
ATTA	Airborne Terain Tracking Altimeter
AVHRR	Advanced Very High Resolution Radiometer
CMOD4	wind retrieval model for the ERS-1 scatterometer, version 4
DLR	German SAR processing facility
ERS-1	Earth Resources Satellite-1
ESA	European Space Agency
FFT	Fast Fourier Transform
IR	Infra Red
MABL	Marine Atmospheric Boundary Layer
PAF	Processing Algorithm Facility
PRI	PRecision Image
SAR	Synthetic Aperture Radar
SLAR	Side Looking Airborne Radar
SST	Sea Surface Temperature
VHRR	Very High Resolution Radiometer
σ_0	backscatter cross section
σ_0'	fully calibrated backscatter cross section
$S\sigma_0$	standardised backscatter cross section
γ	normalised wind speed ratio
θ_n	local incidence angle
f	radar view angle relative to wind direction

ACKNOWLEDGEMENTS

Thanks to everybody for putting up with me,
to Dave who answers all,
to Sue for help in the pursuit of Ian,
to Kate who can make sketches look the business,
to Henry who is always wise
to Phil for coping with my flappers,
and of course to Ian for letting me hassle him.

CHAPTER ONE

INTRODUCTION AND AIMS

1.1 INTRODUCTION

The development of microwave satellite sensors, such as the synthetic aperture radar (SAR), has provided a means of making direct measurements of the small scale topography (roughness) of the sea surface. It is now well established that the modulation of these short waves by surface currents or atmospheric effects enables oceanographic and atmospheric features to be detected by SAR. Images recording mesoscale features, such as the Gulf Stream frontal boundary and associated warm core eddies and mesoscale wind fronts, are now well documented (Hayes, 1981 and Johannessen *et al.,* 1993). The value of SAR lies in the potential not only to locate and observe the spatial distribution of features, but also to obtain quantitative measures of the factors modulating the high frequency wind waves. The benefit of the synoptic view and high temporal resolution offered by satellite instruments has long been recognised as a valuable addition to *in situ* oceanographic measurements.

Following the launch of the first civilian spaceborne SAR on Seasat in 1978 there was a gap of more than a decade before the deployment of the ERS-1 SAR in July 1991. In the interim period research developing the theory and modelling the surface wave spectrum detected by SAR relied on the limited data available from the Seasat mission, short term airborne missions and sensors mounted on towers (Meadows *et al.*, 1983, Gasparovic *et al.*, 1986; Johannessen *et al.*, 1991; Keller *et al.*, 1985). Models of the surface roughness response to variations in the surface current have been developed, but testing their performance was restricted to the few images acquired by Seasat SAR. The launch of ERS-1 SAR, a stable and well calibrated instrument, has provided the user with the first opportunity to make comparisons of backscatter measurements both between images and with model predictions (Laur *et al.*, 1993). Being able to exploit the multi-temporal capability of ERS-1 SAR provides a means of quantitatively assessing the effectiveness of SAR for the investigation of coastal dynamic features on the scale of 10 to 100s of metres. There has been little quantitative assessment of SAR backscatter measurements in terms of the correspondence of the data to real surface roughness features. Determining empirical relationships with factors such as current gradients over different wind and tide conditions and making comparisons with model predictions would considerably improve the understanding of backscatter mechanisms.

An ultimate goal for exploiting SAR would be to obtain quantitative measures of currents and frontal activity in order to validate numerical models of coastal dynamics. Understanding the role of factors such as currents, eddies and frontal boundaries in the transport of sediments, nutrients and pollutants is an important aspect of coastal management.

1.2 AIM OF THE STUDY

This study investigates the application of SAR to dynamical coastal research and in particular, how it could contribute to existing monitoring programmes of the English Channel, such as the Fluxmanche study (Fluxmanche, 1993). The research commenced as part of NERC's ERS-1 SAR Special Topic programme. The emphasis is placed on using the multi-temporal capabilities of SAR to study features such as fronts, currents and bathymetry over varied wind and tide conditions. On an operational basis it is important to understand the conditions required for features of interest to be imaged, since this will influence the opportunies of obtaining usable data from SAR. The influence of different factors, such as tidal currents or marine atmospheric boundary layer (MABL) stability effects are considered in terms of their contribution to the surface roughness signature detected. Comparisons between images of the backscatter signature for specific features and investigations of the surface roughness relationships with wind and tide require accurately calibrated data. As the research programme progressed it became apparent that obtaining a quantitative measure of the backscatter signal from SAR is far from straightforward; there are fundamental problems in calibrating and in determining even relative measures of backscatter variability. The emphasis of the work gradually changed from the detailed study of SAR coastal applications to a methodological study of the quality of SAR data, its calibration and acquiring accurate representations of backscatter variability. The primary aim of this thesis is as follows:

To be able to quantify backscatter variability across specific dynamic oceanographic features imaged by SAR, in terms that are comparable between images and with backscatter model predictions.

1.3 CHRONOLOGICAL OVERVIEW OF THE STUDY

In order to provide the context of the work described in the thesis, it is helpful to summarise the progression of the study as the results and difficulties were encountered. The late launch of ERS-1 in July 1991 and the subsequent delay in the distribution of the digital image data until August 1992 meant the study began with a preliminary assessment of existing Seasat SAR data acquired for the English Channel. This enabled a broad overview to be acquired of the type of coastal dynamical features detectable by SAR and, by using surface wind measurements from synoptic charts, an indication of the types of factors affecting feature detection. The area around the Isle of Wight was identified as a suitable region for the more intensive study of features using ERS-1 data. Although analysis of the hardcopy Seasat SAR data provided an indication of the surface roughness signatures associated with a frontal boundary, a more detailed understanding was sought of the sea surface roughness patterns and mechanisms enabling a small scale frontal boundary to be detected. To achieve this a field experiment was run which was intended to provide comparisons between contemporaneous SAR backscatter patterns, results from a nadir sampling radar, *in situ* measurements and visual observations. Unfortunately the launch of ERS-1 was further delayed by several months, but results from the experiment proved encouraging and identified the need for an extended sequence of fieldwork during the SAR campaign.

The delivery of the first ERS-1 SAR images in August 1992 enabled the digital analysis of the data to begin, providing the opportunity to make quantitative comparisons of relative changes in the backscatter variability across specific features. Investigations of the images are based on the acquisition of two sequences of data centred on the Isle of Wight region: first a series of nine images from the three day repeat phase and then a longer series from January to September 1993, a total of 34 images. By repeatedly covering the same area it was possible to carry out an intensive, systematic study of features in relation to wind and tidal current effects. The first sequence of data was used to identify possible dynamic oceanographic effects and the second to investigate them, combining SAR images with concurrent field experiments. Once all the data were available and could be assessed in relation to the wind and tide conditions it became clear that many features from the first sequence of data considered to be of interest were not repeated. It would appear that many of the features detected by SAR in the coastal zone are a product of ephemeral patterns in the wind field. Consequently, the work progressively moved towards determining both how to identify and quantify the backscatter contribution attributed to a specific wind speed and that resulting from additional modulation of the short wave spectrum by surface currents and other possible oceanographic effects. Estimates of the wind speed effects on the surface roughness signature were obtained using a wind retrieval model for the ERS-1 scatterometer. Results from this analysis enabled the importance of the effects of viewing geometry on SAR images to be assessed. It was realised that where comparisons are to be made between images or with backscatter model predictions the effects of the satellite viewing geometry must be accounted for. A technique was defined for obtaining comparable, quantitative measures of surface roughness variability. The method was tested by carrying out a brief investigation of the backscatter characteristics associated with a bathymetric feature for varied wind and tide conditions. Comparisons between the measured and predicted backscatter across the feature were then used to test the application of a simple first order bathymetric model.

1.4 SPECIFIC OBJECTIVES

The following objectives were identified in response to the primary aim and according to the data availability; the requirements becoming more specific as understanding of the SAR data progressed, emphasising the difficulties associated with obtaining quantitative measures of backscatter from SAR:

- To use the multi-temporal capabilities of SAR to characterise surface backscatter signatures associated with coastal fronts and bathymetric features and to determine the factors affecting their repeated detection.

- To determine the sea surface roughness patterns and the mechanisms which enable small scale frontal boundaries to be detected.

- To be able to determine the backscatter contribution attributed to a specific wind speed and that resulting from additional modulation of the short wave spectrum by surface currents and other possible oceanographic effects.

- To achieve a measure of small scale surface roughness that is independent of the effects of the satellite viewing geometry.

1.5 SUMMARY OF THESIS CHAPTERS

A brief overview of the layout of the thesis is given here, identifying the chapters dealing with the themes discussed previously. Chapter Two contains a brief description of the SAR, the imaging mechanisms and the factors modulating the sea surface roughness. Previous work using SAR or airborne radar to study oceanographic features is discussed and assessed for its quantitative approach and relevance to this study.

The results of preliminary assessment of the Seasat SAR images are presented in Chapter Three and provide a basis for the investigation of the ERS-1 data. The methodology determined to define specific features is described. Chapter Four describes the multi-sensor experiment using airborne radar and multispectral data coincident with *in situ* measurements across a coastal front off Cap Gris-Nez in the Dover Straits.

Once the ERS-1 digital SAR data became available the priority was to calibrate the images. Chapter Five describes the difficulties encountered handling the ERS-1 SAR data and the calibration procedure. Additional corrections, which were found to be necessary to fully calibrate SAR images, were obtained from the ERS-1 SAR calibration and validation team. The significance and effectiveness of using the fullest possible correction is demonstrated. A summary of the results from the visual assessment of the data and a description of the aims and results from the supporting fieldwork programme is given in Chapter Six. Results from the visual analysis suggested it was necessary to fully understand the effects of wind on the image. Chapter Seven develops the use of the ERS-1 scatterometer wind retrieval (CMOD4) to estimate wind speed from SAR. The effectiveness of this approach and the additional information obtained is discussed. Chapter Eight describes the investigation of the effects of satellite viewing geometry on the backscatter detected by the SAR. The importance of removing biases in the data is demonstrated by assessing empirical relationships between the corrected surface roughness measurement and physical factors such as tidal currents. The results from comparing model predictions with corrected backscatter measurements made across a bathymetric feature are discussed. The conclusions and reccomendations made from the research are presented in Chapter Nine.

CHAPTER TWO

REVIEW OF BACKGROUND KNOWLEDGE

2.1 INTRODUCTION

In this chapter a basic review is given of Sythetic Aperture Radar (SAR) imaging techniques. The main emphasis is then placed on what is known about the physical factors which affect the small scale surface roughness and the processes enabling oceanographic features, such as fronts, eddies, currents and bathymetry, to be imaged. Aspects which are of specific interest to the study are considered in more detail in the relevant chapters later in the thesis.

2.2 SYNTHETIC APERTURE RADAR (SAR)

The SAR on board ERS-1 is part of the Active Microwave Instrument (AMI), which operates in the C-band at a frequency of 5.3 Ghz. The SAR is a microwave imaging system which produces a near-instantaneous image across a 100 km swath. The instrument look direction is to the right of the satellite and has a mid-swath incidence angle of 23°.

Over the ocean, variations in backscatter intensity within the image are largely the result of changes in slope and roughness of the sea surface. Electromagnetic waves emitted by the SAR are scattered by the short surface waves and the amplitude of the return signal is a measure of the surface roughness. SAR is a high resolution instrument (12.5m x 12.5m pixels) and this is achieved by using the forward motion of the satellite to synthesize a large aperture for the radar. The position of a target is located in the azimuthal direction by measuring the Doppler shift in frequency between the emitted and returned pulse and in the range direction by using the time taken for the pulse to return (Robinson 1985).

The radar views the surface at an oblique angle (θ) and, to the first order, radar backscattering can be described by Bragg scattering theory (Valenzuela, 1978). That is, constructive interference occurs when the surface waves scattering the radar signal are on a length scale comparable to the radar wavelength (λ_R).

$$\lambda_B = \lambda_R / 2\sin\theta$$

This theory predicts that the normalised radar cross section (the ratio of backscattered to emitted power) is proportional to the spectral energy density of the sea surface waves at the Bragg wavelength (λ_B). Although this theory accounts for a large proportion of the return signal it cannot directly account for many of the backscatter variations and patterns detected by the SAR. In the cases of Seasat SAR (1.28 GHz) and ERS-1 SAR (5.3 GHz) the Bragg wavelengths are approximately 30 cm and 7 cm respectively. According to Phillips (1977), a wind of only 2 to 3 ms^{-1} would be sufficient to produce these high frequency, short waves. As the wind increases the high frequency end of the wave spectrum is believed to saturate and then remain constant while the low frequency, long gravity waves develop.

The wide range of oceanographic features detected using SAR indicates that imaging mechanisms additional to Bragg scattering are influencing the backscatter patterns. Imaging of the longer gravity waves is ascribed to three main theories: hydrodynamic modulation; electromagnetic interaction; and motion effects; all a product of a moving surface. Also contributing to the backscatter signal is random, multiplicative (bright and dark) noise, which is seen on all SAR images and is referred to as speckle. This results from the coherent summation of radar reflections from different areas of a rough surface within one pixel. It can be reduced by adding together several independent looks of an area.

Hydrodynamic modulation results from the orbital motions within the larger waves causing a convergence and divergence of energy of the small Bragg waves superimposed on their surface. It is this effect that partly explains the imaging of swell waves by the SAR. Electromagnetic or tilt modulation is caused by the large waves changing the orientation of the surface to the sensor, resulting in a light and dark banded pattern representing swell. Both of these wave imaging mechanisms apply only for waves travelling in the range direction. Finally, the velocity bunching mechanism is due to vertical motions towards or away from the sensor causing a shift of the position of a facet on the image during aperture synthesis processing. This is the mechanism which enables azimuth travelling waves to be readily imaged. If the waves are propagating with the satellite then the concentration of scattering facets is effectively increased over the troughs and decreased over the crests and vice versa. Detailed explanations of the SAR and ocean surface roughness interaction with electromagnetic waves are given by Allan (1983), Robinson (1985) and Stewart (1985).

2.3 MECHANISMS MODULATING THE SEA SURFACE ROUGHNESS

Before its launch Seasat SAR was expected by some to image only surface swell waves but it rapidly became apparent that the complexity of the surface features detected could be linked to other dynamical processes such as fronts and eddies (Vesecky and Stewart, 1982; Harris *et al.*, 1986). Research using Seasat SAR images has provided the background both for understanding the features observed and investigating the backscattering mechanisms (Alpers, 1983). SAR responds principally to scattering from the short waves, it is modulation of these waves that enables oceanographic features to be detected. Modulation of the surface currents by tidal flow over bathymetry or circulation patterns generated by features, such as fronts and eddies, can cause current shear zones or convergences and divergences to develop, often producing a strong variation in the surface roughness detectable on SAR images. Gravity waves propagating across such features experience a variety of interactions (Phillips, 1981). These interactions may occur between other surface waves (Lake and Yuen, 1978) or with the modulated current field (Hayes, 1981), resulting in refraction (McLeish and Ross, 1985) and sometimes reflection of the wave field, causing perturbations in the spectral density of the waves. Localised atmospheric effects such as wind fronts, cats paws, wind rows, sheltering and changes in air temperature can also be of importance. The effect of these processes on the surface roughness pattern can be considerable, small changes in the wind field, current regime or stability of the MABL resulting in complex patterns of slicks, rough or smooth lines and large adjacent areas of rough and smooth backscatter that often are linked to oceanographic features. The main processes modulating the sea surface roughness are briefly discussed in terms of their cause and appearance on the SAR image; wave-current interaction; wave-wave interaction; MABL stability; and surface surfactants.

2.3.1 Wave-current interaction

Localised circulation patterns develop along frontal margins or result from flow restrictions across bathymetry in coastal regions. At a frontal boundary the horizontal and vertical density gradients can produce different current components, a surface convergence zone and a current shear parallel to the front. Differing flow rates across bathymetric features result in similar effects, convergences and shear zones developing as water is forced to travel faster over shallow regions and slower as it re-enters the deeper water.

Wave-current interaction effects on SAR were studied by Alpers and Hennings (1984), Meadows et al (1983) and Phillips (1981) in relation to the modulation of surface currents by bottom topography. Opposing currents or regions where the flow rate suddenly slows, but the currents are propagating in the same direction, such as on the down tide side of a bank or along a frontal boundary, produce an increase in the surface wave amplitude and a decrease in wavelength. Effectively a convergence of surface currents compresses the wave field, thus increasing the energy density of short waves and the radar backscatter. This often appears as a line feature marking the current boundary. Huang et al (1972) showed that the current fields have only to differ slightly for a large increase in the high frequency wave spectrum to occur. The resulting change in surface roughness is frequently detectable on SAR images as a bright linear feature, 200 to 300 metres in width. Conversely, diverging currents expand the surface wave field and a decrease in radar backscatter (a dark line) is often observed on the uptide side of a bank. The intensity of the returns are linked closely to the current gradients and local wind field at the time of the satellite pass.

Wave interaction with surface shearing and converging currents has also been investigated using modelling techniques to predict changes in the surface wave spectrum (Lyzenga, 1991). The results suggest that the dominant effects on radar backscatter are due to surface waves longer than the Bragg wavelength, since predicted changes in backscatter caused by the 1 to 10 cm waves were very small. At 1 m wavelengths changes in the energy density were predicted to be at their maximum and it is postulated that changes in incidence angle caused by tilting of the surface by the longer waves may explain bright linear features observed on SAR. It is not completely certain that the model fully explains the observed backscatter variations since the effect weakens considerably at incidence angles greater than 20 degrees, beyond which angle the SAR operates.

2.3.2 Wave-wave interaction

Wave-wave interaction is a transfer of energy between waves caused by resonant interactions or a dissipative process, such as wave breaking (Hasselman, 1962). The refraction of long surface gravity waves as they propagate across an area of current shear results in a saturation of the waves and energy is transferred to the shorter wave field, thus affecting the surface radar reflectivity and producing a signature visible on SAR (Vesecky and Stewart, 1982; McLeish and Ross, 1985). It is thought that breaking waves will increase the energy density of waves throughout the spectrum, which will be detected by SAR as an increase in surface roughness (Phillips, 1988). It is likely that this will appear as a narrow line of increased backscatter as the wave field will return to equilibrium as it propagates out of the region.

2.3.3 Marine atmospheric boundary layer stability

Detection on radar images of increased surface roughness and therefore wind stress, over regions of warmer water has been the subject of much interest (Weismann and Thompson, 1977; Wu, 1991). There is considerable interest in the potential of marine radar to improve the understanding of air:sea flux processes (Thorpe 1985). The Frontal Air Sea Interaction Experiment (FASINEX), provided the first comprehensive set of measurements across a well developed thermal gradient (southwest of Bermuda), enabling a detailed study of the response of the lower MABL to sharp changes in sea surface temperature (SST). It is generally agreed that changes in atmospheric stability result from SST changes, producing an increase in convective mixing and wind stress over the warmer water (Greenhut, 1982; Businger and

Shaw, 1984; Keller *et al.,* 1985; Khalsa and Greenhut, 1989; Friehe *et al.*, 1991; Askari *et al.*, 1993). Measurements from tower-based experiments, using X-band radar, demonstrated an increase in the radar cross section in unstable MABL conditions (Keller *et al.*, 1985 and 1989). Models of the effects of atmospheric stability upon the short waves, and therefore the radar cross section, also predict large changes in the backscatter, dependent on wind speed and wind direction relative to the frontal boundary (Hsu *et al.*, 1985; Askari *et al.*, 1993).

2.3.4 Surface slick-like features

Natural slicks of organic material often form in light winds below 6ms^{-1} (Scott, 1986a), appearing as regions of smooth water (dark return) on a SAR image. Dynamical processes involved in the formation of slicks were reviewed by Hartwig and Herr (1984), including a discussion on their detection using remote sensing methods. The effects of viscosity, elasticity and atmospheric surface drag properties of the marine microlayer on the equilibrium of the short surface waves can cause a distinct change in backscattering from regions occupied by a slick. Non organic slicks can also cause an area to appear smooth on a radar image. Slick features are often found to be the product of convergent flow, such as along a frontal boundary or marking internal wave activity, due to the accumulation of surface material dampening the short Bragg waves and can easily be observed *in situ* (Pingree and Mardell, 1987). After the convergence ceases the stability of the slick is likely to decrease, the film patches breaking up into streaks, which may be similar to those observed in the sunglint photos made by Scully-Power (1986) during a Challenger space shuttle flight. Once the winds increase above 7ms^{-1} it is thought surface films would not have a significant effect on the prevention of the formation of short waves.

In some cases, divergent currents produce localised upwelling which may form a thin layer of colder (more viscous) water on the surface, dampening the short Bragg waves over an area and producing a slick-like feature on a SAR image. Narrow bands of smoother water may also be caused by divergent currents (see wave-current interaction section) and are associated with bathymetric boundaries or eddy fields.

2.4 A REVIEW OF PREVIOUS STUDIES OF OCEANOGRAPHIC FEATURES USING SAR

This section gives a brief overview of the dynamical oceanographic and atmospheric features detected using SAR, describing their appearance and associated imaging mechanism.

2.4.1 Mesoscale fronts and eddies

Despite the often considerable ambiguity in understanding and quantifying the backscatter patterns in relation to physical processes in the ocean, the all-weather capability of SAR and diversity of features imaged has made it impossible to ignore the oceanographic potential of the data. The ability to obtain 2-dimensional maps of the spatial distribution of features, such as mesoscale ocean fronts, is an essential aspect of describing ocean dynamics (Tilley and Beal, 1993). A great deal of the work investigating backscatter signatures and mechanisms across fronts has used the Gulf Stream and the associated warm water eddies as a study region. The strong boundary currents and marked SST variation across the front have made it an ideal feature to examine the imaging mechanism theories, such as wave refraction, wave-current interaction, MABL stability and slicks, enabling the front to be detected by SAR.

Bright lines on SAR images along the boundary of the Gulf Stream are attributed to increased surface roughness in the area of high velocity shear between the near-stationary shelf water and the main current (Vachon *et al.*, 1992). The effects of wave-wave interaction as waves are refracted or break along the current boundary are also considered to contribute to the narrow line of increased surface roughness detected on SAR (McLeish and Ross, 1985). Similar factors produce the distinctive streaks on SAR which define the Gulf Stream cold core eddies (Cheney, 1976). Results from a number of other experiments also detect abrupt changes in the sea surface roughness along frontal boundaries: airborne laser profilometer measurements made across the Labrador Current (McClain *et al.* 1982); ERS-1 SAR images of the Denmark Strait front, where the warm and cold Atlantic and Arctic water masses meet (Scott and Brownsword, 1994); and at the boundary of the Rhine-Meuse plume discharge front with the deeper North Sea water (Ruddick and Moens, 1993).

Radar images of thermal fronts may also detect a large change in the backscatter in the vicinity of the SST boundary. Several researchers have observed the Gulf Stream front and warm water eddies to appear brighter on the radar image than the adjacent shelf waters (Weisman and Thompson, 1977; Hayes, 1981; Ross 1981; Lichy *et al.*, 1981; Vachon *et al.*, 1992). An experiment in the Sea of Okhotsk also noted a stronger radar return over the warmer water (Ivanov *et al.*, 1986). Results from these studies suggest that thermal gradients identified by sharp variations in surface roughness can only be detected by radar in light to moderate wind conditions. Investigations of the backscatter response across an eddy system in the Tyrrhenian sea observed a strong, positve correlation in light wind conditions between the SST and radar spatial patterns; a subsequent increase in the wind conditions resulted in a negative correlation (Topliss *et al.* 1994). All researchers noted the dependence of sea surface roughness on the wind direction relative to the frontal boundary and that the backscatter signature can be offset relative to the SST boundary. These results are all based on continental shelf investigations of mesoscale features with SST signatures in the order of 3°C. In the coastal zone SST variations across a frontal boundary are in the order of 1° C or less and their influence on the stability of the MABL is unknown.

Determining the threshold current and atmospheric conditions required for specific features to be detected using SAR is a subject of continuing interest. Seasat SAR images of the Gulf Stream frontal boundary, acquired in light to moderate winds (< 7 ms^{-1}), were successfully used to track the signatures of warm water rings. Winds exceeding 10 ms^{-1}, however, were found to mask any modulation of the waves generated by the relatively weak current shears (Hayes, 1981; Lichey *et al.*, 1981). Johannessen *et al.* (1992) studied methods of distinguishing between the surface manifestations of the different factors which modulate the short wave energy detected by SAR. Their work provides a qualitative definition of the characteristic backscatter profiles expected for wind fronts, surface current boundaries and internal waves detected on SAR images. Large scale experiments, such as JASIN in 1978 (Allan and Guymer, 1984) and NORCSEX'91 (Johannessen *et al.*, 1993), combined *in situ* measurements with near contemporaneous satellite SAR overpasses. The spatial distribution of the scattering patterns has been demonstrated to correlate with features generated by wind effects and mesoscale ocean circulation patterns, such as wind rows, frontal boundaries and eddies. Johannessen *et al.* (1993) used the ERS-1 SAR in near real time to direct ships in the field to particular features of interest. Definitions of empirical relationships between backscatter values for specific currents or wind front signatures remain to be achieved.

2.4.2 Internal waves

Internal waves have been observed on a variety of radar images. Wave-current interactions strain the surface short wave spectrum generating a surface roughness signature detectable by radar. A well known example is the Seasat SAR image of the Straits of Messina, which provided the first experimental evidence that internal waves occurred in the channel (Alpers and Salusti, 1983). An X-band radar proved a successful method of monitoring internal wave propagation through the Straits of Gibraltar, providing evidence of an internal bore and the speeds at which the waves travel (Watson and Robinson, 1990). Kasischke *et al.*, (1983) carried out an intensive study of internal waves in the eastern North Atlantic using SAR and *in situ* data. It was demonstrated that internal waves occur only in the vicinity of a bottom feature, although they may propagate up to 10 km away. Observations of internal waves have also been made along the continental shelf off the coast of Portugual (Allan, 1983).

2.4.3 Atmospheric features

Instabilities in the MABL can produce a temperature invervsion in the lower troposphere, resulting in internal, low frequency gravity waves trapped in the layer above the weak marine boundary layer. Periodic variations in the pressure and horizontal wind velocity within the temperature inversion can be transmitted virtually unchanged to the base of the MABL (Gossard and Munk, 1954). The rapid response of the small waves to dynamic pressure and wind perturbations produces a characteristic signature of the atmospheric wave pattern in the surface roughness field. The first investigation of these atmospheric boundary rolls made using SAR was carried out by Thomson *et al.* (1992). Periodic linear bands of relatively rough and smooth regions, varying in wavelength from 1 to 3 km, and aligned with the wind direction, are imaged. The launch of ERS-1 has revealed that atmospheric rolls are common in exposed oceanic regions. Observations of atmospheric rolls in the coastal zone were made by Alpers and Brummer (1994).

Orographic modulation of the MABL can produce lee waves, which are oriented orthogonal to the local wind direction. Observations of these features from their associated cloud patterns seen on visible wavelength satellite images is common, but Vachon *et al.* (1994) demonstrate that they also modulate the surface wind field sufficiently to be detectable as a surface roughness signature by SAR.

2.4.4 Bathymetric features

Bathymetric features in continental shelf and coastal regions have been observed by many researchers using SAR images. The backscatter signature observed is attributed to wave-current interaction resulting from modulation of the currents as they propagate across a topographic feature (De Loor, 1981; Kenyon, 1983; Meadows *et al.*, 1983; Vogelzang *et al.*, 1992). Models of the effects of wave-current interaction across bathymetric features on the surface roughness pattern detectable by SAR have been derived by Alpers and Hennings (1984), Shuchman *et al.* (1985) and Holliday *et al.* (1986). The results are moderately successful, generally predicting similar trends to those observed in the radar backscatter patterns. Radar backscattering across bathymetric features is discussed in more detail in Chapter 8.

2.4 INVESTIGATIONS OF WIND SPEED RETRIEVAL FROM SAR

The backscatter patterns detected by SAR often reflect the modulation of the small scale sea surface roughness response to local and mesoscale wind events. It is well recognised that the backscatter response is directly related to the surface wind stress, but measuring this value is complex and more simple relationships with wind speed have been adopted as a means of relating the surface roughness signature to a physical property. The potential for using SAR to quantitatively analyse the wind field was first investigated by Gerling (1986). More recent work, using the CMOD4 to derive wind speed modulations across a lee wave feature seen on an ERS-1 SAR image, produced encouraging results when compared with predictions from an atmospheric model (Vachon *et al.*, 1994). Further investigations using CMOD4 to estimate wind speeds in the deep ocean have been made by Johannessen *et al.* (1993). Research in progress by Shuchman *et al.* (1994), using an alternative scatterometer model (Wismann, 1992), is also obtaining good results. The results from these studies further emphasise the potential of SAR data to provide quantitative information about sea surface roughness conditions; a measure of considerable importance to calculations of air:sea exchanges. The higher resolution achievable with a SAR compared to a scatterometer is of considerable value near fronts and in the coastal environment and other regions of high wind gradients. The subject is discussed in more detail in Chapter 7.

CHAPTER THREE

EXAMINATION OF SEASAT SAR DATA

3.1 INTRODUCTION

Sixteen years ago Seasat was launched with a suite of experimental microwave instruments, including SAR. This chapter presents a preliminary assessment of all eleven Seasat SAR swaths acquired over the English Channel. The work was carried out prior to the launch of ERS-1. The aim was to assess the contribution a satellite imaging radar could be expected to make to monitoring coastal dynamical processes.

Due to the unexpectedly short lifetime of the Seasat satellite contemporaneous *in situ* and SAR data were not acquired for consecutive overpasses of an individual area and hence, previous attempts have not been made to carry out a multi-temporal analysis of the images. Considering the relatively well documented nature of the physical oceanography in the English Channel, the availability of tidal atlases, synoptic daily weather charts and SST data, it was anticipated that this would be sufficient information about the prevailing oceanographic conditions to make a useful contribution to the understanding of L-band radar surface roughness signatures. Surveys using airborne X- and C-band SAR and SLAR surveys have demonstrated that despite the difference in the operating frequencies and therefore the length of surface waves affecting the backscatter, the features detected and their appearance remains similar to that observed on the longer wavelength L-band Seasat SAR (De Loor, 1981; La Violette, 1983; McLeish and Ross, 1985).

The principal objective is to provide a starting point for the subsequent investigation of the ERS-1 SAR data. Before attempts can be made to quantify backscatter signatures it is necessary to determine the type of oceanographic features detectable by SAR in the coastal environment. It was considered that this could be achieved using the Seasat SAR data. The relationships between distinctive variations in the surface roughness patterns and oceanographic events were investigated; not all backscatter variations are linked to oceanic processes. The objectives were to determine whether dynamic surface signatures can be associated with specific backscatter patterns and to gain an indication of the wind and tide conditions required for the feature to be detected using SAR. In particular, a systematic method was sought to categorise features detected using SAR. A further objective was to use the results from this analysis to determine a region of interest for further investigations using the ERS-1 SAR data.

In the following section the physical oceanography of the English Channel is briefly reviewed. The availability of the Seasat SAR and supporting data, the methods used to analyse the images and results achieved are then discussed. The main interest lay with identifying frontal boundaries, different current flow regimes and bathymetric features and relating them to the backscatter patterns. The characteristics of these features, the imaging mechanism enabling them to be detected and the number of obsevations on additional passes is discussed.

3.2 THE ENGLISH CHANNEL

Over the past hundred years the English Channel has been relatively well studied, providing a good knowledge of the positions and characteristics of frontal boundaries and flow patterns. Strong coastal currents are driven by tides, wind and density gradients and in the centre of the channel average flows of 1.5 ms^{-1} are present, with tidal extremes of 3.6 ms^{-1} and 4.6 ms^{-1} recorded around Portland Bill and Cap de la Hague (Sager and Sammler 1964 and 1968). The residual flow is west to east and the rectilinear tidal streams run parallel to the coast.

Fronts developing in the Channel may result from seasonal stratification of the water column or from freshwater input and tidal mixing effects. In late spring surface warming along the Celtic Sea shelf break, at the western end of the Channel, generates a thermocline separating the stratified deep water from the well mixed Channel water (Simpson *et al.*, 1978; Pingree and Mardell, 1981). Horizontal temperature changes in the order of 1°C enable the irregular boundary to be identified using infra red (IR) imagery and it remains an established feature across the Western Channel throughout May to September. The exact position of the front may shift according to wind and tidal movement of the surface water and in exceptionally warm years it may extend considerably further up the Channel. Using tidal mixing theory, Simpson *et al.* (1977) obtained a stratification parameter and predicted the positions of frontal boundaries throughout the English Channel, taking into account the depth and tidal amplitude throughout the water column.

Convergent tidal fronts separate the warmer, less dense coastal water from the well mixed main channel water. An example is the Jersey front where the boundary is defined by a line of current shear and an abrupt temperature change (Pingree and Mardell, 1981). These fronts are best defined during February to March and more weakly throughout the summer months (Pingree *et al.*, 1974). The less dense coastal waters and sediment load are confined to areas within the 50 m depth contour.

Strong tidal currents result in areas of high levels of energy dissipation and bottom stress and often correspond to areas of current shear and regions of overfalls, such as around Cap de la Hague, Les Heaux and through the Alderney race. Studies of current patterns through the Dover Straits estimate an average flow rate of 2.2 cms^{-1}. In the restricted channels between sandbanks, residual flow rates of up to 6 cms^{-1} have been recorded (Carruthers, 1928). Investigations of sediment transport through the straits by Dewez *et al.* (1989) suggest that sediment transfer towards the North Sea occurs within a broad band along the French coast, whereas in the central part of the Straits of Dover, current meter data indicate that sediments are transported westward into the Channel. Visible band satellite images have been used to deduce a residual coastal flow to the west, starting from near Beachy Head and ending in a small gyre just east of the Isle of Wight (Boxall and Robinson, 1987).

3.3 DATA AVAILABLE

Eleven Seasat SAR swaths were acquired over the English Channel in 1978 and were examined in this study. The data are recorded in chronological order in table 3.1. The study was based on hard copy images. The poor state of the digital data, in addition to the fact that Seasat SAR was not well calibrated, means there is little advantage in using the digital data; categorising features in terms of dB or comparing images would not have been viable. The far more extensive coverage provided by the continuous swaths of optically processed data was considered preferable for the overview nature of this work. The area covered by each swath is mapped on figure 3.1, along with a diagrammatic representation of the features observed.

Satellite IR images were used to relate variations in SAR backscatter to SST frontal features. Contemporaneous data are not available, the majority of archived tapes having degraded, and only one VHRR IR image could be obtained for the entire three months that Seasat was in operation (24.8.78, figure 3.2a). Data acquired by the AVHRR sensor, on the later TIROS-N platforms, were obtained for the same months a year later, August to October of 1979. However, due to cloud cover only five images were found to provide a good view of the entire English Channel. An example is the AVHRR IR image acquired on 3.8.79 (figure 3.2b). Comparison of the VHRR image from 1978 with a sequence of images acquired in 1979 and with historical SST monthly mean data, shows that during summer (the time of the Seasat mission) the SST trends are relatively stable. The contemporaneous VHRR IR image is therefore considered a good indication of SST conditions for comparison with the SAR. In addition, the satellite data provide more detailed information on the small coastal fronts and the nature of the boundary, not available from models or monthly mean data.

The distribution of suspended sediments can also be used to provide an indication of the frontal boundaries and flow regimes within the Channel. Satellite imagery from the Coastal Zone Colour Scanner (CZCS) gives an overview of these patterns (figure 3.3), clearly separating the coastal and deeper water regions.

Local current information and expected frontal regions were deduced using charts, tidal atlases, satellite SST images, results from previous field studies and model predictions. Weather conditions concurrent with the SAR swaths were taken from the Meteorological Office synoptic charts. Table 3.1 includes a summary of the wind and tide conditions within the English Channel at the time of the Seasat pass.

Table 3.1 Seasat SAR coverage of the English Channel and a summary of the wind and tidal information at the time of each image.

Date	Time (GMT)	Seasat SAR orbit	Wind speed and direction (Beaufort) (00 / 1200 GMT)	Tidal information†	
				HW Dover (GMT)	Hours (:min) +/- HW
4.8.78	06:05	547	W2 / WSW3	11:27	-5
7.8.78	06:12	590	W2 / WNW3	00:42	+6
10.8.78	06:19	633	NW1-2 / W1	02:25	+4
16.8.78	06:35	719	WSW4 / WSW4	08:56	-2:20
20.8.78	21:32	785	W1 / W3	12:13	-3
21.8.78	07:16	791	W1	12:57	-5:30
24.8.78	07:20	834	SSW1	02:46	+5
1.9.78	22:09	957	NW2 / NW2-3	22:45	-0:30
2.9.78	07:52	963	N2	11:05	-3
5.10.78	00:28	1430	NE2 / NW2-3	00:23	HW
8.10.78	00:40	1473	N4	02:24	-2

† taken from Admiralty Tidal Atlas

3.4 METHODS

Although it is inevitable that a degree of subjective judgement is involved in all descriptive analysis of SAR image data, a procedure to enable cataloguing of features and relative backscatter variations (σ_0) in as objective a way as possible was sought. Comparisons could then be achieved between both repeat swaths and similar features throughout a region, enabling a systematic approach to be adopted, which would depend less on specific user experience.

Analysis of the data for the English Channel was based on a definition of what comprised a feature on a SAR image. Five main backscatter signatures were distinguished, which appeared to correspond to oceanographic or atmospheric features:

- Tonal variations in σ_0: large areal changes in the uniform backscatter pattern, such that a boundary appears relatively bright on one side and dark on the other.

- Line features: distinct bright or dark lines around 50 to 100 m in width and generally aligned with the current flow.

- Texture-like variations: areas of high brightness variations, often appearing as distinct bands, in the order of 250 to 500 m width.

- Slick-like features: dark filamented streaks, in the order of 100 m width.

- Banded (light and dark) tonal changes at kilometre scales.

Once specific backscatter features were identified their cause, location and frequency of occurrence on SAR was examined. Diagrammatic representation of backscatter patterns overlaid on a 1:500 000 Admiralty chart enabled comparison of the location with bathymetry, with known frontal features, with other remotely sensed data (figure 3.1) and with historical wind and tide information (table 3.1). Coastal reference points were used to co-register overlays of the images for repeat SAR swaths, enabling comparison of backscatter patterns and changes in feature positions to be noted between overpasses. Using this information and *a priori* knowledge from previous studies of SAR, the backscatter categories could then be associated with specific types of dynamic oceanographic features (eg. swell, frontal boundaries, current patterns, coastal effects and bathymetry).

Texture-like variations in backscatter appear to occur over or adjacent to bathymetric features (eg. around the Channel Islands, C on figure 3.4). Line features may appear individually or as a sequence of adjacent light and dark lines in regions of strong current activity. A distinctive single line often marks a frontal boundary such as the Jersey front (1 on figure 3.4). The series of continuous lines across Les Roches Douvres can be seen from the tidal atlas to be an area of intense current gradients across the shallows (D on figure 3.4). Tonal variations in backscatter can indicate a SST front. For example the large scale variation in surface roughness on SAR 791 is thought to correlate with the seasonal thermal stratification boundary at the western end of the channel (9_a on figure 3.4). It should be noted that sudden variations in the backscatter have also been observed to be a product of wind fronts, particularly where the boundary is very straight (Johannessen *et al.*, 1993). The likelihood of these effects generating the features observed on the images was investigated using synoptic meteorological charts to identify events such as rain or fronts passing across the study region and the orientation of features relative to the local wind direction.

The different categories of backscatter signatures were then described in terms of scale, relative strength (estimated subjectively) and whether the feature was detected on further images of the area. General trends of a feature are noted, such as its orientation, its size and the type of boundary (whether the margin is straight or is marked by a line). Estimates of the length and width of the backscatter signature are compared with the size of the feature thought to be the cause. The results for each category of features are tabulated, thus beginning a database of coastal dynamical oceanography detectable by SAR in the English Channel that contains both qualitative and quantitative information. Investigations of the imaging mechanisms of the SAR could then be based on the probable physical cause of the feature and the surface roughness signature.

Tables 3.2 to 3.5 summarise the features detected throughout the English Channel, dividing them into the categories: frontal boundaries; current shear; bathymetry; and coastal effects. The letters or numbers associated with particular features in the tables are used to label the same features on the figures. Symbols used within the tables denote the appearance of the signature, indicating whether it is a tonal (*), texture (+) or a line (#) feature, appearing bright (b) or dark (d) on the image. The strength of the signature corresponds to the number of symbols used (eg. * indicates a just perceptible tonal feature, while *** indicates a strong signature). If a feature is not covered by an image then the table is left blank. However, if a location is imaged but a known feature (i.e. detected on a previous pass) is not detected then it is referred to as a 'miss' and denoted by 0 in the tables. The tables provide a basis from which to analyse the various features detectable by SAR, and to compare their appearance in different overpasses, assessing the oceanographic and meteorological conditions required for a feature to be imaged.

3.5 ANALYSIS OF THE SAR IMAGES

3.5.1 Thermal Fronts

Fronts in the English Channel are essentially tidal fronts and in some cases mark a division between stratified warm water and well mixed water. The SST distribution was determined from the satellite IR images. It can be demonstrated that the Seasat SAR covered various examples of frontal boundaries with temperature gradients in the order of 0.5 to 1°C, in varied wind and tide conditions. The appearance and strength of the backscatter features are summarised in table 3.2.

The major front in the study region is the seasonal stratification front that occurs in the western approaches between May and September. During the time the images were acquired (August to October) this is well established (the predicted frontal position is marked on figure 3.1 as the double line and can be seen on the IR image, figure 3.2a). At this time of year light winds frequently prevail, providing conditions considered favourable for the detection of thermal gradients (refer to Chapter 2). As the air flows across a region of warmer water the marine atmospheric boundary layer (MABL) can become unstable resulting in an increase in the surface stress and therefore the surface roughness detected by SAR. The transition across a SST boundary may appear as a large tonal variation in the backscatter intensity. SAR passes 791, 590 and 547 all cover the western English Channel region. Only on SAR 791 is a marked tonal change in σ_0 detected (marked 9a on figure 3.4) in this region. The VHRR IR image acquired three days later on 24.8.78 clearly shows the presence of the SST front (figure 3.2a), very close to the position of the surface roughness signature observed on the SAR image. The region of increased surface roughness is over the area of warmer water and the colder water adjacent to the coast (to the west of Prawle point) appears dark. In addition, the boundary on the SAR is very filamented and closely matches that seen on the IR image. The high pressure zone just southwest of the region and the light wind speeds (2 ms^{-1}) recorded at 00:00, 06:00 and 12:00 GMT on the synoptic meteorological chart suggest that the feature is unlikely to be the product of a wind front (the image was acquired at 07:16 GMT). The images were all acquired in similar tidal conditions, but only 791 was acquired in winds of 2ms^{-1} or less. At the time images 590 and 547 were acquired the wind speeds were estimated to be around 5 ms^{-1} or more; the wind speed threshold for detecting SST variations is estimated by several workers to be around 3 to 4 ms^{-1}. The results suggest that the surface roughness signature on SAR 791 marks an SST frontal boundary.

In summer smaller, weak stratification fronts occur throughout the English Channel in the shallower, nearshore water. The headlands tend to produce separate circulation patterns within the bays, resulting in local fronts separating the inshore water from the main, faster flow in the centre of the channel. In summer the shallow water becomes warmer, but the SST gradient is weak, as shown by the IR data (figure 3.2). A distinctive tonal variation in backscatter across a shallow coastal front is observed across the Baie de Brieuc, the boundary approximately following the 20 m contour (marked 7 on figure 3.4). Winds at the time of the image were 3 ms^{-1} or less. A bright line along the margin suggests current shear is occurring between the deeper water and that in the bay. The tidal stream atlas shows currents to be very weak inshore (0.1 to 0.25 ms^{-1}) and slightly stronger further offshore (0.8 ms^{-1}) at the time the image was acquired. Simpson's stratification parameter can be used to demonstrate that at these current speeds a SST boundary could occur in the region of the 20 m contour. The transition between stratified and mixed water at this depth is calculated to occur at current speeds of 0.6 to 0.7 ms^{-1}. The results suggest that the surface roughness signature marks a SST boundary, which is detected by SAR due to instabilities in the MABL over the warmer inshore water.

Three SAR swaths covered the eastern channel, but only SAR 791 detected variations in backscatter that can be associated with SST features. Regions of darker (smoother) water are observed to the east of Dungeness and along the French coast, extending west of the River Somme to just north of Dieppe (marked as 11 and 10_b respectively on figure 7). Both features closely match the position of the warm inshore water observed on the IR image (figure 3.2a). The mechanism modulating the small scale surface roughness, enabling these features to be detected by SAR cannot be attributed to instabilities in the MABL; the warmer water is smoother and the image was acquired in moderate wind conditions (around 12 ms^{-1}). The regions of water can be seen to extend 10's of kilometres along the coast but only a relatively small distance offshore. They may be a product of fresher coastal water inputs or slick material confined inshore, dampening the short waves. Evidence that fresher water outflows can influence the surface roughness signature is given by the small region of darker water at the mouth of the L'Orne river plume (just west of the Seine) observed on SAR 633 (figure 6a).

Other cases of tonal variations in the backscatter were observed along the coastline, the inshore water appearing brighter (eg. the boundaries marked 9_b and 10_a on figures 3.4, 3.5 and 3.6). However, these features are weak, with very straight boundaries and are most likely to be a product of local variations in the wind; they were all acquired early morning and a land breeze could have been present.

The strong tidal mixing around the Channel Islands produces anticlockwise jets and gyres around the main islands, forming frontal zones clearly identifiable on the IR imagery (figure 3.2). The main front occurs between Jersey and Guernsey and is known to be well defined in summer, during the time of the Seasat orbits (refer to § 3.2). Both passes across the region, swaths 791 and 590 acquired during a range of different wind and tide conditions, show a bright line of increased backscatter marking the Jersey tidal boundary in virtually the same position on both passes (marked 1 on figures 3.4 and 3.5). Field studies indicate the front is around 18 km long which is in close agreement with the observations from the SAR images. A strong thermal gradient can also exist across the front, the inshore waters are warmer and less saline. On SAR 791, acquired in light wind conditions, the feature is also seen as a clear tonal variation in backscatter, the band of rougher water occurring inshore. The strong tidal current gradients maintain turbulent conditions along the boundary and *in situ* observations have recorded that both slicks and areas of rough water and breaking waves occur in the region. Convergent currents along the boundary would be expected to steepen the short waves, producing the band of increased surface roughness observed on the SAR images. The weaker front around Guernsey is also observed on SAR 785 (figure 3.8).

Table 3.2 Summary of the frontal features detected in the English Channel.

Frontal boundary feature (numbered as on figures)	SAR pass										
	547	590	785	791	633	834	963	719	957	1430	1473
1.Jersey Front		##b	##d /b	##b **b WW							
2.Front E Guernsey		##b	0								
3.Front W Guernsey		0	##b	*b WW							
4.Cap de Carteret Front		*b CW									
5.Front E Illes de Chausey		*b CW									
6.Front S Minquiers		##b		0							
7.Front across Baie de St Brieuc	0	0	0	##b **b WW							
8. Weymouth & Portland Bay fronts			#d *b WW								
9_a.Channel Front	0		0	**							
9_b.Lyme Bay Front		*d WW	0	**							
10_a.UK Coastal Boundary Fronts					**b WW	**b WW					
10_b. French Coastal Boundary Fronts a)Baie de Somme	a)								#b	0	0
b)E of Cherbourg	b)				**d WW	**d WW					
c)Dieppe-Baie de Somme	c)							*d WW	0	0	0
11. Dungeness Stratification Front								**d WW			

* Tonal variation in backscatter: *b = bright, *d=dark.
WW or CW respectively denote whether the area of return correlates with warm or cold water.
\# Line feature: #b = bright, #d = dark.

Unless a thermal front is also marked by a strong current gradient across its boundary, then the likelihood of detecting the feature using SAR in anything other than very light wind conditions is poor (Hayes, 1981 and McLeish and Ross, 1985). The images available for this study only represent relatively light to moderate wind conditions (maximum 8 ms^{-1}) and firm conclusions about the ability of SAR to detect current boundaries at all wind speeds can not be made.

3.5.2 Current Features

Strong currents occur throughout the English Channel and current shear zones are observed on several of the SAR images, along tidal fronts, across banks and in areas of intense current streaming around headlands. The results are summarised in table 3.3. As observed in § 3.5.1, converging currents can produce a bright line feature of the order 0.3 km in width. Conversely, divergences appear as a narrow dark line, as the short surface wave field is expanded, and are often observed adjacent to the roughened signature. The importance of wind and tidal effects on the capability of SAR to image these features is considered in terms of current speed, direction and gradient, with respect to the local wind speed and direction.

The strong tidal streams around Cap de la Hague and through the Alderney race were imaged by SAR passes 633 and 834 and provide good examples of current shear features (dashed lines marked * on figure 3.6 a and b respectively). In both cases the current shears are imaged as adjacent bright and dark lines, appearing to curve around the headland with the tidal flow. The variable current gradients generate rough and smooth regions as the currents propagate through the shallower water. The lines are strongest on 633, when the ebb flow is at its strongest and current speeds range from 1.7 ms^{-1} offshore to 1 ms^{-1} inshore. Although the lines appear continuous they are at the most 5 km in length, 0.1 km wide and roughly 0.5 km apart. Similar features were observed across shoal areas around the Channel Islands, such as the Minquiers and Roches Douvres. Again, these are attributed to filaments of water moving at different speeds as the depth of the water varies, creating the distinctive surface roughness pattern (dashed lines marked D on figures 3.4, 3.5 and 3.8). Small circular features (up to 2 km in diameter) observed on SAR 834 throughout the Alderney race are thought to relate to the overfalls known to occur in this area (figure 3.6b).

One of the most interesting features, not mentioned in any of the oceanographic literature was a dark V-shaped band (approximately 5 km in width) stretching across the Dover Straits, imaged by SAR 1473 (figure 3.9). Although the area was imaged again by Seasat SAR the feature was only observed once. The image was acquired at 2 hours before high water Dover, as the tide begins to turn in the Dover Straits (figure 3.10). It is hypothesised that the band of smooth water separates two different current regimes during the change from one tidal phase to the other. The distribution of the surface residual currents in the Straits of Dover implies divergent conditions during slack water (Dewez *et al.,* 1989). A further narrow dark band was observed extending parallel to the French coast from Cap Gris Nez to the Sandettie Bank. This may relate to the tidal state, the currents ebbing first along the French coast, creating a zone of shear between the currents still flooding eastwards. Investigations of the general sediment transport across the English Channel - North Sea boundary by Dewez *et al* (1989) indicate a bed-load boundary extending parallel to the French coast in a position very similar to the feature observed on the SAR. The winds were around 6 to 8 ms^{-1} and it would be unlikely that surface films would be sufficient to dampen the short waves in these conditions; slicks are not normally detectable in winds above 7 ms^{-1} (Scott, 1986).

A combination of mechanisms is thought to contribute to the appearance of current shear features, including wave-current interaction, wave refraction and converging and diverging currents as described in Chapter 2. A major factor influencing the detection of current shear by SAR is the strength of the current gradient across a region. Results from this work suggest that a difference in current as small as 0.3 ms^{-1} is sufficient to generate a region of rougher water detectable using SAR. The features are therefore imaged at virtually all tidal states. Although the maximum winds encountered were 8 ms^{-1}, the mechanism seems to be relatively insensitive to wind effects, areas of current shear being clearly detected on all the images.

Table 3.3 Summary of current shear features detected in the English Channel.

Current shear feature	SAR Pass										
	547	590	785	791	633	834	963	719	957	1430	1473
South of Minquiers		##		0							
Roches Douvres	0	##	##	##							
Les Heaux to Isle de Brehat	0		##	##							
Banc des Langoustiers	0		##	##							
Alderney race & Cap de la Hague		0	#		###	##					
East of Vergoyer bank								0	##d	0	0
Dover to Calais								0	##d		##d
Cap Gris-Nez to Sandettie bank									0		##d

Line feature (unless labelled as dark (d) the signature has a light/dark banded appearance).

3.5.3 Bathymetry

Bathymetric features, varying in depth from 2 to 100 m, are detected throughout the English Channel under a wide range of wind and tidal conditions. In most cases the backscatter signature closely overlays the charted feature, the appearance varying with the type of bathymetry (table 3.3). Shoals, rocky coastlines and some sandbanks tend to generate a texture-like return, appearing mottled. Examples of these features are marked D on the figures.

Features such as Prawle Point or St Albans ledge extending out into the sea produce a well defined band of increased surface roughness with a smooth region behind. Shallow water banks, such as the Shingles and others around the Isle of Wight produce similar signatures. These light and dark banded signatures are characteristic of sudden changes in shallow water bathymetry (10 to 15 m) and are visible in virtually all tidal conditions (down to 0.3 ms^{-1}). Examples of these features are marked as A_{1-8} on figures 3.4, 3.5, 3.6(a,b) and 3.8. The signature (bright/ dark bands) reverses with the current flow. This is clearly demonstrated by the images covering St Albans ledge (A_3). SAR passes 633 and 834 were acquired during ebb tides and the bright return occurs as the currents converge on the downtide side of the ledge (west). SAR 785 represents flood tide conditions and the area of rough water occurs to the east. The intensity and contrast in the backscatter signature appears to increase with the currents, appearing brightest on SAR 633.

The well documented sandbanks in the eastern channel are detected on two of the three SAR passes over the area. SAR 791 was acquired when the tidal current conditions were weak across the region (< 0.4 ms^{-1}). In only slightly stronger current conditions (0.6 ms^{-1} or more) at the time of SAR passes 957 and 1473 (figure 9) the banks are clearly imaged. Adjacent light and dark bands approximately aligned with the bank mark the feature. These admittedly limited results suggest that the deeper water features require slightly stronger currents to generate a surface roughness signature detectable by SAR.

An unexpected bathymetric feature detected using SAR was the Hurd Deep (marked B on figures 3.4, 3.5 and 3.8). This is a narrow, 100 m deep channel, orientated east to west in the Western Channel. It was observed on all the SAR passes covering the region as adjacent bright and dark bands. The appearance on the image and the section of the Deep detected varied between overpasses, appearing to depend on the tidal conditions. Oblique currents crossing the Deep at the time of SAR 785 produced texture variations in the backscatter and a line feature that was 3km wider than the charted feature (figure 3.8). The hypothesis is that as the water flows over the boundary of the Hurd Deep, where the depth changes from 60 to 100 m over 2 km, the currents throughout the water column are modulated sufficiently to cause wave refraction (causing wave-wave interaction) in addition to weak convergences and divergences of the surface currents. All these factors affect only a narrow band (maximum in the order of 3km) of the surface wave field which is consistent with the signatures observed on all but one of the images.

3.5.4 Coastal features

Along the UK coastline several dark, slick-like plumes are observed on the SAR images, generally coinciding with river mouths and urban areas. Table 3.5 summarises the features observed along the English coastline. The features tend to be contained within 3 to 5km of the coast. It is hypothesised that the more buoyant fresh water flowing out from the rivers overlies the denser saline water, effectively dampening the small surface waves. The features

Table 3.4 Summary of bathymetric features detected in the English Channel.

Feature	SAR Pass										
	547	590	785	791	633	834	963	719	957	1430	1473
A_1 The Lizard	**d										
A_2 Prawle Point	**b+	**b+		**b							
A_3 St Alban's Head			***b		**bd	#b/d					
A_4 Portland Bill & The Shambles			**d/b		***b	*,+					
A_5 Eddystone Rocks	+			##,++b							
A_6 The Shingles					**b,++b	##b					
A_7 St CatherinePoint, IOW					**b/d,++b/d	0					
A_8 East of Shanklin, IOW					**b/d						
B Hurd Deep	##d	##b	##b/d, +	##b/d							
C Channel Islands & Casquets		***, +++	***, +++	+++							
D Illes de Chausey, Minquiers, Roches Douvres & Banc des Langoustiers		+++	**b/d	+++							
E Brittany Coast	++		++	++							
F Cherbourg Peninsular					##d,++	##d,++					
G Dover Straits, 10/20m contour features								0	##d		##b/d
G_a Goodwin Sands									++		**b/d
G_b Le Cobart								0	##d		0
G_c Les Ridens								0	++		++
G_d Bassurelle								0	*d		0
G_e Deep SE of Bassurelle								**d/b	*d		0
H Sandbanks north of Cap Gris-Nez									++b/d	+b/d	++b/d

+	Texture variations in backscatter
*	Tonal variation in backscatter (b/d)
#	Line feature (b/d)

would not be expected to be long lived, nor to exist in strong wind conditions; maximum winds were 8 ms^{-1} for features observed in this study. In most cases the wind conditions varied from southwest to northwest at the time of the images and are not thought to be indicative of wind sheltering effects (table 3.1). Similar features were observed on the French coast. However, without information of local wind conditions at the time of the image the imaging mechanism is uncertain.

Table 3.5 Summary of river/ freshwater inputs into the English Channel.

Feature	SAR Pass										
	547	590	785	791	633	834	963	719	957	1430	1473
Helford and Falmouth	**d										
Fowey	**d			**b							
Tamar	*d			**d							
Salcombe	*d	*r,d		**d/ b							
Dart		*d		**d							
Teigh		**d		0							
Exe		**d		*r,d							
Poole Harbour			*d		**d	**d/ b					
Weymouth Bay			**d		0	**d					
West Solent			**d		**d	*d					
Southampton Water			*d		*d						
Bognor Regis to Newhaven							**d				

* Plume (b/d), where only the river has a signature it is denoted *r.

3.5.5 Atmospheric effects

Wide dark bands, spaced several kilometres apart, were observed on SAR passes 834 and 785 to the west of Portland Bill (figures 6a and 8 respectively). The features occur close inshore, extending across Weymouth Bay and curving round into Poole Bay. The relatively large scale of the surface roughness patterns suggests the feature is of atmospheric origin. Features such as internal waves have a wavelength of the order 200 m and would not be established in a shallow water region (30 to 50 m), which is likely to be well mixed around the headland. The bands are oriented roughly parallel to the headland and in the case of SAR pass 785 are orthogonal to the westerly winds. A wind roll effect generated as the air flows over the headland might be expected to create features on this scale; whether the wind was strong enough (5 ms^{-1}) is uncertain. At the time SAR 834 was acquired the winds were even less. On SAR 785 the feature appears to have propagated to the east with the tidal flow, a distinct kink in the bands occurring as the currents bend round into Poole Bay. It is possible that in light winds the feature can be maintained over a tidal cycle. That atmospheric rolls can be detected by SAR has been established using airborne data (see Chapter 2). It is expected that lee waves would have a similar signature.

3.6 PROBABILITY OF FEATURE IMAGING

The consistency of SAR in the detection of the various features can be deduced from the information presented in Tables 3.2 to 3.5. Zeros entered indicate the failure of the SAR to record a feature which shows up on another overpass of the same area. Ten of the total of twelve frontal boundary zones detected throughout the English Channel were covered by repeat overpasses. Of these only five were detected on more than one of the repeat passes. It is clear that if a frontal boundary is not associated with strong current shear activity then the SST boundary will only be detected in very light wind conditions (< 3 ms^{-1}). The main tidal mixing front across the western approaches was known to be present at the time of most of the SAR passes but the only time a backscatter signature was detectable by SAR was during very light winds. The strong current shear zone defining the Jersey front was imaged on all passes covering the region and the spatial characteristics observed matched closely.

As expected assessment of the current shear features shows an improvement in the detection rate, five out of the eight cases were imaged on other passes over the area. Shallow water (< 20 m) bathymetric features are detected by every overpass, although the intensity and pattern of the backscatter signature vary according to the current strength, direction and the type of feature. The dark backscatter signatures associated with river discharges along the English coastline are imaged consistently by the SAR, only two non-detections of a feature occurring.

3.7 DISCUSSION AND SUMMARY

Analysis of the optical hardcopy Seasat SAR imagery has produced a surprisingly detailed view of physical oceanographic features within the English Channel. The method of analysis and terms of description developed for this study have proved an effective means of assessing and comparing spatial and temporal variations in features observed on the images. The objectives defined at the beginning of the chapter have been met, identifying the types of features detectable by SAR and their associated surface roughness signature for specific wind and tide conditions. Many of the backscatter features were found to correlate closely with SST frontal features, tidal effects, bathymetry and fresh water inputs.

Data from this study forms the beginnings of a database cataloguing the features detected by SAR in the English Channel. Several of the features imaged would not have been observed using traditional survey methods or visible satellite imagery. Of particular interest were the parallel streaks indicating tidal streams; examples of these features had not been observed prior to Seasat. Strong current shear filaments were detected around Cap de la Hague; whether they have a vertical structure in addition to a horizontal signature is unknown. It is hypothesised that they result from horizontal current gradients. Observations of varied current shear features suggests that differences in currents of only 0.3 ms^{-1} across a 500 m region are sufficient to generate a narrow band of surface roughness detectable by SAR. Another unexpected feature, not previously documented, were narrow bands of smoother water appearing to separate a change in the current regime and potentially marking sediment transport boundaries. Two very distinct bands were observed in the Dover Straits and another possible case was imaged extending off Cap de la Hague. Verification of the cause of these features and an explanation of their effect on the surface roughness pattern will require *in situ* investigations of the surface and vertical current profiles.

The detection of SST variations using SAR is clearly extremely sensitive to the local wind conditions, as indicated by other researchers. Detection of SST fronts in the English Channel will depend greatly on the presence of strong current shears occurring along the boundaries. River inputs appeared as dark regions on the images. Whether these are a product of sheltering, a different wind flow regime down a valley or dampening of the small scale waves by the less saline water is uncertain.

Imaging mechanisms suggested in the literature can be used to explain some of the backscatter signatures and line features. However, the maximum coverage of any one area of the English Channel was three overpasses and therefore the imaging criteria could only be assessed for limited wind, tide and the summer density stratification conditions. Drawing conclusions about the ability of SAR to monitor dynamical features throughout the year from these data was not possible. The results do point towards promising possibilities which can be explored further with ERS-1 SAR multi-temporal data. The English Channel is considered to offers excellent conditions for such experiments, considering that such a wide variety of phenomena are found in close proximity.

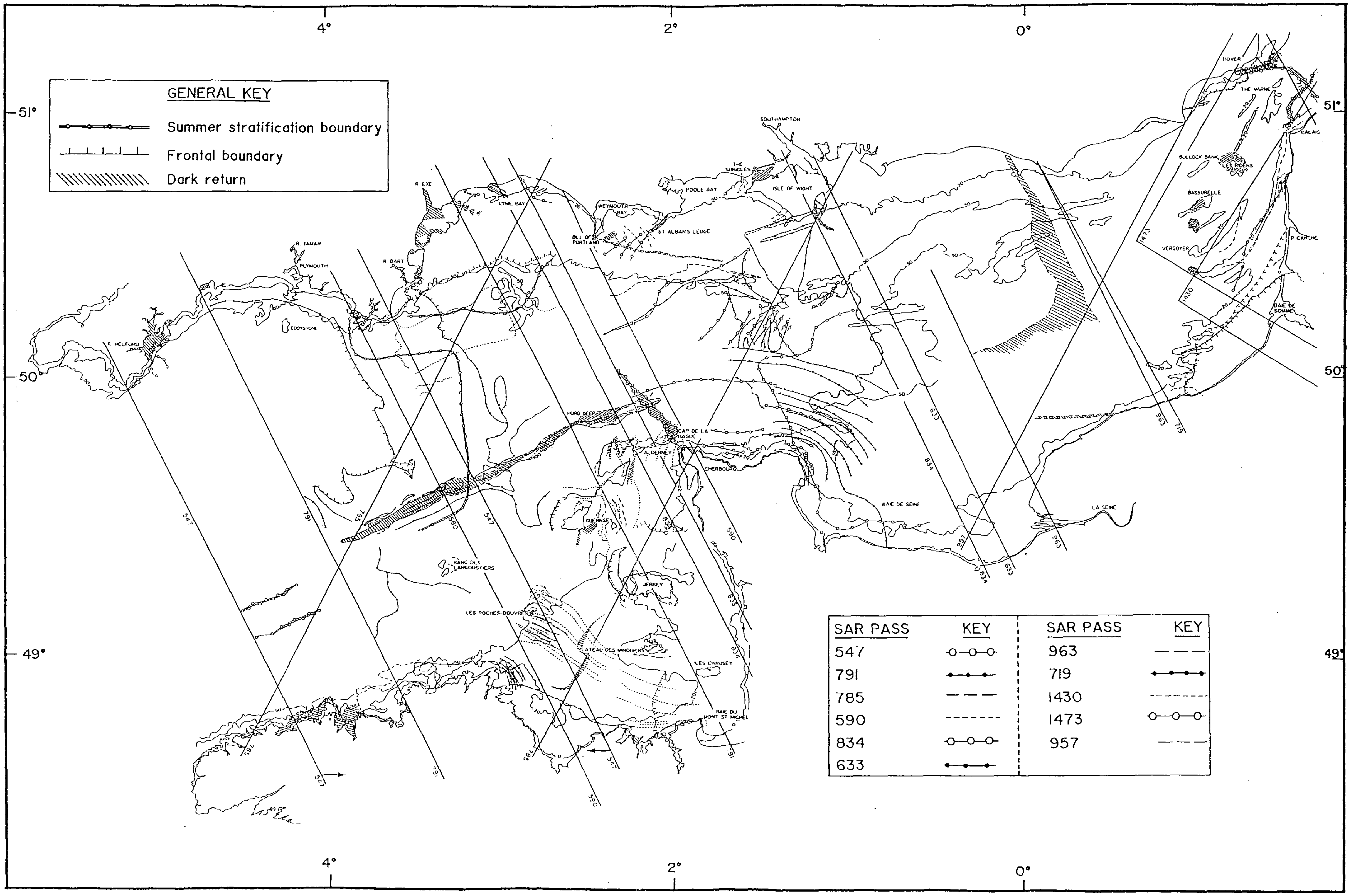

Figure 3.1 A sketch map showing the interpretation of all the Seasat SAR swaths covering the English Channel.

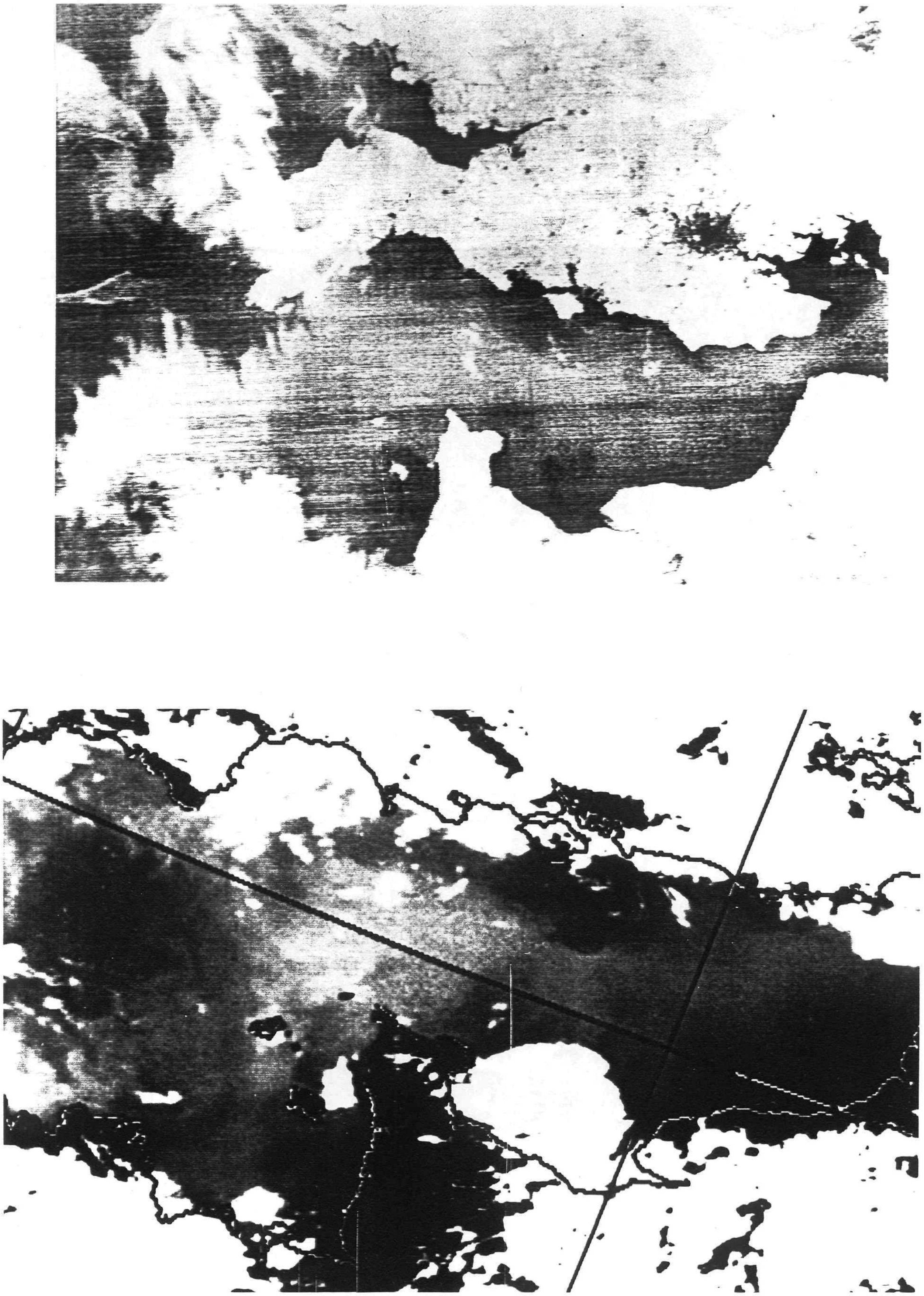

Figure 3.2 a) Top: VHRR (24.8.78) and b) Bottom: AVHRR (3.8.79) IR images. Showing the SST distribution in the English Channel (darker returns indicate warmer water).

Figure 3.3 CZCS image (13.2.86).
Shows the suspended sediment distribution in the English Channel. The lighter return indicates higher levels of sediment confined inshore by coastal boundary front.

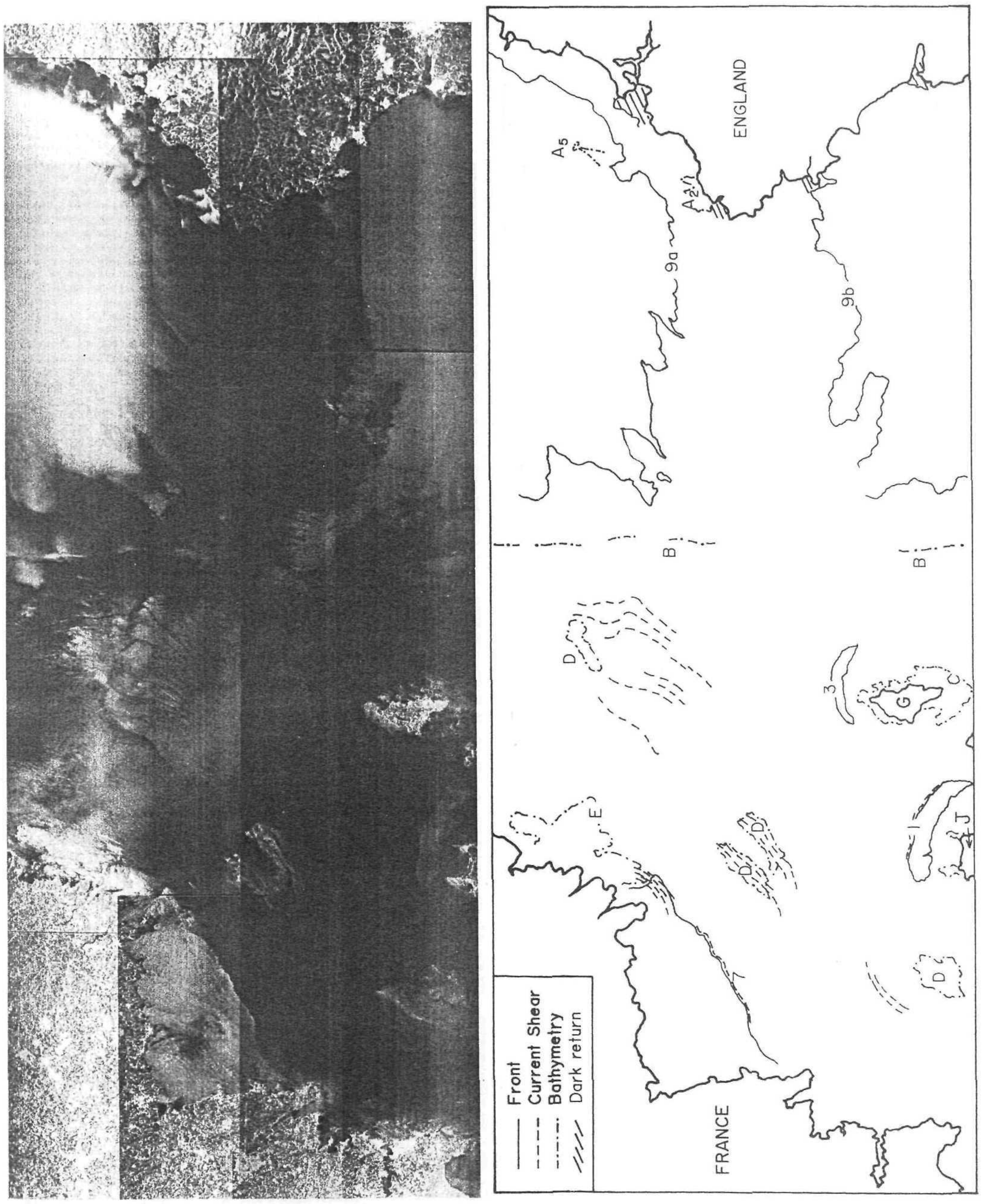

Figure 3.4 Seasat SAR 791 and sketch map.
The image shows the SST stratification boundary (9a), tidal fronts around the Channel Islands (1 and 3); shallow water bathymetry (B and C) and lines of current shear (1 and D). The map outlines the features, the fronts are numbered as in table 3.2. The letters correspond to the bathymetric features recorded in table 3.4.

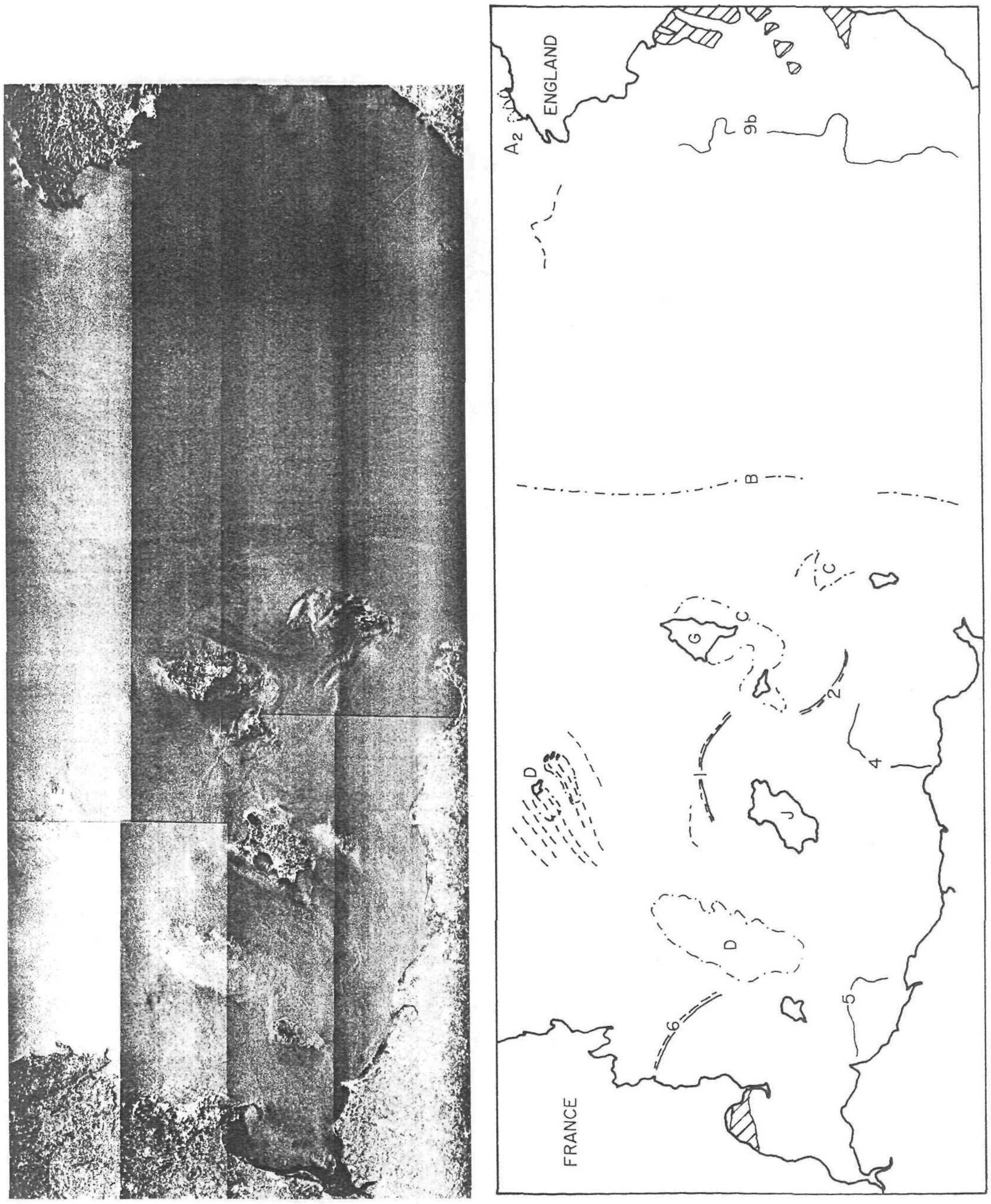

Figure 3.5 Seasat SAR 590 and sketch map.
The image shows the tidal fronts around Jersey (J) and Guernsey (G). The map outlines the features, the fronts are numbered as in table 3.2. The letters correspond to the bathymetric features recorded in table 3.4.

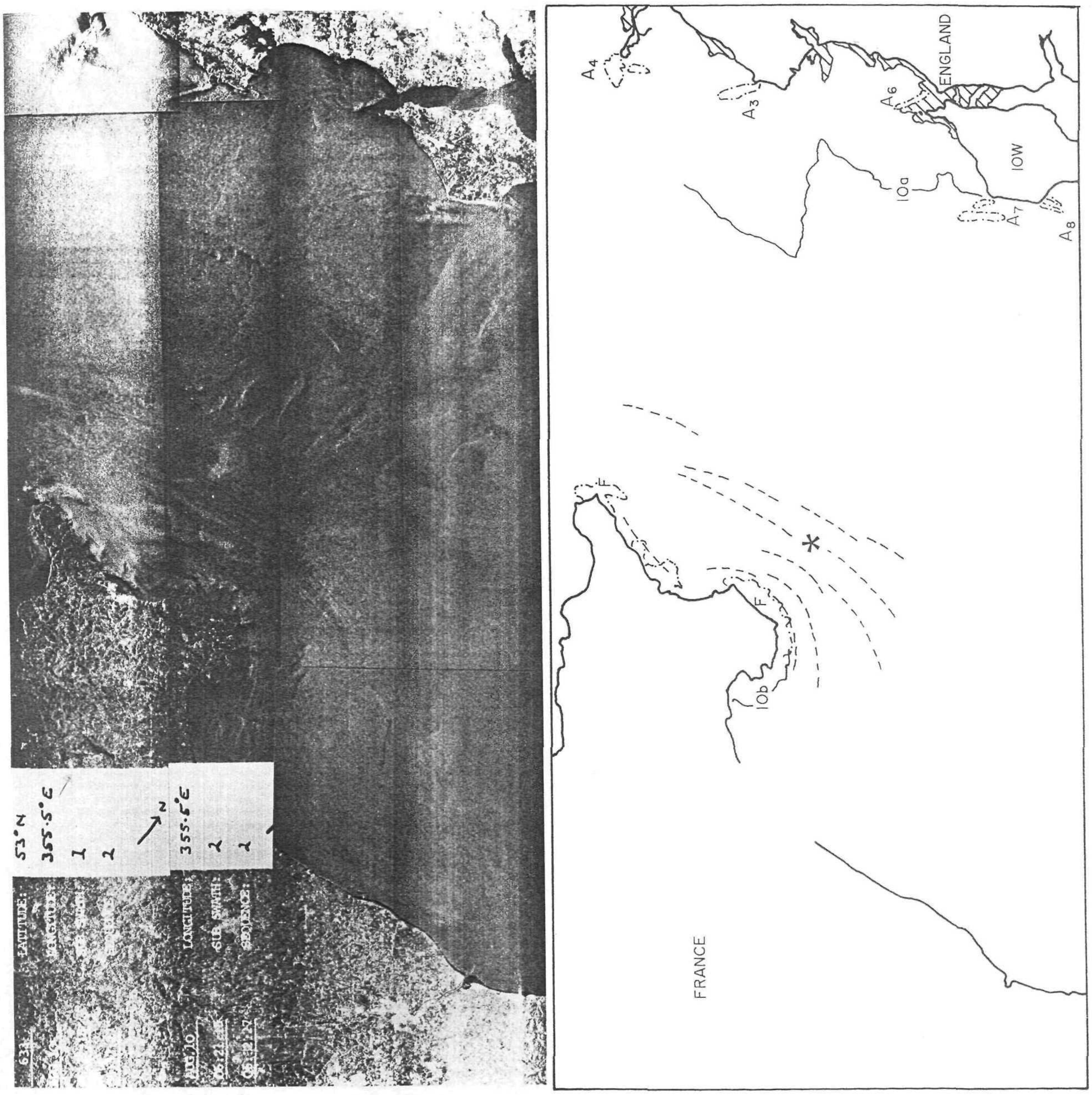

Figure 3.6(a) Seasat SAR 633 and sketch map.
The image shows the current streams around the Cap de la Hague (*). The map outlines the features, the fronts are numbered as in table 3.2. The letters correspond to the bathymetric features recorded in table 3.4.

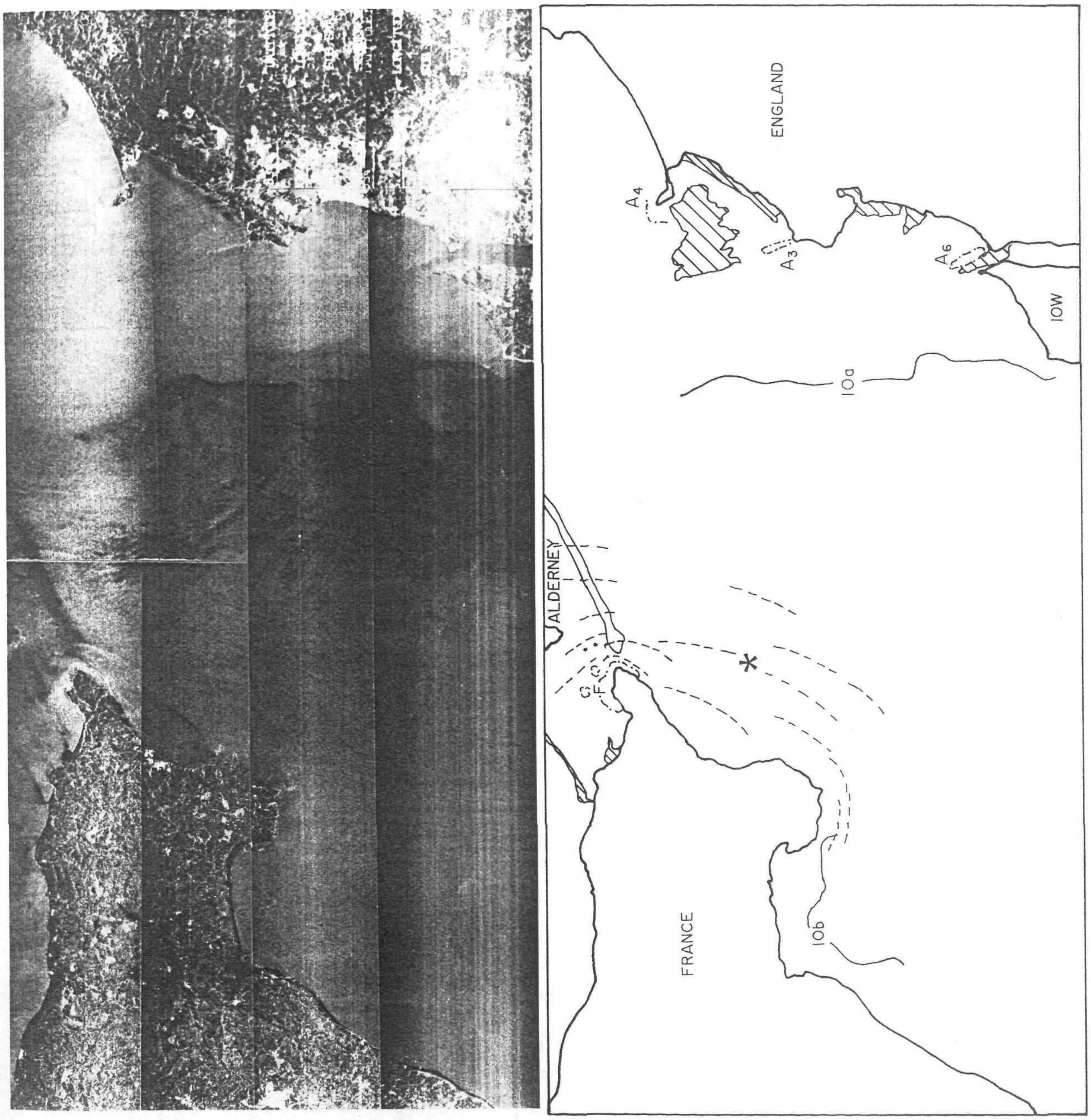

Figure 3.6(b) SAR 834 and sketch map.
The image also shows current streamimg around the Cap de la Hague (*).
The map outlines the features, the fronts are numbered as in table 3.2. The letters correspond to the bathymetric features recorded in table 3.4.

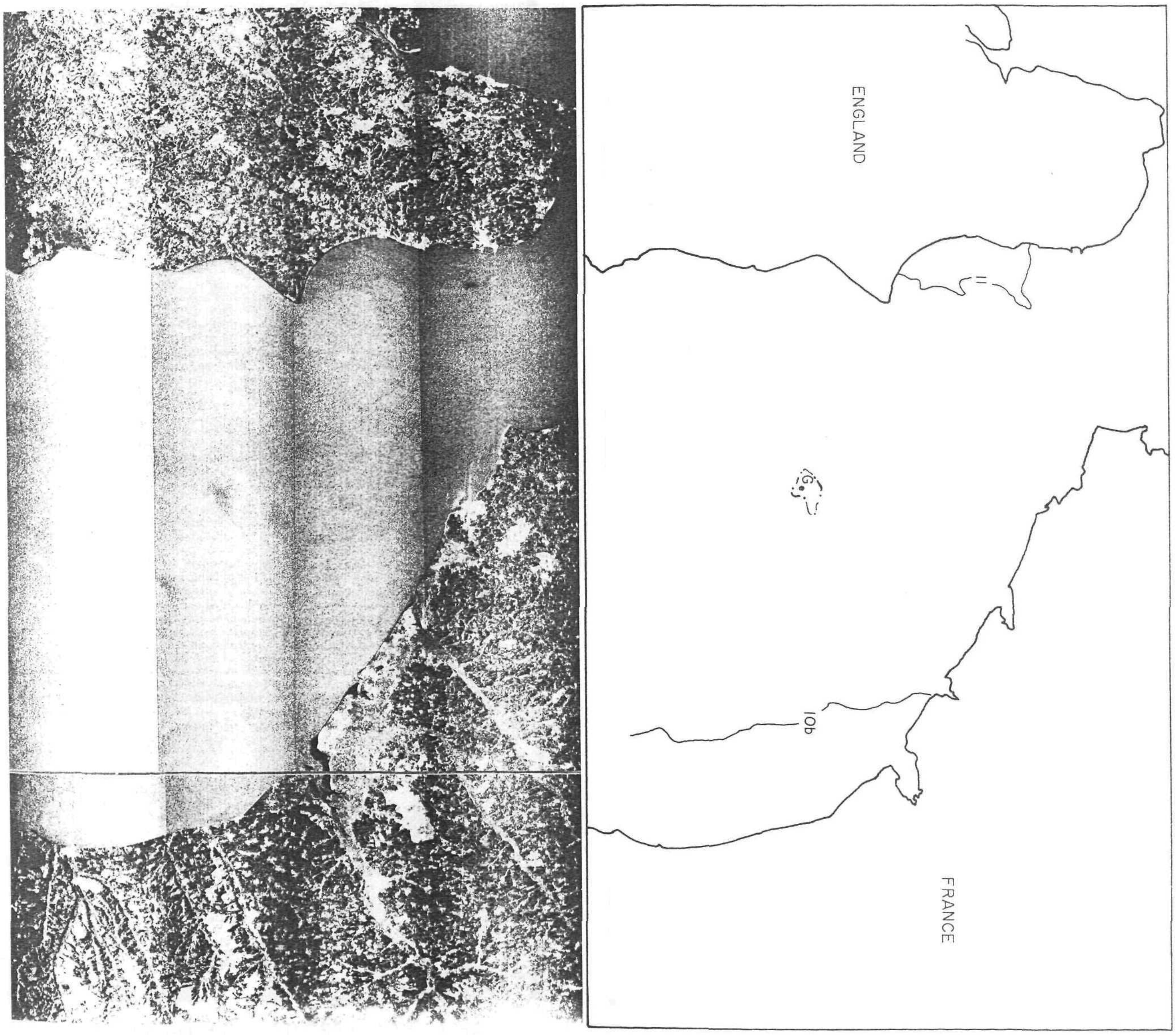

Figure 3.7 SAR 719 and sketch map.
The image shows a stratification front off Dungeness (11), note the decrease in backscatter over the coastal water. The map outlines the features, the fronts are numbered as in table 3.2. The letters correspond to the bathymetric features recorded in table 3.4.

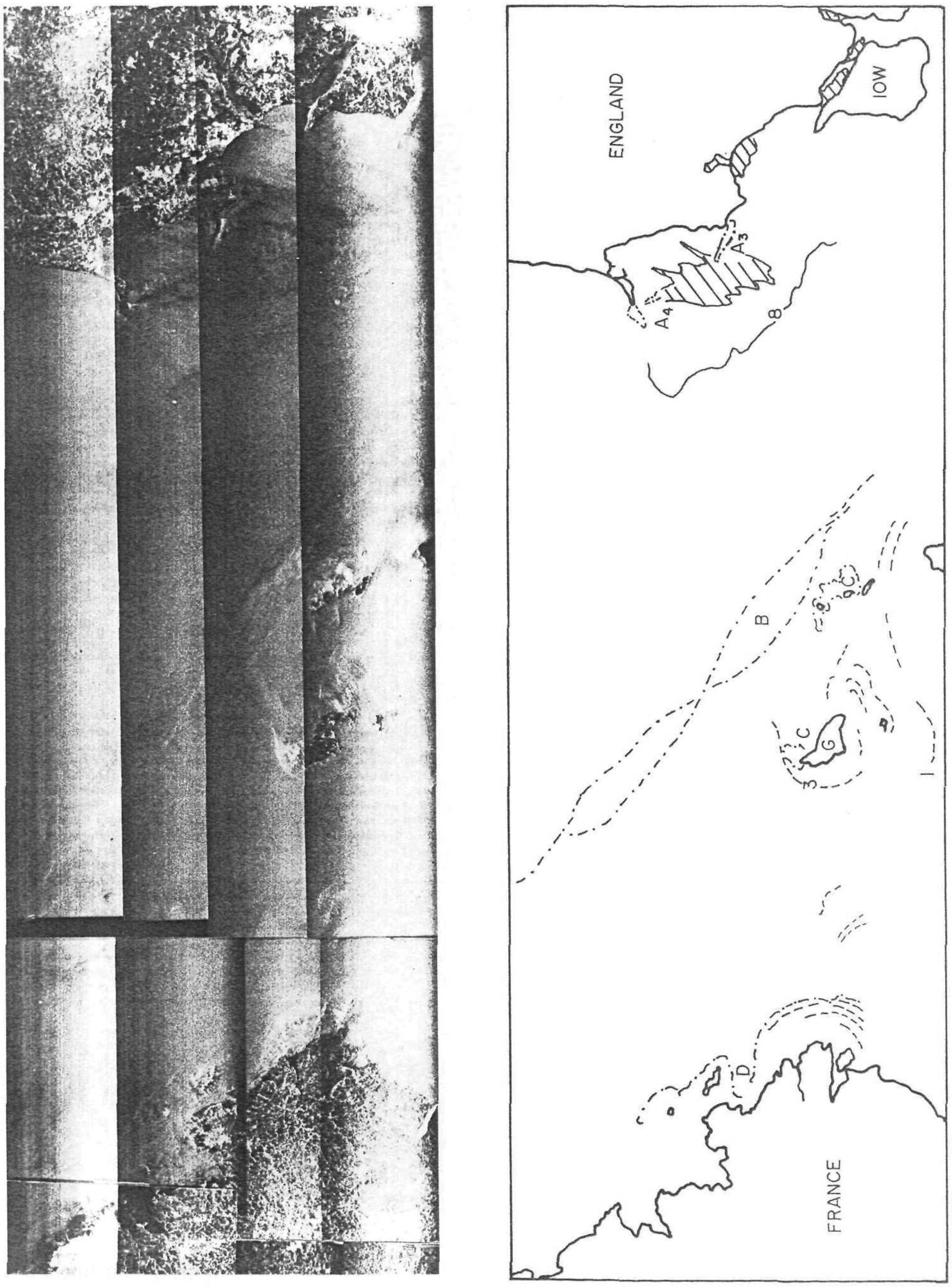

Figure 3.8 SAR 785 and sketch map.
The image shows the tidally convergent frontal boundaries around the Channel Islands (1 and 3), lines of current shear (D) and the Hurd Deep (B). The map outlines the features, the fronts are numbered as in table 3.2. The letters correspond to the bathymetric features recorded in table 3.4.

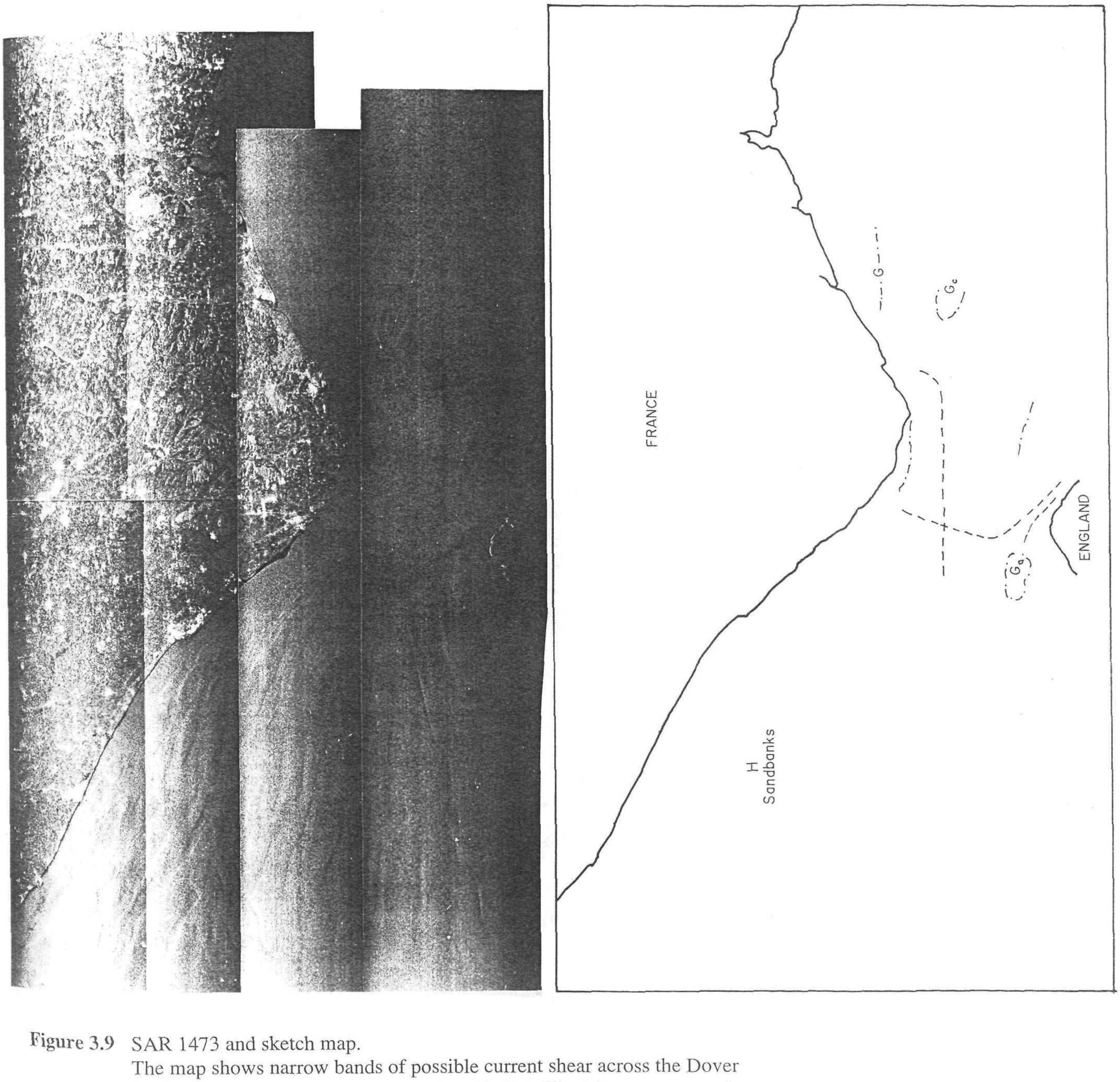

Figure 3.9 SAR 1473 and sketch map.
The map shows narrow bands of possible current shear across the Dover Straits. The fronts are numbered as in table 3.2. The letters correspond to the bathymetric features recorded in table 3.4.

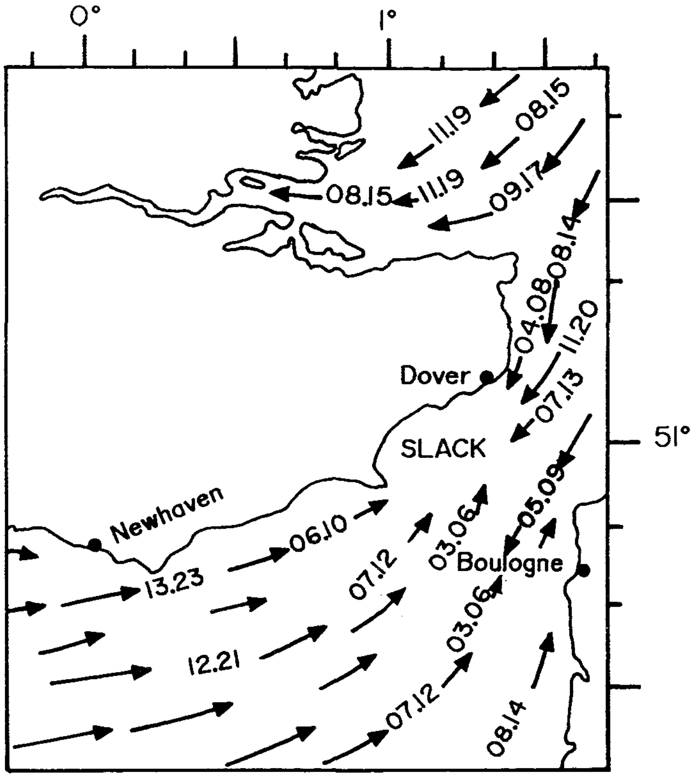

Figure 3.10 Tidal streams from the Admiralty Atlas: 2 hours before high water.

CHAPTER FOUR

AN INVESTIGATION OF A COASTAL FRONT USING AIRBORNE ALTIMETER AND IMAGING RADAR DATA

4.1 INTRODUCTION

The analysis of the Seasat SAR data provided an indication of the characteristic backscatter features associated with coastal frontal boundaries detectable using a spaceborne imaging radar. A more quantitative understanding is sought of the surface roughness patterns generated across a density boundary. The primary purpose of the experiment described in this chapter was to investigate the surface roughness signature associated with a small tidal front, where variations in temperature and salinity variations are of the order 1 to 2°C and 0.5 psu respectively. To achieve this an Airborne Terrain Tracking Altimeter (ATTA) and a Side Looking Airborne Radar (SLAR) were flown across a coastal front as part of a contemporaneous ship and airborne experiment. Concurrent surface observations enabled *in situ* measurements of the SST gradients and wind conditions to be compared with the backscatter signature.

The investigation concentrates on a narrow frontal zone along the French coastline in the eastern English Channel, referred to throughout this chapter as the Cap Gris-Nez front. The work was planned in conjuction with an exisiting airborne and field campaign monitoring flow through the channel over a three week period during April and May 1991 (Fluxmanche, 1993). It was intended that the experiment would coincide with ERS-1 SAR data acquisition across the area. However, the ERS-1 launch was further delayed by several months and SAR data of the area were only acquired at a later date. Analysis of these ERS-1 data did not identify any features considered to be associated with the Cap Gris-Nez front and without coincident *in situ* observations further investigation of these images would have been inconclusive and therefore was not pursued.

4.2 RATIONALE

The analysis of the Seasat SAR images has demonstrated that coastal fronts are generally detected as a narrow line feature. This denotes either an increase (bright) or decrease (dark) in surface roughness across a boundary of 100 to 250 m in width. In some instances, the SST gradient can be detected due to a large scale variation in backscatter. Deployment of the ATTA was aimed specifically at investigating the narrow surface roughness signature across the frontal boundary, although it would also be expected to detect other spatial variations in the short wave energy field. The SLAR was flown to provide a synoptic view of the region and for comparison with features detected using ERS-1 SAR. Previous studies using x-band radar have demonstrated that it detects features similar to those observed on C- and L-band SAR (De Loor, 1981). Acquiring data from different radar instruments across the same feature, enabled assessment of the suitability of the systems for the investigation of small scale frontal features. In addition, the synergistic approach assisted in the recognition of continuity between features detected crossing several ATTA tracks.

The use of an airborne radar in the experiment brought the benefits of the flexibility of an aircraft, in that repeat coverage of an area is easily achieved, enabling systematic investigation of features over a range of tide and wind conditions. For an intensive survey, a combination of concurrent airborne missions and *in situ* fieldwork can readily be carried out, repeat coverage occurring daily (or even hourly), enabling radar signatures of front-like features to be examined in different oceanographic conditions.

4.3 THE AIRBORNE RADAR SENSORS

ATTA is an altimeter type of sensor which samples at discrete points along track. The SLAR is an imaging radar that views 20 km either side of the aircraft track. Both instruments provide a relative measure of backscatter. A brief description is given of their operating parameters.

4.3.1 ATTA

An altimeter is a nadir viewing radar which records over time the power return from the surface. The amplitude of the return can provide an inverse indication of the sea surface roughness. The ATTA is a pulse limited system which operates at 13.75 Ghz. The spatial resolution depends on the pulse repetition frequency and the aircraft speed. In this experiment the system was operated at 0.25 m resolution. Table 4.1 summarises the system performance.

Table 4.1 ATTA operating specifications

radar frequency	13.75 Ghz ± 0.3 GHz
transmitted pulse width	12 μs
compressed pulse width	2.2 ns
transmitted power	400 mWatts
range measurement: resolution	0.25, 1, 4 or 16 m
pulse repetition frequency	350 Hz
antenna beamwidth	10 °
optimum operating altitude	above 2,500 m

The signal received by the altimeter depends on energy reflected from any surface facet within the field of view of the incident pulse. Facets perpendicular to the direction of illumination will produce a stronger return. A pulse reflected from a rough surface includes random backscatter from the various wave facets, producing a signal dominated by noise. To reduce this the ATTA signals are logged at an average of 64 pulses per record generating a pulse profile every 5.4 seconds, which is equivalent to 32 metres ground resolution. The slope of the leading edge of the pulse profile can be used to calculate wave heights. However, this study was aimed at detecting the small scale sea surface roughness and therefore it is the maximum amplitude of each record that is used. The magnitude of the signal is strongly influenced by small scale roughness and by the effect of longer waves tilting the surface. The returned power varies inversely with the surface roughness, a smooth surface presents near-perpendicular facets and appears as a peak in the along track pulse amplitude. A rough surface will scatter the radar energy away from the instrument resulting in a weaker return signal.

4.3.2 SLAR

The SLARs flown in this experiment are real aperture radars, which only measure the amplitude of the sea surface radar cross section; there is no phase input. The UK and Dutch SLAR are both x-band (9.4 GHz) instruments. The UK SLAR was flown too far inshore and the data were not useful to this study; the instrument is not described here. Table 4.2 provides a summary of the Dutch SLAR imaging specifications. For this study the SLAR was operated at the optimum swath width of 20 km, an antena is mounted either side of the aircraft providing a total of 40 km coverage.

Table 4.2 Summary of Dutch SLAR technical specification

horizontal beamwidth	0.5 °
vertical beamwith	37 °
polarisation	vertical
frequency	9.4 GHz
pulse repetition frequency	1.0 kHz
pulse width	0.5 μs
noise factor	8 dB
amplifier	logarithmic
azimuthal resolution	60 m
range resolution	75 m
swath width	15 - 40 km
optimal altitude	500 m

4.4 PREVIOUS INVESTIGATIONS OF FRONTAL BOUNDARIES USING POINT SAMPLING RADARS

Surface roughness modulations associated with frontal boundaries have been investigated using airborne scatterometer type instruments to study the Gulf Stream boundary (Weisman *et al.*, 1980) and the margin of the Rhine plume (Matthews *et al.*, 1992). These features are well established and comprise salinity, current and temperature boundaries. Although the Gulf

Stream and Rhine Plume are warmer than the surrounding water, the margins are defined differently. Visual records note the Gulf Stream to be significantly rougher than the water on the continental shelf, whereas the Rhine plume has been observed to be characterised by a frontal slick.

The radar measurements across the Gulf Stream (Weisman *et al.,* 1980) had a consistently higher backscatter cross section per unit area than the surrounding colder, shelf water. Variations across the boundary of the square root of the wind stress variations were found to correlate well with the normalised radar backscatter cross-section (σ_0) observations. The influence of the SST gradient on the surface wind stress was noted to be an important factor affecting the radar signal. AVHRR measurements of SST variations across the frontal boundary were around 4 to 5 °C over distances of 50 to 75 km. During the five day sampling period the winds ranged from 3 to 5 ms^{-1} and MABL conditions were both stable and unstable. Over this period the differences in σ_0 ranged from 0.5 to 2.8 dB. Wind against current effects were not considered to have a significant role.

The heliborne radar flown across the Rhine plume by Matthews *et al.* (1992) was operated in multi-frequency mode and the frontal boundary was detected as a reduction in backscatter of about 10 dB at both X- and C-bands. During the experiment the wind conditions were light (< 3 ms^{-1}) and the sunglint patterns on visible band images were used to confirm the frontal margin to be an irregular slick-like feature, roughly 100 m wide. The small scale roughness was noted to rapidly re-establish after crossing the boundary. Analysis of airborne thermal IR data detected a marked SST signature which was linked to the surface roughness variations. The *in situ* observations identified the frontal boundary as a low salinity, higher temperature (> 0.5 °C) feature. The mechanism is not considered to be linked to the SST effects on wind stress, since the warmer water appears smoother. Nor can the dampening of the short surface waves of Bragg dimension be attributed to biological activity or current shears within the region. It was considered that, given the light wind conditions, the weakly converging currents would be sufficient to accumulate abiotic surfactant material, generating a slick-like feature.

The airborne scatterometer measurements used in conjunction with supporting data provide a surprising degree of information about the frontal boundaries, despite the differences in scale. The imaging mechanisms are different in both cases: the Gulf Stream is a mesoscale feature defined by a large temperature step which influences the wind stress across the frontal boundary; the Rhine plume is a coastal feature of similar proportions to features within the English Channel, the frontal zone being defined by a narrow region of reduced roughness along the boundary. A point sampling radar of suitable resolution can therefore be sensitive to different imaging mechanisms associated with frontal features. It was therefore reasonable to assume that the ATTA could provide a valid method for measuring relative changes in surface roughness across a frontal boundary in the English Channel.

4.5 THE CAP GRIZ-NEZ FRONT

The Cap Gris-Nez front is a small section of an intermittent sequence of coastal fronts extending along the north coast of France, often referred to as 'coastal rivers'. Freshwater outflows from the major rivers, such as the Seine and Somme, are trapped near the coast by the local bathymetry. The sandbanks, such as the Bassure de Baas, deflect the ebb current back onshore and constrain the flood tide to the shallow water, resulting in parallel flow along the coast. The residual flow is thought to be northwards and it is the distance over which materials (such as pollutants) are transported along the coast and the level of mixing between the coastal and central waters of the Channel that is the subject of the Fluxmanche studies (Fluxmanche, 1993). Visible analysis of data from Landsat thermal images and airborne thermatic mapper (ATM) images identified two frontal boundaries within the region (Matthews and Boxall, 1994). The features consist of a stable, narrow turbidity boundary, which extends a maximum of 2 km offshore and a SST front, varying in location between 5 to 9 km offshore. An estimated 2 °C increase in temperature occurs across the SST front in the transition from the main channel to the inshore waters. A distinct spectral signature marked a sharp increase in the chlorophyll concentrations inshore. Along the frontal margin, patches of cooler water, of 70 to 200 m in width, were also noted on the Landsat thermal image.

The fieldwork carried out at the time of this study (April 1991) was concentrated on the main frontal zone 5 to 10 km offshore. An analysis of the sediment and chlorophyll distribution was carried out using an airborne visible waveband sensor (the CORSAIR). A sharp boundary was observed denoting an increase in chlorophyll concentration in the coastal waters (Mathews, 1994). During this survey the frontal zone was defined by an inner and outer boundary (figure 4.1). The outer margin lay roughly 7.4 km offshore (Front 1) and the inner 5.5 km offshore (Front 2). Results from the *in situ* survey identified the front as a sediment, organic and salinity boundary. Figure 4.2 shows the surface salinity and temperature distributions during the experiment. The salinity increases by 0.5 psu or more in the main channel. Differences in SST are less pronounced at this time of year, although an increase of 0.5 °C occurred just north of the river Somme.

A continuous field programme, throughout 1990 and 1991, found the boundary to be maintained throughout the year (Nash and Boxall, 1993). In summer the offshore water is around 2 °C warmer and a distinct horizontal thermal boundary is present; although associated with the front, the vertical stratification of the offshore water cannot account for the presence of the front throughout the year. In winter it is the coastal water that becomes stratified. However, the freshwater input is insufficient to maintain a normal density front. Results from a study of the currents using a surface radar and *in situ* current meters showed persistent horizontal divergence and upwelling along the outer boundary, approximately 10 to 13 km offshore (Castaneda, 1994). This is consistent with field observations of upwelling cold 'bubbles' and visual surface roughness observations of a narrow slick (50 to 100 km wide) along the boundary.

The processes controlling the frontal boundary are still not fully understood, although its position is attributed to local bathymetry and tidal current effects. According to calculations of horizontal eddy diffusivity the front should be destroyed, but clearly there is some form of vertical mixing maintaining the density gradients (Boxall pers. comm.). The mechanism suggested is based on the stratification parameter defined by Simpson and Hunter (1974). The value h/u^3, where h denotes the depth and u the current speed, is used to define a depth at which the effects of bottom friction and tidal mixing become small and the water column can become stratified. This occurs acround the 30 m contour off Cap Griz-Nez, the position at which the front persists. The theory cannot account for the stratified coastal waters in winter, when it is assumed that the freshwater and buoyancy flux increases.

4.6 EXPERIMENT PLAN AND DATA ANALYSIS METHODS

A multi-sensor experiment in which *in situ*, airborne visible waveband (CORSAIR) and radar (SLAR and ATTA) measurements were obtained was conducted off Cap Gris-Nez during April and May 1991. Results from the *in situ* and visible imagery verified the presence of a frontal zone, showing its position and appearance as described in § 4.5. The aim of this work was to assess the surface roughness signatures associated with the frontal zone using the ATTA and SLAR. The *in situ* and CORSAIR data (figure 4.1) were used to verify the results from the radar surveys. Visual observations, such as that from a video recording acquired by the UK aircaft (16.4.91), provide additional information about the surface signature of the frontal boundary. A summary of both air and ship sightings of surface roughness variations in the vicintiy are recorded in table 4.3 and mapped on figure 4.1.

4.6.1 ATTA

Ideally, the ATTA experiment would have been carried out simultaneously with the *in situ* survey and CORSAIR campaign. This was not possible due to limits on aircraft availability and the ATTA was flown two weeks later. Studies of the front indicate it is a relatively stable feature, that exists on a timescale of months rather than weeks, moving a maximum of 1 km east or west. The delay in the ATTA flights was therefore not considered to affect the interpretation of the results. It was planned to fly the instrument over the same area for three consecutive days, twice a day. However, the ATTA signal is strongly attenuated by rain and cloud and coverage was limited to one day (3.5.91). Ten latitudinal flight paths were flown over a 11x11 km area at 1.852 km (1′ latitude) intervals covering the predicted position of the frontal boundary and including the coast line for navigation between data (figure 4.1). The flights crossed orthogonal to the front, optimising the opportunity of detecting variations in surface roughness.

Table 4.3 Summary of visual surface roughness observations from air and ship surveys

Date	**Platform**	**Position (latitude and longitude, decimal)**	**Description of feature**
10.4.91	ship	50° 47.85; 01° 28.82	Long slick approx. 20 m wide orientated N-S, near 30 m contour. > SST and < salinity inshore. More slick-like features seen inshore.
		50° 51.88; 01° 33.19	E-W line (possible increase in roughness inshore).
11.4.91	ATM aircraft	50° 51.54 ; 01° 31.24	Line division of water.
		50° 50.99; 01° 31.06	Change in surface roughness, smoother inshore, filamentatous boundary orientated N-S.
		50° 50.27; 01° 30.19	Rough line approx. 20 m wide.
16.4.91	UK aircraft (video)	50° 48.4; 01° 28.9	2 narrow lines of breaking waves. Approx. 100 m apart (figure 4.3).
1.5.91	Dutch SLAR	/	Wind rows.
2.5.91	ATTA aircraft	50° 55.1; 01° 28.9	White line approx 1.5 km offshore.
3.5.91 (observations numbered as on figure 4.1)	ATTA aircraft	50° 54.1; 01° 36.8 (2)	Wave refraction, see clear line of breaking waves.
		50° 53.2; 01° 39.9 (3)	Faint streaks across track.
		50° 52.0; 01° 32.3 (4)	White lines approx N-S.
		50° 50.9; 01° 34.5 (5)	White lines appear associated with wave refraction (N-S).
		50° 50.0; 01° 25.3 (6)	Dark lines N-S.
		50° 49.0; 01° 35.8 (7)	White lines near coast.
		50° 47.9; 01° 32.2 (8)	Very distinct white lines
		50° 46.9; 01° 35.0 (9)	2 white lines, N-S.

The analysis began with an investigation of the data quality, assessing any systematic trends which might distort the underlying amplitude values. A plot of the backscatter power return along each track identified a low frequency sinusoidal wave pattern causing artifical highs and lows in the high frequency data returns. The aircraft altitude measured by the ATTA show a similar periodicity. Figure 4.4 shows three examples of the along track variations from runs 1, 3 and 10 on 3.5.91. The aircraft altitude is superimposed in bold over the raw (grey) and averaged amplitude (thin line). The peaks and troughs in the amplitude signal can be seen to match closely the peaks and troughs in the aircraft altitude but, with a slight time lag occurring. The amplitude of the sinusoidal variance along track differs between flight paths. Maximum power returns would be expected when the instrument is nadir pointing (at minimum and maximum aircraft altitude). However, the peaks occur as the aircraft is increasing in altitude and not when it would be expected to be level. The effect may be ascribed to the pitch of the aircraft causing the sensor to point off nadir. Another possible explanation may be linked to the effect of changes in altitude on a pulse limited system. As the altitude increases the angles of illumination over the footprint decrease (are closer to nadir) and consequently the backscatter received by the ATTA increases.

Although the effect cannot be fully explained, the similarity between the range and low frequency amplitude signals is sufficient to confirm a correlation between signal strength and the variations in the aircraft altitude. Since these long wavelength modulations are unconnected with the surface roughness state being investigated, they are removed using a high pass filter. Using Nyquist sampling theory, a time window was chosen of sufficient duration to span half the wavelength of the shortest variation in aircraft altitude for each track. The raw amplitude profile was then subtracted from the smoothed profile leaving the residual power returns for analysis. *In situ* observations and thermal imagery suggest the width of the frontal slick-like feature to be in the order of 50 to 150 m (two to five ATTA resolution cells). Hence, to preserve spatial resolution further filtering was not carried out. The residual values are plotted along track, west to east, along a longitude scale (figure 4.5). Two standard deviations (SD) either side of the mean are marked. The distribution of the values within 2 SD of the mean were found to be normal, fitting the Chi-squared test at the 5% level. It is therefore reasonable to assume that these data represent the background surface roughness signal from a uniform wavefield. When data points outside 2 SD are included the distribution is not normal, indicating that these points are the result of non-random effects and can be interpreted as evidence of real features in the surface roughness field. Data outside 2 SD appearing as distinct peaks and consisting of 3 to 6 stepped points are considered to represent a feature. A spike of only one data point may be spurious and is ignored, such as occurs in Run 7 adjacent to the feature marked F2 (figure 4.5). This method achieved a semi-automated approach for the separation of possible features of interest from the background surface roughness field.

4.6.2 SLAR

Three SLAR passes were flown across the front on 16th, 17th April and 1st May 1991, as near contemporaneous with the CORSAIR, ATTA and *in situ* data as possible for comparison of results. Two passes were flown by the Dutch coastguard SLAR along a north to south transect approximately 3 km offshore. The radar look direction was orthogonal to the predicted frontal position to maximise feature detection. The object of flying at different times was to obtain data under different wind and tide conditions for investigation of the factors affecting surface roughness patterns detectable by an imaging radar.

The digital image data were analysed qualitatively. Quantitative assessment of the data is not viable, since calibration parameters for the effects of aircraft pitch and roll are not included in either of these systems. The spatial distortions and variable backscatter intensities across the range direction within the image cannot accurately be accounted for. For the purpose of this study, the spatial information on the size, position and appearance of a feature, such as a slick or line, was the main requirement. For comparison with the field data and results from the ATTA, features of interest are mapped (figure 4.1) and their distance along the ATTA track calculated.

4.7 RESULTS AND DISCUSSION

The location of the frontal boundaries are based on data acquired on 11.4.91 (CORSAIR) and 10.4.91 (*in situ*). The direct visual observations of slicks along the frontal margin from both ship and airborne platforms (summarised in table 4.3 and marked $_S$ on figure 4.1), combined with informaton on surface current patterns, suggests the frontal boundary is often marked by a region of smooth water varying in width from 50 to 200 m; a divergence or conversely an accumulation of abiotic or biological material would generate a feature of this type. Observations from the aircraft of occassional bright line features thought to indicate breaking waves in regions of wave refraction, were noted in the survey region, although in general these features occurred further inshore (marked as $_R$ on figure 4.1). An airborne video visible still of the front taken during the UK SLAR flight (16.4.91) provides a good example of these bright line features (figure 4.3). The position of the feature is plotted on figure 4.1 and corresponds to the southern end of front 1 detected from the CORSAIR spectral data. It would be expected that such variations in surface roughness would modulate the backscatter signature received by ATTA, SLAR or ERS-1 SAR. Table 4.4 summarises the wind and tide conditions at the time of data acquistition from the airborne and *in situ* surveys. A summary of the results is also recorded.

4.7.1 The SLAR

The results from the SLAR passes flown across the area on 17.4.91 and 1.5.91 showed no evidence of any variations in surface roughness corresponding to fronts 1 or 2 on either day. The parallel bright streaks seen on the 1.5.91 image are orientated with the wind direction (SW to NE) and, given the wind conditions (8 to 10 ms^{-1}), are thought to denote wind rows (figure 4.6a). Wind speeds greater than 7 ms^{-1} would be expected to effectively obscure any slick-like features associated with the frontal boundary. However, on 17.4.91 light winds prevailed (1 to 4 ms^{-1}), which are optimum for detecting slick-like features or SST effects on the surface roughness (as described in Chapter 2). The absence of a backscatter signature on this SLAR image would suggest either the resolution of the SLAR was too low to detect the feature or that there was no surface roughness signature at the time of the image. The slick along the boundary is estimated to vary between 50 to 200 m in width; the SLAR range resolution is 75 m. That the conditions were optimum for the detection of slick-like features is demonstrated by the distinct large scale change in backscatter observed to the south of this image (figure 4.6b). The transition to a smoother sea surface (dark) closely corresponds to the position of the river plume from the Somme. The filamentatary appearance of the boundary and the narrow tongue of darker water extending northwards with the tide, increases confidence that the tonal variation in backscatter is linked to a frontal feature. The mechanism is uncertain, since the SST gradient across the front is slight (0.5 °C maximum), although a strong salinity front exists. A Landsat Thematic Mapper image acquired in January 1988 showed suspended particulate matter contained within a similar boundary. Dampening of the shorter waves by the bouyant outflow of fresher water could account for the smoother sea surface roughness pattern observed. Unfortunately, the feature was not covered by the ATTA flights.

A weak, north-south, line feature (slightly brighter than the background signal) was also observed on SLAR pass 17.4.91. This is thought to correspond to the turbidity front along the 20m contour (figure 4.6b and plotted as a dashed line on figure 4.1). At the time of the pass the tide was still ebbing in the channel (0.4 ms^{-1}), but had begun to flood inshore (0.2 ms^{-1}). Although the opposing currents are weak the current shear appears sufficient to produce a slightly rougher line of water parallel to the coast, which is observed on the SLAR image.

4.7.2 The ATTA

To obtain a detailed look at the ATTA data the residual amplitudes are plotted along track for runs 1 to 10 (figure 4.5). Runs 3 to 7 cross the frontal boundary detected using the CORSAIR data and the discussion concentrates on these passes. Runs 1 and 2 are to the north of the frontal zone and 8, 9 and 10 are to the south of the study region. Any possible features on the ATTA data along these tracks can therefore only tentatively be identified, using the spatial continuity of features between tracks to estimate the likelihood of their being genuine. Potential features observed on tracks 3 to 7 are verified by spatial matching with frontal features deduced from the CORSAIR, SLAR and *in situ* data (figure 4.1). Peaks or troughs in backscatter found to correspond to fronts 1 and 2 are labelled F1 and F2 on figure 4.5. A peak in the signal corresponding to the position of a weak inshore front identified on the SLAR image is labelled S. The troughs in the amplitude signal, on Runs 4 and 7 (marked +), are thought to be associated with Front 2. Discrete features were recorded on every run, with the exception of Run 1. Run 1 measured peaks greater than 2.5 SD along the entire track. This track is to the north of the frontal zone and the peaks are thought to be associated with wave refraction and modulations of the sea surface as the currents propagate around the headland (table 4.3). The data are not included further in the discussion of the results.

Table 4.4 Summary of airborne and *in situ* data acquired for the experiment.

Instrument	Date & time (GMT)	Wind Speed (ms^{-1})	Tide +/- HW Dover & Conditions at Cap Gris-Nez	Summary of Results
In situ Data	10.4.91 11.4.91			CTD, sediment, visual observations and current data identify a frontal boundary.
CORSAIR (spectral)	11.4.91 14:00		+5:20 weak ebb	Detect 2 fronts, 7.4 & 3.4km off-shore (fronts 1 & 2).
UK SLAR (imaging radar)	16.4.91			Flight path too close inshore
Dutch SLAR (imaging radar)	a)17.4.91 09:45 b)1.5.91 13:20	a) 1-3 ms^{-1} b) 8-14 ms^{-1}	a) -2.5 weak opposing current, ebb offshore, flood inshore (@ 0.2 ms^{-1}) b) +1 flood 0.7 ms^{-1}	a) Weak line of current shear along 20m contour. Large change in backscatter at Somme river front. b) Very bright return across entire study region.
ATTA (RAL) (nadir radar)	3.5.91 09:20 - 10:25	5-10 ms^{-1}	-3.5 ebb 0.7 ms^{-1}	Runs 3-7 show evidence of Front 1 and generally Front 2, plus the line of current shear observed on the SLAR at the 20m contour.

Figure 4.7 summarises the distribution of the residual amplitudes from each run. Plotting the data to scale along lines of latitude enables the spatial information to be assessed relative to each flight path. By interpolating between the peaks in the backscattered power (lying above

2.5 SD's from the mean) the three line features are defined orientated north to south, except to the north were the front bends around to the east. The peaks and troughs considered to represent the frontal boundaries are again labelled F1, F2 and S. The dotted sections of the lines indicate regions where the signature on the ATTA data was less distinct or else two or three adjacent peaks occurred.

Front 1 is detected on Runs 3 to 7 as a clear spike (>2.5 SD) and on Runs 8 to 9 two or three peaks, estimated to be in a similar position, are seen. A peak in the data indicates an area of smoother water, which is consistent with the narrow slick-like feature observed at the frontal boundary. A peak in the data comprises of 3 to 6 data points, which is representative of a region 90 to 190 m in width. These values are consistent with the thermal and *in situ* observations of the front.

Front 1 does not appear in the expected position on Run 2 (figure 4.5). Mapping the data to scale on figure 4.7, enabled the positions of features to be compared with visual observations from the ship and Front 1 on figure 4.1. Run 3 virtually follows the front as it changes in orientation from north:south to east:west. The two peaks marked * on figure 4.5, initially thought to be spurious features, are found to correspond to the position of the established frontal boundary as it curves round. The position of the distinct peak on Run 2 would then correspond to the position of front 1 and is mapped accordingly on figure 4.7. For the aircraft to drift off track by 0.2 km or for the front to have moved (less than 0.25 km) or to undulate across the flight path can be considered reasonable. The peaks are therefore thought to represent the frontal boundary, although without *a priori* knowledge of the area from earlier surveys it would have been difficult to categorise these features.

The secondary front is a weaker feature, but is also detected as a peak in backscatter on Runs 3 to 7, with the exception of Run 4. The signature is more diffuse and on Run 7 corresponds to two or three peaks and a weak trough (marked + on figure 4.5) in the backscatter. Visual observations of slick-like features and narrow lines of rougher water were made in the region where front 2 crosses track 7. On Run 4 the trough in the backscatter also matches the position of front 2. The transects further to the south of the study area (8 to 10) are more confused and only 10 shows a distinctive peak in the region of front 2. The estimated position of front 2 is plotted on figure 4.7. Confidence that the features are representative of the position of front 2 is given by the spatial consistency between the observations on each flight path. On Run 7 the three peaks are spread over a region of 500 to 1000 m; whether they are connected to frontal current activity is uncertain.

The feature observed along the 20m contour on the SLAR image is also identified on Runs 3 to 9, the amplitude of the signal varying greatly. On runs 3, 5, 6 and 9 the peak is adjacent to a trough in the backscatter signal. This would suggest a narrow band of rougher water adjacent to a smooth region. This is a surface roughness signature which is characteristic of the effects of bathymetry on the short wave energy field (as described in chapter 2).

All three frontal features observed on the ATTA data closely match the positions and spatial shape of the fronts established from the spectral and ship data. The slight variations in the position and shape of the front predicted using the ATTA data are well within estimated frontal movements. The calculated widths of Front 1 are in close agreement with estimates of the width from ship observations using thermal images.

4.8 SUMMARY

The analysis of the ATTA data demonstrates the potential of using a high resolution, nadir sampling airborne radar to investigate coastal frontal features. Distinct changes in the radar backscatter signature were found to correspond closely to the boundaries, identified from the *in situ* and visible airborne experimental work, marking fronts 1, 2 and the weaker feature inshore. This verifies that frontal features can be associated with variations in surface roughness and hence, given a suitable resolution instrument, are detectable using a radar type sensor.

Factors such as slight differences in current speed and direction, either as the flow enters the shallower water or opposing flows as the tide turns first inshore, generate small regions of intermittent upwelling, current shears, convergences and divergences. These effects appear sufficient to modulate the sea surface short wave field, producing narrow regions of smooth or rough water (50 to 200 m width) along the frontal boundary, which are detectable by the ATTA. The failure to detect the main frontal features using the 75 m SLAR is ascribed to the lower resolution and high level of noise in the images. The images acquired by ERS-1 SAR at a later date also show no evidence of the frontal boundaries; given the well established nature of the frontal zone this was a surprising result. However, without contemporaneous field data to confirm the existence of the frontal boundaries at the time of the SAR image acquisition it is difficult to draw any conclusions.

The aim of this experiment was to assess the backscatter signatures associated with coastal frontal features for different wind and tide conditions, but poor weather conditions disrupted the flight schedule and only one day's data were obtained. The success of the analysis of the ATTA data confirms the potential for using an altimeter type instrument for the detection of the small scale changes in surface roughness, which are attributed to weak variations in the horizontal current gradients occurring along frontal boundaries. However, without supporting *in situ* and visible airborne data, verifying the presence of the frontal boundaries, it would have been difficult to assess how representative the changes in backscatter were as evidence of real oceanographic features in the surface roughness field. Although an imaging radar would provide a more spatially continuous view of features within a region, the results from this experiment suggest that it may not be as sensitive as an airborne altimeter type instrument, such as the ATTA.

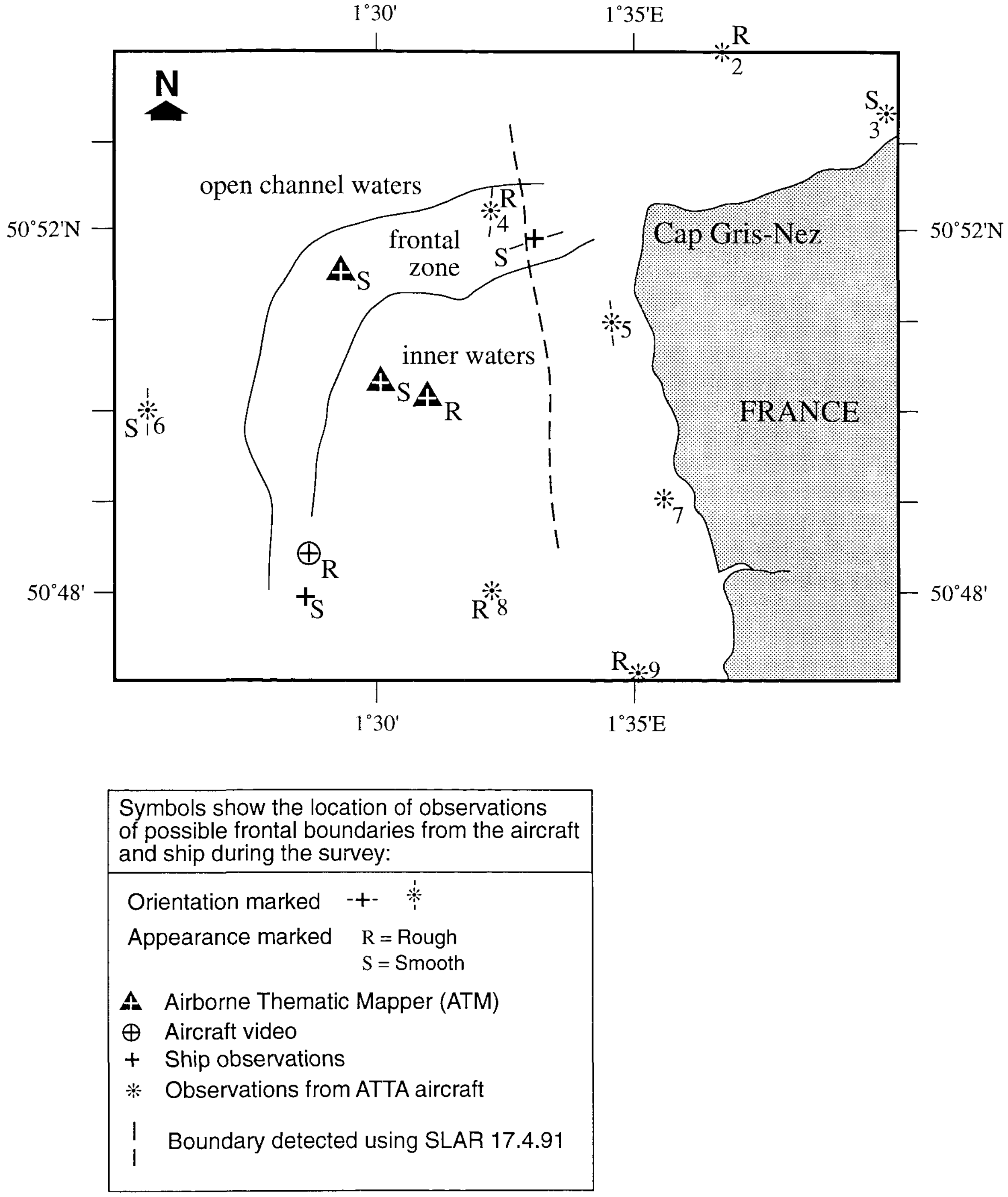

Figure 4.1 Diagram of the Cap Gris-Nez frontal zone.
Frontal boundaries 1 and 2 were determined from the visible remote sensing results (Matthews and Boxall, 1994). The dashed line marks an inshore boundary observed on the 17.4.93 SLAR image. Observations of possible frontal boundaries made from the aircraft and ship deployed during the experiment are also marked, including information on the orientation and appearance (rough or smooth) of these line features. The numbers correspond to the observations made from the ATTA aircraft, as recorded in table 4.3.

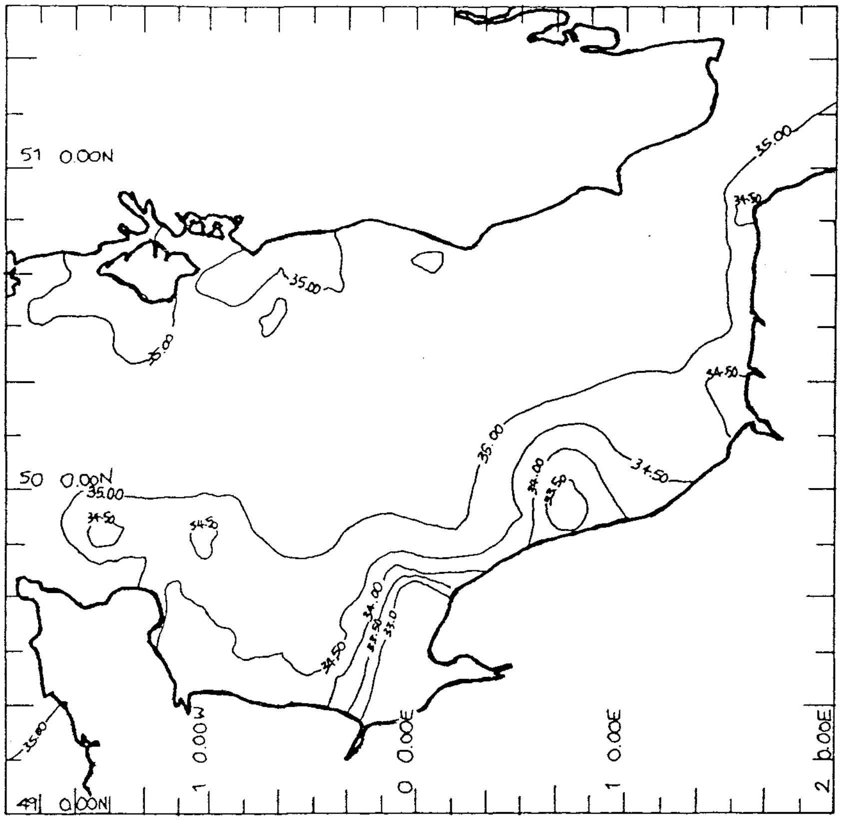

Figure 4.2 Spatial variation of salinity in the Eastern Channel for April 1991. From the Challenger 77 cruise (Nash and Boxall, 1991).

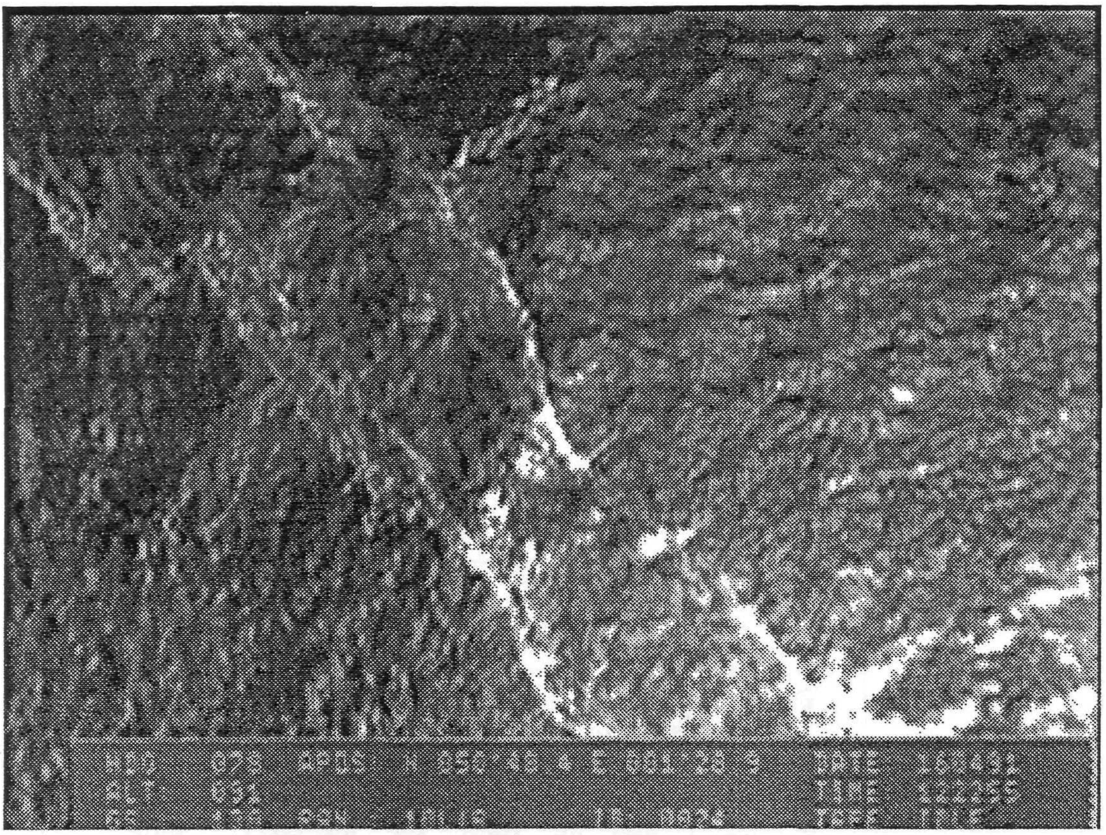

Figure 4.3 Visible video still of the southern end of the Cap Gris-Nez front on 16.4.91. Taken from the UK aircraft carrying a SLAR, the two bright lines mark narrow bands of breaking waves approximately 100 m apart.

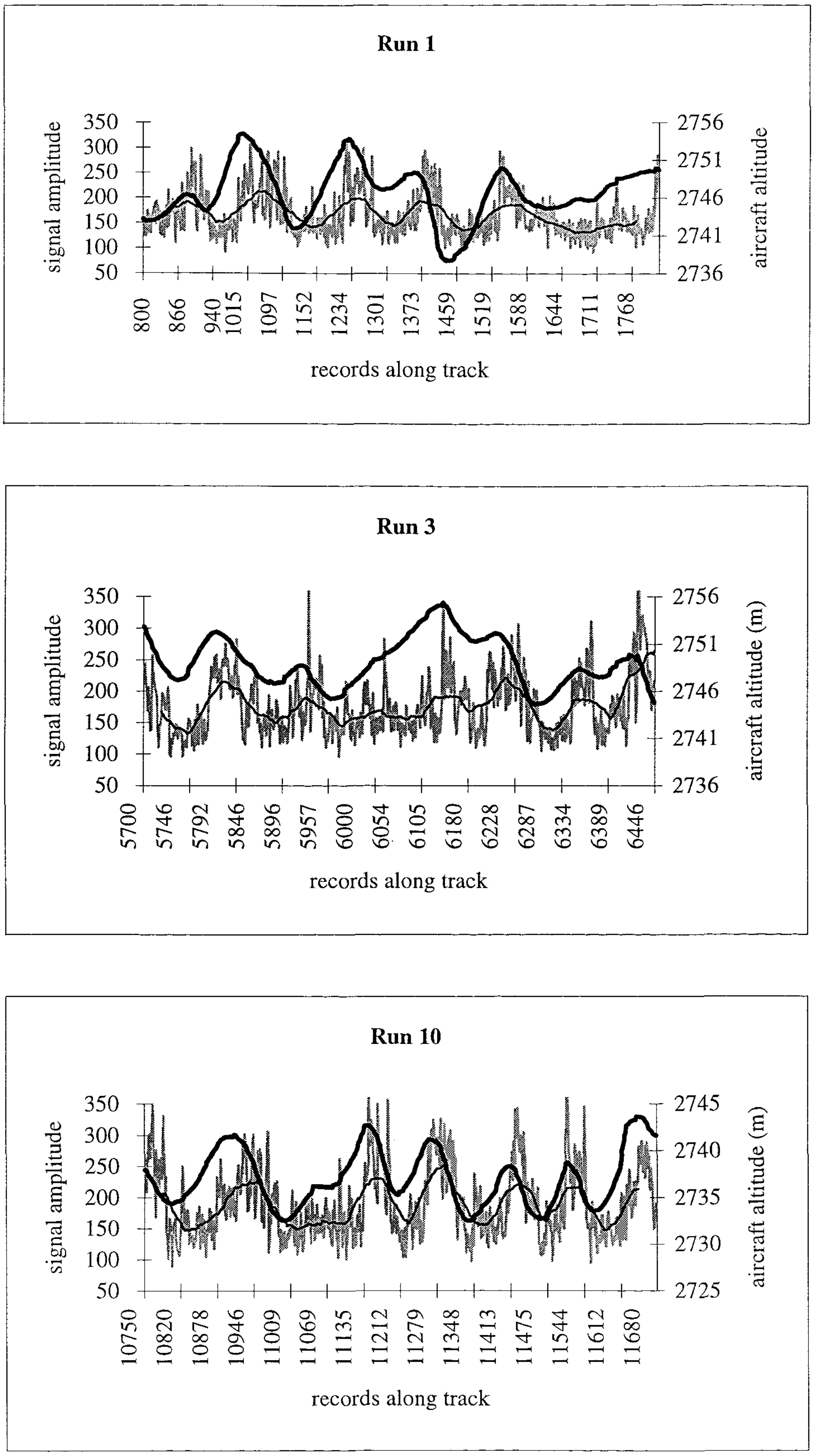

Figure 4.4 Comparison between aircraft altitude and ATTA signal amplitude variations. Examples taken from runs 1, 3 and 10 acquired on 3.5.91. The grey line represents the full resolution signal amplitude and the light line through these data a low pass filter. The bold line overlain shows the low frequency variations in the aircraft altitude, the effects on the amplitude signal are most apparent on run 10.

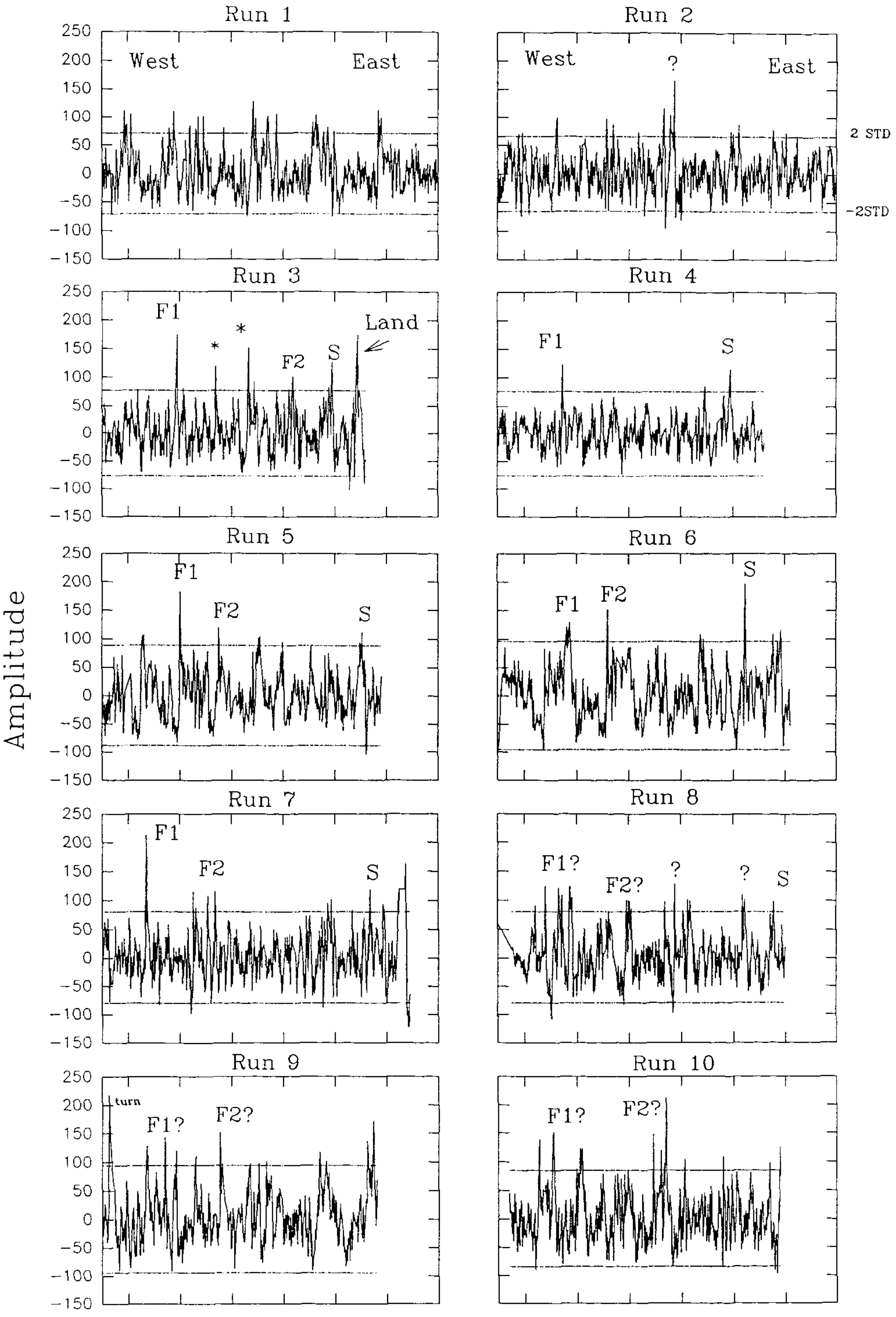

Figure 4.5 ATTA residual amplitude signals for runs 1 to 10 on 3.5.91.
The straight lines marked SD of ± 2. Distinct peaks or troughs above or below these lines are considered to mark a significant change from the mean surface roughness. A high return represents a smooth region of water. Features corresponding to the frontal boundaries 1 and 2 are labelled F1 and F2, S indicates a feature corresponding to the inshore boundary observed on the SLAR. The peaks labelled * are also thought to represent front 1 as it curves to the west (refer to figure 4.1).

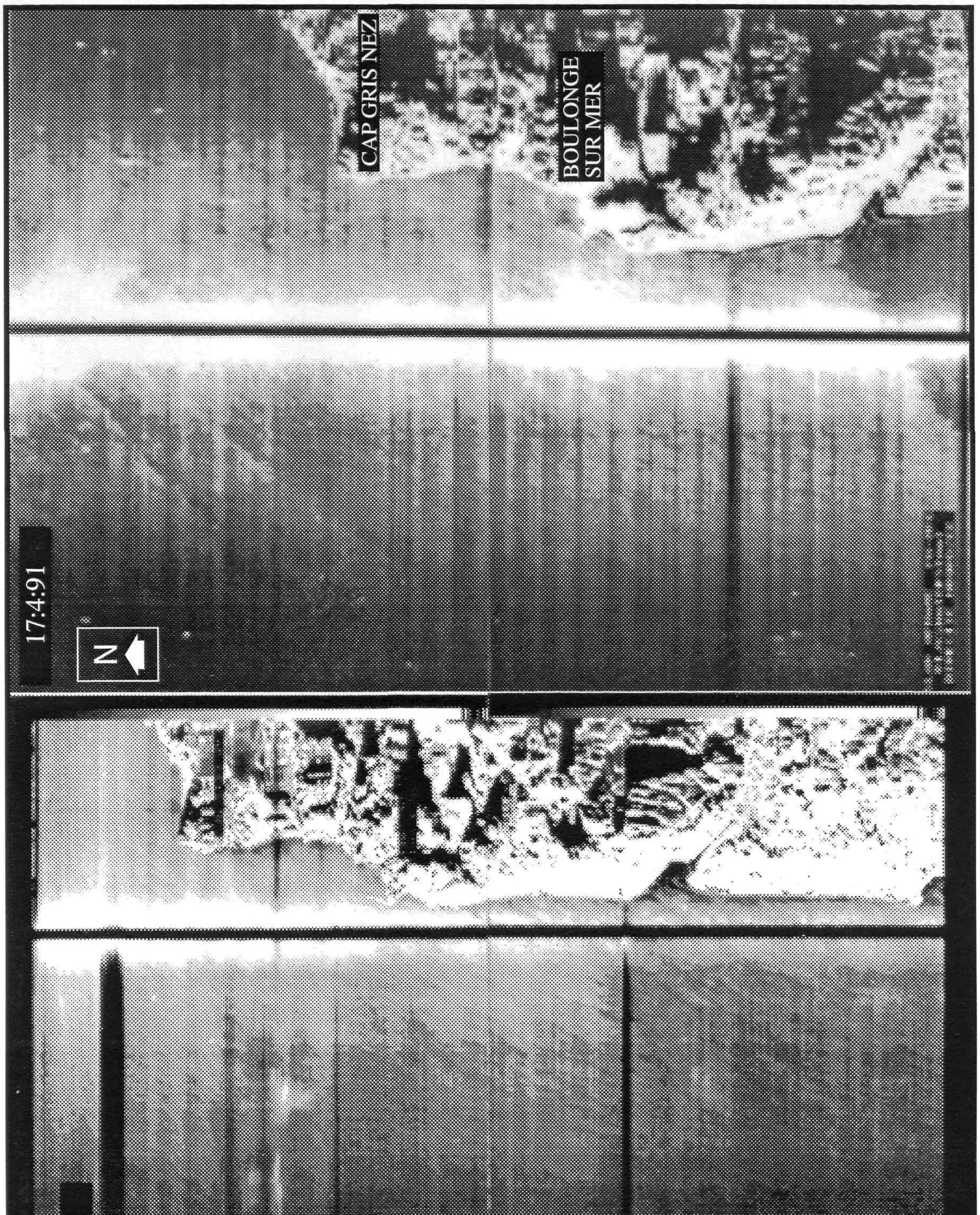

Figure 4.6 SLAR images acquired over the Cap Gris-Nez front by the Dutch coastguard. Note the tonal change in backscatter (bright to dark) in the southern corner of the image for 17.4.91. The bright streaks on 1.5.91 represent wind rows.

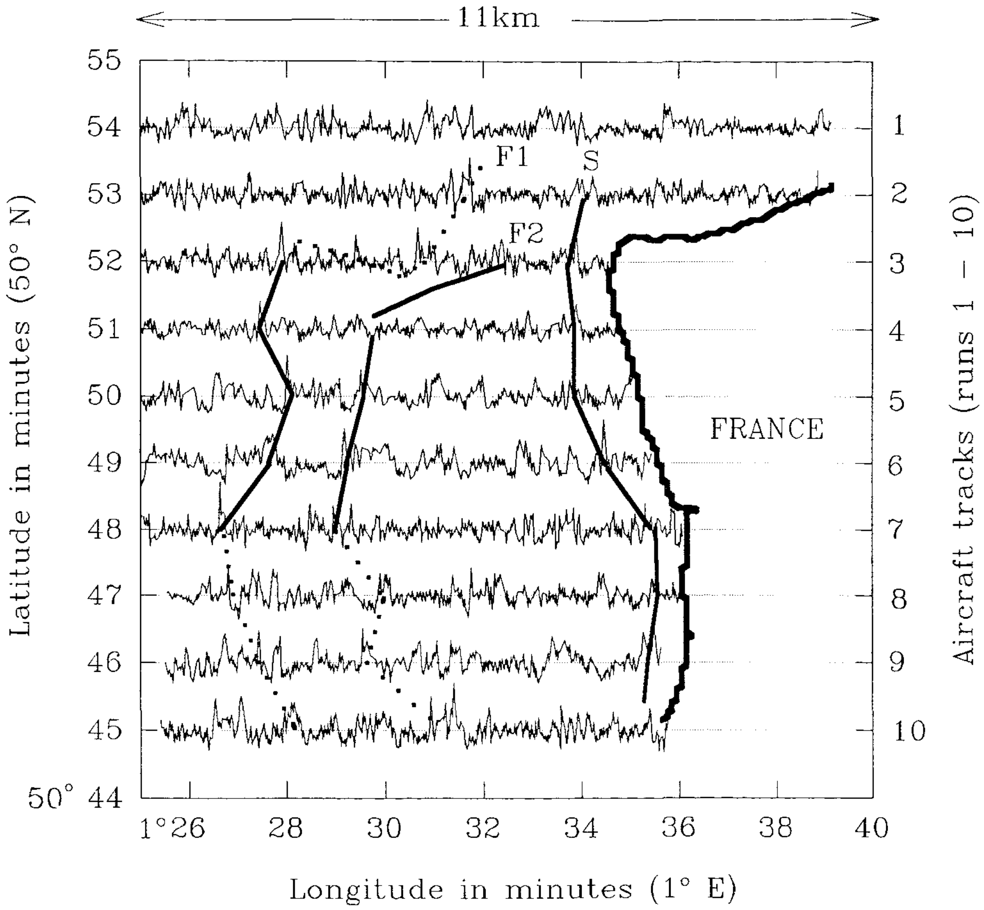

Figure 4.7 Summary map of the residual ATTA amplitude returns plotted along track. The positions of the fronts determined from the ATTA survey are marked, linking the features identified in figure 4.5. Dotted lines are used where the features are less distinct. F1 and F2 correspond to fronts 1 and 2 and S represents the boundary detected by the SLAR (as on figure 4.1).

CHAPTER FIVE

ERS-1 SAR PRI IMAGE ACQUISITION, HANDLING AND CALIBRATION

5.1 INTRODUCTION

The delivery of the first ERS-1 SAR data in August 1992 enabled the digital analysis of radar imagery to begin. The emphasis of this phase of the study is to use the multi-temporal capabilities of the SAR to study oceanographic features over varied wind and tide conditions. Comparisons of relative differences in backscatter signatures across specific features between images and rigorous investigations of the factors modulating the short wave spectrum require accurately calibrated data. The ERS-1 SAR is a stable and well calibrated instrument, which is intended to provide the user with the first opportunity to make quantitative assessments of the backscatter measurements (Laur *et al.*, 1993).

This chapter catalogues the ERS-1 SAR data acquired for the study and notes the difficulties associated with handling large quantities of SAR images. A description is given of the calibration procedure outlined by ESA. The technique is used to obtain backscatter profiles across the entire range direction of the image for all the data acquired for this study. The performance of the procedure was then examined, using a standard model describing how backscatter is expected to vary with viewing geometry and wind speed, to determine if any spurious perturbations occur within the calibrated data. The suitability of the existing PRI.SAR product for operational use is then discussed in the summary.

5.2 THE SAR DATA

The SAR images are transmitted to ESA ground stations, Kiruna in Sweden receiving the data for the English Channel region, and then distributed to the Processing and Archiving Facilities (PAF's) located in Italy, Germany and the UK for the generation of off-line products, such as the SAR.PRI images, as documented in ESA SP-1149 (1992).

The data acquired for this study are Precision Images (PRI) supplied mainly by the UK-PAF. PRI data are a multi-look (3), ground range, digital product generated from raw SAR image mode data. The summing of 3 non-overlapping contiguous frequency bands (multi-look) is used to achieve speckle reduction and generates a product with a spatial resolution of 26 m in range and between 6 m and 30 m in azimuth, which is sampled by 12.5 x 12.5 m pixels. The product is described as being calibrated and corrected for the antenna elevation pattern and range spreading loss; it was designed such that radar backscatter cross sections (σ_0) could easily be derived. PRI.SAR images were intended to supply accesible radar data for use by the applications scientist.

5.2.1 Data Acquisition

ERS-1 was launched on 17th July 1991 in a 3-day repeat cycle known as the commissioning and first ice phase for calibration and validation of the sensors. At the beginning of April 1992 it was transferred to a 35-day repeat phase, not returning to a three day repeat until the end of 1993 when it entered the second ice phase. Since April 1994 ERS-1 has been in the geodetic phase with a 168 day repeat cycle. A preliminary sequence of nine images was requested for the period September 1991 to March 1992 to provide a first assessment of the capabilities of ERS-1 SAR and to provide a basis for planning a more comprehensive study. These first data were not received until August 1992, due to operational problems at ESRIN and the PAFs.

For the main study 26 images were acquired from January 1993 until September 1993. Although in the 35-day repeat mode, the large overlap of swaths at 50° N provides coverage of the study region at intervals of 7 to 14 days apart, enabling a multi-temporal data base to be created. Tables 5.1(a) and (b) catalogue the SAR data acquired for the entire study, including the PAF.

Table 5.1(a) Summary of SAR images acquired from the 3-day repeat phase for the preliminary analysis of the data.

Date	Time (GMT)	Orbit	PAF (†)
3.9.91	22:13	700	DLR*(†)
6.9.91	22:13	743	DLR(†)
9.9.91	22:13	786	DLR(†)
25.1.92	10:59	2757	UK(†)
28.1.92	10:59	2800	UK(†)
13.3.92	10:59	3445	UK(†)
16.3.92	10:59	3488	UK(†)
19.3.92	10:59	3531	UK(†)
22.3.92	10:59	3574	UK(†)

* DLR = German PAF

Table 5.1(b) Summary of SAR images acquired in 1993 for the main multi-temporal study.

Date	Time (GMT)	Orbit	PAF (†)
8.1.93	11:00	7754	UK(†)
24.1.93	11:00	7983	UK(†)
12.2.93	11:00	8255	UK(†)
28.2.93	11:00	8484	UK(†)
19.3.93	11:00	8677	UK(†)
4.4.93	11:00	8985	UK
17.4.93	23:00	9178	UK
23.4.93	11:00	9257	UK
3.5.93	23:00	9407	UK
9.5.93	11:00	9486	UK
22.5.93	23:00	9679	UK
28.5.93	11:00	9758	UK
7.6.93	23:00	9908	UK
13.6.93	11:00	9987	UK
26.6.93	23:00	10180	UK
2.7.93	11:00	10259	UK
12.7.93	23:00	10409	UK
18.7.93	11:00	10488	UK
21.7.93	11:00	10531	UK
31.7.93	23:00	10681	UK
6.8.93	11:00	10760	I
16.8.93	23:00	10910	UK
22.8.93	11:00	10989	UK
4.9.93	23:00	11182	UK
10.9.93	11:00	11261	I

†Data Processed before 8.4.93.

5.2.2 Data Handling Methods

A total of 34 SAR images were acquired at intervals throughout the ERS-1 mission and, although mainly supplied by the UK-PAF, data have also been received from the Italian and German PAFs. Inconsistencies between the PAFs in the processing of the PRI.SAR product have added to various practical problems associated with reading the data. The Committee on Earth Observation Satellites (CEOS) designed a uniform header format for the provision of imaging specifications and calibration parameters. Although the general format is observed, account must be taken of variations in implementation between the PAFs.

A PRI.SAR product consists of 131 megabytes (MB) of 16-bit binary data plus a CEOS header containing standardised information about each image. To read images this size requires dedicated disk space. The first task was to reduce the data to 8-bit, a format compatible with image processing systems, enabling the images to be studied and areas of interest extracted.

5.2.2.1 Data Compression

Compression of the data to 8-bit was carried out to assist data handling in terms of disk space, memory capabilities and screen display. To avoid loss of information the dynamic range, mean and noise within the 16-bit data were studied for the maximum wind speed (17.5 ms^{-1}), moderate and low (2.5 ms^{-1}) wind speeds (figure 5.1). Spreads between 10-1500, -1300 and -1150 DN respectively were found. The standard deviation within the data also increased with higher wind speeds suggesting that the high frequency variability is noise related and could be removed.

The routine developed for this study was to block average the data over 2x2 pixels, reducing the pixel size to 25 m, the nominal resolution of the SAR. That there is no significant data loss, just smoothing of spurious points, is apparent from comparisons of statistical results from the raw and compressed data; diffferences in the mean DN values are less than 1 and the standard deviation is reduced (figure 5.1). Reduction of the 16-bit data to 8-bit byte format was then achieved by dividing the values by 6. This contained even the highest values (1500 DN) within the 8-bit range (0-255), with minimal loss of radiometric resolution, whilst ensuring there was no loss of data at the maximum end of the spectrum or spurious points introduced at the low end due to 'wrap round' of the data. The result is a 16MB image that can easily be stored, viewed and efficiently calibrated for derivation of the radar cross section.

5.3 CALIBRATION OF ERS-1 SAR PRI PRODUCTS

For SAR PRI data to be of operational use to the applications scientist it must be possible easily to make quantitative comparisons between pixel values from targets within a single image or with those in another image, irrespective of the range position and different wind conditions. To achieve this the data must be accurately calibrated, by relating image intensity (I) to the radar backscatter cross section coefficient (σ_0), which is scaled logarithmically in dB.

The dependence of the backscatter cross section on incidence angle has been well described for various wind conditions (Jones *et al.*, 1977; and Long, 1985). An empirical model of the relationship was used to determine the effectiveness of the ESA SAR.PRI calibration procedure, comparing the backscatter gradient across the range of the SAR swath with that derived from the model for the relevant wind and SAR look direction. It was demonstrated for the first time that the calibration scheme given by Laur (1992) requires considerable modification. A final correction determined only recently (March 1994) remedies an underestimate in σ_0 for high backscattering regions and is particulary relevant over the oceans (Meadows and Stapleton, 1994). Implementation of the full calibration enabled the quantitative analysis of the images to proceed. The full calibration is not yet published by ESA. The factors additional to the original ESA calibration to be taken into account when calibrating a SAR PRI image are summarised below:

- Implementation of an incorrect antenna pattern by UK-PAF on data processed between

1.9.92 and 8.4.93.

- Insufficient range timing information for UK-PAF imagery before April 8th 1993.
- Correction of the calibration constant for power loss effects (Laur *et al.*, 1993).
- Correction of the replica pulse variations (Laur *et al.*, 1993).
- Raw data saturation leading to a σ_0 underestimate across the entire image, particulary over sea (Meadows and Wright, 1994).

These factors have all been accounted for in the calibration of the images used for this work. The following sections describe the status of the radiometric calibration, looking first at the procedures given by ESA and the PAFs. The steps taken to identify a calibration problem and the inclusion of a correction for power loss are then discussed.

5.3.1 The Preliminary ESA Calibration

The SAR.PRI backscatter cross section is calibrated with respect to the antenna pattern, the range spreading loss, the incidence angle and the processor dependent calibration constant using the procedures described by Laur (1992). The procedures to be applied depend on the SAR processing date, so far three versions of the SAR.PRI product have been released, with slight variations occurring between PAFs. Data processed prior to 1st September 1992 are not corrected for the antenna pattern and only the UK-PAF included a compensation for the range spreading loss. For products processed post 1st September 1992 both corrections were applied. Some UK-PAF images displayed strong intensity variations in the range direction of up to 3.5dB and investigations showed the antenna elevation pattern was applied incorrectly, the problem being caused because the definition of the antenna boresight assumed a nominal earth radius and satellite altitude. This caused an offset of the antenna pattern from its correct position across track, producing the intensity fluctuations across the range. The corrections required for imagery processed up to 8th April 1993 are described by the UK-PAF ERS-1.SAR.PRI

Health Report (1993). Subsequent SAR.PRI products contain the correct antenna pattern and range spreading loss corrections. That the antenna pattern is now implemented correctly was confirmed by a study carried out by DRA, the sinusoidal variation caused by the incorrect elevation pattern has been completely removed (Hutchins, 1994).

The following sections describe the relationship between image intensity and the backscattering coefficient (σ_0), according to Laur (1992) and outline the basic parameters required to calculate a local σ_0. A summary is given of the derivation of the calibration constant (K), including the updated version, and the range spreading loss and antenna corrections applied by the PAF's to the PRI product. Corrections applied to data processed before 8th April 1993 are included in these sections. Figure 5.2 illustrates the importance of the different corrections on the backscatter across range for a SAR image acquired on 24.1.93. Where the antenna pattern was incorrectly implemented corrections may be up to ± 2 dB and power losses can be in the order of 3 dB; the total effect of these corrections is shown by the bold line in the final plot.

5.3.2.1 Derivation of the Backscattering Coefficient

The derivation of the backscattering coefficient is given by Laur (1992). In simple terms:

$$\langle I \rangle = K \, . \, \sigma_0$$

where:

$\langle I \rangle$ = average pixel intensity measurements
σ_0 = backscattering coefficient of the distributed target
K = the constant of proportionality or the calibration constant

K is dependent on incidence angle and ESA determine K at a reference incidence angle of 23°: $K = K(\alpha_{ref} = 23°)$

To determine a local $K(\alpha)$: $$K(\alpha) = K \, . \, \frac{\sin \alpha_{ref}}{\sin \alpha}$$

The local incidence angle at pixel n is determined using the SAR viewing geometry as derived by Laur (1992):

$$\cos \alpha_n = \frac{(R_T+h)^2 - R_n^2 - R_T^2}{2R_n . R_T}$$

Figure 5.3 The SAR viewing geometry

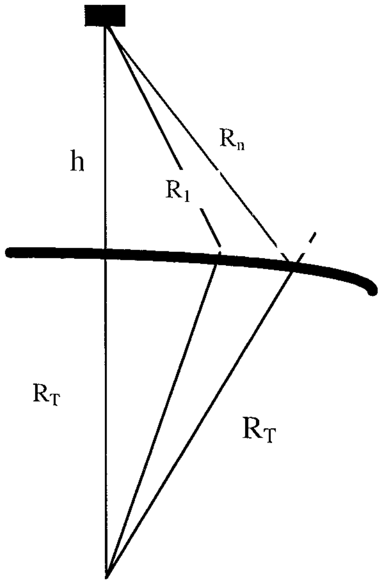

Calculating this parameter requires an accurate derivation of the satellite altitude (h), local earth radius (R_T) and the local slant range (R_n) using the following parameters from the CEOS header:

The geodetic latitude, λ, of the image centre at mid-azimuth is used to calculate R_T.

- The zero-doppler range time, t_1, of the first range pixel (the value lies between 5500×10^{-6} and 5550×10^{-6} seconds) and is used to calculate R_1.

- The incidence angle, α_1, of the first range pixel at mid-azimuth (values lie between 19.2° and 19.8°) is used with R_T and R_1 to determine h.

These values are found in the CEOS header file, exact positions are given in the ESA format document.

For images processed before 8.4.93 the zero-doppler range time is coded into the header in seconds (not nanoseconds as it is now) and is not sufficiently accurate to determine the satellite altitude for the calibration of the radar backscatter cross section. It is recommended that the 4th orbit state vector position (in the leader file) is used to calculate the altitude according to Meadows (UK-PAF Health Report, April 1993).

To determine the backscattering coefficient (σ_0) of an area located at incidence angle α_n:

$$\sigma_0 = \frac{<I>}{K(\alpha_n)} = \frac{<I>}{K} \cdot \frac{\sin \alpha_n}{\sin \alpha_{ref}}$$

The mean intensity (<I>) is directly proportional to the sum of the digital numbers (DN) squared for given pixels in the image:

$$<I> = \frac{1}{N} . \Sigma DN^2$$

N is the number of pixels sampled, which for statistical validity, should be sufficiently large for the coefficient of variance to be less than 0.34, indicating a homogeneous sample.

<I> should be derived by summing the squares of the individual points and then taking the average DN square. For this work 25 m resolution pixels are averaged in blocks of 5 x 5 to 125 x 125 m resolution and the mean value squared to calculate <I>. This technique is intended not only to reduce speckle effects in the image but also to simplify the programming methods and reduce processing time. Variance within the image produces an estimated error of +8% (0.4dB) using this technique (Meadows, pers. comm.) and is compensated for in the final stage of the calibration program.

To express backscatter in decibels (dB):

$$\sigma_{0\,(dB)} = (10.\log_{10}\langle I\rangle) - (10.\log_{10} K) + (10.\log_{10}(\sin \alpha / \sin \alpha_{ref}))$$

or: $$\sigma_{0\,(dB)} = \langle I\rangle_{(dB)} - K_{(dB)} + \beta_{(dB)}$$

where: $$\beta_{(dB)} = 10.\log_{10}(\sin \alpha / \sin \alpha_{ref})$$

In PRI images the range of incidence angles (α) is roughly 19.5 to 26.6°, the correction factor β can vary from -0.7 to + 0.6 dB across the image swath.

These formulae assume that the PRI products are corrected for the SAR antenna pattern and the range spreading loss. SAR images used in this study were all collected after 1.9.92 and therefore include these corrections, but data processed between 1.9.92 and 8.4.93 must be corrected for the anomalous antenna pattern before deriving σ_0 (§ 5.3.2.4).

5.3.2.2 The Calibration Constant

The derivation of a calibration constant for the SAR is performed by comparing radar cross section returns with the nominal cross section of a corner reflector or transponder. For ERS-1 SAR transponder 2 deployed by ESA in Flevoland, Netherlands was used for this purpose (Meadows, 1993). The calibration constant is only valid for one specific product (such as the PRI) and one specific SAR processor (eg. the UK-PAF), the different gains of the PAFs resulting in different K values. The K values for the different PAFs are provided by ESA. The constant was recently updated after the discovery of a power loss for the transponder caused by raw data saturation of the Analogue to Digital Converter (ADC) for higher backscattering targets. The correction applied to K is 0.39dB (Laur *et al.*, 1993).

$$\text{Kupdated (Ku)} = K + 0.39 \text{ dB}$$

During data acquistition for this study ERS-1 SAR maintained high radiometric stability and the calibration constant remained the same from the 5th September 1991 to the end of September 1993 (Laur *et al.*, 1993). The radiometric stability is defined as the standard deviation of the (time series) measurements of the radar cross section of a calibration target (using the same calibration constant). Once all corrections are included the stability measured over the past two years is about 0.22dB.

5.3.2.3 The Range Spreading Loss

The range spreading loss accounts for power attenuation, which increases with distance from the satellite. Excepting the UK-PAF, images processed before 1.9.92 do not include the correction:

Range spreading loss, $\Omega_{(dB)} = 10.\log_{10} (R^3/R^3_{ref})$

where:

R = slant range distance at the target location and is derived geometrically, and

R_{ref} = reference slant range distance at mid swath (23°), R_{ref} = 847.0km.

Slant range values (R) are from 825km near range to 871km far range and the correction factor can vary from -0.3dB to +0.4dB across the image swath (figure 5.2c).

5.3.2.4 The Antenna Pattern

Research carried out at ESRIN, ESA estimated the ERS-1 in-flight antenna pattern using images of the Amazon rain forest, assuming the region to have a uniform backscatter. For data processed prior to 8.4.93 at the UK-PAF the antenna pattern was applied incorrectly, assuming a nominal earth radius and satellite alititude. The corrections for this are tabulated in the UK-PAF Health report (1993) for the 3-day and 35-day repeat cycle in terms of the latitude at which the image was acquired and the look angle in degrees. Figure 5.2 shows the correct elevation pattern (a) and the correction to be applied to images acquired before 8th April 1993 (b). Images for this study were acquired around latitude 50° North and during the three day repeat the error in the antenna pattern was minimal, varying from -0.01dB in the near range to +0.01 in the far range, and can be ignored. In contrast, during the 35-day repeat phase the antenna mispointing was much more severe at mid latitudes, with a look angle error of 1.057° compared to -0.007° during the 3-day phase. The corresponding corrections are significant varying from +1.85 to -1.94 dB. Corrections were derived from the tables using linear interpolation for the local look angle at the target pixel. The correction is added to the deduced radar cross section.

5.4 MODIFICATION OF THE CALIBRATION

5.4.1 Identifying a Calibration Problem

To enable a thorough assessment of the ESA calibration, ' range profiles' taken across the entire 100 km SAR swath were examined from 30 overpasses of the English Channel. The backscatter gradient determined across the range of the SAR swath was compared with that derived from a model for the relevant wind and radar look direction. The relationship between backscatter and incidence angle for various wind conditions is given by a wind retrieval model for the ERS-1 scatterometer, known as CMOD4. The model is described fully in Chapter 7. Figure 5.4 illustrates that for the incidence angles 19.5° to 26.5° viewed by ERS-1 SAR, the model predicts a decrease in backscatter of 8.5 to 6 dB from near to far range for 3 to 11 ms^{-1} wind conditions; the smoother the surface (less wind) the greater the backscatter gradient.

The profiles were taken from a region of deeper water to the south of the Isle of Wight, thought to be unaffected by bathymetry or localised strong currents. Hence, assuming a steady wind, the backscatter across range would be expected to be relatively uniform. A 'wide profile' of 8000 x 256 pixels was extracted from each image, spanning the entire range (hence, referred to as range profiles). The data were block averaged 10 x 10 to reduce speckle effects, calibrated according to the ESA procedure and then further averaged over 51 pixels in the azimuth to a single line of data 800 pixels long. The resulting range transect of 800 points describes a 100 km x 6.4 km area across the SAR image. Figure 5.5 displays the range profiles of the backscatter (dotted lines) superimposed on the CMOD4 lines, which predict σ_0 dependence on incidence angle (straight lines). A flattening of the measured backscatter profiles from mid to near range is clearly apparent, the SAR values falling below the prediction lines by at least 1 dB. The shallowest range gradient (2 dB across the entire swath) was observed on 24.1.93, suggesting the problem is greatest for images acquired in high wind conditions (11 ms^{-1}). The consistency of the problem over the relatively large number of images analysed, all for approximately the same region but for varied wind and tide conditions, meant the shallow backscatter gradients could not be dismissed as natural variation in the sea surface or wind field as suggested by earlier researchers.

The origin of the problem was initially unclear. Consultation with the UK-PAF and the ERS-1 SAR calibration and validation team at Marconi Research Centre (MRC) revealed the problem of inaccuracies in the replica pulse and later power losses in the raw data caused by saturation of the Analogue to Digital Converter (ADC). The latter effect is particularly relevant to data collected over the oceans. The errors are consistent with saturation of the ADC, producing a power loss in the raw data, particularly in the near range. The importance of power losses at higher backscattering levels (>-7 dB) is most clearly illustrated by the extract from 24.1.93, referred to above. Although the power loss appears to be the most significant correction for the data used in this study, at certain times in the lifetime of ERS-1 replica pulse errors could be greater than 1dB (Laur *et al.*, 1993). Both corrections are discussed in detail in the following sections.

5.4.2 The Replica Pulse Correction

Problems encountered in the implementation of the replica pulse within PAF SAR processors were reported by Laur *et al.* (1993). The replica pulse is an internal calibration parameter and is a copy of the SAR pulses, which is transmitted to ground with the raw data. The replica pulse is intended to compensate for drift of the SAR system during the imaging sequence. The assumption was made that the power of the replica pulse is directly proportional to the transmitted pulse power, unfortunately this is not the case (Smith *et al.*, 1994). Consequently the replica pulse variations introduced by the SAR processors, which vary depending on the PAF, need to be removed. This correction is achieved by comparison of the replica pulse power used to generate the image (available in the CEOS leader file) with the value used to generate the reference image of Flevoland from which the calibration constant was derived. Quality checking of the data has now been implemented at the UK-PAF since April 1993 and at the D-PAF since May 1993.

$$\text{Replica Pulse correction} = \frac{\text{image replica power}}{\text{reference replica power}}$$

The reference replica power is 205229.

5.4.3 The ADC Power Loss

Power losses were first recognised from their influence on the ESA transponder measurements (Meadows, 1993). That power losses would occur was predicted before ERS-1 was launched (Lancashire, 1987), but it is only recently that the extent of the problem has been identified, a higher SAR gain being used than originally envisaged. The research was performed at MRC for the Defence Research Agency (DRA) by Meadows and Wright (1994) and is summarised by Hutchins (1994). Power losses in the raw data are reflected in a corresponding image power loss. It is estimated that approximately 40% of ERS-1 SAR images will have an image power loss of greater than 0.5 dB (and up to 2 dB). The problem is most significant for regions having a high backscattering level, such as images covering areas of ocean and certain snow covered regions and increases near range. For comparisons of radar cross section measurements from a coastal region, such as the Isle of Wight, the calibration procedure must therefore include corrections for power losses; in high winds the effect will be particularly severe. These findings have yet to be published by ESA as part of the calibration procedure, but have been reported at the EARSeL Symposium on Sensors and Environmental Applications, June 1994, by P. Meadows.

The investigation of the power loss is based on ERS-1 SAR raw data. The SAR raw analogue data are quantitised to 5-bits within the ADC. The distribution is expected to fit a Gaussian curve which should be presevered when the data are transformed to a digital image. If the input signal level to the ADC is high, a large number of values will occupy the lowest and highest quantisation levels, thus saturating the instrument. Saturation of the ADC results in a lower output power than the input power (ie. there is a power loss). An indication of power loss is given by the I or Q channel STD value in the CEOS header. If the STD is between 2 and 6 the power change produced by the ADC is small (<0.1 dB). For higher STDs there is significant power loss. The header value is an average for the whole scene and may be misleading where land as well as sea occurs in an image. Hence, all images analysed in this study are investigated for power losses. Losses tend to be greatest in the near range, the backscattering being higher as a result of the radar dependence on incidence angle.

Ideally, to derive an accurate ADC power loss for the PRI image the corresponding raw SAR product should be examined. However, transformations from image locations to the corresponding raw data block are complex. Combine this with the additional burden of increased data distribution by the ground segment and such a procedure is seen to be impractical. Instead it is recomended by Meadows (pers comm. 1994) that the power loss be estimated directly from the PRI product. This involves simulating the raw data by removal of the antenna pattern and range spreading loss corrections from the PRI image. Estimates of the raw radar cross-section used for the calculation of power loss are then made from blocks of approximately 5km in azimuth and 15km in range, equivalent in size to the instantaneous field of view (IFOV) of the raw SAR footprint. Table 5.2 gives the power loss as a function of PRI Intensity/K_{ref} rather than radar cross section. Linear interpolation or extrapolation can be used to determine the power loss in dB, which is then added to the calculated radar cross section. It is estimated that power loss derived from the SAR.PRI compared to values from the raw SAR data differ by less than 0.25 dB (Peter Meadows, pers comm.). Figure 5.5 illustrates the difference in gradient across the range profile between the full calibration accounting for power loss (solid line) and the recommended ESA calibration (dotted line), for a number of images acquired in varied wind conditions. All the images suffer power losses to some degree and in most cases the effect extends across the entire range.

Table 5.2 Predicted power loss (dB) as a function of PRI intensity/K:

PRI / K_{ref} (dB)	Power Loss (dB)
-2.63	3.41
-4.21	1.43
-5.09	0.80
-6.32	0.45
-7.17	0.23
-8.25	0.09
-9.82	0.01
-20.18	-0.06

5.5 THE FULL CALIBRATION

The full calibration expression for the derivation of the backscattering cross section (σ_0) from a SAR.PRI image of an area located at incidence angle, α, includes corrections for the replica pulse power and the power loss:

$$\sigma_{0(dB)} = \langle I \rangle_{(dB)} - K_{(dB)} + \beta + \text{replica pulse correction}_{(dB)} + \text{power loss}_{(dB)}$$

The ADC power loss corrections implemented in the revised calibration procedure are illustrated by the example in figure 5.2 for the image from 24.1.93. Curve (i) in figure 5.2(f) gives the backscatter range profile according to the standard ESA calibration. The corrections for the antenna pattern (a) and range spreading loss (c) are incorporated in the SAR.PRI product and must be removed from (i) in order to recover the original raw power (curve (ii) in (f)). Figure 5.2(d) shows the relationship (table 5.2) between power loss and raw image intensity, which is applied to the raw power (ii) to derive the corresponding power loss in dB shown by (e). The final range profile (iii) results from adding the power loss to (i). For data processed before 8.4.93 figure 5.2(b) replaces (a) for the removal of the antenna pattern.

That the radar image cannot be examined, even in terms of relative differences, without first calibrating the data is demonstrated by comparison of the histograms for an extract taken directly from the image of DN values with the fully corrected σ_0 values. Figure 5.6 shows how the distribution and shape of the histogram changes once the data are calibrated, from being slightly biased towards the high end, to having a normal distribution with more values in the high ranges.

5.6 CONFIDENCE IN THE IMPROVED CALIBRATION

The improved calibration procedure was applied to the range profiles for all 30 images, as shown in figure 5.7. The approximate wind speed derived from the synoptic meteorological charts, indicated above each figure, shows the wide range of wind conditions sampled. Correcting for power losses has significantly improved the relationship between SAR measured backscatter (bold line) and the model estimates for given wind conditions. Confidence in the full calibration is increased by the close conformation of the slope of the range profile with the CMOD4 gradients. This is particularly well illustrated by range profiles for 24.1.93, 12.2.93, 28.2.93, 9.5.93 and 22.8.93 for wind conditions of 5 to 11 ms^{-1}. Where calm conditions occur the recovered backscatter magnitude is below the noise threshold for the SAR (-25 dB), as shown by profiles for 19.3.93, 3.5.93 and 7.6.93. The highest winds in the sequence occurred on 13.3.92 when meteorological charts recorded 17 ms^{-1}. This maximum value is reached in part of the image whereas, prior to implementing the revised calibration, the maximum wind speed estimated from the SAR data was 12 ms^{-1}. Deviations from the CMOD4 predictions can be credited to natural variations in the wind field caused for example by orographic effects or atmospheric fronts. High frequency variations in σ_0 may be due to sea surface dynamical processes, but do not influence the overall trend of the profile. Where the profile crosses land (Isle of Wight) it is labelled on the figures.

5.7 CONCULSION

The SAR.PRI product was intended to give the end user easy access to quantitative measurements of surface roughness. However, to achieve a satisfactory calibration of the images is a complex and time consuming process, requiring substantial data manipulation to determine the power loss. Confidence that the calibration is now fully implemented is demonstrated by the linear dependence of measured backscatter on incidence angle, closely corresponding to the CMOD4 predictions. The uniformity of the wind, in many cases over distances of 25 km or more, is the factor which enables this approach to be used for testing the variation of σ_0 across range. Backscatter estimates derived from the SAR images can now be considered as reliable estimates, enabling comparisons of relative changes in surface roughness across features within or between images to be made. Absolute σ_0 values associated with specific features cannot be compared unless they are in the same range positon, due to the natural variation in backscatter with incidence angle. Once calibrated the SAR is a robust instrument, having maintained a radiometric stability of 0.22 dB since its launch (Meadows and Wright, 1994) and in this respect is highly suited to multi-temporal and spatially comparitive type studies.

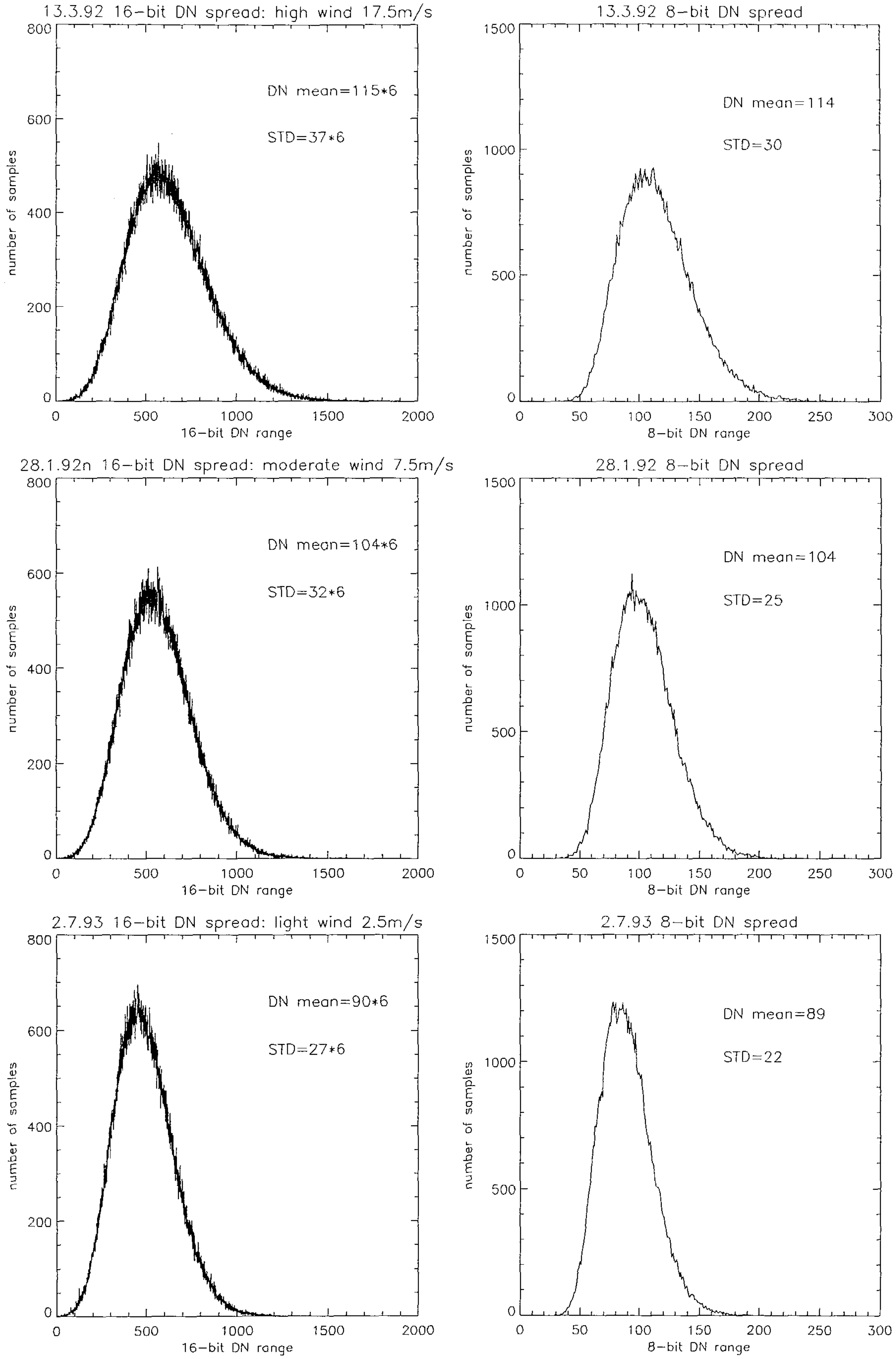

Figure 5.1 Histograms showing the data distribution for 16- and 8-bit data. Examples are given for high, moderate and low wind speeds, demonstrating the minimum and maximum spread of the 16-bit data and the preservation of the shape and mean data values once the data are transformed to 8-bit.

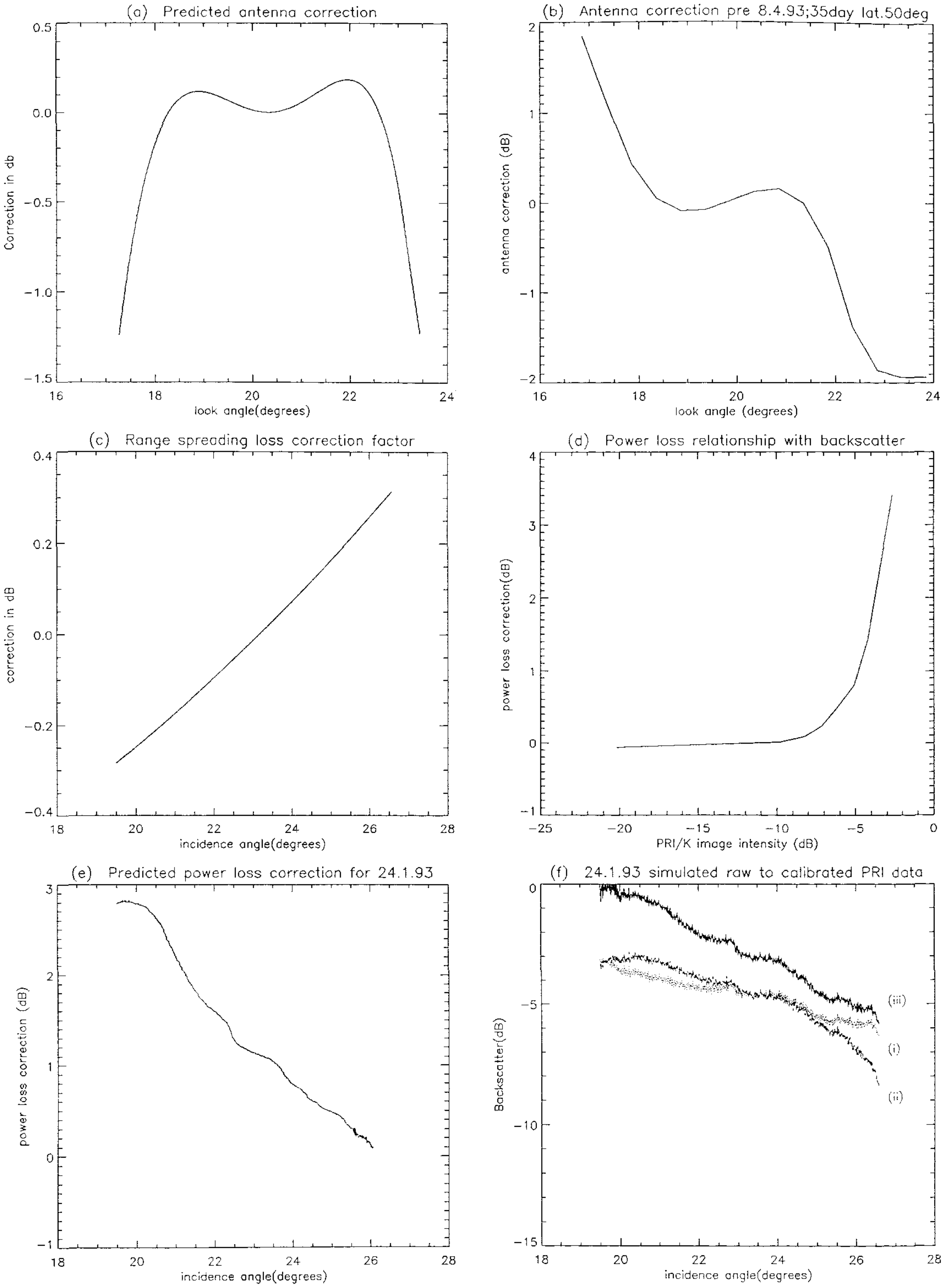

Figure 5.2 The corrections required to fully calibrate ERS-1 SAR data. Examples based on the 24.1.93 image, which required: the antenna pattern correcting from (b) to (a); the removal of the range spreading loss correction (c) and antenna pattern to calculate the power loss (e) using curve (d); giving the backscatter profiles across range for the ESA calibration (i), simulated raw power (ii) and full calibration (iii).

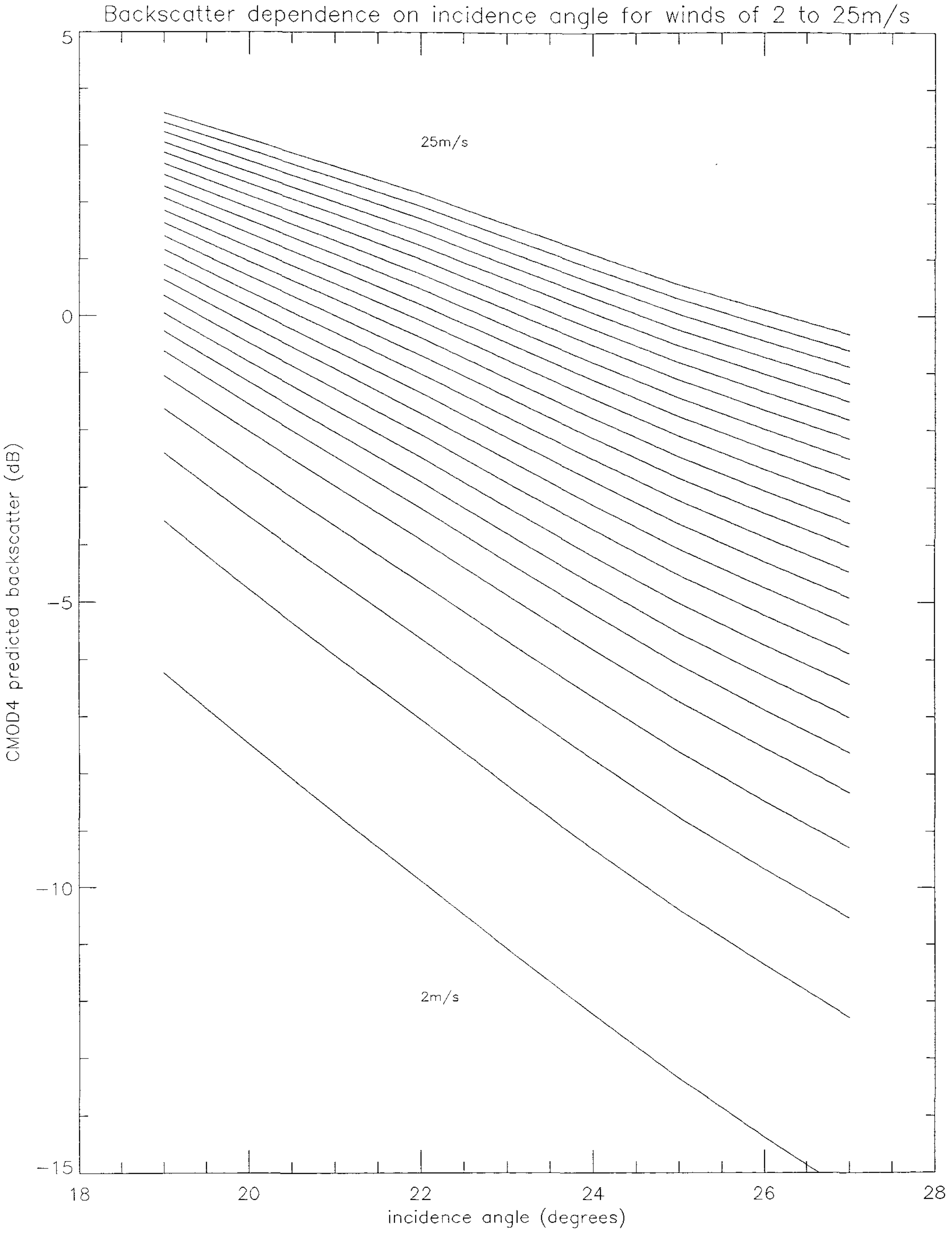

Figure 5.4 Predicted backscatter dependence on incidence angle.
Derived using CMOD4 for upwind (0°) viewing geometry and wind speeds ranging from 2 to 25 ms^{-1}.

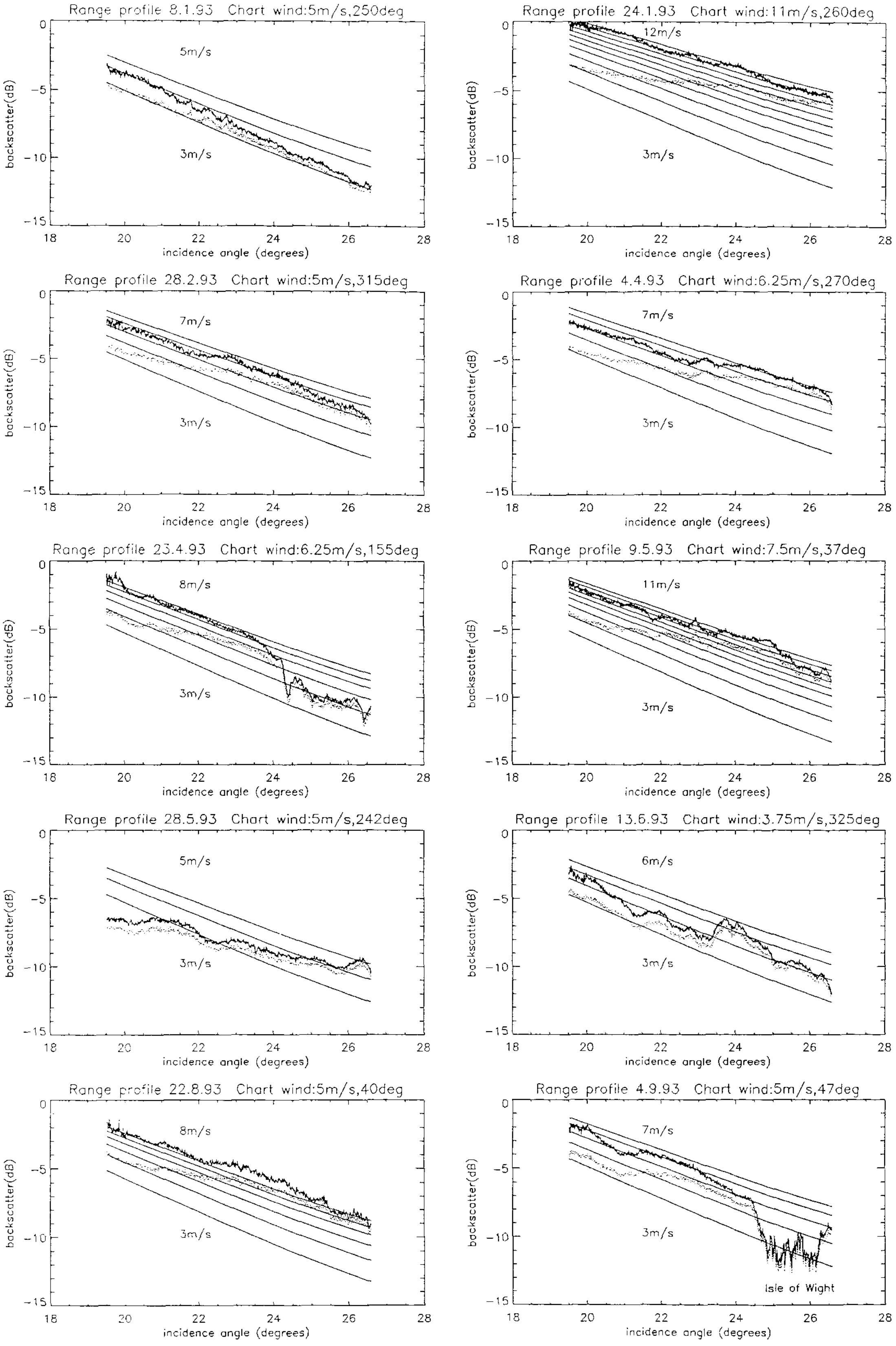

Figure 5.5 Comparison of ESA calibration and full calibration including power loss. Examples of backscatter values taken across the entire SAR range for varied wind conditions: the dotted lines demonstrate the results achieved using the ESA calibration routine and the bold lines the improved results obtained by including the ADC power loss in the procedure. The data are overlain on the CMOD4 predicted backscatter values (straight lines) for the specific imaging conditions for each image.

(a) Distribution of uncalibrated DN values

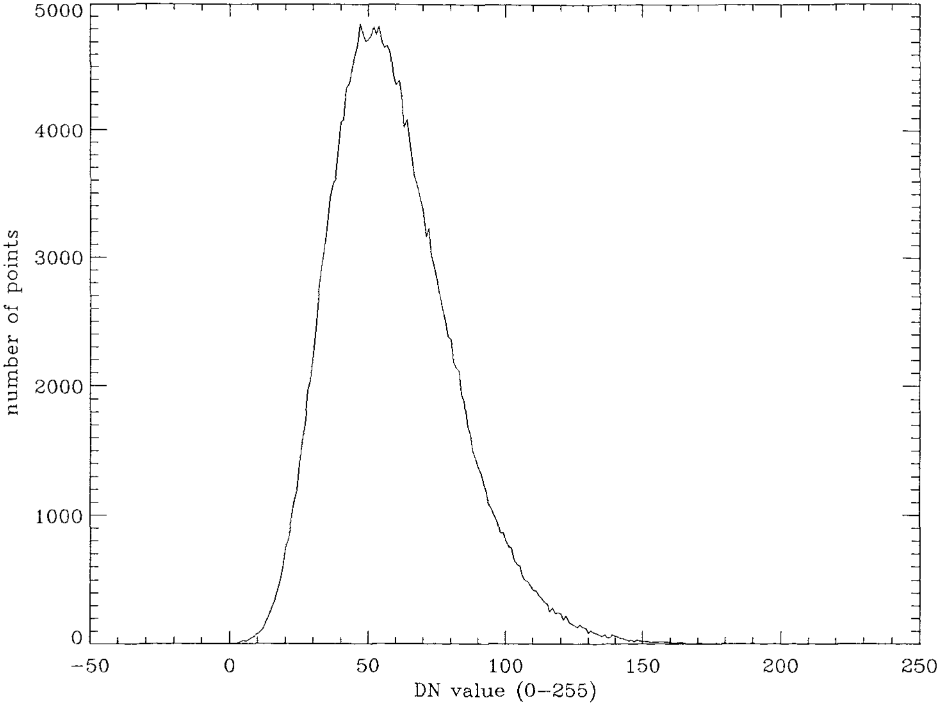

(b) Distribution of fully calibrated log dB values

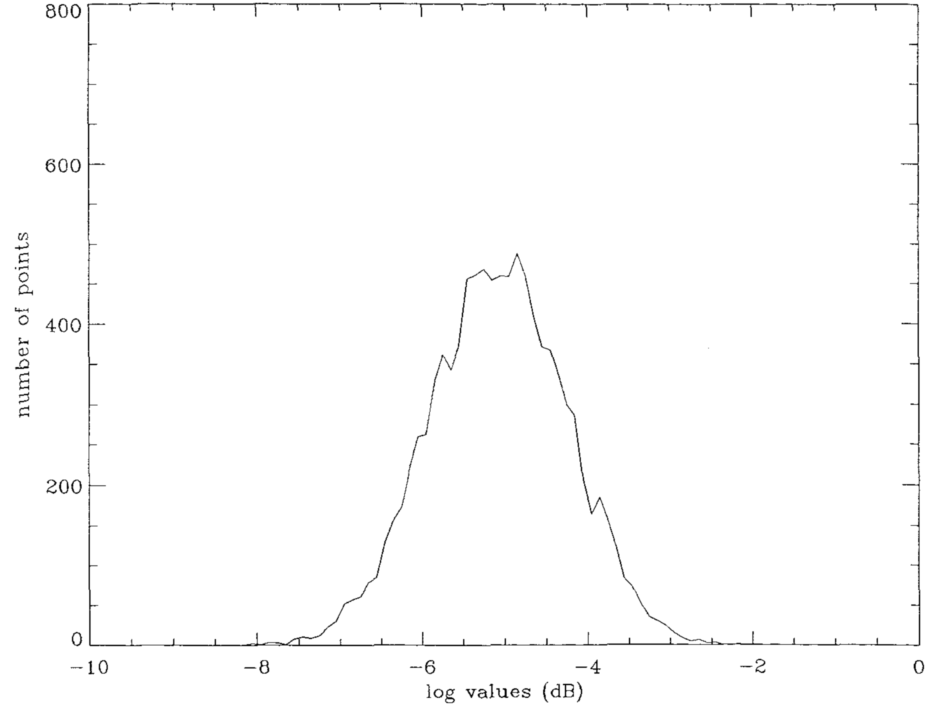

Figure 5.6 Data distribution for uncalibrated DN and calibrated dB values.

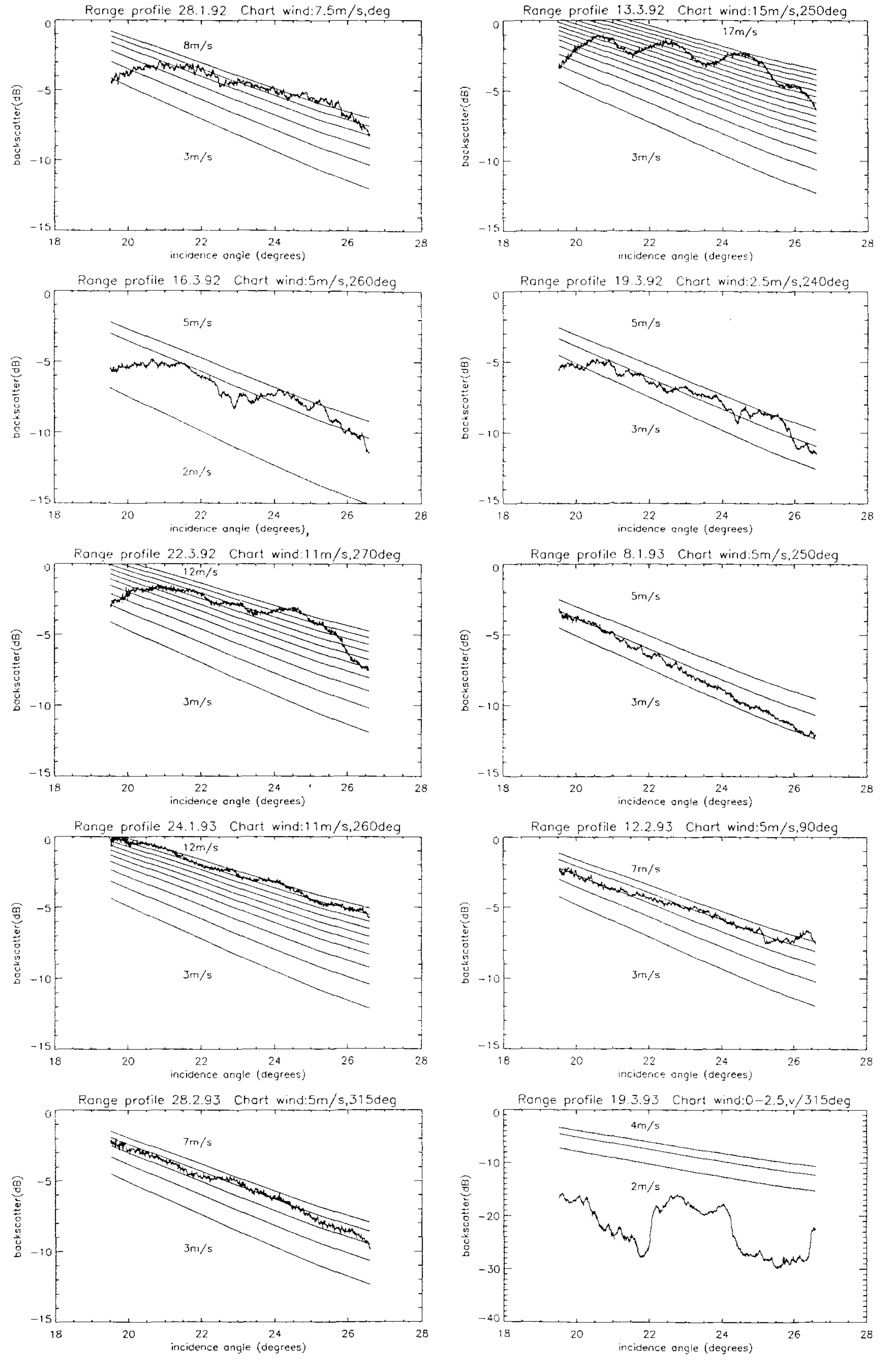

Figure 5.7 Fully calibrated backscatter profiles across range for all the images. Bold line denotes the backscatter profile, overlain on the CMOD4 predicted backscatter values (straight lines) for the specific imaging conditions for each image. The wind speed and direction taken from the meteorological synoptic charts are given for each profile.

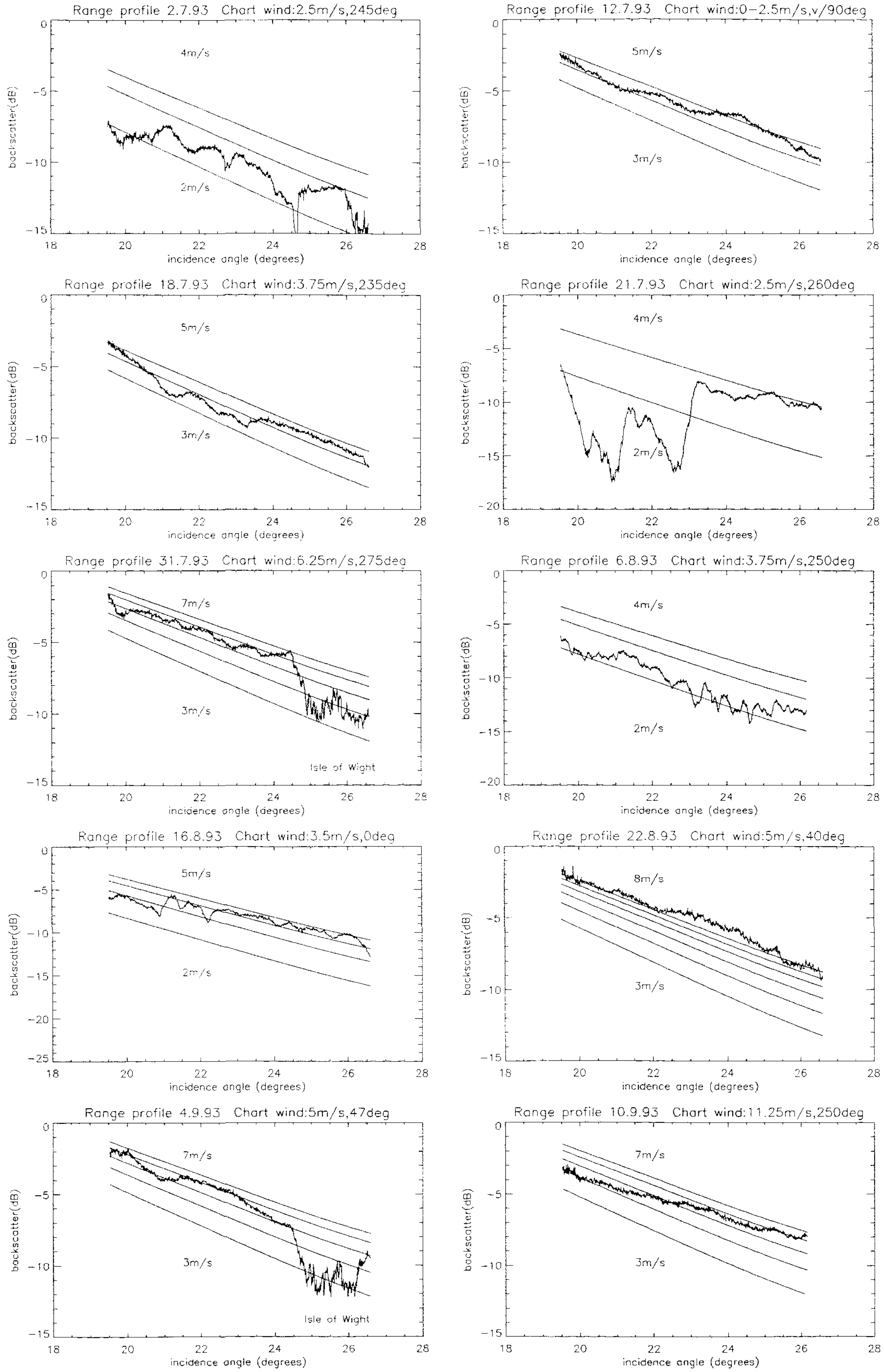

Range profile 2.7.93 Chart wind:2.5m/s,245deg

Range profile 12.7.93 Chart wind:0–2.5m/s,v/90deg

Range profile 18.7.93 Chart wind:3.75m/s,235deg

Range profile 21.7.93 Chart wind:2.5m/s,260deg

Range profile 31.7.93 Chart wind:6.25m/s,275deg

Range profile 6.8.93 Chart wind:3.75m/s,250deg

Range profile 16.8.93 Chart wind:3.5m/s,0deg

Range profile 22.8.93 Chart wind:5m/s,40deg

Range profile 4.9.93 Chart wind:5m/s,47deg

Range profile 10.9.93 Chart wind:11.25m/s,250deg

Figure 5.7 (cont.)

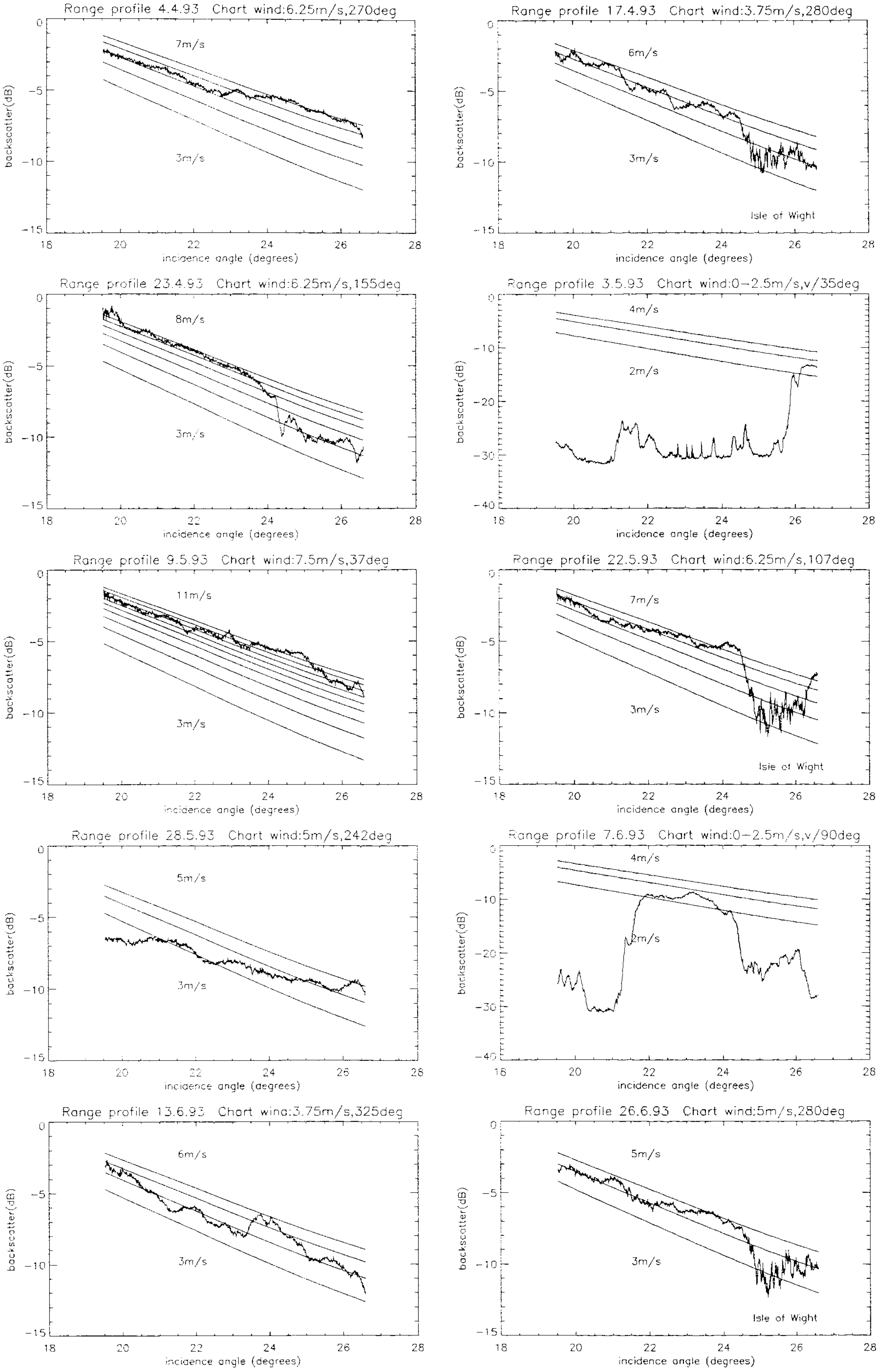

Figure 5.7 (cont.)

CHAPTER SIX

PRELIMINARY ANALYSIS OF THE ERS-1 SAR IMAGES

6.1 INTRODUCTION

The broad overview of oceanographic features associated with a surface roughness signature obtained using Seasat SAR, combined with the results from a detailed study of a SST front using the ATTA, has clearly demonstrated the potential of using SAR data for coastal oceanography. The successful acquisition of data from ERS-1 SAR provided the opportunity to repeatedly cover an area, enabling comparisons of relative changes in the backscatter signatures across specific features to be made. This chapter continues with the qualitative analysis of the images begun using Seasat, assessing the capabilities of a SAR to detect dynamic oceanographic features in the coastal environment, such as frontal boundaries and bathymetry. The aim was to characterise the surface roughness signatures associated with features and to determine the factors affecting their detection by SAR. To achieve this it was planned to undertake a series of contemporaneous SAR and *in situ* experiments during the data acquisition period.

An initial sequence of 9 images was obtained whilst ERS-1 was in the 3-day repeat phase. It was on the basis of the preliminary analysis of these data that the acquistion of a further series of 25 images and the experimental fieldwork programme were planned. In this manner a systematic study of dynamic features over varied wind and tide conditions was achieved. The region investigated is roughly defined as the area between Portsmouth and Anvil Point, but the study concentrates on the area to the west of the Isle of Wight. Figure 6.1 outlines the overall study area and the region identified for a more intensive analysis of the SAR and *in situ* experimental work. The headlands, bays and bathymetric features referred to throughout the chapter are marked.

To view the images the data have been reduced to 8-bit and block averaged to 25 m resolution as described in Chapter 5. This sufficiently reduces the speckle without any significant loss of resolution, which is an essential requirement of feature mapping. In order to display the images for presentation in this chapter the data are further averaged to 200 x 200 m pixels, enabling the entire 100 x 100 km area imaged to be displayed. Where higher resolution extracts are included the plate caption states the pixel size and the distance spanned.

6.2 PRELIMINARY ANALYSIS OF THE FIRST ERS-1 SAR IMAGES

The work described here is based on 9 ERS-1 SAR images of the south coast of Britain, covering an area centred on the Isle of Wight (figure 6.1). The data were acquired during the satellite's 3-day repeat phases from September 1991 to March 1992 (table 6.1). The wind and tide conditions at the time of the SAR pass are also recorded. The aim of this preliminary analysis was to identify any dynamic oceanographic features of interest which have been imaged, to provide the subject for a more detailed, multi-temporal study, combining information from *in situ* studies with SAR data. Similarities in any backscatter patterns between images are of particular interest, the object being to investigate the repeat detection of features. To aid interpretation of the SAR data, AVHRR IR images were acquired throughout the study period. Of these, only 5 were sufficiently cloud clear to provide an indication of the SST structure in the study region (table 6.1).

The analysis of the Seasat SAR images showed a possible frontal boundary occurring to the west of the Isle of Wight; the potential for detecting coastal frontal boundaries using SAR data is of particular interest. Changes in surface roughness observed on the images, such as large scale tonal variations in backscatter, or line features, were compared with the SST boundaries observed on AVHRR infra red (IR) images. The criteria used to define the backscatter signatures associated with frontal boundaries are those derived from the analysis of the Seasat SAR data in Chapter 3.

Table 6.1 Summary of first sequence of ERS-1 SAR images and the wind and tide conditions at the time of data acquisition.

Image	Wind at St Catherines Point (also given inshore when differences occur)		Tide		Closest cloud free cover by AVHRR IR
date & time (GMT)	speed (ms^{-1})	direction	+/-HW Dover†	direction & speed at 20m contour*	
3.9.91 22:13	5	NNE	+4:40	0.2 ms^{-1} ebb (possible flooding inshore)	4.9.91
6.9.91 22:13	3	E	+0:40	0.7 ms^{-1} ebb	7.9.91
9.9.91 22:13	5 <3 inshore	E	-1:30	0.4 ms^{-1} flood (weak ebb inshore)	21.11.91
25.1.92 11:00	<1.5	WSW	-4:00	0.7 ms^{-1} flood	24.1.92 (and 6.12.91)
28.1.92 11:00	8 <3 inshore	E	-6:00	0.5 ms^{-1} flood	/
13.3.92 11:00	17 10 inshore	W	+6:00	0.2 ms^{-1} flood	/
16.3.92 11:00	8 <3 inshore	WNW	+2:00	0.8 ms^{-1} ebb	/
19.3.92 11:00	<3	WSW	HW	0.2 ms^{-1} ebb	/
22.3.92 11:00	13 10 inshore	W	-2:00	0.5 ms^{-1} flood	/

* position of tide estimate marked on figure 6.1

† Admiralty Tidal Atlas

Figure 6.2 summarises the varied positions of the SST boundaries derived from the IR data. A thermal gradient was identified on all the available, cloud clear IR images acquired during the SAR survey (table 6.1), approximately following the 20 m contour line across the bay, separating the very shallow inshore waters from the main channel flow. The inshore water appears warmer (darker) and stratified, possibly due to increased freshwater inputs along the coast during winter. This was found to be the case off Cap Gris-Nez, as described in Chapter 4. On two images (4.9.91 and 7.9.91), a plume of warmer water is observed extending out past the Needles and also out from Poole Harbour on the western side of the bay. A distinct sub-region of slightly warmer water is observed on virtually all the thermal imagery, which appears to be confined within Poole Bay by Christchurch Ledge.

Of the 9 SAR passes acquired covering the study region, possible frontal features were identified on 6 of the images and are plotted on figure 6.3. Table 6.2 summarises the backscatter signature, whether it is a line or tonal variation in backscatter, and the position in relation to SST features. The data were acquired as three short series of images, during September 1991, January 1992 and March 1992, which are separated by 3 days. It was hoped that features might be maintained over these periods, enabling some continuity between backscatter signatures to be established. The only instance where some similarity between the surface roughness signatures on two consecutive images occurred, was for the images acquired on 16.3.92 and 19.3.92 (plate 6.1). Both show a large scale variation in backscatter across Christchurch bay, which corresponds to the SST boundaries identified on several of the AVHRR IR images (figure 6.2). On the second day the feature is considerably more extensive, closely matching the SST signatures on 4.9.91, 21.11.91 and 24.1.92. The differences between the images are ascribed to the change in the wind conditions, on 19.3.92 wind speeds of <3 ms^{-1} prevailed throughout the region, conditions which are associated with observations of large scale variations in backscatter across a SST feature (as described in Chapters 2 and 3). In contrast, on 16.3.92 while the chart records winds below 3 ms^{-1} along the coast, offshore they increase to 8 ms^{-1}, which would account for the more uniform surface roughness distribution.

A persistent surface roughness feature was identified on five of the SAR images, defining a distinct boundary, which also approximately follows the 20 m bathymetric contour, east to west across Christchurch and Poole Bays, extending over a distance of 28 km (figure 6.3). The features corresponded closely to the SST margins observed on the IR images acquired during the period of the study and are not attributed to lee shore (sheltering) effects. The IR data obtained only one day before the SAR image for 25.1.92 (plate 6.2) shows the SST boundary to occur in virtually the same position as the line of increased roughness detected by the radar (figures 6.2 and 6.3). Hence, the variations in surface roughness described in table 6.2 are considered to represent a SST and possibly a salinity frontal boundary. Refraction of the swell waves in the region of the line feature on 25.1.92 image suggests that changes in the current regime are also influencing the nature of the boundary.

Table 6.2 Summary of the potential SST frontal features observed during the 3-day repeat survey.

Date	Feature	
	Backscatter signature line/ tonal, bright or dark	Location and correspondence to SST features on the IR images
9.9.91	Tonal signature, darker inshore, increasingly so in Poole Bay (to west).	Main boundary from IOW* to just south of Poole, roughly following the 20 m contour. Darker area in Poole Bay limited by CCL†. Boundaries correspond to observations from IR images: 4.9.91; 21.11.91; 6.12.91.
25.1.92	Strong line feature, bright to east and dark to west. Tonal variation, slightly darker inshore of line and very dark zone in Poole Bay.	Line feature extends from IOW west to Anvil Point. Slight decrease in backscatter inshore to west. Dark region confined to west in Poole Bay by CCL. Line boudary matches closely the IR image 24.1.92 indicating colder region of water inshore.
13.3.92	Large tonal variation - very bright inshore with darker region along boundary.	Extends from IOW to Anvil Point. Very similar to SST boundaries on 21.11.91 and 6.12.91 IR images.
16.3.92	Tonal variation - darker region inshore.	Feature mainly confined to Poole Bay, a few filaments extending east of CCL. Similar to several of IR images showing warmer water in Poole Bay.
19.3.92	Large tonal variation - darker water inshore.	Extends furthest offshore to east, along the coast of the IOW, then trends inshore and westwards to Anvil Point. Very similar to SST trends on 21.11.91 and 6.12.91
22.3.92	Large tonal variation - very bright inshore with darker region along boundary.	Extends from IOW to Anvil Point. Very similar to SST boundaries on 21.11.91 and 6.12.91 IR images.

*IOW = Isle of Wight
†CCL = Christchurch Ledge

The shape, position and surface roughness signature of the boundary vary considerably, from a curved line on the 25.1.92 image, a filamentatous tonal variation on the 19.3.92 image, to a much flatter boundary on the 13.3.92 and 22.3.92 images (plates 6.2, 6.1 and 6.3a,b respectively). The differences observed in the shape of the feature can be associated with changes in the wind conditions, since the margin persists over varied tidal states between 0.2 and 0.8 ms^{-1}, for both ebb and flood currents. The idea is reinforced by Salomon's (1991) numerical model of tidal trajectories in the English Channel. This predicts that in light wind conditions a tracer would follow a curved path across the bay, but in stronger wind conditions (independent of wind direction) the trajectories are much flatter; this is very similar to the differences detected on the SAR images.

On four of the images the frontal zone is defined by a large tonal variation in backscatter, the inshore water appearing relatively dark (smoother). Considering these images were acquired in light wind conditions the differences might be attributed to instabilities in the ABL causing a slight increase in the surface wind stress. However, the thermal imagery show that it is the inshore waters that are warmer and another mechanism must be sought to explain the surface roughness patterns. Given the light wind conditions, it is possible that the riverine inputs contain sufficient slick-like material to dampen the short waves detectable by SAR. That this is a potential mechanism is reinforced by the separate region of smooth water (darker) that persists within Poole Bay on several images and the distinct narrow darker bands observed extending up to 7 km offshore along both the mainland and Isle of Wight coasts (9.9.91 and 16.3.91, plates 6.4 and 6.1); both features are consistent with the effects of freshwater runnoff from the land. The effects of riverine inputs were also used to explain the region of dark water associated with the Somme river plume, which was detected on a SLAR image also acquired in light wind conditions (described in Chapter 4).

Although the very bright regions observed on the images for 13.3.92 and 22.3.92 are the product of wind effects, it was considered whether the position of the boundary of the feature was influenced by the front. There is no evidence of an atmospheric front crossing the region at the time of either of the images The very bright return inshore cannot easily be explained, the meteorological records at the time of the SAR passes indicate lower winds inshore of around 10 ms^{-1}, compared to up to 17 ms^{-1} offshore. It is possible that funnelling of the winds as they flow off the land may be responsible, although the westerly wind direction does not entirely back this up. Another theory suggested is that the shallower inshore waters are more easily mixed throughout the water column and, are therefore more turbulent, hence the change in roughness in the 20 m depth region (Boxall, pers. comm., 1994). The darker region observed along the entire edge of the zone is also unexplained.

A feature more consistent with expected variations in surface roughness associated with a wind front occurs on the image from 28.1.92 (plate 6.5). Here, the rougher region occurs offshore and there is a gradual decrease in backscatter further inshore, matching the wind speed records (table 6.1). The wind is from the east and the differential sheltering effects of the Isle of Wight and the mainland can clearly be seen in the positions of the distinct graduations in the surface roughness patterns, corresponding to the southern extent of the island and the mouth of the Solent.

6.2.1 Summary of the preliminary ERS-1 SAR data

The synergistic approach to the analysis of the SAR, using SST information from AVHRR IR data aided the interpretation of the surface roughness patterns. The results suggest that on several of the SAR images the backscatter features correspond to a coastal SST front. It was hypothesised that the variation in the small scale surface roughness is an effect of dampening of the short wave field by slick-like material of riverine origin. This is reinforced by observations of lines of smoother water extending out from the coast and adjacent to the coast. To test the theory a field study was proposed, concentrating on the region just south of the Needles, at which point the front appears to curve into the coast and where groundwater inputs are thought to occur.

6.3 ANALYSIS OF CONTEMPORANEOUS ERS-1 SAR AND *IN SITU* DATA

This section presents the fieldwork programme and the results from the comparisons of contemporaneous *in situ* and SAR data. The aim was to obtain quantitative oceanographic information about the features observed on contemporaneous SAR images, in order both to verify features and to improve the understanding of the factors influencing the surface roughness signature. A multi-temporal SAR survey was planned, beginning in January 1993 and ending in September 1993, by the end of which a total of 25 SAR images would be acquired covering the study region to the west of the Isle of Wight (figure 6.1). Although ERS-1 was in the 35-day repeat phase at this time, overlap between swaths at this latitude enabled the area to be covered at intervals varying from 7 to 14 days. During this time a series of *in situ* experiments were planned, in order to cover a range of tide and wind conditions. Throughout the experiment AVHRR IR images were acquired to aid interpretation of the SAR and *in situ* data.

6.3.1 The fieldwork plan

The fieldwork was concentrated on a SST frontal boundary detected just south of the Needles in the preliminary analysis of the ERS-1 SAR and IR imagery (§ 6.2). Six days of fieldwork were planned over a period from 28.5.93 to 10.9.93 (table 6.3). By carrying out the experimental work in spring and summer it was hoped to increase the potential of obtaining concurrent SAR and *in situ* data during light wind conditions, when sea surface warming effects might be expected to result in large scale variations in surface roughness. The sampling procedure and meaurements were therefore also aimed at identifying any frontal boundaries, including the effects of freshwater inputs along the coast for comparison with the backscatter patterns. The analysis of the IR and SAR data in § 6.2 indicated the SST front to be variable in location hence, to improve the sampling on the day of the SAR coverage the area was also surveyed the day before. It was hoped that it would be possible to obtain near-simultaneous *in situ* measurements across a SST boundary at the time of the SAR pass.

To achieve these goals a continuous surface (top 0.5 m) profiling programme was carried out measuring SST and salinity across the study region. Wind speed and direction and humidity measurements were also acquired. Air temperatures were taken to provide an indication of the stability of the ABL, a mechanism often linked to large scale backscatter variations. Sampling was begun 2 hours before the SAR pass and continued for 2 hours afterwards. In this manner, near-simultaneous SAR and *in situ* data could be acquired, in addition to determining the horizontal SST and salinity distributions across the study region on each day. The assumption is made that providing no large scale, sudden change in the atmospheric conditions occur, then comparisons between the spatial SAR data and temporal *in situ* measurements can be made either side of the satellite pass.

Observations of any region of smooth (slick-like) water, rough lines or foam lines were recorded for comparison with the image. Any variations in temperature or salinity across such features was noted. It was intended to take measurements of the water quality within slicks, but sampling techniques available could not offer a continuous measurement method, nor a means of distinguishing whether the material was of riverine origin. The vertical temperature and salinity distribution throughout the water column was investigated at four sites within the study region. The samples were taken inshore and offshore of the SST frontal margin and hence the positions of the stations varied each day. Once SST or salinity gradients of interest had been identified in the early stages of fieldwork it was planned to deploy an Acoustic Doppler Current Profiler (ADCP). The objective was to determine if the front(s) are associated with any convergent or divergent current activity and to provide a quantitative measure for comparison with the SAR data.

The field study was carried out using the Departmental research vessel, the *Bill Conway*, a 12 m launch. This imposed limitations on the study regarding the area sampled (distance offshore) and the weather conditions for sampling (not in winds greater than 8 ms^{-1}). Visual observations of surface roughness variations across the study region were also requested from a Sealink ferry operating in the area on a regular basis from April to September 1993.

6.3.2 Comparing the *in situ* and SAR data

Six days of fieldwork were planned, of which four provided contemporaneous *in situ* and SAR measurements within the study region and provided an indication of the horizontal temperature and salinty distributions. Adverse weather limited observations on 10.9.93 to the Western Solent, but wind speed and direction measurements were measured. Only one day of fieldwork was entirely cancelled. Unfortunately it was not possible to obtain ADCP measurements during the experiment. Table 6.3 summarises the *in situ* measurements made and the main observations, including the information recorded from the Sealink ferry.

Table 6.3 Summary of fieldwork plans, measurements achieved and the main observations.

Date coincident with SAR pass (day before where possible)	Vessel	Measurements *	Main observations
3.5.93	Sealink ferry	visual observations, wsp, wdir, rain	50°.37.2', 1° 37'W wsp ≤ 3 ms^{-1}, wdir 225°, no rain Distinct rough line orientated west to east, slightly rougher to south. Darker water to south of line
28.5.93 (27.5.93)	Bill Conway	SST, S, wsp, wdir, Ta, visual observations 5 vertical dips of T & S‰	27.5.93: SST front 1°C/2km 28.5.93: SST front 0.8°C/2km surface S variations < 0.2 psu vertically homogeneous wsp = 4.6 ms^{-1}, wdir = 210° ABL Neutral
13.6.93	Bill Conway	SST, S, Ta, visual observations, hand held wsp and wdir, 3 vertical dips of T & S	SST front close to Needles 1°C/1km surface S variations < 0.2 psu Several observations of slicks vertically homogeneous wsp ≅ 6-7 ms^{-1}, wdir ≅ 280° ABL Stable
22.6.93 (closest SAR pass 26.6.93)	Sealink ferry	visual observations, wsp, wdir, rain	50°.39', 1° 36'W wsp 3-5 ms^{-1}, wdir 225°, no rain Line of frothy bubbles orientated west to east. No difference either side.
2.7.93 (1.7.93)	Bill Conway	SST, S, wsp, wdir, Ta, visual observations 4 vertical dips of T & S	1.7.93: surface S variations < 0.2 psu slick lines observed SST change 0.5°C at Needles 2.7.93: 0.5 psu change off Needles SST front E-W 0.6°C/2km - begins just south of Freshwater Bay. Lot of slick material observed Thermocline in top 5 m, vertical change of 0.5 offshore and 1°C inshore. wsp = 3.1 ms^{-1}, wdir = 237° ABL stable
6.8.93 (5.8.93)	Bill Conway	SST, S, wsp, wdir, Ta, visual observations 2 vertical dips of T & S	Temperature and S horizontally and vertically homogeneous on both days. (large swell and strong winds all previous week). wsp = 6.8 ms^{-1}, wdir = 242° ABL stable
22.8.93	Bill Conway	/	Cancelled due to adverse weather.
10.9.93	Bill Conway	SST, S, wsp, wdir, Ta, visual observations	Confined to Solent due to adverse weather.

*abbreviations used in table: S = salinity; wsp = wind speed; wdir= wind direction; and Ta = air temperature

The *in situ* observations verified that a weak SST front persists just south of the Needles. Figure 6.4 is a summary map of the results, showing the position and temperature gradient across the frontal boundary for comparison with the SAR images. Changes in SST across the frontal boundary varied, but were in the order of 0.5 to 1°C over a distance of 1 to 2 km. The boundary trended approximately east to west, sometimes extending into the Solent, as on 13.6.93. Differences in the horizontal salinity distribution across the area were slight (< 0.2 psu) on all the days sampled. Generally the region was vertically well mixed throughout the survey period. The exception was on 2.7.93 when a distinct thermocline was found to exist around 4 m depth. This was an exceptionally calm, hot day (wind speed < 3 ms^{-1}) and the effects of solar heating are thought to have increased the SST by 0.5 to the south of the region and 1°C further inshore, weaking the horizontal temperature gradient.

The SAR images showed no evidence of backscatter signatures corresponding to the SST feature. This is consistent with the absence of *in situ* observations of any lines of rougher water or large scale changes in roughness, other than those linked with bathymetry or slick-like features. It was noted that after a period of strong wind conditions, such as occured prior to the fieldwork on 6.8.93, the entire study region became well mixed and any SST structures were broken down. Hence, variations in surface roughness, such as those observed on SAR images for 13.6.93 and 22.8.93 (plates 6.19 and 6.28 respectively), acquired in winds of around 7 and 10 ms^{-1} respectively are unlikely to be associated with an SST front boundary. The light wind conditions at the time of the image on 2.7.93 would have been considered ideal for the detection of a SST feature, however the SAR image does not show any large scale tonal changes in backscatter (plate 6.21).

Two observations of changes in surface roughness in the vicinity of the frontal boundary were made from the Sealink ferry. Both were of line features trending east to west. On the 3.5.93 the distinct rough line appeared to mark a change in roughness between inshore and offshore waters (marked on figure 6.4). A similarly located distinct change in the backscatter pattern (dark to the south and bright to the north), orientated roughly northeast to southwest was observed on the SAR image acquired later on 3.5.93 (plate 6.14). At the time the image was acquired the synoptic chart records winds below 3 ms^{-1} and an unstable MABL. The backscatter signature is characteristic of those associated with SST fronts in these conditions. However, interpretation of the feature is treated with caution; the margin denoting the change in roughness is very straight and the orientation is slightly different to that observed, more closely matching the wind direction. In addition, a similarly orientated backscatter boundary is observed close to the eastern edge of the SAR image, suggesting the features are the effect of local variations in the wind field.

Several slick-like features were observed from the boat on 13.6.93 and 2.7.93, but the surface measurements did not identify any distinct variation in salinity and differences in SST were in the order of 0.03°C, the values decreasing slightly within the slick area. It is probable that the material comprising the slick is only present in the top microlayer and hence, the sampling method employed here would not be an effective means of investigating this material. The features were up to 30 m in width and extended over 100 m or more. Similar slick-like features (dark lines) were detected on SAR images acquired on these days (plates 6.19 and 6.21). On 2.7.93, in calm conditions, the features appeared to be orientated randomly, with narrow lines linking the regions together, whereas, on 13.6.93 the slick-like zones were elongated in the direction of the prevailing wind. Unfortuately the cause of these features was not identified.

Although near-simultaneous *in situ* measurements were obtained for direct comparison with the SAR data and SST frontal boundaries were identified, the experiment was not considered successful as an investigation of frontal features detectable by an imaging radar. What did prove invaluable were the continuous meaurements of wind speed and direction, which enabled comparisons to be made on 3 days between estimates of wind speed derived from the SAR and *in situ* measurements. Analysis of these data is described in Chapter 7.

6.3.3 Recognised limitations of the *in situ* experiment

The main aim of the fieldwork was to combine contemporaneous SAR and *in situ* data to examine a coastal frontal boundary. This could have been achieved more effectively by choosing a well established frontal feature, for which any tidal or seasonal variations in its appearance or extent are well recorded. In addition the feature should be known to be associated with a distinct current gradient across the boundary, which can be measured and compared to the backscatter signature. The fieldwork reported here has demonstrated that it is unlikely that a boundary will be detected by SAR if it is not defined by a distinct surface roughness signature, such as results from convergence or divergence of the surface currents.

The fieldwork plan could also have been improved. It was intended for this work to gradually increase the number of parameters measured *in situ* as successive factors were assessed. However, given the variable weather conditions that occurred during the study this was not a practical approach to undertake, as is demonstrated by the lack of surface current data. The study would have also benefited from a more flexible approach, that is once it became apparent that a frontal boundary was not being detected by the SAR then it might have been wiser to investigate another feature of interest. The acquisition of real time data onboard the vessel would also have been of considerable assistence to the *in situ* survey, enabling specific backscatter features to be investigated.

6.4 QUALITATIVE ANALYSIS OF THE MULT-TEMPORAL SURVEY SAR IMAGES

This section presents a qualititative investigation of all the ERS-1 SAR images acquired between January and September 1993 in a continuation of the work begun using the Seasat SAR. The multi-temporal sequence of data covering virtually the same area offers the opportunity to extend the analysis of backscatter signatures over varied wind and tide conditions. Table 6.4 summarises the wind and tide information at either end of the ERS-1 SAR pass, using the data from the meteorological office synoptic charts and Admiralty Tidal Atlases. Any SST features using AVHRR IR images are also recorded. This section then presents a record of variations in the appearance and detectability of features under specific imaging conditions, providing a basis for the main analysis of the data. The categories, such as bathymetry, frontal boundaries, and criteria defined in Chapter 3 are applied and the results tabulated and discussed in the following sections.

Table 6.4 Summary of multi-temporal ERS-1 SAR survey

Date & Time (GMT)	Wind information from Meteorological Charts west and east extremes imaged		Tidal Conditions at time of image (from Admiralty Tidal Atlas)		AVHRR IR data (where available cloud clear coverage of study region)
	wind speed (ms^{-1}) W-E	wind direction (degrees) W-E	+/- HW Portsmouth (hours)	Ebb/ Flood (tidal state given for Needles)	
8.1.93 11:00	5-5 (inshore 2.5)	250-270	HW -2days springs	begin ebb	
24.1.93 11:00	12.5-10	260-260	-1 springs	end flood (slack)	
12.2.93 11:00	5-5	090-100	-4 +2days springs	strong flood	
28.2.93 11:00	7.5-7.5	315-v	-4 -2days neaps	strong flood	CW† inshore margin S of IOW*
19.3.93 11:00	calm	315-v	+2 +2days neaps	strong ebb	
4.4.93 11:00	7.5-5	270-270	+2 +2days neaps	strong ebb	
17.4.93 23:00	5-2.5	260-315	+2 +1day neaps	strong ebb	
23.4.93 11:00	5-7.5	180-135	-1 springs	end flood (slack)	
3.5.93 23:00	calm	035-v	+2 +3days neaps	strong ebb	4.5.93 (05:11Z) > SST inshore
9.5.93 11:00	10-7.5	040-035	-2:30 +2days springs	weak flood	
22.5.93 23:00	5-7.5	130-085	-1 -2days springs	end flood (slack)	
28.5.93 11:00	5-2.5	225-260	-5:30 -3days neaps	weak flood	
7.6.93 23:00	calm	090-v	-2:30 +2days springs	strong flood	
13.6.93 11:00	5-2.5	280-005	+6 neaps	begin flood	
26.6.93 23:00	5-5	270-290	-5:15 +3days springs	weak flood	
2.7.93 11:00	2.5-2.5	245-245	+1 -3days springs	moderate ebb	E-W SST front as *in situ* result
12.7.93 23:00	2.5-2.5	090-v	-6 -1day neaps	moderate flood	
18.7.93 11:00	5-5 (inshore 2.5)	180-245 (insh.225)	+0:30 +3days neaps	weak ebb	
21.7.93 11:00	2.5-5	260-270			
31.7.93 23:00	5-7.5	280-270	+1 neaps	moderate ebb	
6.8.93 11:00	5-5	250-270	-1:30 +3days springs	end flood	>SST close inshore
16.8.93 23:00	5-calm	010-v	+1 +3days neaps	moderate ebb	
22.8.93 11:00	7.5-7.5	040-040	-3:30 +2days springs	strong flood	
4.9.93 23:00	5-5	050-045	-2 +2days springs	strong flood	
10.9.93 11:00	12.5-10	250-250	+6/-6 neaps	weak flood	

v=variable wind direction, † CW= cold water, * IOW = Isle of Wight

6.4.1 Bathymetry

The major bathymetric features within the study region (as marked on figure 6.1), which are covered by most of the SAR passes, have been examined. The results are recorded in table 6.5, using the same terms of description as in Chapter 3; a subjective asssessment of the strength of the signature is give in terms of weak, moderate or strong (marked by +, ++, +++ respectively). The b or d recorded denotes whether the signature is bright or dark. Typically a bathymetric bank is associated with a double, bright and dark signature (denoted by b/d), an increase in the surface roughness occurring on the downtide side of the bank. Any instances where the signature is reversed are noted. If the feature is not covered by a SAR pass then a '/' is entered, whereas if it is not detected then a '0' is recorded.

Table 6.5 Summary of bathymetric features

SAR pass	Feature				
	St Albans Ledge	Christchurch Ledge	Shingles Bank	Banks south of St Catherines Point	Shallows off Selsey Bill
8.1.93	++b/d	++b/d	++b/d	+b	/
24.1.93	/	/	+b	+b	b+
12.2.93	+b/d	+b/d	++b/d	++b	/
28.2.93	/	/	+b	+b	+++d
19.3.93	+b	+b	+b	+b	/
4.4.93	/	/	+b	+d	++b
17.4.93	+b (diffuse)	++b/d	++b/d	/	/
23.4.93	+b/d (wide d band)	0	+d	+b	/
3.5.93	/	/	+++b	+b	++b
9.5.93	/	/	+b	+b	++b/d
22.5.93	+b/d	0	+b	/	/
28.5.93	++d/b	+d/b	+++d/b	++d	/
7.6.93	/	/	+++b	+b	+b
13.6.93	/	/	+b	0	+b/d
26.6.93	++d/b	+d	++d/b	/	/
2.7.93	++b/d	++b/d	++b/d	+b	/
12.7.93	/	+d/b	++b	+b/d	+b
18.7.93	/	/	+b	+b	++b/d
21.7.93	++d/b	/	/	/	/
31.7.93	+b	++b/d	++b/d	/	/
6.8.93	++d/b	0	++d/b	+d	/
16.8.93	/	/	++b/d	+b	+++b/d
22.8.93	/	/	++b/d	++b/d	++b/d
4.9.93	+b	+d/b	++d/b	/	/
10.9.93	+d/b	0	+d/b	+b/d	/

+ = texture-like signature, b/d = light and/or dark return, 0 = covered by SAR pass but not detected, / = not covered by SAR pass

Features comprising a distinct bank (increase and decrease in depth over distances of approximately 1 km) are characterised by a double signature (bright/dark) on virtually all the images. In all examples where this is the case, the downtide side is rougher, clearly demonstrating the direction of the tidal flow. The 100 km swath of the SAR enables a large section of the coastline to be imaged near-simultaneously and the strength of the backscatter signature across similar features could provide an indication of the current strength. A good example of this is given by the image for 28.5.93 (plate 6.17), where the greater strength of the signature across the Shingles bank compared to that marking St Albans Ledge, corresponds to the progressive increase in the current speeds to the east at this stage of the tidal cycle. Similarly, it can be seen from the backscatter signature marking Christchurch Ledge that the currents in the bay are significantly less than those around the headland or streaming into the Solent. Although this feature is narrower than that off St Albans, it is also shallower and for given current speeds it would not be unreasonable to expect the modulation of the surface roughness to appear similar to the eye.

Drawing quantitative conclusions from these features will require a detailed understanding of the backscatter signature resulting from changes in the bottom gradient, the strength of the currents and the direction of flow over the feature of interest. In the case of a rocky ledge extending off a headland (eg. St Albans and Christchurch Ledges) the tidal currents are likely to flow directly across the feature. The backscatter signature might then be expected to conform to the simple wave:current interaction theory proposed by Alpers and Hennings (1984) for surface roughness modulations across a bank (as described in § 2.1.1). If the feature is a mobile bank, such as the Shingles, then researchers have demonstrated that the flow is predominantly around the bank (Pattriarachi and Collins, 1987). In this case, although a double signature is observed, it may not be the result of the same mechanisms modulating the surface roughness.

The visibility of different features to the radar under different wind and tide conditions could provide information on the surface roughness mechanisms contributing to the SAR backscatter imaged. For example, the Shingles bank and St Albans Ledge are detected under all the wind and tide conditions during the time of the multi-temporal experiment. In high winds the features appear weaker, the signature is often only a region of bright, diffuse backscatter adjacent to the bank. However, in very calm wind conditions (<3 ms^{-1}), such as occurred at the time the images for 19.3.93, 3.5.93 and 7.6.93 were acquired (plates 6.10, 6.14 and 6.18), these features can be associated with a distinct increase in surface roughness. The features appear bright against the dark background. It is normally considered that bathymetric signatures detected using SAR are a product of additional modulation of the small scale wind waves by variable surface current effects. However, the very distinct backscatter patterns associated with these features in calm conditions, in particular the signature across the very shallow region (approximately 3 m) off Selsey Bill (3.5.93, plate 6.14), suggests an alternative source of short wave energy may be contributing to the backscatter signal. Whether this is a product of wave:wave interaction due to breaking of the swell waves across the bank or wave refraction effects is uncertain. Without *in situ* observations possible mechanisms can only be speculative.

The only feature not detected under all the conditions encountered is Christchurch Ledge, which at wind speeds of around 7 ms^{-1} and weak tidal flow conditions (<0.2 ms^{-1}) does not appear to significantly contribute to the surface roughness signature.

6.4.2 Fronts

One of the main aims of this work was to assess the potential of SAR for the detection of small frontal boundaries. The preliminary assessment of the ERS-1 SAR data from the 3-day repeat phase showed large tonal variations in backscatter to the west of the Isle of Wight on several of the images, which were thought to represent a frontal boundary. The presence of an SST boundary in the area was confirmed both by the *in situ* fieldwork and the IR images. However, examination of the SAR images throughout the timeframe of the field study showed no evidence of the feature. Light wind conditions were recorded several times during the period of the image acquisition programme, but the backscatter patterns seen on the preliminary sequence of data are not repeated. Several of the images do display large tonal variations in backscatter, but these were acquired in high wind conditions. Examples are the images for 24.1.93, 28.2.93 and 22.5.93 (plates 6.7, 6.9 and 6.16), when the wind speeds were 7.5 ms^{-1} or more. The effects of sheltering within Poole and Christchurch Bays should be considered as a possible explanation for the variations in backscatter observed on the images. However, without *in situ* measurements it is difficult to determine whether the backscatter patterns detected by SAR represent an oceanographic feature, or are simply the result of ephemeral wind effects.

6.4.3 Riverine inputs

Freshwater runoff from the land often contains surfactant material and the images were examined for possible features that appeared linked to riverine inputs. The data received during 1991 and 1992 imaged dark lines extending out from the coast and regions of low backscatter within Poole Bay, which appeared to correspond to fresher water outflow. On 9.9.91 (plate 6.4) narrow bands can be seen all along the coastline bending to the west, possibly responding to the tidal streams which have begun to ebb inshore. That the features were maintained long enough to extend 5 km offshore may be explained by the weak tidal conditions (slack water) at the time the image was acquired. Regions of smooth water observed within the bay occur on 25.1.93 and 16.3.92 (plates 6.2 and 6.1). Possible examples of river input were not observed on any of the images acquired during 1993 and only on 8.1.93 (plate 6.6) and 6.8.93 (plate 6.26) did the area in Poole bay appear dark. These later results suggest that the early observations of feature may simply have been a product of very localised variations in the wind field.

6.4.4 Long wavelength features

Many of the images display long wavelength features, the varied appearance and scales of these backscatter patterns suggest they are a product of long wavelength fluctuations in the lower atmospheric boundary layer. A record of all the images acquired for this study, that show these types of features, is given in table 6.6. Information on the scale of the feature, its alignment with the wind direction and the stability of the MABL at the time the image was acquired is also recorded.

Table 6.6 Summary of long wavelength features observed on the ERS-1 SAR images

Image (plate number)	Alignment with the wind direction (°)†	Mean wind direction (°)	Length (km)	Spacing (km)	ABL conditions‡
13.3.92 (6.2)	0	250	25 - 50	8 - 10	+
16.3.92 (6.3)	90	260	25	2	+
22.3.92 (6.5)	0	270	25 - 50	5 - 10	+
24.1.93 (6.7)	0	260	25	5	-
12.2.93 (6.8)	0	90	20	5	-
17.4.93 (6.12)	20	260	20	5 -10	N
23.4.93 (6.13)	0	180	15	1	N
22.5.93 (6.16)	90	90	10	1	+
13.6.93 (6.19)	0	0	5 - 20	3 - 8	+
2.7.93 (6.21)	0	245	10 - 20	2 - 3	+
6.8.93 (6.26)	0	260	20 - 30	3 - 5	+
16.8.93 (6.27)	0	10	15 - 20	2 -5	N
4.9.93 (6.29)	0	45	10 - 15	2 - 5	-
10.9.93 (6.30)	0	250	25 - 50	1 -3	N

† 0 = aligned, 90 = orthogonal
‡ - = unstable, + = stable, N=neutral

Topographic effects funnelling the wind as it streams off the land explain several of the narrow bands of increased roughnesss observed, such as on 12.2.93, 13.6.93, 16.8.93 and 4.9.93. However, where the wind is parallel to the coast or onshore then other mechanisms are sought. Atmospheric boundary layer rolls are normally the explanation given to long wavelength features observed on the SAR images. Although many of the features are aligned with the wind direction as would be expected, the MABL conditions were in general neutral or stable and the wavelengths are mostly considerably longer than the 1 to 2 km spacing associated with ABL rolls. A backscatter signature considered characteristic of ABL rolls occurs on 23.4.93 (plate13), but the air temperature is recorded as warmer than the sea on that day. The image for 24.1.93 was acquired in unstable ABL conditions and the very long wavelength dark bands may be attributed to these effects. Similar, but more distinct features are seen on 13.3.92 and 22.3.92, when the boundary layer was stable. In all these these cases the banding is aligned with the wind direction and the signature is noticeably stronger inshore where it appears to approximate to the 20 m contour, becoming fainter further offshore. The effects may be a result of instabilities in the flow in the area of transition from land to sea. The very patchy dark banding to the southwest of the image for 6.8.93 and the narrow bright streaks seen on 10.9.93 cannot be accounted for. On 2.7.93

the streaks appear to be a product of the wind extending surfactant material, but the spacing and the distance over which the features extend are similar to the above examples and may be an indication of the length scales of flow patterns within the wind field.

Periodic banding of the surface in coastal waters have been observed in light wind conditions. Smooth streaks occur which are in the order of 50 m wide and many kilometres long, separated by rougher water about 300 m wide (Ewing, 1950). In shallow water these features follow the bottom contours and have been attributed to internal waves in a shallow thermocline. The backscatter patterns observed in these images are all considerably larger scale than these features.

Where the wind is orthogonal to the feature ABL rolls can be ruled out. On 22.5.93 the distinct long waves seen to the west of the Isle of Wight are attributed to lee waves in the atmosphere, generated as the wind flows over the island. The features seen on 16.3.92 cannot be explained in this manner. These features are investigated in more detail in Chapter 7.

6.4.5 Wind fronts

The occurrence of wind fronts on SAR images of the open ocean has been reported by Johannessen *et al.* (1993). The changes in the wind regime are noted to be abrupt, generating a distinct step-like feature in the backscatter signature, in the transition from rough to smooth water (bright to dark) and are generally marked by a very straight boundary. A feature meeting this description was observed on the image acquired on 21.7.93 (plate 6.24). The synoptic chart records light winds, varying between 2.5 to 5 ms^{-1} and a wind direction of 260°, orthogonal to the feature, agreeing with observations made by other workers. However, the synoptic chart does not show a front in this region. Where this is the case, the backscatter signature is very different. On 23.4.93 an occluded front is shown on the weather chart orientated north to south and extending across the study region (figure 6.5). The band of dark return seen on the image (plate 6.13) corresponds closely to the position of this feature. The reduced roughness may be a result of rain occurring along the frontal boundary, dampening the short waves; rain is recorded all along the boundary. The area ahead of the front (to the east) appears rougher.

In the coastal environment distinct differences occur between the coastal and offshore wind patterns, which are seen on several images. On the 13.3.92 and 22.3.92 (plate 6.3) the very bright returns inshore appear in narrow bands, possibly caused by funnelling of the wind, whereas the offshore wind direction is predominantly westerly. On the image for the 19.3.92 (plate 6.1) the transition from rough offshore to smooth inshore appears to be in process, the wind is light (5 ms^{-1}) and southwesterly and 'fingers' of slightly rougher water extend inshore.

6.4.6 Summary of the qualitative analysis of the ERS-1 SAR images

The results from the qualitative analysis of the ERS-1 SAR images demonstrate that bathymetric features can be detected under virtually all wind and tide conditions. It is also apparent that they have the potential to provide information on the direction and variations in strength of the tidal flow along the coastline. This could be a valuable tool for coastal management in areas where the tidal regime is not well documented.

The potential of SAR for detecting weak temperature gradients, not associated with a current shear along the boundary, was found to be poor in this region. The features observed in the first sequence of data were not repeated and although the *in situ* study identified an SST boundary on several occassions it was not observed on the SAR images. Similarly, the features thought to be associated with riverine inputs in the preliminary analysis were not observed on the later sequence of images.

Evaluating a large number of images over a long period enabled the complex backscattering features caused by variations in the wind field to be recognised. Images such as these improve the understanding of the variability of coastal wind fields, providing a synoptic view of conditions. Combined with *in situ* measurements they could be useful in the study of transitional winds, such as sea breezes.

6.5 CONCLUSIONS

The importance of obtaining a multi-temporal dataset for the investigation of features using SAR is clearly demonstrated by this work; the variability of the wind field in the coastal environment producing a complexity of surface roughness patterns, which might be falsely interpreted when using a single image. To improve the understanding of the backscatter patterns and to validate features observed it is essential to carry out contemporaneous *in situ* measurements. The reliability of being able to detect bathymetry makes it a good feature to use where quantitative comparisons of the relative changes in backscatter occurring over different wind and tide conditions are sought.

The qualitative analysis of the data has led to the following conclusions. If the SAR data are to be quantitatively assessed then sufficient understanding of the features associated with the wind field must be gained in order to identify the oceanographic contribution to the surface roughness signature. It is not only necessary to be able to understand the wind contribution in terms of σ_0, but also the natural fluctuations associated with wind in the coastal zone and the effects on the surface roughness patterns detected by SAR. The following chapters concentrate on investigating these factors.

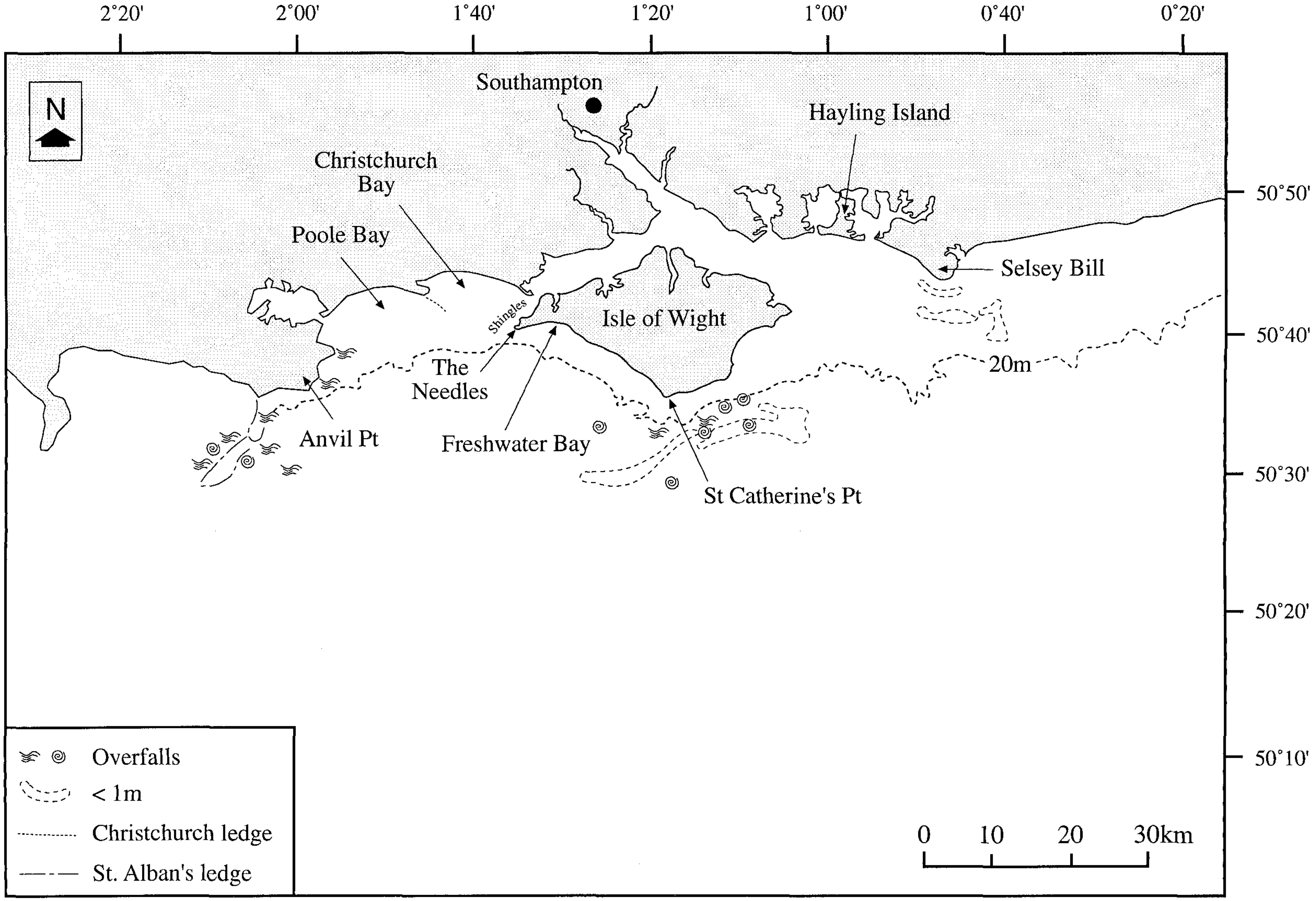

Figure 6.1 Map showing the area studied using ERS-1 SAR data and the sub-region where the *in situ* experimental work was carried out. The headlands, bays and ledges referred to in the text are labelled.

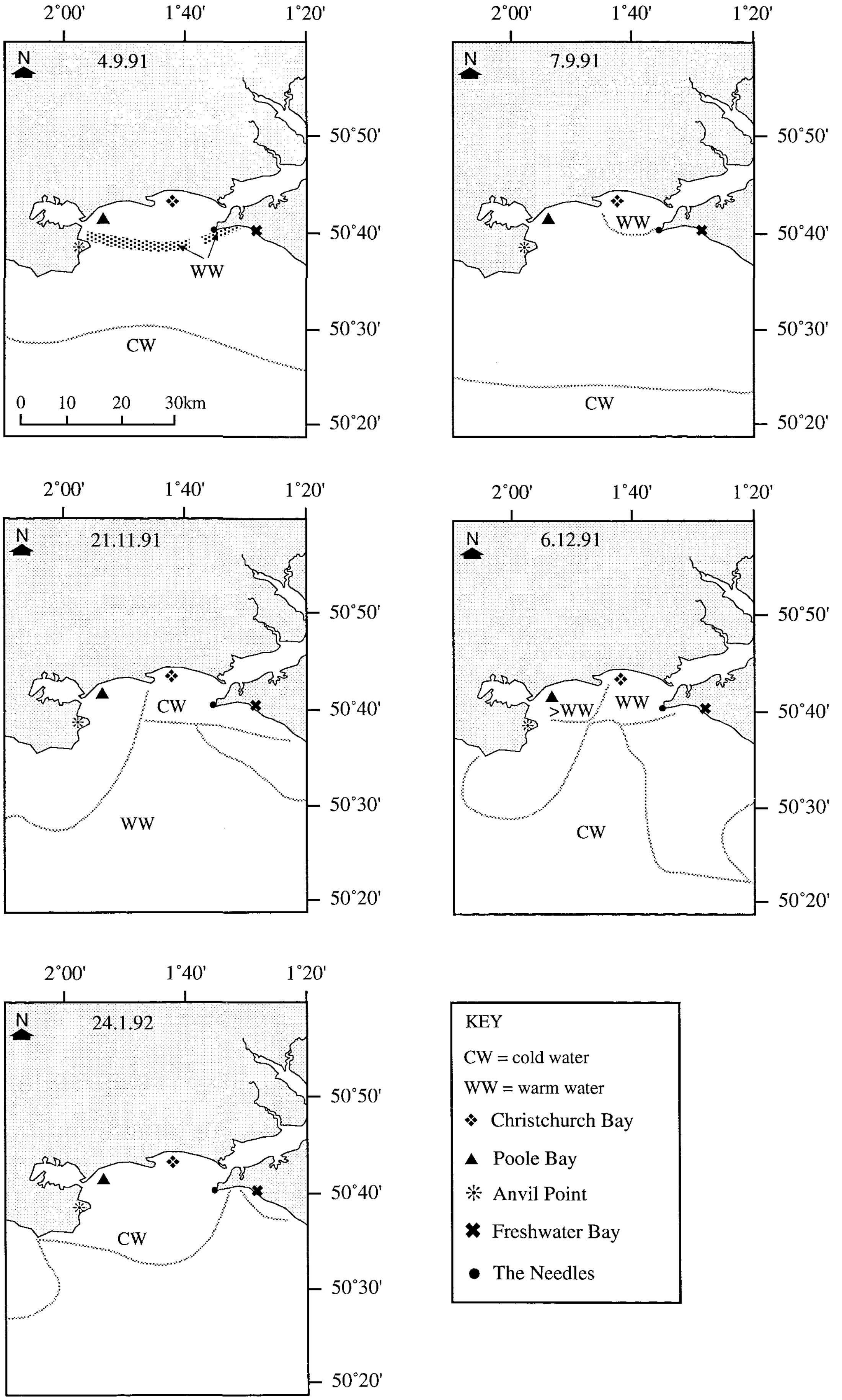

Figure 6.2 Map summarising the positions of the SST boundaries observed on the AVHRR IR images for the preliminary study period (September 1991 to March 1992).

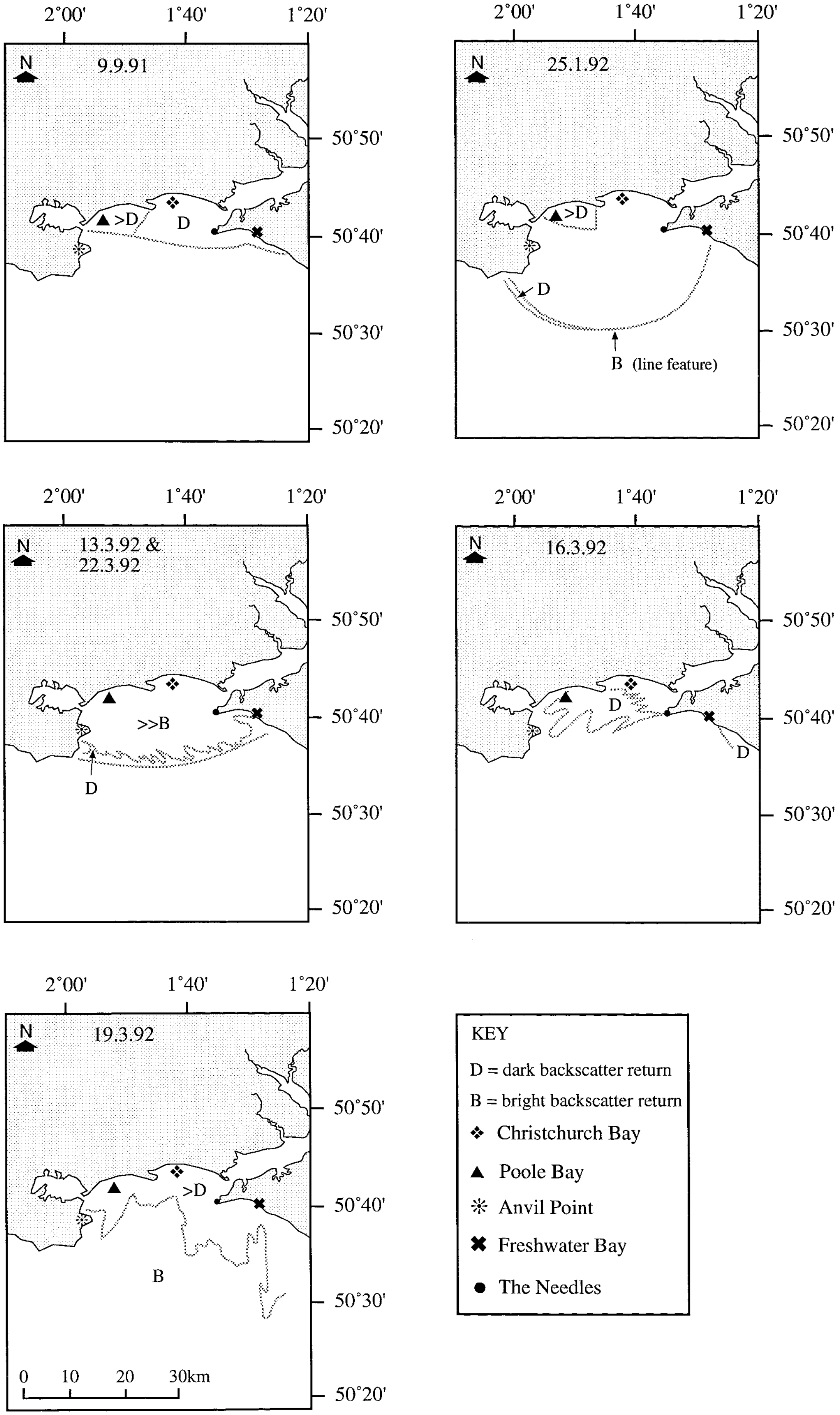

Figure 6.3 Map summarising possible frontal boundaries delimited by variations in backscatter on the ERS-1 SAR images for the preliminary data acquisition period (September 1991 to March 1992).

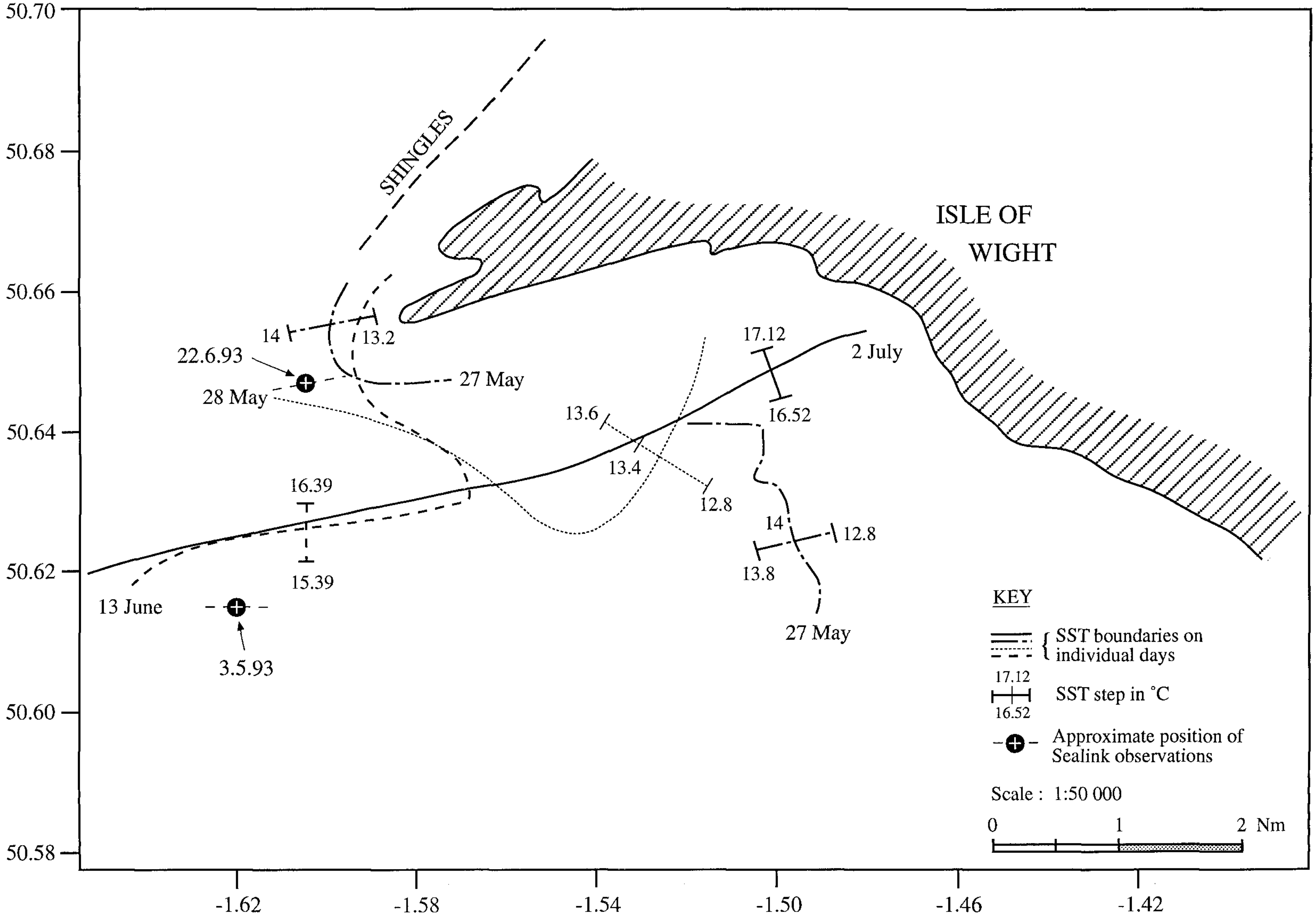

Figure 6.4 Map summarising the SST distribution and gradients across boundaries derived from *in situ* measurements during the main SAR data acquisition period, 27.5.93 to 2.7.93.

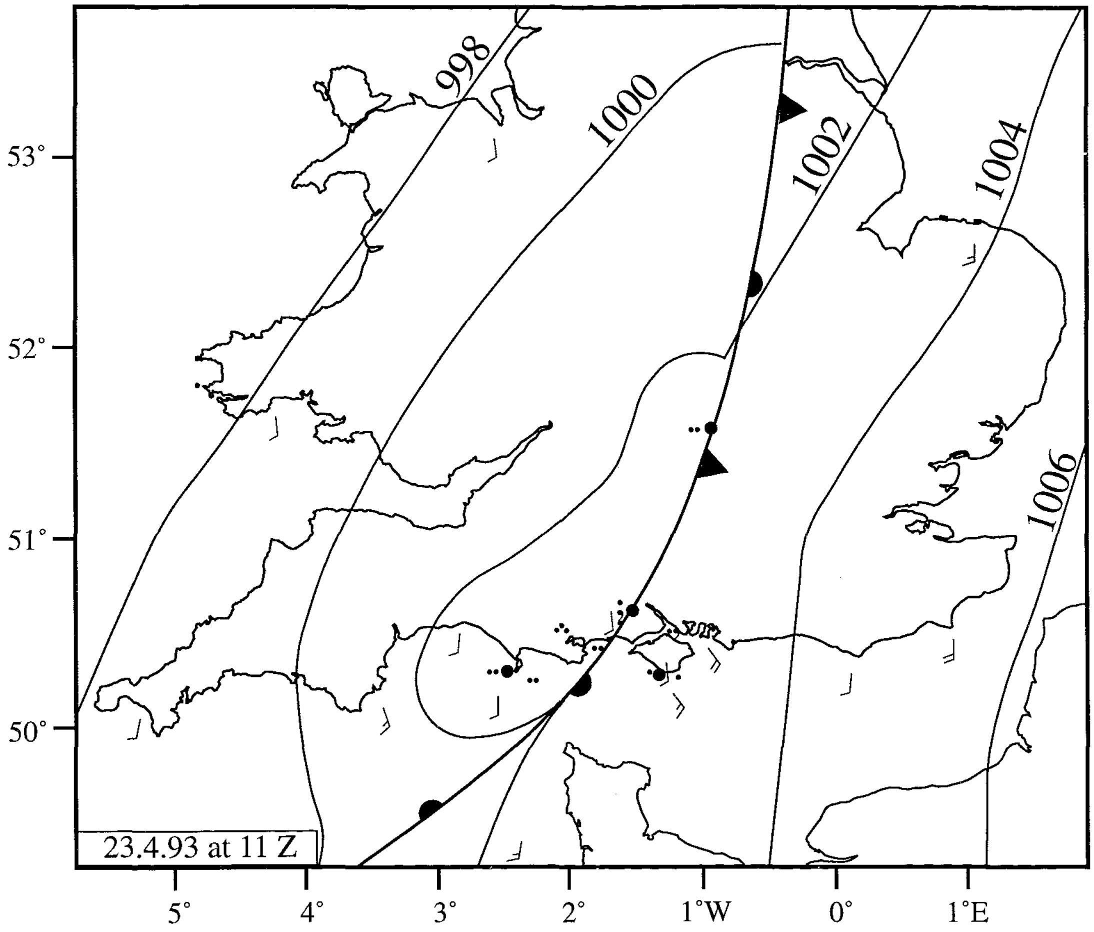

Figure 6.5 Extract from meteorological synoptic chart showing the presence of an occluded front across the study region on 23.4.93 at 11:00 GMT (time of SAR pass). The • indicates rain occuring along and behind the front.

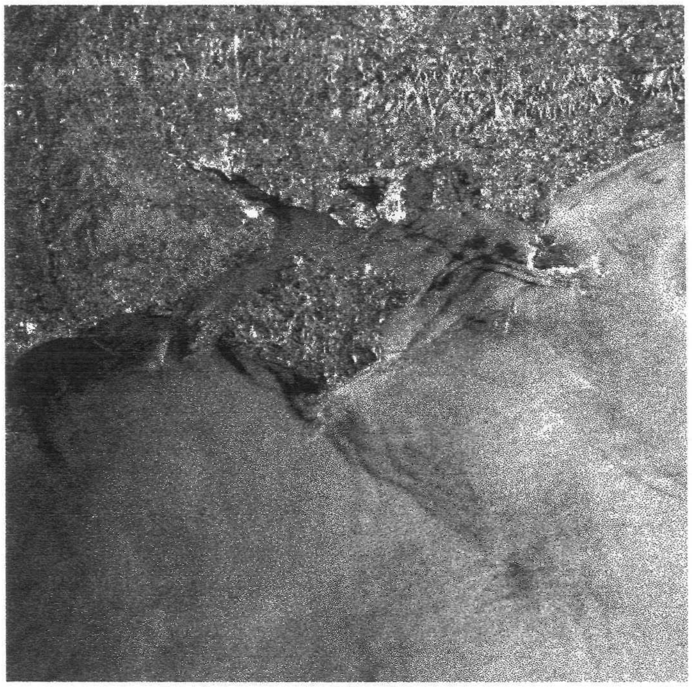

Plate 6.1 (a) ERS-1 SAR image 16.3.92

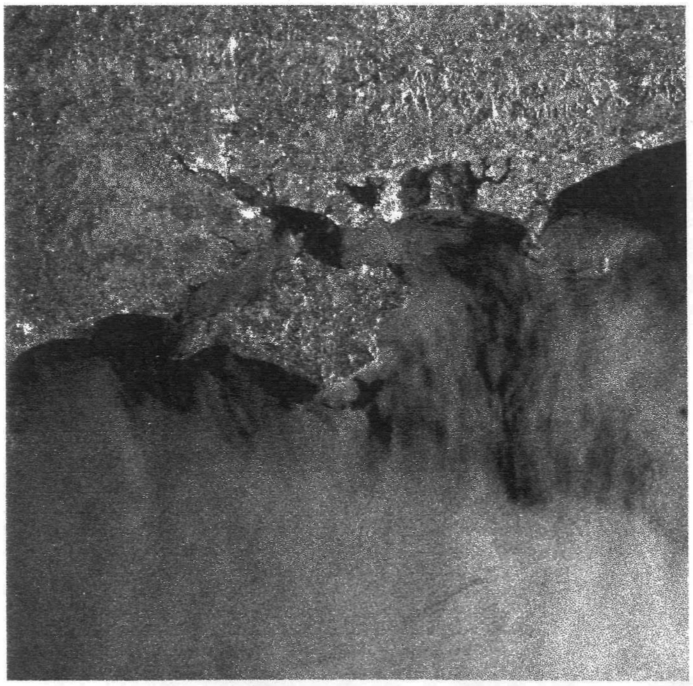

Plate 6.1 (b) ERS-1 SAR image 19.3.92

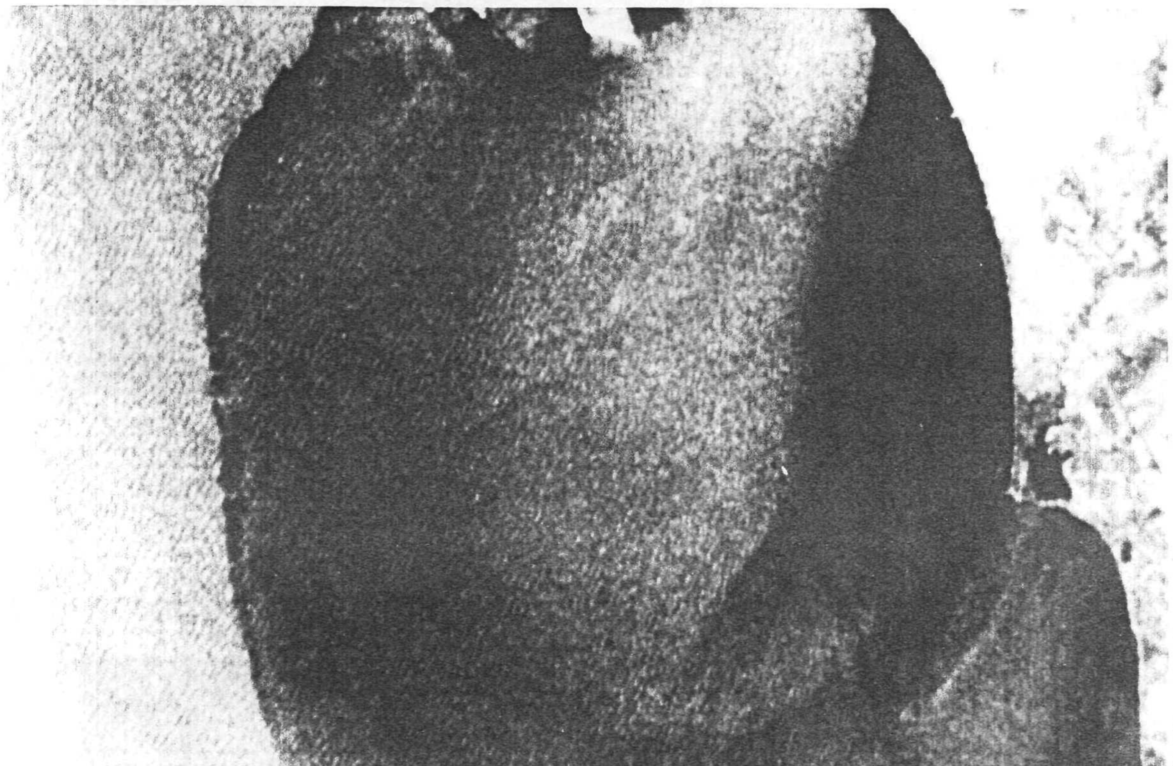

Plate 6.2 Extract from ERS-1 SAR image 25.1.92.
The image shows a possible frontal boundary extending across Christchurch and Poole Bays. The distance covered is approximately 19 km.

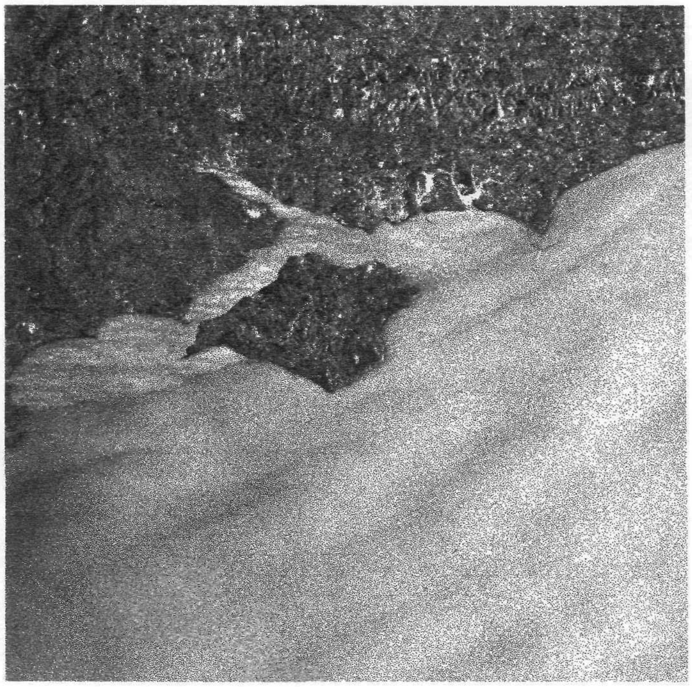

Plate 6.3 (a) ERS-1 SAR image 13.3.92

Plate 6.3 (b) ERS-1 SAR image 22.3.92

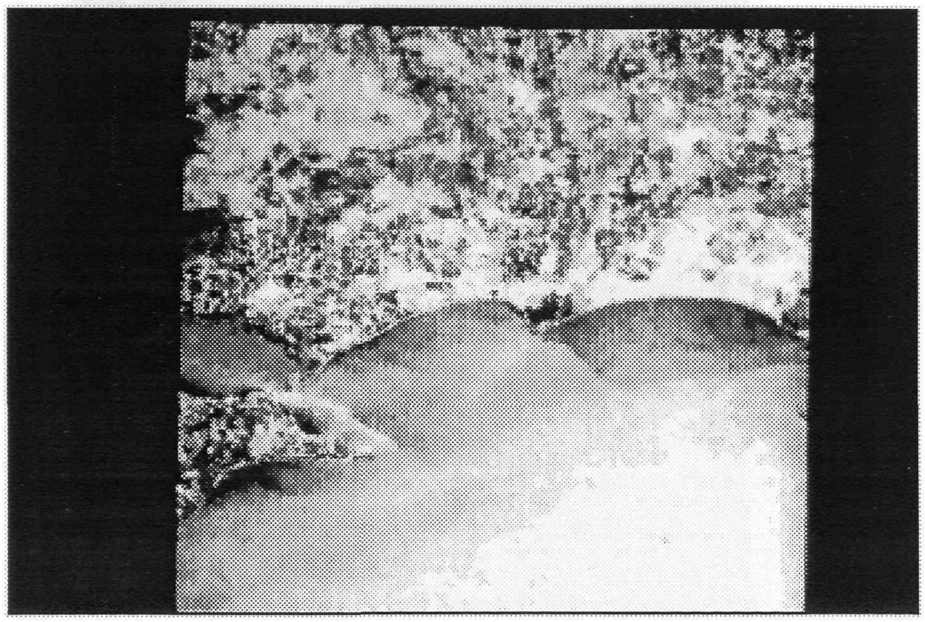

Plate 6.4 ERS-1 SAR image 9.9.91.
The pixels have been averaged 6 x 6, resulting in 75 x 75m resolution and spanning a distance of 38.4 km.

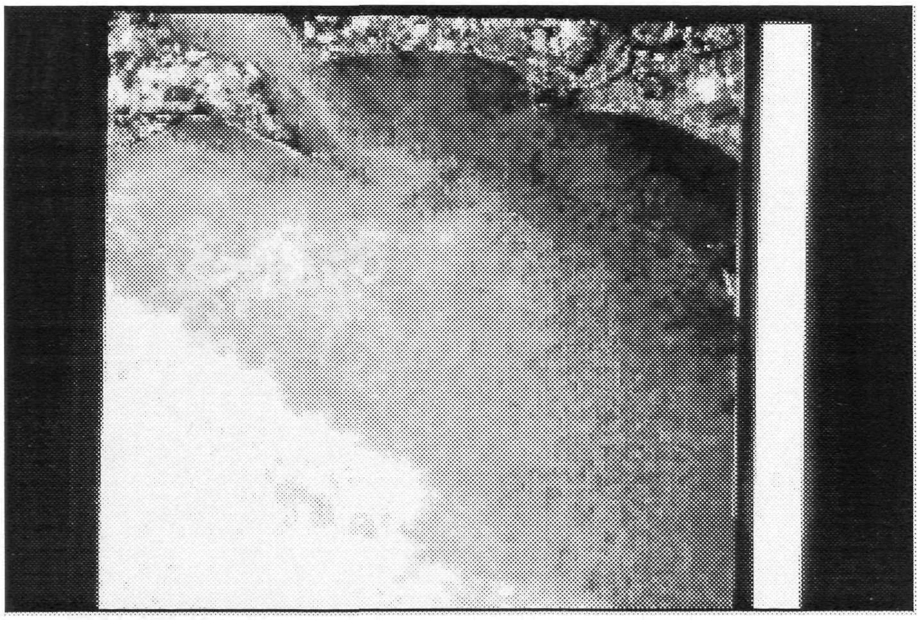

Plate 6.5 ERS-1 SAR image 28.1.92.
The pixels have been averaged 6 x 6, resulting in 75 x 75m resolution and spanning a distance of 38.4 km.

Plate 6.6 ERS-1 SAR image 8.1.93

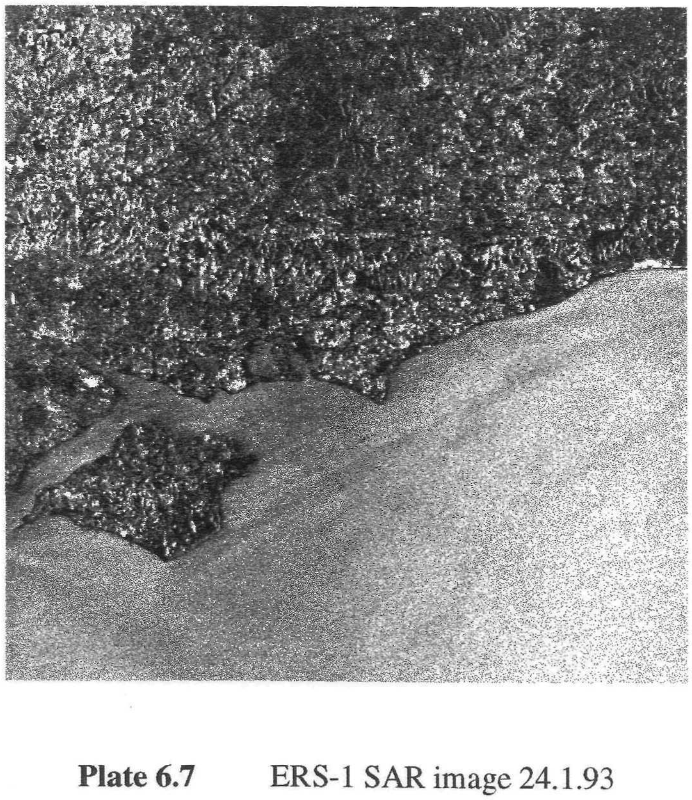

Plate 6.7 ERS-1 SAR image 24.1.93

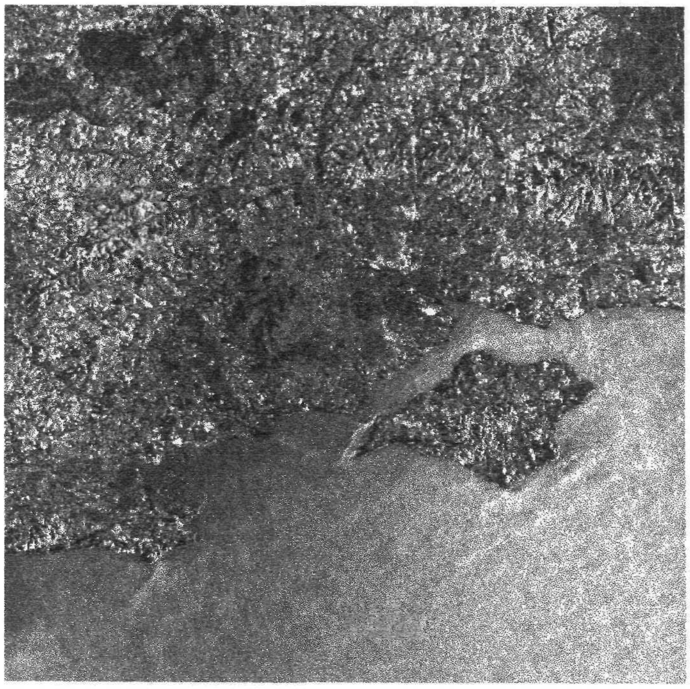

Plate 6.8 ERS-1 SAR image 12.2.93

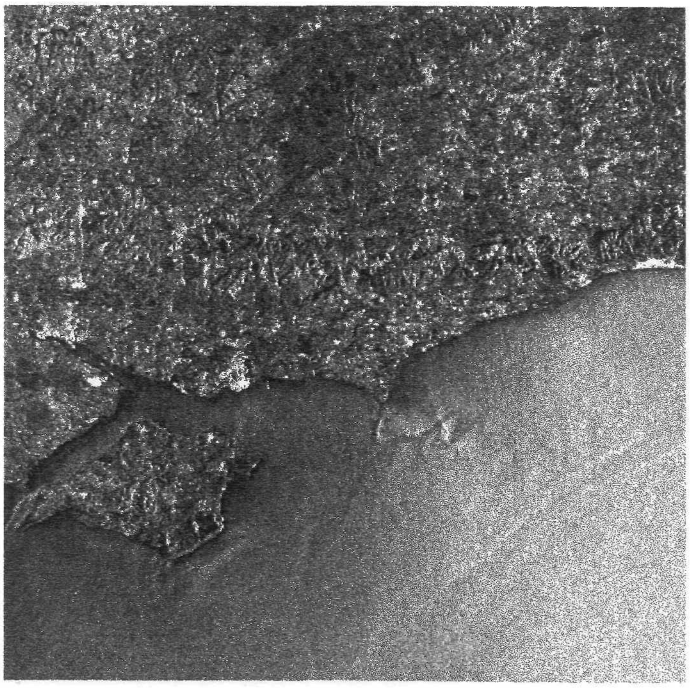

Plate 6.9 ERS-1 SAR image 28.2.93

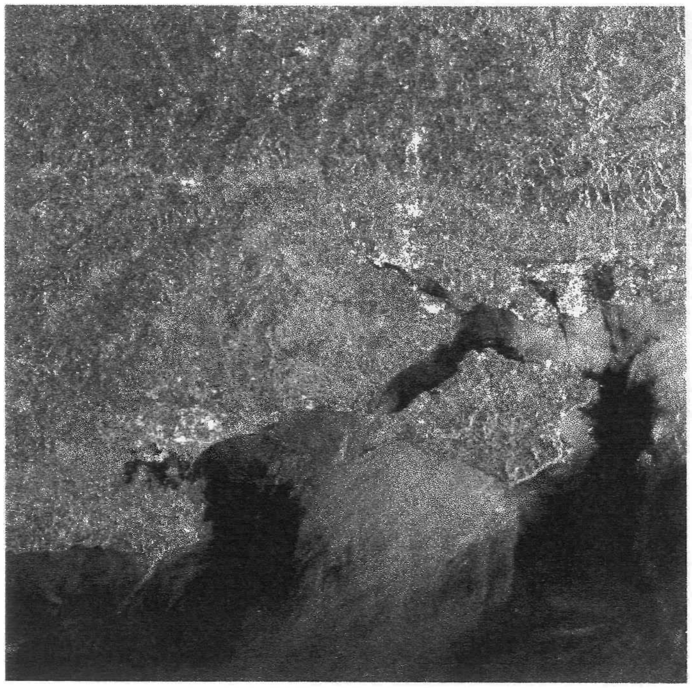

Plate 6.10 ERS-1 SAR image 19.3.93

Plate 6.11 ERS-1 SAR image 4.4.93

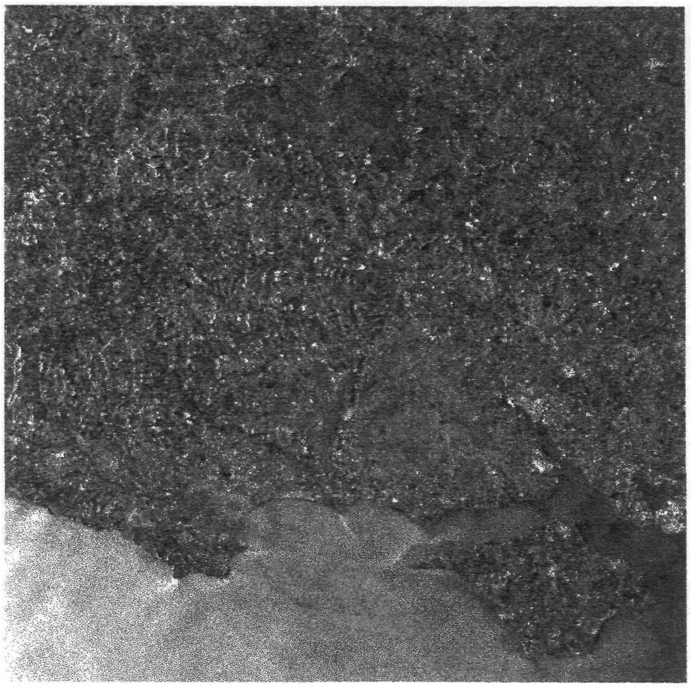

Plate 6.12 ERS-1 SAR image 17.4.93

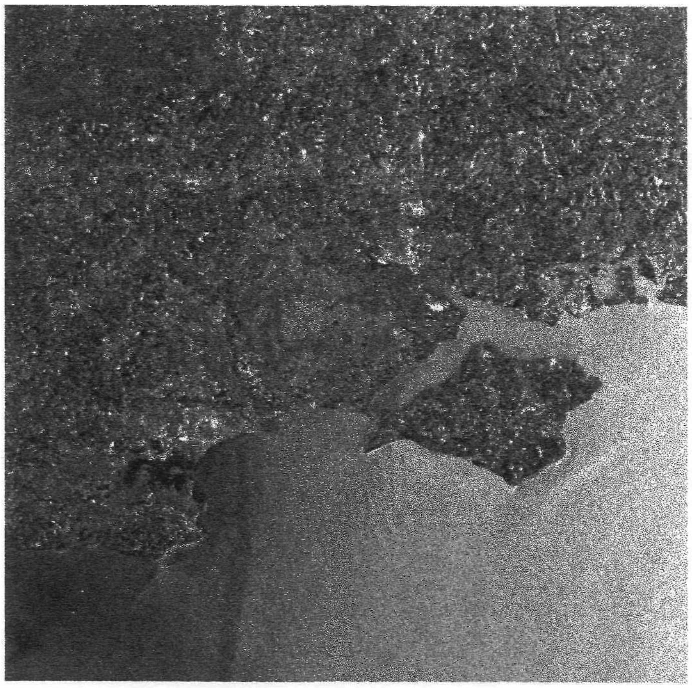

Plate 6.13 ERS-1 SAR image 23.4.93

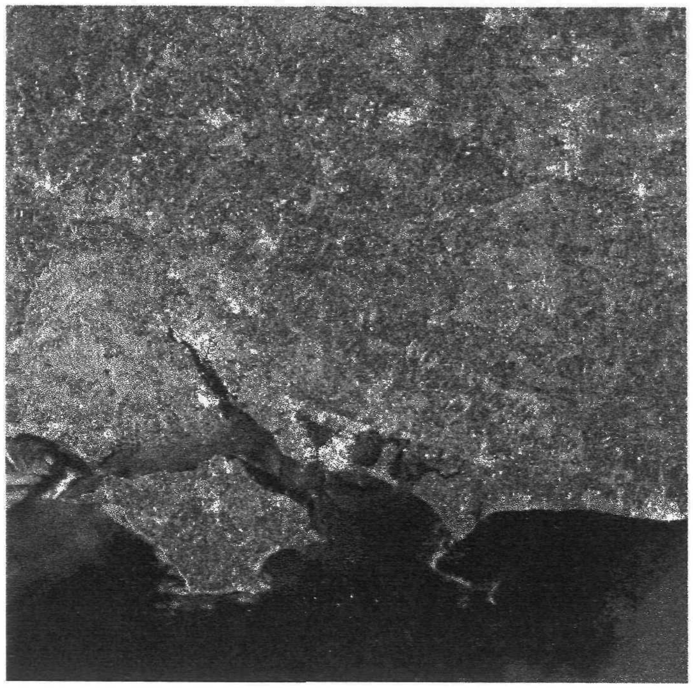

Plate 6.14 ERS-1 SAR image 3.5.93

Plate 6.15 ERS-1 SAR image 9.5.93

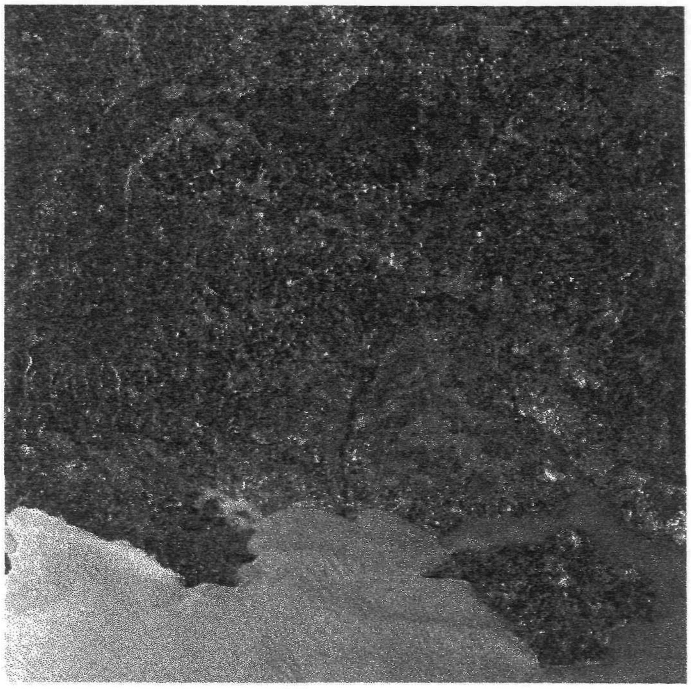

Plate 6.16 ERS-1 SAR image 22.5.93

Plate 6.17 ERS-1 SAR image 28.5.93

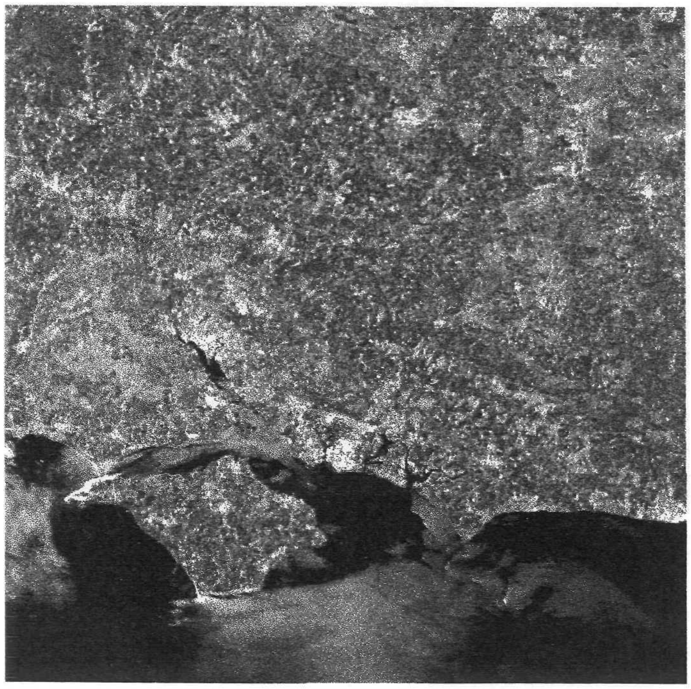

Plate 6.18 ERS-1 SAR image 7.6.93

Plate 6.19 ERS-1 SAR image 13.6.93

Plate 6.20 ERS-1 SAR image 26.6.93

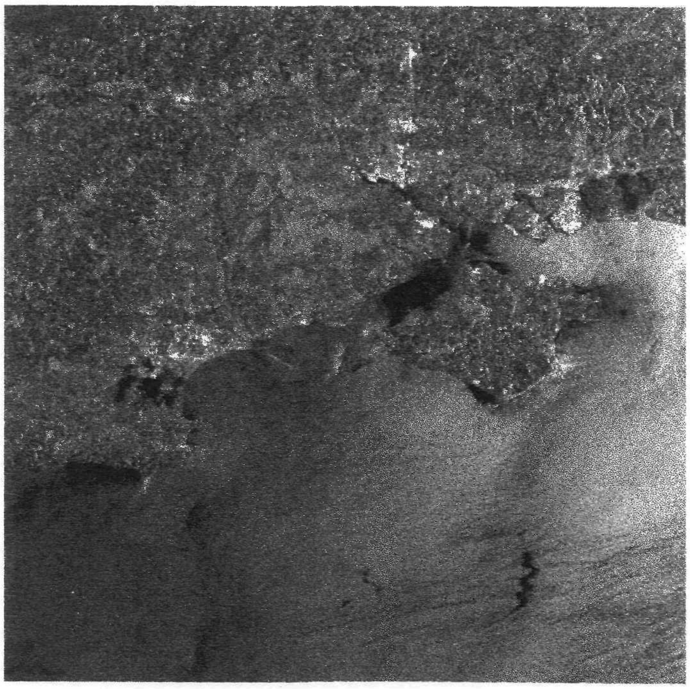

Plate 6.21 ERS-1 SAR image 2.7.93

Plate 6.22 ERS-1 SAR image 12.7.93

Plate 6.23 ERS-1 SAR image 18.7.93

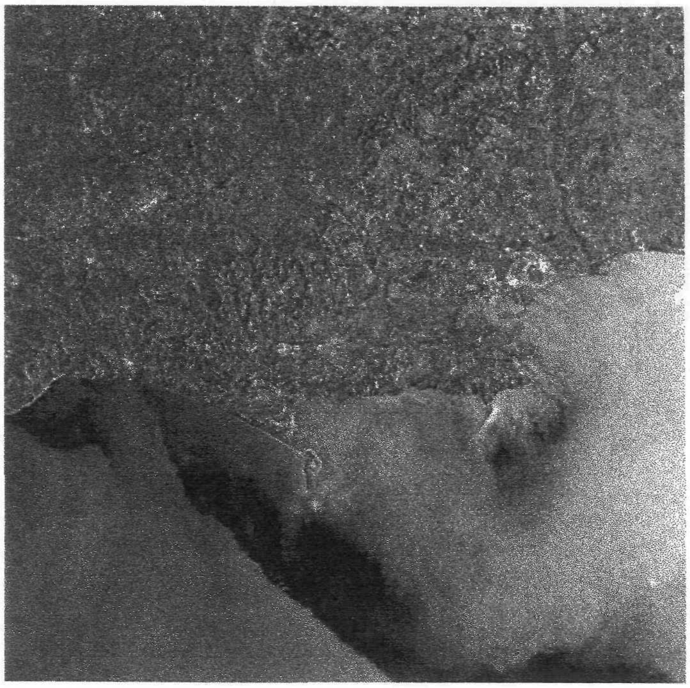

Plate 6.24 ERS-1 SAR image 21.7.93

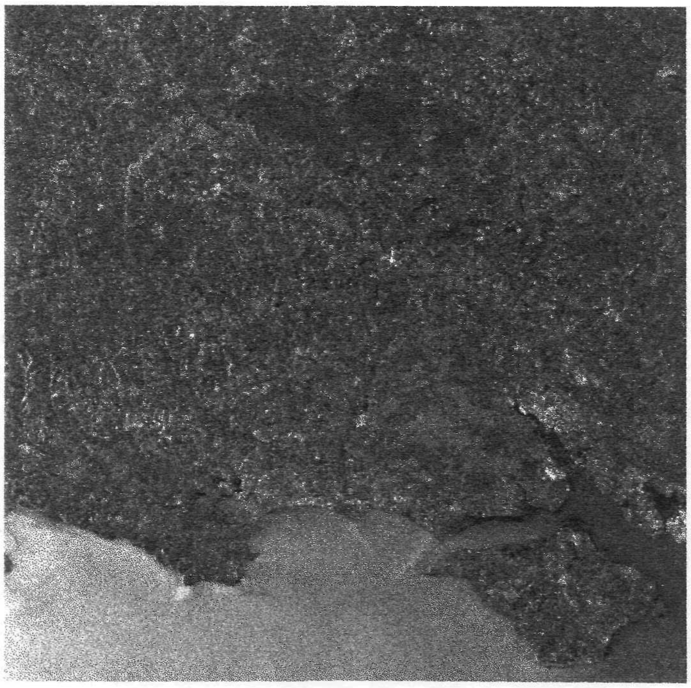

Plate 6.25 ERS-1 SAR image 31.7.93

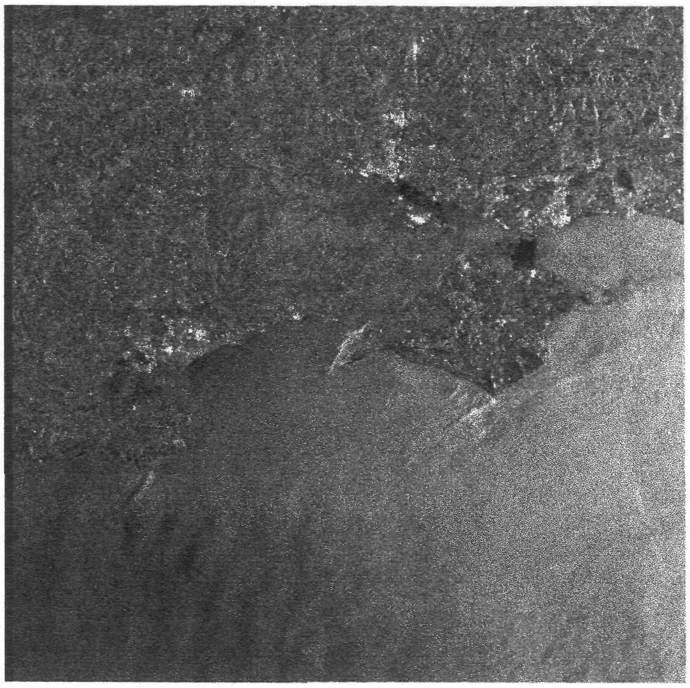

Plate 6.26 ERS-1 SAR image 6.8.93

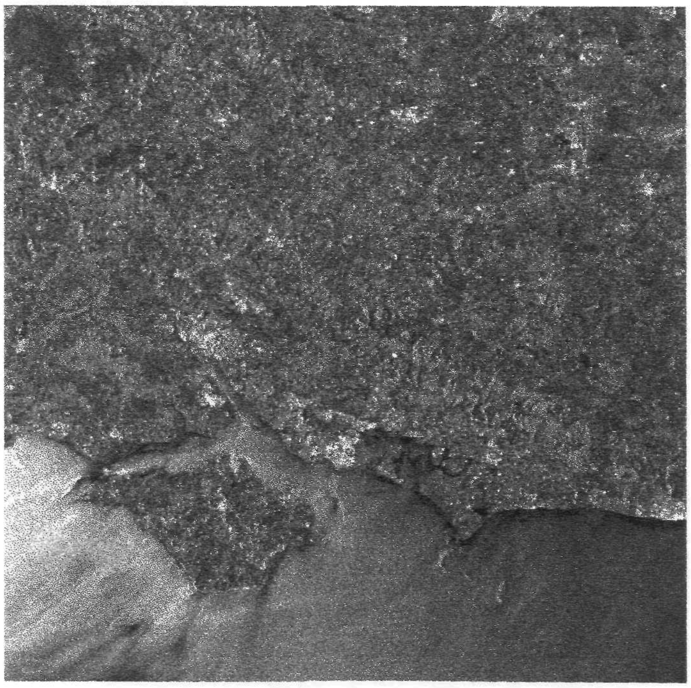

Plate 6.27 ERS-1 SAR image 16.8.93

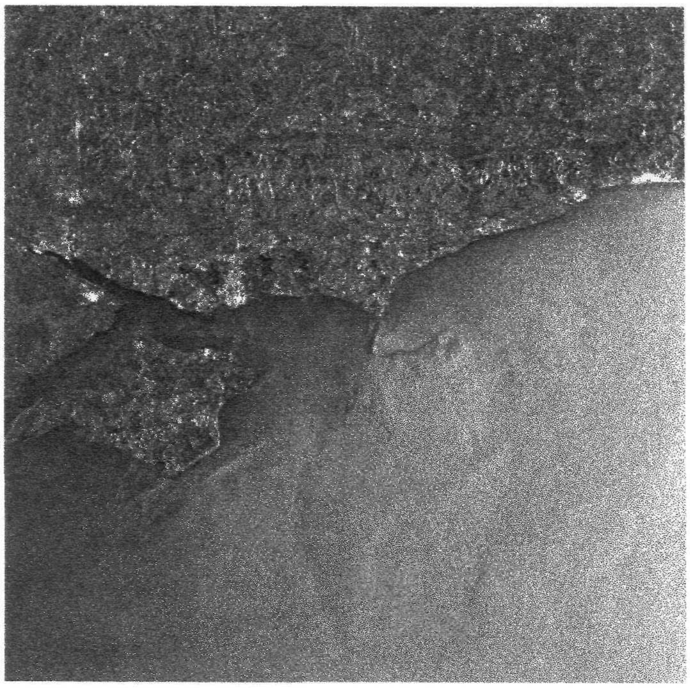

Plate 6.28 ERS-1 SAR image 22.8.93

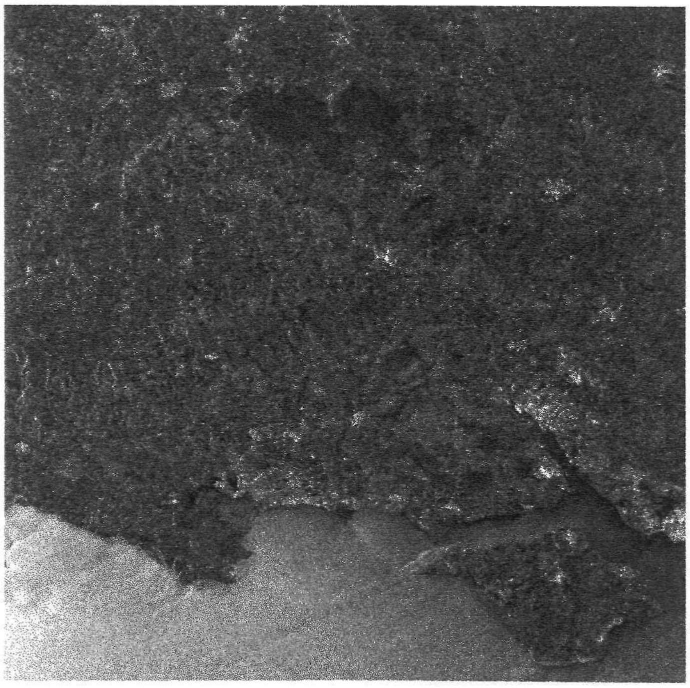

Plate 6.29 ERS-1 SAR image 4.9.93

Plate 6.30 ERS-1 SAR image 10.9.93

CHAPTER SEVEN

WIND SPEED ESTIMATES FROM ERS-1 SAR

7.0 INTRODUCTION

The backscatter patterns detected by SAR often reflect the modulation of the small scale sea surface roughness by both local and mesoscale wind events. Being able to measure and characterise the events generating these features would considerably aid the quantitative analysis of SAR. The first analysis of the wind field using SAR was carried out by Gerling (1986), using a power law model to relate SEASAT SAR-measured backscatter to estimates of wind from the Seasat-A scatterometer. In this study, the potential of the ERS-1 scatterometer wind retrieval model (CMOD4) is examined for estimating wind speeds from ERS-1 SAR. The model is empirically derived (Stoffelen and Anderson, 1993). The potential for using CMOD4 for wind speed retrieval from ERS-1 SAR in the open ocean has been demonstrated by Vachon *et al.* (1994). The applicability of using the model to derive winds from SAR images in the coastal zone is considered in this study. SAR-derived wind speed estimates are compared with *in situ* measurements and meteorological synoptic chart records of surface winds. A detailed analysis of the fluctuations and reproducibility of features observed from the resulting wind speed profiles is made, studying the factors influencing wind speed variability in the coastal zone. Such high resolution, synoptic measurements have not formerly been available from existing techniques. That SAR is capable of providing synoptic wind information on the 1 km scale is demonstrated by research in progress by Shuchman *et al.* (1994). They are currently investigating the potential of using the simple C-band scatterometer model developed by Wismann (1992) for obtaining 1 km resolution estimates of wind speed from SAR.

Scatterometer type instruments provide global coverage, but the 50 km resolution cell is too coarse to resolve strong wind gradients and localised storms or rain cells often bias their wind predictions (Jones *et al.* 1982). The small scale local variability of the wind field is particularly well illustrated by SAR images collected near atmospheric fronts. Indeed, it was the discovery of such ephemeral features which initiated the quantitative investigation of wind effects.

7.1 DERIVING WINDS FROM RADAR BACKSCATTER

From the earliest work by Moore and Pierson (1966) using satellite scatterometers to obtain oceanic wind and wave predictions it was clear that the 1-5 cm scale waves interacting with the radar signal were approximately proportional to the energy transfer from the atmosphere to the ocean (the wind stress). The major question was whether or not the normalised radar cross section (NRCS), σ_0, could be successfully correlated with wind speed. The partition of wind energy between short and long wavelengths and the possibility of saturation above moderate wind speeds of 7-8 ms^{-1} were also debated. Prior to the launch of the Seasat scatterometer (SASS) in 1978 comprehensive field experiments were carried out using airborne scatterometers. Circle flights, performed at different bank angles, provided measurements of the dependence of σ_0 on incidence angle and a strong empirical correlation was established between ocean surface wind velocities and σ_0 (Jones *et al.*, 1977).

SASS operated at 13.9 GHz (L-band) whereas the new generation scatterometer on ERS-1 operates at 5.3 Ghz (C-band), for which the dependence of σ_0 on wind speed and direction was not well known. Further experiments were undertaken during the ESA C-band scatterometer 'Haltenbanken' field campaign off the coast of Norway, studying the dependence of σ_0 on the wind vector and incidence angle (Feindt *et al.*, 1986). Their results indicated that parameters such as the long wave slope should also be investigated. Donelan and Pierson (1987) compared observations with theoretical predictions, showing the weakness of the power law and, suggested that due to viscosity effects, a simple relationship between increased wind speed and increased σ_0 is impossible. However, an empirical relationship between σ_0 and wind speed and direction for neutral stratification at 10 m height was found to be moderately successful and was called CMOD2/3 (Long, 1985). The non symmetric nature of a wave with respect to wind direction causes σ_0 to vary harmonically with the angle between the radar beam and the wind direction. Further calibration and validation activities for the ERS-1 scatterometer carried out at the European Centre for Medium-Range Weather Forecasts (ECMWF) revised the pre-launch transfer model to the form called CMOD4, significantly improving the accuracy of wind retrieval (Stoffelen and Anderson, 1993). An alternative wind retrieval model for ERS-1 SAR is also being developed by Shuchman *et al.* (1993) using data from the NORCSEX'91 field experiments. At present this is still at the developmental stage and is based on a limited number of measurements. In contrast, CMOD4 is a well researched model, which is based on a σ_0 to wind relationship for neutral stratification at 10 m, containing 18 tuning coefficients to account for the asymmetry of the wave field. The model has been tested using global wind data and is designed to have world wide application.

The updated wind retrieval model is based on a σ_0 to wind relationship improved by using wind vector data from the ECMWF. The temporally variable wind fields associated with frontal boundaries and light winds often confuse the wind estimates and averaging over the 50 km resolution cell can blur out frontal details altogether. The wind retrieval from the scatterometer, therefore, also relies on background wind direction information in the retrieval at each node taken from the ECMWF (Stoffelen and Anderson, 1993). The model surface wind predictions show a bias 10% lower than conventional observations, estimated as 2.25 ms^{-1}, for which correction is made. CMOD4 does not include corrections for other geophysical parameters, such as SST or swell influences on surface roughness but, being based on world-wide wind data, calculates an average wind vector for neutral conditions. Investigations of the noise contribution for varying SST values between 0°C and 30°C found no differences in the scatter of σ_0 for winds below 3 ms^{-1}; it would appear that CMOD4 effectively estimates wind speed even where any σ_0 dependancy on SST occurs (Stoffelen and Anderson, 1993). The transfer function is sensitive to slight variations in wind speed, but there are indications that σ_0 saturation occurs for wind speeds above 18 ms^{-1}. The accuracy of CMOD4 is given as a standard deviation of 2 ms^{-1} for wind speed estimates, but directions are only to within 90° of the ECMWF predictions.

The model as implemented by ESA is described by Lecomte (1993) and can be summarised as follows:

$$\sigma_0 = b0\ 1+b1.\cos f+b3.\tanh\ (b2)\ \cos\ (2f)^{1.6}$$

The coefficients b0, b1 and b2 depend on the radar beam incidence angle and wind speed. In simple terms, Stoffelen and Anderson refer to the largest term b0 as the 'bias' term, b1 as 'upwind/ downwind amplitude' and b2 as 'upwind/ crosswind amplitude'. The difference between the wind direction and radar look direction is given by the variable *f*; this angle is zero when the wind is blowing towards the radar. The model is used to generate σ_0 values for specific wind and radar look angles. Given calibrated SAR σ_0 data and wind direction information it may thus be used as a look-up table to estimate wind speed for specific imaging conditions.

7.1.1 Applicability of CMOD4 for wind retrieval from ERS-1 SAR

The CMOD4 was developed for the retrieval of wind information from the ERS scatterometer. In this study its application to ERS SAR is investigated. The justification for applying the model to the SAR is discussed, considering both the instrumental and model requirements.

7.1.1.1 The Instrument - SAR

The SAR and scatterometer on board ERS-1 are both part of the AMI and hence, operate at the same freqency (C-band). In view of the similarity in the operational parameters of the instruments and because they interact with surface waves of the same order of magnitude, it was considered likely that the CMOD4 would provide useful wind speed data when applied to the SAR. Vachon *et al.* (1994) examined an unusual SAR image of atmospheric lee waves behind the island of Hopen, using the model to derive wind speed estimates from the image for comparison with a one-layer linear model for atmospheric lee waves. A good correlation was found and it was estimated that CMOD4 calculated winds to +/-3 ms^{-1} accuracy, suggesting that SAR could provide a useful tool for the study of localised wind events.

7.1.1.2 The Model - CMOD4

There were three potential problems associated with using CMOD4 for wind retrieval from SAR within the terms of reference of this study:

- The model was developed for deep ocean conditions but this investigation is based in the coastal waters of the English Channel.

- The model uses the 3 independent measurements of σ_0 by the scatterometer to deduce the wind direction. Although in some circumstances SAR images long wavelength features which can provide wind direction information, often it cannot be obtained directly from the image.

- The model is based on large spatial averages of radar cross section for each wind speed (50 x 50 km for scatterometer) whereas, when applying it to SAR, areas of 100 x 100 m would be used, which may introduce a bias into the wind speed estimation.

The model is based on average deep ocean conditions and has no provision for the effects of a varied wave field, which in a coastal area may consist of fetch limited, shorter and steeper waves. The importance of hydrodynamic and current modulation of the small scale surface waves is still not fully researched. Local wave current interaction may roughen or smooth the sea surface but the effect is generally spatially confined to a narrow region and is unlikely to be large enough to influence wind estimates using average backscatter values from large areas. Estimation of the wind speed using CMOD4 should therefore be analysed bearing these points in mind.

As mentioned previously, given the asymmetric nature of a wave the expression relating wind speed to σ_0 is highly dependent on the viewing angle of the radar relative to the wind direction, hence an accurate wind direction input to the CMOD4 is essential. This is illustrated by figure 7.1. The curves relating σ_0 to wind speed for the possible angles between wind direction and the radar look angle (denoted as f) show the compensation made by the model for cross wind viewing angles. That is, when f equals 0° (upwind) the maximum σ_0 is measured and the estimated wind is therefore lower than that for the same σ_0 value corresponding to f equals 90° (cross wind). Although it has proved successful when used with scatterometer data, the CMOD4 can fail close to fronts and in low winds (< 4 ms^{-1}) where, across a sampling area of 50 x 50 km, the wind direction is highly variable. A similar wind extraction model for the scatterometer data developed by Wismann (1992) also found problems estimating low wind speeds. The CMOD4 adopts an approach using directional wind data from external sources, such as forecasts from the ECMWF, to improve quality (Stoffelen and Anderson, 1993). The lack of directional information from SAR is not considered to be a problem, because wind direction is available for first comparisons from *in situ* measurements and on an operational basis from surface measurements recorded on meteorological synoptic charts. Directional wind information may also be derived directly from the image, either by eye, using features such as wind streaks off the land or atmospheric rolls (Gerling, 1986). Where such information is available it may be used to verify or improve the chart data, increasing confidence in the result.

7.2 FACTORS AFFECTING THE BACKSCATTER RELATIONSHIP WITH WIND SPEED

The influence of wind fetch, wind direction, wind speed, atmospheric boundary layer (ABL) stability, sea surface temperature (SST), wave slope and weather fronts on the small scale surface roughness fluctuations detected by SAR need to be considered. This section summarises the research to date on these factors.

Measurements by Large and Pond (1981) showed that, in unstable conditions the convective mixing from the upper layer transfers energy down to the sea surface. The only quantitative measurements of backscatter variations obtained over a range of wind and atmospheric conditions were made by Keller *et al.* (1989), using a tower-based C-band scatterometer with an incidence angle of 45° in the North sea. Measurements show an increase in backscatter for given wind speeds in unstable conditions. They computed a vertical wind speed profile for unstable conditions, which demonstrates the increase in wind speed at the sea surface, accounting for increased σ_0 in unstable ABL conditions. According to their results the relationship is not linear and air:sea temperature differences beyond ± 2°C do not significantly vary the backscatter. Results from Alpers and Brummer's (1994) work in the German Bight also suggest ABL instabilities are associated with increased backscatter for given wind speeds.

Backscatter dependence on factors such as SST becomes apparent at low wind speeds of the order 3 to 6 ms^{-1} (Liu, 1984 and Topliss *et al.*, 1994). Local instabilities in the ABL across a SST front can also generate transient convection breezes that, in light winds, can cause changes in the sea surface roughness detectable by radar (Askari *et al.*, 1993). In a coastal region SST features are unlikely to be sufficient to generate this effect, although, localised instabilities in the ABL caused by land-sea convection breezes, transition from a land to marine wind regime or atmospheric fronts could produce a similar result.

Wind direction, on or offshore, is considered to have an important effect on wind turbulence in the coastal zone. According to Large and Pond (1981), turbulence decreases with increased fetch across the sea. Their research identified selected cases where higher drag coefficients were caused by transient winds; a land breeze or offshore wind generates a new wave field which would be expected to have a greater surface roughness. Smith (1988) estimates that, for offshore winds, it may take a fetch of up to 100 times the measurement height (10 m) before the marine wind profile is established (1 km). Anemometers located at a shoreline will therefore often underestimate marine winds during periods of offshore winds.

According to Keller *et al.* (1989) the effects of wave slope on σ_0 are neglible and can only be detected in stable ABL condtions, that is when turbulence is low.

7.3 VALIDATING WIND SPEED ESTIMATES FROM SAR

Testing the validity and utility of CMOD4 as a routine method for deriving wind speeds from SAR requires an investigation of both the accuracy and sensitivity of the technique. The accuracy of the chart winds and the possible errors inherent in comparing SAR wind speeds with these data are discussed. The influence of factors such as: wind fetch; localised land effects; atmospheric boundary layer (ABL) stability and weather fronts; are considered in the analysis of the results.

7.3.1 Analysis of *in situ* measurements compared with SAR-estimated wind speeds

In order to study the accuracy of the mean wind speed and the spatial variations in estimates from SAR the data were compared with *in situ* measurements. Comparing spatial (SAR) with temporal (*in situ*) measurements along a transect involved using ship data collected 30 minutes either side of the SAR overpass. The assumption is made that the statistics of any variability seen in space are equivalent to those measured over time, provided no large scale disturbances, such as an atmospheric front, pass through the area during sampling. In an attempt to overcome the fundamental problems when comparing space with time measurements the ship sampling interval was set as near as possible to the SAR nominal resolution (25 m). Sampling at 10 second intervals at a boat speed of approximately 3 ms^{-1} is spatially equivalent to 30 m intervals. Any processing of the data, such as averaging, could then be carried out at similar periods.

Contemporaneous *in situ* time series measurements of wind speed and direction were made for SAR overpasses acquired on the following days: 28.5.93; 2.7.93 and 6.8.93. Figure 7.2 shows the ships tracks sampled for each day. *In situ* weather conditions were relatively constant on all three days, a standard deviation (SD) of 0.68 ms^{-1} was the maximum wind speed variability observed (table 7.1); it is reasonable to expect that the mean *in situ* measured wind speed would be equivalent to the average wind speed derived from the sea area viewed by SAR. The *in situ* wind speed measurements were corrected to the reference height of 10 m (U_{10}) to represent surface winds. *In situ* air and sea surface temperature measurements were used to determine the stability of the ABL and the wind speed data were adjusted accordingly, using the relevant coefficient derived from tables compiled by Smith (1988); where the sea is warmer than the air constitutes unstable ABL conditions. Surface current effects on the wind profile were also accounted for before comparison with the CMOD4 results.

The ship tracks were registered to the SAR images in order that pixels coincident with the sample lines could be identified and backscatter evaluated without distortion by resampling of the radar radiometric values. To obtain a SAR sample considered representative of the average conditions at each point along the track the data were block averaged by 5 x 5 pixels (to 125 x 125 m resolution), as described in § 5.4.1. SAR-derived wind speed estimates were then calculated using the mean *in situ* measured wind direction as the input to the CMOD4. To maintain comparability between the data sets the *in situ* wind speeds were averaged at 40 second intervals, approximately equivalent in temporal terms to a 100 m sample interval.

The representativeness of the SAR-derived wind speeds relative to the direct measurements made *in situ* was then assessed. Figure 7.3(a) shows the mean SAR estimates and the mean *in situ* meaurements for the three days sampled. The results for 2.7.93 match closely, the means are considerably less than 1 SD apart (error margins shown). The values for 28.5.93 are also considered a good result, with SAR estimates well within the error bands of the CMOD4 model of ± 2ms^{-1}. The mean values differ by 1.2 ms^{-1} and 0.3 ms^{-1} respectively (table 7.1). The results from 6.8.93 were markedly different, estimates of wind speed from SAR being 3 ms^{-1} or more below measured values. This image, and another for 10.9.93, were supplied by the I-PAF and both considerably underestimate the wind speed. Since these were the only images supplied by the I-PAF it was not possible to determine whether there is a systematic error or whether the low σ_0 values, and therefore wind speed underestimates, are a real feature. Effects such as the suppression of σ_0 in atmospherically stable conditions are not thought to explain the problem, given that the 2.7.93 image was obtained in similar conditions.

Second, a comparison was made between the trends and magnitude of the variability of the synoptic (SAR) and temporal (*in situ*) data. Figure 7.3(b) displays the *in situ* measurements (dashed) and wind speed estimates from SAR (solid) along the transects. Similarities in trends in the data are best on 6.8.93, but the match with absolute values was worse. The beginning of the profile on 28.5.93 also follows the ships data very closely, but as on 2.7.93 dips in the *in situ* data are not detected by the SAR. At the point of nearest coincidence with the SAR overpass (marked by the arrow on the profiles) the match is very good for 28.5.93 and 2.7.93, differences between the *in situ* and SAR-derived wind speed estimates being less than 0.5 ms^{-1}, on both days. Values of SD calculated for the data show that in terms of magnitude the variability of the data compare favourably, the maximum difference in SD is 0.22 ms^{-1} on 28.5.93 (table 7.1). The effects of tide on the sea surface roughness are not considered to account for the variations in the trends between the estimated and measured wind speeds. The maximum variability in both the ship and SAR wind profiles occurred on 28.5.93, when virtually slack water conditions existed (< 0.1 ms^{-1} current), compared to slightly stronger currents of 0.5 ms^{-1} on 2.7.93. The SST was constant along the profiles and is not considered a significant influence. A more valid explanation is thought to be provided by the very variable nature of the wind direction along the ship's track. On the 28.5.93 the wind direction varied from 135° to 335° and, given that the CMOD4 uses the mean wind direction to estimate wind speed, it is not unreasonable to suggest that variations from the measured winds may be a result of localised changes in the wind direction. The model is extremely sensitive to wind direction input (§ 7.2.1.2) and studies of inshore wind field variability on scales of the order of 100 metres would require synoptic *in situ* wind direction measurements, such as from buoys, to achieve an accurate picture of local winds. However, for the study of mean trends at longer scales (km) the results are encouraging.

The field study was limited by physical practicalities, the region being close inshore and therefore subject to local wind variability and possible tidal interaction with bathymetry. Despite the complexities of the area, the results from the 28.5.93 and 2.7.93 comparison of the mean *in situ* measurements and SAR estimates of mean wind speed were very encouraging, indicating that further investigations would be worthwhile.

Table 7.1 Statistical comparison of *in situ* measurements and SAR estimates of wind speed.

Date	Wind speed statitstics (ms^{-1})								ABL stability (Ta-Ts)
	mean wind speed		maximum wind speed		minimum wind speed		standard deviation (SD)		
	in situ (±2)	SAR (±2)	*in situ* (±2)	SAR (±2)	*in situ* (±2)	SAR (±2)	*in situ*	SAR	
28.5.93	4.6	5.8	6.6	9.17	3.4	4.1	0.64	0.86	neutral
2.7.93	3.1	2.8	4	4.6	1.6	2	0.46	0.52	stable
6.8.93	6.8	3.2	8.8	5.4	5.3	2.3	0.68	0.55	stable

7.3.2 Comparison between SAR wind speed estimates and Meteorological chart data

Further validation of the CMOD4 as a technique to estimate wind speeds from ERS SAR was achieved by using the hourly British Isles synoptic charts as a source for wind information; chart wind directions were used as the input to the model and the chart measured wind speeds were used for comparison with values derived from SAR. Using this method enabled quantitative analysis of all 30 images acquired for this study, giving wind speed estimates over varied meteorological and tidal conditions. Confidence in the chart records of wind speed and direction was given by the close match with *in situ* wind measurements (average ship wind directions were within 10° of the St Catherines Point measurements on all 3 field experiment days). The suitability of using these data was further tested by plotting average chart wind speeds against average backscatter from the range profiles (figure 7.4). Apart from a few outliers a monotonic, almost exponential curve is observed from the SAR backscatter relationship with wind speed. The scatter is greater about the mean at the lower end of the wind spectrum (<5 ms^{-1}), suggesting other factors are influencing σ_0 at low wind speeds. Variable wind direction is considered to be the main source of error when estimating low wind speeds using CMOD4 (Stoffelen and Anderson, 1993) and may account for the scatter.

The 'wide range profiles' extracted to investigate backscatter dependence on incidence angle (described in § 5.4.1) were used to calculate wind speed across the entire 100 km SAR range.

The sample size (5 x 5 pixels) is effectively the same as that used for comparison between the SAR and *in situ* measurements, but with further averaging applied in the azimuthal direction to cover a wider area, reducing speckle effects and producing estimates of wind speed at 125 m intervals in the range direction. It was established in the analysis of the backscatter across range (Chapter 5.4.3) that surface backscatter can be surprisingly uniform over distances up to 100 km. Investigation of wind field variability across the range, using surface wind measurements from meteorological stations at either end of the transect as reference points, is therefore considered a valid approach. The following stations were used: Channel Lightvessel; Portland Bill; Isle of Wight; Portsmouth; Beachy Head; and occasional ship reports when available. The stations are mainly land based and care was taken to gain an overview of weather patterns throughout the English Channel, to avoid biasing the data for land conditions.

To assist comparison, the estimated U_{10} values from SAR are plotted from west to east across the range and a line is overlain depicting a simple linear interpolation between the wind speeds taken from meteorological stations at each end of the transect (figure 7.5). This enables the overall trend of the CMOD4 wind speeds to be compared with the inferred trend in wind speed across range, as well as with mean chart values. Chart surface winds are measured to ± 1 ms^{-1} accuracy and the SAR derived winds to ± 2 ms^{-1}, error bars on the graphs show the overlap between the data. The Isle of Wight occurs in a few profiles (where it is labelled, figure 7.5) and was left to show the proximinity of land and the effects on the local wind field. In many cases the wind speed profiles were uniform across distances of 25 km or more and could easily be matched to chart observations. Range profiles for 12.2.93, 4.4.93, 22.5.93, 28.5.93, 2.7.93 and 31.7.93 closely conform to chart predictions for wind speeds ranging between 2.5 and 6.25 ms^{-1}. It is encouraging that even where the wind speed varies considerably across the profile, the trend in many of the profiles still closely conforms to the chart observations, for example: 19.3.92; 24.1.93;17.4.93; 9.5.93.

The sensitivity of the SAR to variations in wind speed of at least 1 ms^{-1} is demonstrated by the trough in the data observed on the image acquired on 23.4.93. The passage of an occluded front through the imaged area, shown by the synoptic chart, corresponds to a sudden decrease in the wind speed estimate. The overall trend in the data still closely matches that of the chart values. Images collected during calm conditions record backscatter values below the noise threshold for SAR (-25 dB). The CMOD4 sets the wind speed to a virtually horizontal profile between 1 and 2 ms^{-1}. These conditions occur on 19.3.93, 3.5.93 and 7.6.93. The latter two exhibit slight variability in the profile to the east and in the middle respectively, again demonstrating the sensitivity of the technique to very slight changes in wind speed. The highest winds in the sequence occurred on 13.3.92 when the chart records surface values of 17 ms^{-1} at the western end of the transect. This maximum is reached in part of the image but large fluctuations in the wind speed of up to 5 ms^{-1} take the average value below that predicted, although the overall trend is similar.

There is only one case, out of the thirty images analysed, in which there is no overlap between the estimated wind (± error bars) and the chart wind. This occurs on 10.9.93 when the model calculates an average wind speed of 5.2 ms^{-1} compared to the chart average of 11.25 ms^{-1} and *in situ* measurements within the western Solent of 10.5 ms^{-1}. As discussed in § 7.3.1, this image was one of the two processed by the I-PAF. The other is the image for 6.8.93 which underestimates the wind speed by more than half. Of the remaining data, all from the UK-PAF, only the 12.7.93 gives an underestimate of wind speed similar to that on 6.8.93. Whether there is a problem with the I-PAF data is at present undetermined; samples of the land have a similar mean and range as the UK-PAF data, so a simple difference in offset is probably not the cause of the anomally.

7.3.2.1 Statistical analysis of the CMOD4 wind estimates across range

The relationship between the mean SAR-derived wind speeds across the range profile and the mean chart wind speeds was investigated to determine the validity of using CMOD4. Figure 7.6 shows that the data follow a positive linear trend with only one anomalous value from 10.9.93. Omitting this value from the calculation of the regression statistics improved the standard error of the estimated wind speeds from 1.27 ms^{-1} to 0.98 ms^{-1} and the regression coefficient (r^2) by almost 10% to 0.87. That a good correlation exists between the data is demonstrated by the low degree of scatter about the predicted regression line, 95% of the data falling within ± 0.74 ms^{-1} of the predicted CMOD4 wind speed at the intercept and within ± 0.12 ms^{-1} at the mean. Notably, the scatter about the mean is greatest at the lower wind speeds (4 ms^{-1} and less), similar to the distribution of points for the simple fit of σ_0 to wind speed in figure 7.4; the effects of other parameters on σ_0 at low wind speeds remains to be investigated. Confidence in the results is increased by the proximity of the regression line to the ideal relationship where the gradient is 1. The distribution of points about the calculated regression line may reflect the natural occurrence of stable or unstable conditions. The data are therefore examined according to their position about the line of equivalence, which passes through the origin (marked on figure 7.6).

Possible causes of scatter of the data about the regression line were investigated in terms of ABL stability and wind fetch. Figure 7.6 divides the data according to the stability of the ABL, solid markers denoting stable and empty markers unstable conditions. The wind direction is separated into two groups and plotted according to whether it is off the sea (fetch unlimited) or offshore (fetch limited) conditons, wind off the land being plotted as squares and off the sea as diamonds. The following hypotheses were examined in relation to the data:

- Points above the equivalence line correspond to unstable ABL conditions and those on or below the line indicate a stable situation.

- Offshore winds will be associated with an increased sea surface roughness and therefore estimates of wind speed from SAR in these conditions will lie above the equivalence line.

The majority of stable points do lie on or below the equivalence line, only two cases overestimating the wind speed (17.4.93 and 9.5.93). These two may be accounted for by underestimates of the marine wind field by the coastal station, since the wind direction is offshore. Orographic acceleration of the wind may be also be affecting the σ_0, but are unlikely to be registered on the synoptic chart. However, although four of the unstable points are clearly above the line and only two are below, several points in both categories lie on or very close to the equivalence line, implying that ABL stability is not a major influence on σ_0 in this region.

Where the wind is offshore five of the twelve points indicate an overestimate of wind speed using SAR. Whether these differences can be attributed to underestimates of the wind by the meteorological stations, or are a localised effect of the transition from land to marine flow on the sea surface roughness, is uncertain. In light, offshore wind conditions (<5 ms^{-1}) the wind estimates mainly fall below the line. The one instance of offshore, light wind conditions where the SAR-derived wind is an overestimate, the wind is from the east. It is suggested that as the wind flows across the Isle of Wight it becomes increasingly turbulent and produces a corresponding increase in the small scale surface roughness. The unusual circular pattern in the σ_0 signature observed inshore, to the west of the Isle of Wight on this image (12.2.93, plate 6.8), reinforces this idea. Furthermore, the range profile for this day (figure 7.5) shows the wind estimate to be much closer to the chart value to the east, where it is unaffected by orographic influences. The effects of local convection winds associated with cumulus clouds were also considered, but the synoptic chart and AVHRR visible image record 100% stratus cloud cover. Fourier analysis of the image gives a wavelength of roughly 6 km for these features (§ 7.5). Although two other images exist with similar wind direction and speed, the surface roughness pattern is not detected again.

7.3.3 Summary of wind speed estimates

Estimates of wind speed from SAR were surprisingly good, the profiles in figure 7.5 are virtually superimposed in several cases and for most instances the error bars for the CMOD4 estimates and chart values overlap, the profiles following similar trends. Given that the chart profile is based on surface wind speeds measured approximately 100 km apart, at either end of the SAR profile, and the chart and CMOD4 data are accurate to ± 1 ms^{-1} and ± 2 ms^{-1} respectively, the standard error of ± 0.98 ms^{-1} achieved in the comparison of average chart and estimated wind speeds is considerably better than expected. The sensitivity of the SAR data to slight changes in wind speed illustrates the importance of using the most accurate calibration procedure available.

The effects of ABL stability and wind fetch did not appear to influence the total backscatter measured by SAR. Differences between SAR estimates of wind speed for varied fetch and ABL conditions, for the same chart wind speeds, are slight (in the order of 2 ms^{-1} for winds ranging from 2 - 12 ms^{-1}) and insufficient numbers of points fall into the same wind speed groups. In addition, the strong dependence of the CMOD4 estimate of wind speed on wind direction relative to the SAR look angle (figure 7.1) means any deviations from chart winds could easily be credited to inaccuracies in the wind direction. For this study wind directions are an average between the two stations at either end of the profile and the assumption is made that the wind direction is uniform across the SAR swath. The correspondence between the SAR and chart wind speed trends, even when an atmospheric front occurs within the sample region, considerably increases the confidence in the results.

In light wind conditions σ_0 is more easily influenced by factors other than direct wind speed, such as ocean surface dynamics and surface surfactants. Considering over half of the images sampled for this study were acquired in winds of less than 6 ms^{-1}, this may account for the spread of results about the line of equivalence. There is scope for further work, possibly best suited to repeatable airborne or tower experiments or 3-day repeat data from a SAR, using an open ocean region to decrease the number of factors influencing sea surface roughness.

CMOD4 was derived in open ocean conditions and its applicability to a coastal region was in question. For example, according to Smith and Banke (1975) waves in the coastal region are steeper and have a higher aerodynamic roughness than open ocean conditions. Whether this affects the backscatter measured by SAR is uncertain, although the SAR derived wind speeds for the present study are surprisingly accurate if this were the case. The technique has proved sufficiently successful to enable it to be used to investigate small-scale and mesoscale variability in the wind field.

7.4 EXAMINING HIGH FREQUENCY WIND SPEED VARIABILITY USING SAR

To investigate high frequency variability the low frequency wavelength features are removed from the range profiles. A high pass digital filter was designed using a frequency cutoff which left only spatial scales between 125 m and 800 m for analysis. The SD of each filtered profile was then calculated and plotted against mean SAR-derived wind speeds (figure 7.7).

High frequency variations in the wind speed profiles could be attributed to small scale turbulence in the wind field, sea surface processes or instrument noise. If it is assumed that the values estimated are representative of the wind speed, then the variability of the profiles can be examined for dependence on the following factors, which are hypothesized to increase the high frequency variability of the wind field and therefore, the high frequency variability of the Bragg waves:

- Increased wind speed.
- Turbulent flow off the land.
- Decreased fetch.
- An unstable ABL.
- Wind against tide.

In figure 7.7 the data are grouped according to ABL stability and fetch. The graph shows a strong, positive linear relationship between fluctuations in the wind speed and the mean; the variability increases with wind speed as hypothesized. Scattering of the data is within one SD for wind speeds below 7 ms^{-1}, irrespective of fetch and stability conditions. Calculation of the regression statistics gave an r^2 value of 0.947 and a standard error of ± 0.014 ms^{-1}. Between wind speeds of 7 to 8.8 ms^{-1} there is a noticeable gap in the observations and data lying in the higher wind speed group are scattered either side of the line.

The results support the hypothesis that high frequency variations in the SAR-derived wind speed profiles are associated with small scale near-surface turbulence in the wind field. The degree of gustiness or local variability of the wind field is directly proportional to the mean wind speed; increases in wind speed result in an increase in the variability. This must also indicate that the small scale surface waves respond directly to variations in the near-surface wind conditions. Any deviatations of the data from the linear relationship (outliers on figure 7.7), indicate that factors external to the natural variance of the wind speed are contributing to the small scale sea surface roughness.

Wind direction was expected to be an important factor, affecting the small scale turbulence detected by the wind speed profiles in the coastal region. Wind blowing offshore is both more turbulent (gusting) and fetch limited. A developing wave field is generated, which may be associated with a rougher sea surface than for fetch unlimited conditions. Localised orographic modulation of the wind field, caused by friction, funnelling, eddying and sheltering effects, produces features on the SAR images, such as dark regions in the lee of the land or streaks of bright or dark backscatter extending several kilometres offshore. Although examples of these features are seen on several images (12.2.93, 17.4.93, 16.8.93 and 4.9.93 with wind directions 90°, 315°, 10° and 45° respectively, plates 6.8, 6.12, 6.27 and 6.29), there is no evidence that the surface wind field is more turbulent in these regions. The points marking wind off the land (square) or sea (diamond) appear to be equally distributed about the regression line on figure 7.7. Similarly, other long wave trends observed in the wind speed profiles, such as on 13.3.92, 22.3.92 and 23.4.93 (plates 6.2, 6.5, 6.13), possibly caused by ABL instabilities generated in the transition from land to marine flow, do not appear to increase the variability relative to the mean wind speed.

The influence of ABL instabilities on the high frequency variability of σ_0 in the coastal zone was the next factor to be considered. The air:sea temperature difference is calculated for all the images using air and sea temperature information from the synoptic charts. It should be noted that this is only a rough indication of ABL conditions. In the coastal region instabilities in the boundary layer are likely to be present much of the time due to the transition from the land to sea environment (Guymer, pers. comm.). The empty boxes plotted on figure 7.7 denote unstable ABL conditions (sea warmer than air). Their relatively uniform distribution about the regression line suggests that instabilities in the ABL do not significantly change the variability of the small scale roughness in the coastal environment. Atmospheric rolls are often a result of instabilities in the boundary layer and are detected on several of the images. Profiles including these features do not exhibit any increase in the variability of the wind speed. In the light of these results and work by Keller *et al.* (1989) it is unlikely that ABL instabilities can be used to explain the high variability observed on 28.2.93 (point B on figure 7.7), although extremely unstable ABL conditions (+8 °C) existed. Another instance of very unstable conditions (>+2 °C) did not influence small scale boundary layer turbulence either.

In a region of strong tidal currents such as the English Channel, it might be expected that wind against tide would steepen the small wind waves, effectively increasing σ_0. The high frequency variability of the profiles was therefore examined in terms of tide relative to wind direction. A range of tidal states was covered by the images, including a wind of 5 to 8 ms^{-1} against a 2 ms^{-1} tidal current on 12.2.93, but there is no evidence that steepening of the small wind waves by tidal current interaction with the wind results in any increase of the small scale sea surface roughness detectable by SAR. It is probable that turbulence in the coastal zone will be relatively high at all times, obscuring any slight modulation of the wind waves by tides.

The close conformation of the data to the regression line despite the diversity of fetch, orographic, wind versus tidal currents and ABL effects, suggests that these factors are not producing a significant contribution, additional to the effects of wind speed, to the small scale sea surface roughness. The occurrence of an atmospheric front within the area imaged is associated with a high degree of variability, as shown in the wind speed profiles for 23.4.93 and 22.8.93. The SD calculated for both these days lies above the regression line (points A and C on figure 7.7). On 23.4.93 the transition across the boundary is clearly marked by a dark band on the image, orientated north to south (plate 6.13). On the range profile this can be seen as a large dip in wind speed, to the east of which the surface wind turbulence increases (figure 7.5). This sharp transition in the wind field does not occur on the 22.8.93 range profile, which also appears more variable (figure 7.5). Considering the relatively lower SD of the data acquired in higher wind speed conditions on the 13.3.92 (point F on figure 7.7) and 24.1.93 (point G on figure 7.7), these effects cannot be attributed to wind speed alone.

The high variability relative to the mean SAR-derived wind speed is indicative of the effects of sudden increases in atmospheric turbulence on the sea surface. The concept of the sea surface wave field becoming essentially rougher in response to a disruption in the mean wind flow, such as could be caused by the passage of an atmospheric front or the transition from terrestial to marine flow, was suggested by Smith (1988). The SAR data provide information on the response time, or sensitivity of the short waves, to these sudden changes in the wind field.

In figure 7.8 the data are presented as a plot of the SD of calibrated σ_0 versus mean SAR-derived wind speed. The data are very scattered indicating that direct measurements of the variability of σ_0' do not follow a linear relationship with wind speed. Comparison of figures 7.7 and 7.8 demonstrates the variability of σ_0' due to the effects of changes in incidence angle and wind direction relative to the SAR view angle. The CMOD4 removes these effects (referred to as f and θ_n respectively) for the calculation of wind speed from SAR. It is suggested that using CMOD4 estimates of wind speed from the SAR data gives a better indication of the surface roughness distribution than the directly measured σ_0'.

The good correlation between wind variability and the mean wind speed suggests that the high frequency variability of a wind profile might be used to test the accuracy of the wind estimate. If outliers from the regression line (figure 7.7) are genuine, it would be possible to account for their position in terms of processes affecting σ_0 and wind speed. SAR-derived wind speeds that were considered under- or over-estimates, with reference to the synoptic chart surface values, would therefore be true representations of local conditions, as long as the SD of the high frequency variability lies on or very close to the regression line. Outliers would be considered to indicate that factors additional to the mean wind speed, such as oceanographic processes or air:sea interaction effects, are modulating the small scale sea surface roughness.

7.4.1 Tidal current interaction with bathymetry

The initial factors which were hypothesized to increase the variability of the short wave field do not account for the main outliers from the regression line on figure 7.7. Tidal current interaction with bottom topography was therefore considered as an explanation for these outliers. This possibility had previously been discounted, since the range profiles were taken in a region of deeper water, generally greater than 25 m in depth. Visual analysis of the data did not initially suggest bathymetric signatures. After more detailed analysis, with reference to the high frequency variability, faint lines observed on some images could be associated with topographical modulations (9.5.93 and 22.8.93, plates 6.15 and 6.28). A transition in the bathymetry occurs at 1°20′W, just south of the Isle of Wight, between a relatively uniform region (30 m or more) to the west, and a slightly shallower and more variable regime to the east. A corresponding variability in the tidal currents is found across the region, weak currents to the west, on average 0.5 to 1 ms^{-1}, compared to 1 to 2.25 ms^{-1} to the south and east of the Isle of Wight. The transition between regions can be detected in the small scale variability of the sea surface, as illustrated by the plots of differences in the profiles of SAR-derived wind speeds across range for 22.3.92 and 28.2.93 (figure 7.9). Where the profiles enter the slightly deeper water in the far range (at 700 pixels across on 22.3.92 and 600 pixels across on 28.2.93) the variability decreases by approximately a third.

Accounting for the outliers in terms of tidal currents proved convincing; the points B, C, D and E on figure 7.7 were all collected at a time of strong flood tides (around 1.35 ms^{-1}) and slight changes in the bottom slope were found to correlate with the long wavelength trends observed in the wind speed profiles (figure 7.5, 9.5.93 (D) and 22.8.93 (C)). In comparison points F and G, lying below the regression line (figure 7.7), were acquired in slack water conditions.

7.4.2 Categorising sea surface variability turbulence parameters

It was sought to relate the high frequency variability of the wind field (in terms of the SD) with the factors modulating the sea surface roughness. The ability to categorise factors affecting small scale sea surface roughness within a coastal region, using the variability of the wind speed, would be a useful analytical tool. This could offer the user a means of distinguishing between ephemeral wind driven features and dynamic oceanographic signatures. The ratio between SD and wind speed was investigated to determine whether characteristic values of the ratio could be defined, which would separate the data in terms of the factors contributing to the sea surface roughness. For example, if the surface roughness is purely wind driven then dividing the data into different wind speed categories (criteria I given in table 7.2) would suggest that high winds are associated with a higher degree of variability than moderate winds. That this is not the case, is demonstrated by figure 7.10(a), the minimum and maximum values for groups 2 and 3 (moderate and higher wind speeds respectively) completely overlap. Only when light winds prevail (group 1) does the ratio unambiguously categorise the conditions.

Using the results from the analysis of the high frequency variability of the wind speed, the criteria are re-defined to include the effects of factors additional to wind speed that are considered to contribute to the sea surface roughness variability (criteria II in table 7.2). Group 1 is a low wind speed category and again is based solely on wind speed. Group 2 is considered to represent average conditions and the main criteria are: a lower wind speed limit only and no current interaction with bottom topography. Group 3 defines the outliers in figure 7.7, where the variability of the wind speed is relatively high in comparison to the mean. The criteria include the passage of an atmospheric front across the study region and, or current interaction with bottom topography, in addition to using wind speed. Zones of current shear would also be expected to fall in this category, but have not been examined in this study.

Figure 7.10(b) illustrates the effectiveness of this classification. The range between the minimum and maximum data is small within the three groups defined in the second set of criteria. Allowing for the importance of current interaction with bottom topography and the impact of weather fronts on the variability of the wind speed profiles gave a successful division of the data into distinct classes. The separation and very small spread of the points within groups 2 and 3 is a surprisingly good result. Looking at the shape of the histograms for detrended wind speed data belonging to the groups defined by category II does not provide a means of recognising the occurrence of factors external to the mean wind speed on the backscatter measured by SAR. As can be seen by figure 7.11 the wind speed data all display a roughly gaussian distribution, irrespective of whether they belong to group 2 (a to d), or fall into group 3, either as a product of tidal current interaction with bathymetry (e and f) or atmospheric frontal effects (g and h).

Table 7.2 Categories defining high frequency wind speed variability

Groups	Criteria			
	Criteria I wind speed	ratio SD/mean wsp min. & max.	Criteria II wind speed, direction, weather fronts & bathymetry	ratio SD/mean wsp min. & max.
1	2-4 ms^{-1}	0.0105-0.0153	< 4 ms^{-1}	0.0105-0.0153
2	4-8 ms^{-1}	0.0158-0.0226	> 4 ms^{-1} no bathymetric effects	0.0158-0.0183
3	> 8 ms^{-1}	> 0.0206	> 4 ms^{-1} bathymetric effects 3-12 ms^{-1} atm. front in image	0.026 - 0.0234

These results could be applied to automatic analysis of SAR images. Examination of the SD/mean ratio could be used to separate images where bathymetric or atmospheric frontal signatures are indistinguishable from the patterns generated by local variability of the wind field. A local weather forecast would determine whether atmospheric frontal effects were a factor. Ideally, a study of the ratio of SD of backscatter relative to mean wind speed (chart or SAR-derived), either along a profile or for a sample area (for example 256 x 256 pixels), would determine to which category the area belongs using the values in table 7.2. If the data fall into group three then it is probable that events additional to wind speed effects are contributing to the sea surface roughness variations.

Of considerable interest are the ratios for the two fetch unlimited high wind speed points (F and G, figure 7.7), which fall well within group 2. Where the wind fetch is unlimited a fully developed wave field would be expected and this may explain the relatively low surface roughness. These two points were acquired in slack water conditions and it was considered whether the regression line is biased to stronger tide conditions. However, using only data acquired for tidal current conditions less than 0.3 ms^{-1} to re-calculate the regression line would not noticeably decrease the gradient. This may indicate that the σ_0 relationship with wind speed becomes non linear at higher wind speeds (above 8 ms^{-1}), marking the beginning of saturation of the backscatter signal at high wind speeds. Alternatively, other unknown processes may be dampening the small scale turbulence in these cases; no rain was recorded on these days.

7.4.3 Summary of high frequency variability

The high frequency variability of the wind speed shows a strong linear relationship with mean wind conditions. The original hypotheses proposed could not account for the variability observed in the wind speed profiles. Although the effects of the local orography noticeably modulate the large scale features observed on the profiles (figure 7.5, 17.4.93) they do not appear to influence the small scale roughness. It was found that factors external to the natural variance of the wind speed, such as the occurrence of an atmospheric front or tidal interaction with bathymetry, result in an increase in the small scale variability. The results from the range profiles examined indicate that only when the flood tide is in the order of 1.25 ms^{-1} was the current interaction with bottom topography sufficient to modulate the backscatter signal. Averaging of the data is considered to have removed the effects of instrument noise and speckle, enabling variations in the wind speed of the order 0 to 0.25 ms^{-1} to be detected. The reduced spatial resolution to 125 m is considered adequate for studies of sea surface variability in the coastal zone. The sensitivity of the SAR to what are considered real variations in wind speed is a surprising result, which is reinforced by the strong linear relationship of the small scale variability with wind speed.

The linear relationship between the high frequency SD of the wind field and the wind speed could prove a useful tool for the investigation of SAR data. If it is assumed that the wind speed estimates are genuine, then data can be categorised in terms of the factors affecting the surface roughness signature measured by SAR. This would not only help the user to separate oceanographic signatures from ephemeral wind features, but also provides a technique for investigating the effects of factors additional to the mean wind speed roughening the sea surface. If average variability can be defined for given wind speeds then backscatter measurements, in an area less complex than a coastal zone, could be used to empirically study deviations from the model in relation to factors such as MABL stability and wave slope.

7.5 LONG WAVELENGTH VARIABILITY IN THE RANGE PROFILES

Longer wavelength variations in the wind field were observed on spatial scales of 1 km upwards from the range profiles of wind speed (figure 7.5). The profiles vary between a surprising uniformity (10.9.93) and large scale fluctuations in the order of 15 km wavelength (13.3.92). The following section seeks to characterise the factors generating these features.

The range profiles provide an indication of the wavelength and amplitude of the surface roughness variations in terms of wind speed (ms^{-1}). However, the profiles may not necessarily cross features orthogonally and therefore estimates of wavelength may not be wholly accurate, nor do they give any directional information. To improve on this, the long wave features on the images were investigated using 2-D Fast Fourier Transform (FFT) techniques. For computational ease a square region was extracted from each image for FFT analysis, covering as much of the sea region as possible. To enhance low frequency wavelengths, remove swell waves and other high frequency wind variability the data were averaged to 200 x 200 m pixels and then smoothed using a 3 x 3 running average, effectively removing any information below 600 m wavelength. Examples of images containing long wavelength features detectable on a power spectrum are shown in plates 6.3, 6.8 and 6.12. Figure 7.12 shows two examples of power spectra, frequency plots of the signal amplitude, for

24.1.93 and 12.2.93. Where a strong power signal occurs on a plot the wavelength and direction are extracted.

Results from the FFT analysis identified a range of wavelengths on scales of 2 to 10 km that are comparable with the features observed on the images and profiles. Observations of persistent long wavelengths (> 4 km) occurring across SAR images have not previously been documented. To study the features in relation to wind driven effects the following two hypotheses were investigated:

- the crests of longer wavelength features align with the wind direction,

- increased wind speed results in longer wavelength features.

Figure 7.13 (a) and (b) respectively show the relationship between the wavelength of the features and the wind direction and speed. The majority of the features are orientated within 20° of the wind direction independent of their wavelength, suggesting they are a product of wind related processes. Separating the data into winds off the land or sea did not identify any relationship with the wavelengths of features observed. Wind speed also appears to be unrelated to the wavelength (figure 7.13, b).

In terms of wind direction the features separate into three main classes: those streaming approximately orthogonal to the land, a result of orographic modulation of the wind field; those parallel to the land, possibly due to the transition from flow over the land to the sea; and those with no land effects. The wavelengths and distance over which features extend are discussed according to these classes.

In offshore wind conditions the variations in backscatter often align with the flow and are attributed to local orographic effects. Examples where the surface is roughned vary in wavelegth from 2.4 km (4.9.93) to 6.8 km (16.8.93). Wind directions between 300° to 50° appear to result in dark bands, such as on 13.6.93, 16.8.93 and 4.9.93 (plates 6.19, 6.27 and 6.29). Modulations of the wind field are in the order of 0.25 to 1 ms^{-1} (figure 7.5), suggesting that only a slight variation in wind speed is required to modulate the backscatter sufficiently that it appears as a strong feature on the image. These effects may extend up to 30 km offshore. On 12.2.93 near circular features are observed on the image, thought to be caused by disruption of the wind field as it flows across the Isle of Wight (wind from the east). Although the image appears more turbulent visually, modulation of the wind speed profile is of the same magnitude as for winds directly offshore. FFT analysis identifies two orthogonal long wave features of approximately 6 km wavelength.

Long wavelength features associated with winds approximately parallel to the coast occur when the wind is westerly (250° to 280°) and the crests align closely with the direction of flow. The wavelengths of the features vary from 2 to 10 km, similar to the land effects, but the modulation of the wind field can be as much as 4.5 ms^{-1}, as on 13.3.92. However, in most cases modulation of the wind field is of a similar order to that for events controlled by orography (0.25 to 1.5 ms^{-1}) and, again, the background sea surface roughness decreases, creating dark bands. Examples of these features occur on the 13.3.92, 22.3.92, 17.4.93, 6.8.93 (plates 6.2, .6.5, 6.12 and 6.26) and more weakly on 24.1.93 (plate 6.7), the bands varying between 1 to 2 km in thickness, rather wider than the features generated by flow off the land. Features with narrower banding, but with similar characteristics, occur on 10.9.93 (plate 6.30). The cause of these features is not well known but may be attributed to the transitional nature of the wind field between land and sea, resulting in ABL instabilities.

Long wavelength features aligning with winds off the sea (240°) may result from the wind elongating surfactant material into narrow streaks (approximately 100-200 m in width), effectively dampening the surface roughness signature and producing dark streaks. Images containing these features were acquired in light wind conditions (<3.5 ms^{-1}), during late spring and summer (28.5.93 and 2.7.93, plates 6.17 and 6.21). At which time the organic blooms are a source of slick material. The streaks are several kilometres long and are distributed across the image, the spacing varying between images from 5.8 km to 2 km respectively; whether these long wavelength, wind driven features reflect the mesoscale variability of the wind field is uncertain.

Two images where the crests of the dominant wave features are virtually orthogonal to the wind direction, with relatively short wavelengths (2 to 2.7 km) were acquired on 16.3.92 and 22.5.93 images. These are thought to be caused by atmospheric lee waves as discussed in Chapter 6.

7.5.1 Summary of low frequency variability

Deriving directional and wavelength information from the images and wind speed range profiles proved an effective means of investigating long wavelength features observed on SAR images. The long wavelength surface roughness features are ascribed to mesoscale variability in the wind field rather than dynamical oceanographic processes for the following reasons: the alignment of the features with the wind direction; length scales; lack of distortion of the features and the continuity across the entire 100 km swath. Where land interaction with the wind field occurs the long wavelength variations are sufficient to noticeably modulate the sea surface. Where the wind is directly off the sea variations in the surface wind field are determined from patterns in the distribution of surfactant material. Whether winds off the sea are sufficiently variable to modulate the backscatter is unknown.

Using FFT analysis is a possible means of separating atmospheric and ocean events on SAR. Meteorological features appear more likely to exhibit a repeatable pattern across an image, whereas the localised nature of surface dynamic effects, such as current interaction with bathymetry, will not be identified on the power spectrum. However, the FFT is not an entirely suitable method for studying long wavelength features associated with variability of the wind field because the features are so diffuse. Also, where an image contains the coast it is often difficult to sample a sufficiently large square area to include enough repeats of the feature. The result is a weak power spectrum that requires considerable filtering and much subjective analysis to identify the features. It is likely that if the FFT was applied to the entire sea area the results would be improved, but at this stage better and quicker analysis can be achieved by eye directly from the image.

7.6 CONCLUSIONS

The close match of SAR-derived wind speed estimates using CMOD4 with winds from synoptic charts was extremely encouraging, the errors well within the ± 2 ms^{-1} given for the model. The model requires a wind direction input and, although the information is not measured by the SAR, except by visual inspection when low frequency features such as ABL rolls and orographic streaming occur, this work demonstrates the effectiveness of using routine surface wind direction measurements from meteorological stations for analysis of SAR in the coastal reigon. The high resolution achievable for wind speed estimates enables features, such as atmospheric fronts that are below the resolution of the scatterometer, to be detected by characteristic wind speed variability.

The study was not originally designed with the investigation of wind effects in mind, the complexity of variables affecting sea surface roughness in a coastal zone being far from ideal. However, by sampling a sequence of images across the entire 100 km range it was possible to study in detail the small and mesoscale variability of the wind field over varied wind and tide conditions. The strong linear dependence of the high frequency variability on wind speed not only improved the confidence in the CMOD4 estimates, but enabled features to be characterised in terms of factors affecting small scale surface roughness. If this relationship can be established for other regions, it will provide a technique for separating oceanographic contributions to the surface roughness signal from the effects of natural variations in the wind field. It will also provide a method for further investigating the effects of factors additional to wind speed, such as ABL stability, wind fetch, swell, orography and tidal interaction with bottom topography, on the backscatter signal. Comparisons of SAR-derived estimates of wind speeds from different wave regimes, for example coastal and open ocean conditions, may also provide a method for quantitatively assessing differences in surface roughness for given wind speed conditons; these factors can significantly influence air:sea flux calculations.

It has been established in this chapter that CMOD4 can be used to accurately estimate wind speed from SAR. It can be assumed from the consistent results achieved using wind speed, compared to those from direct measures of backscatter, that the corrections for the dependence of backscatter on incidence angle and radar view angle relative to the wind direction are an important factor in recovering a measure of surface roughness. If comparisons are to be made between SAR images in terms of the backscatter signature of surface roughness then it is essential these effects are removed, maintaining the same linear dependence of image intensity on surface roughness between images. A detailed investigation of the magnitude and importance of these corrections is given in Chapter 8.

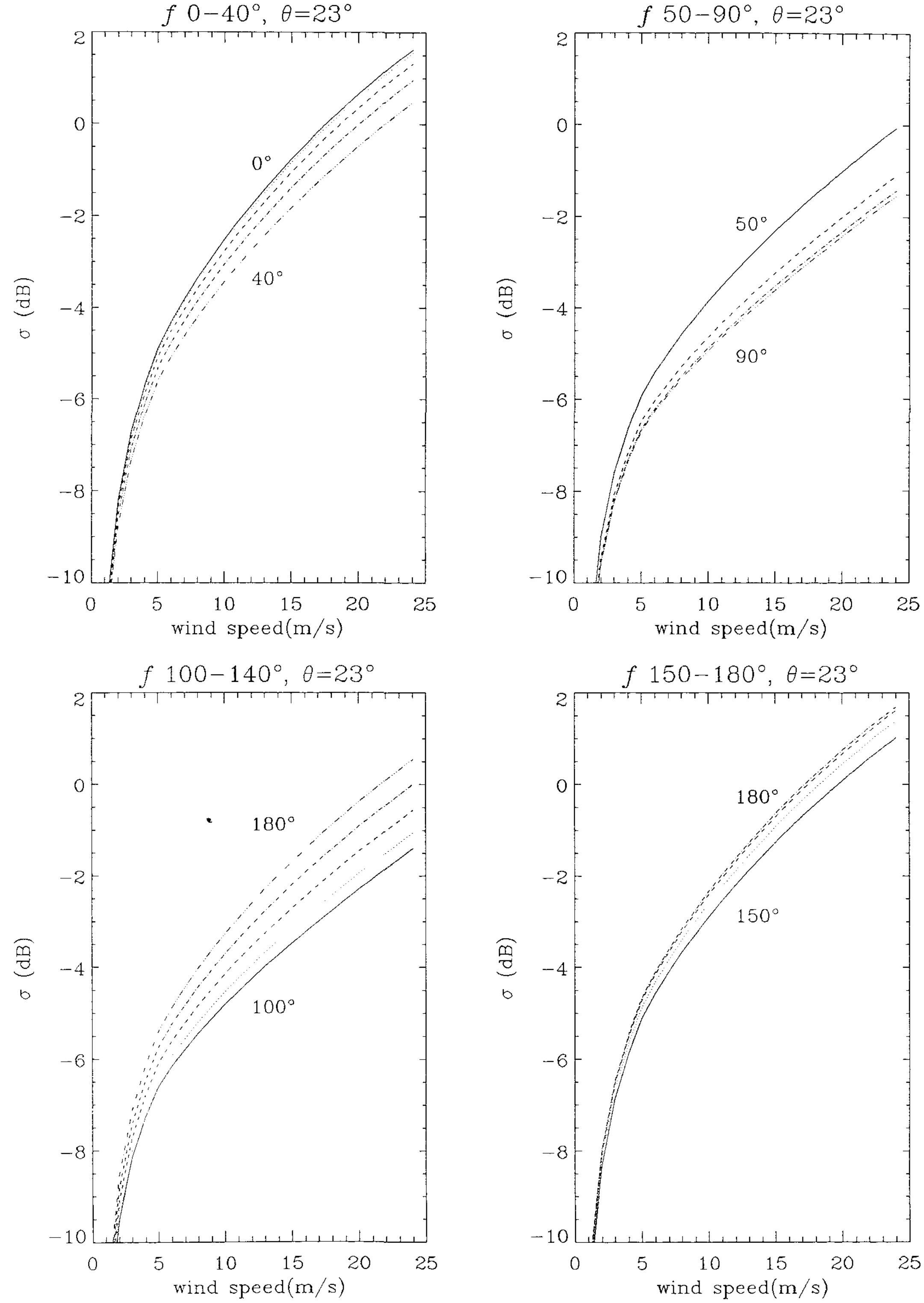

Figure 7.1 CMOD4 empirically derived curves relating backscatter to wind speed. The plots show the dependence of backscatter on the radar view angle relative to the wind direction (*f*) at the SAR reference incidence angle (θ = 23°).

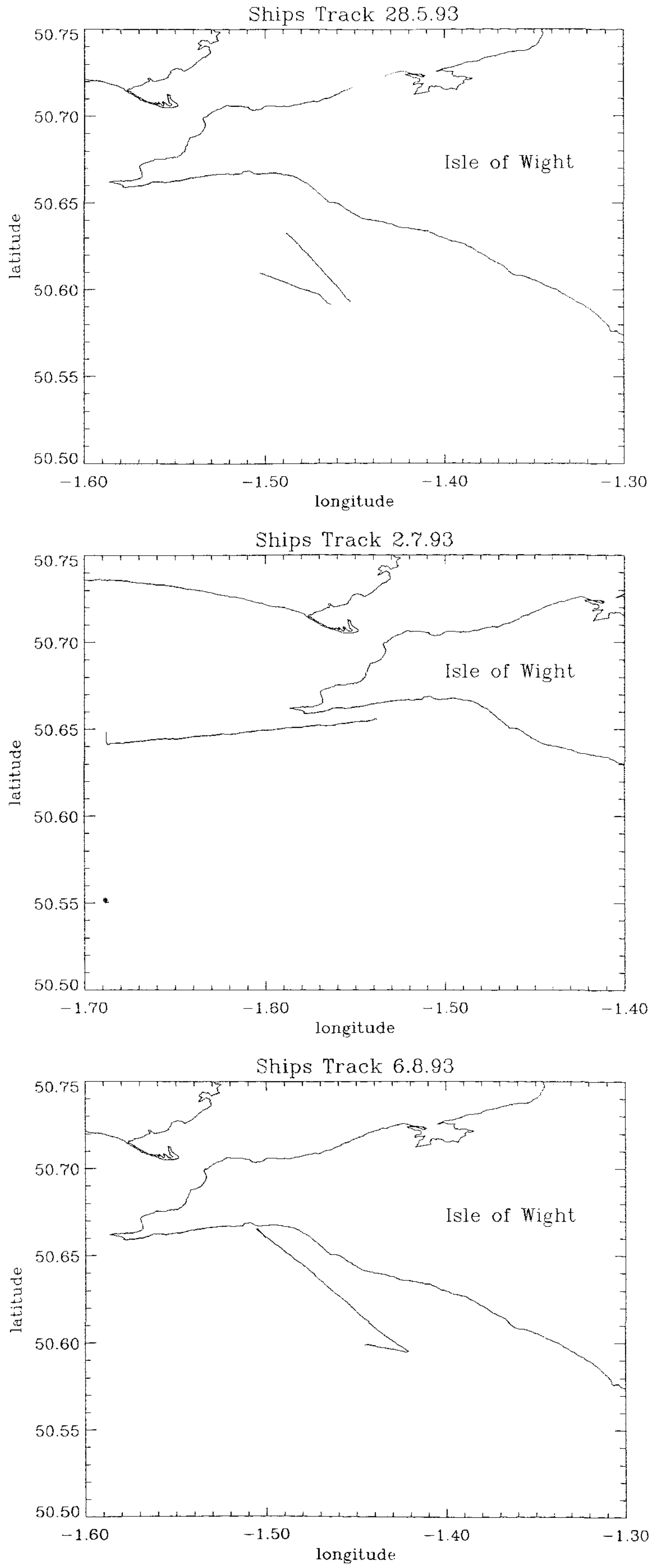

Figure 7.2 Maps showing the ships tracks during the 30 minutes *in situ* sampling period either side of the SAR overpass on 28.5.93, 2.7.93 and 6.8.93.

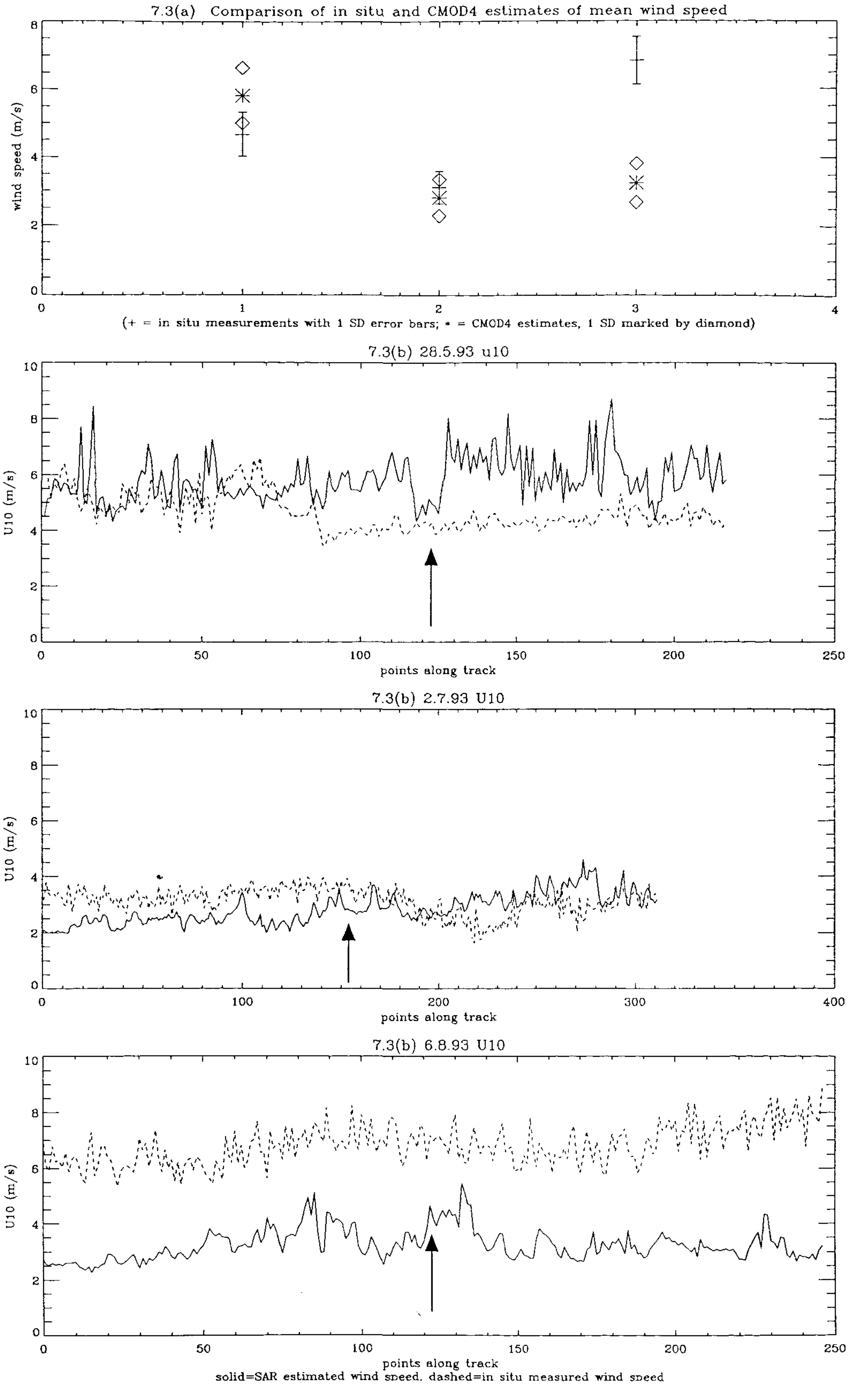

Figure 7.3 Comparison of mean wind speeds and spatial variations between *in situ* measurements and SAR-derived estimates.

(a) Mean *in situ* (+) and SAR-derived wind speed estimates (*) for 28.5.93 (1), 2.7.93 (2) and 6.8.93 (3) with error margins of 1 SD marked on.

(b) Comparison of spatial SAR-derived wind speed estimates with temporal *in situ* wind speed measurements along transects acquired 30 minutes either side of the SAR overpass. Arrows indicate points of nearest coincidence between SAR and *in situ* data.

Figure 7.4 Relationship between average SAR backscatter (dB) and wind speed (taken from synoptic charts).

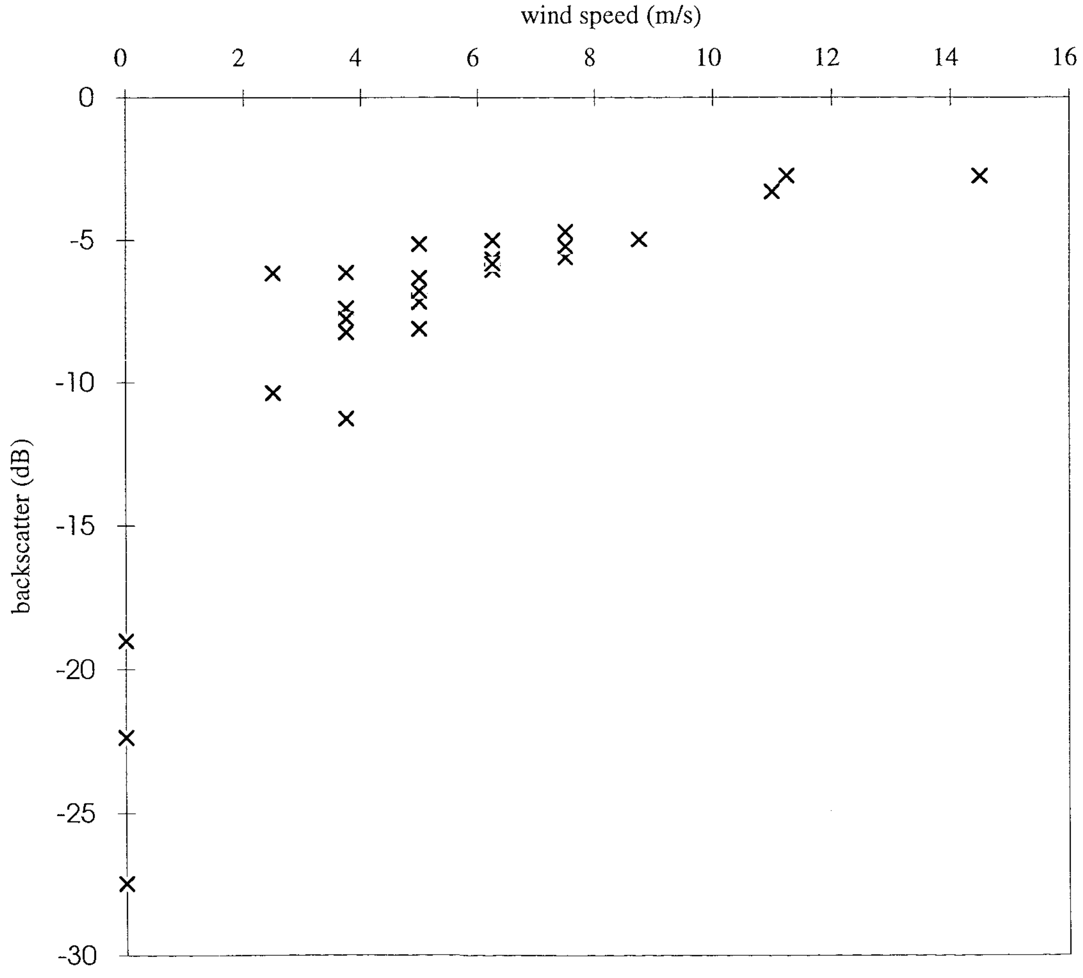

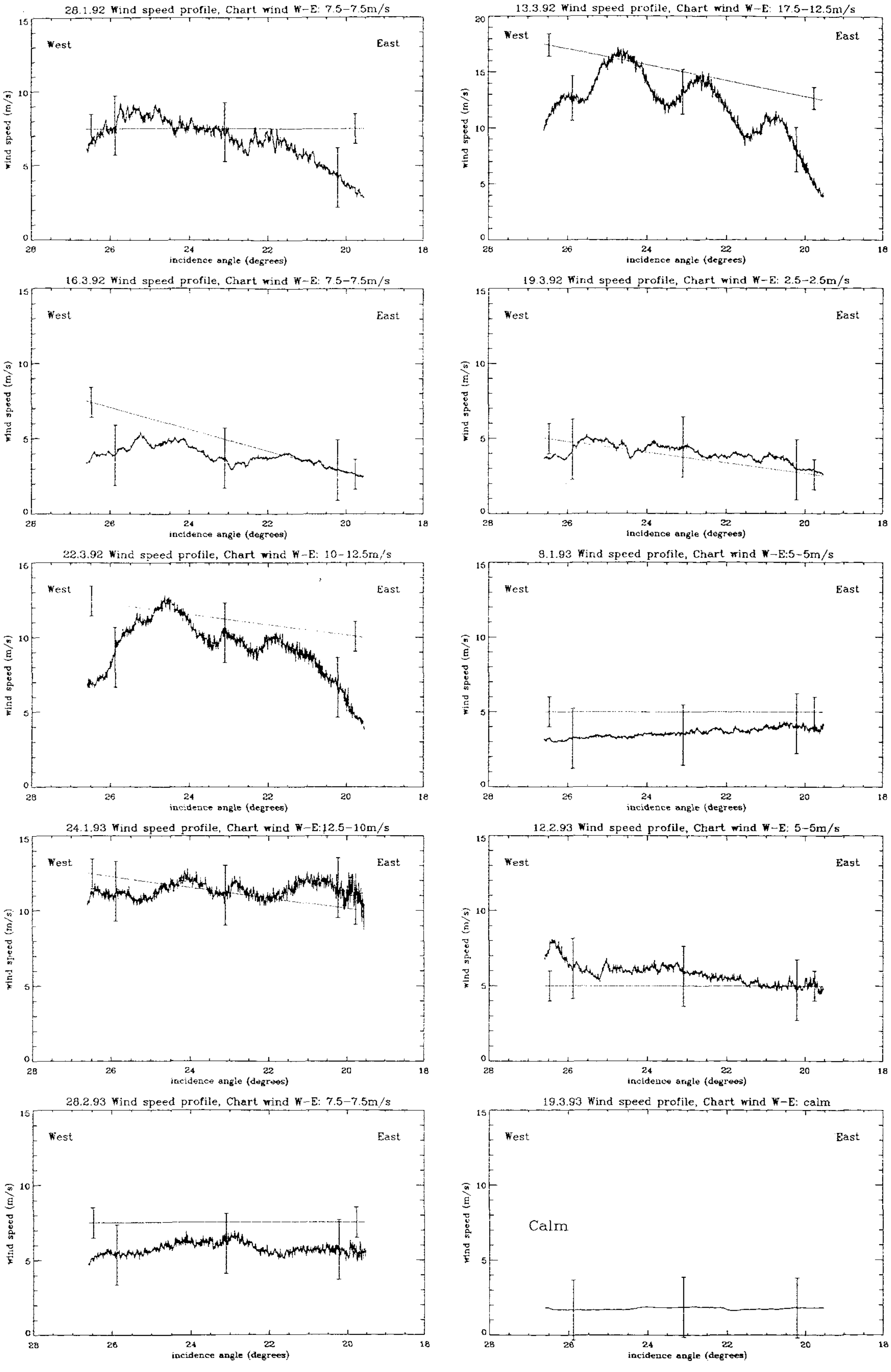

28.1.92 Wind speed profile, Chart wind W-E: 7.5-7.5m/s

13.3.92 Wind speed profile, Chart wind W-E: 17.5-12.5m/s

16.3.92 Wind speed profile, Chart wind W-E: 7.5-7.5m/s

19.3.92 Wind speed profile, Chart wind W-E: 2.5-2.5m/s

22.3.92 Wind speed profile, Chart wind W-E: 10-12.5m/s

8.1.93 Wind speed profile, Chart wind W-E:5-5m/s

24.1.93 Wind speed profile, Chart wind W-E:12.5-10m/s

12.2.93 Wind speed profile, Chart wind W-E: 5-5m/s

28.2.93 Wind speed profile, Chart wind W-E: 7.5-7.5m/s

19.3.93 Wind speed profile, Chart wind W-E: calm

Figure 7.5 Comparison of SAR-derived estimates of wind speed with chart values. The bold line denotes the estimates from SAR of wind speed across range using CMOD4, with error bars of ± 2 ms^{-1} overlain. The straight line shows the wind speeds taken at either end of the SAR image from the synoptic charts, indicating the general trend and average conditions; these data are accurate to ± 1 ms^{-1}.

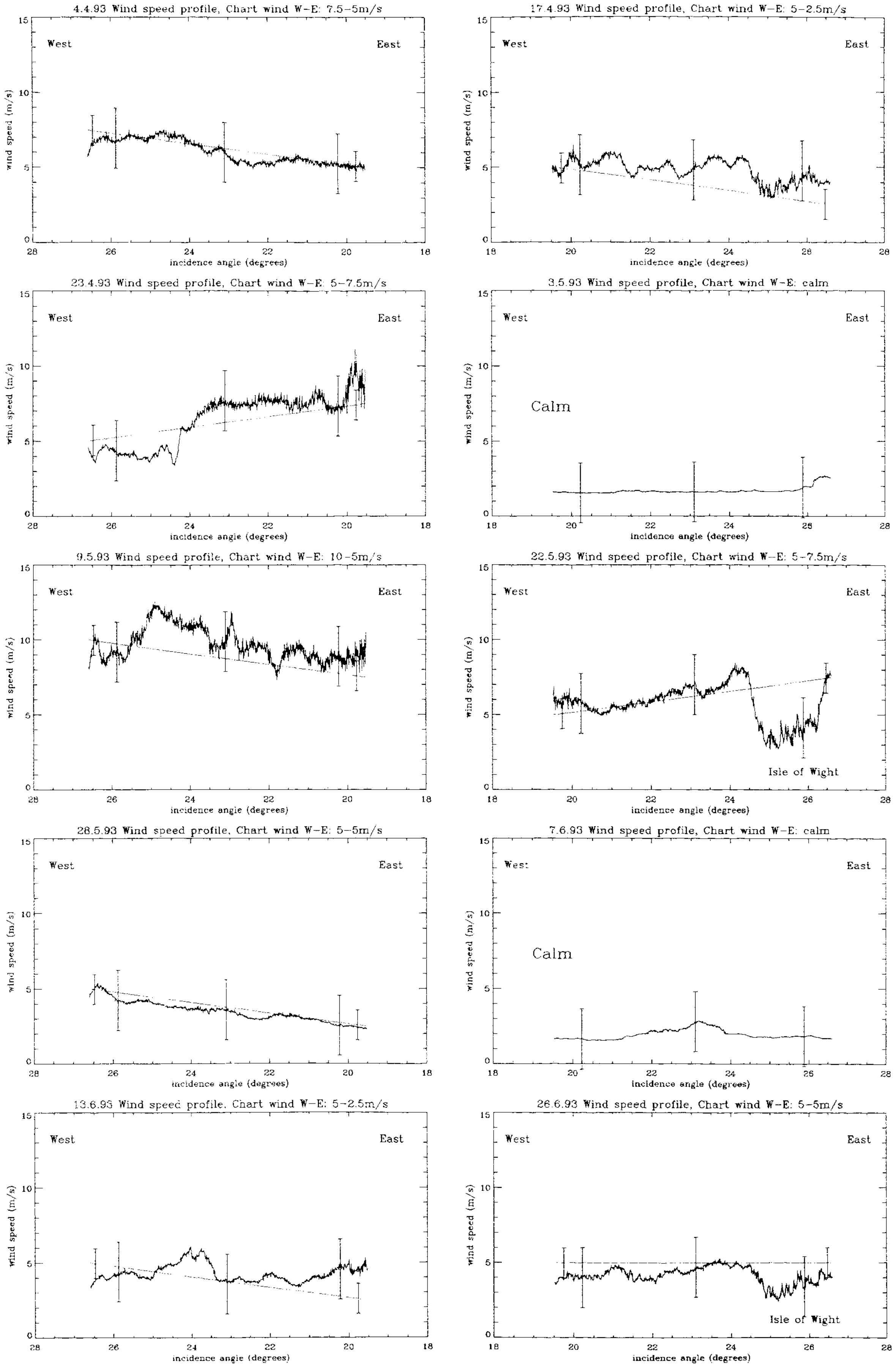

Figure 7.5 (cont)

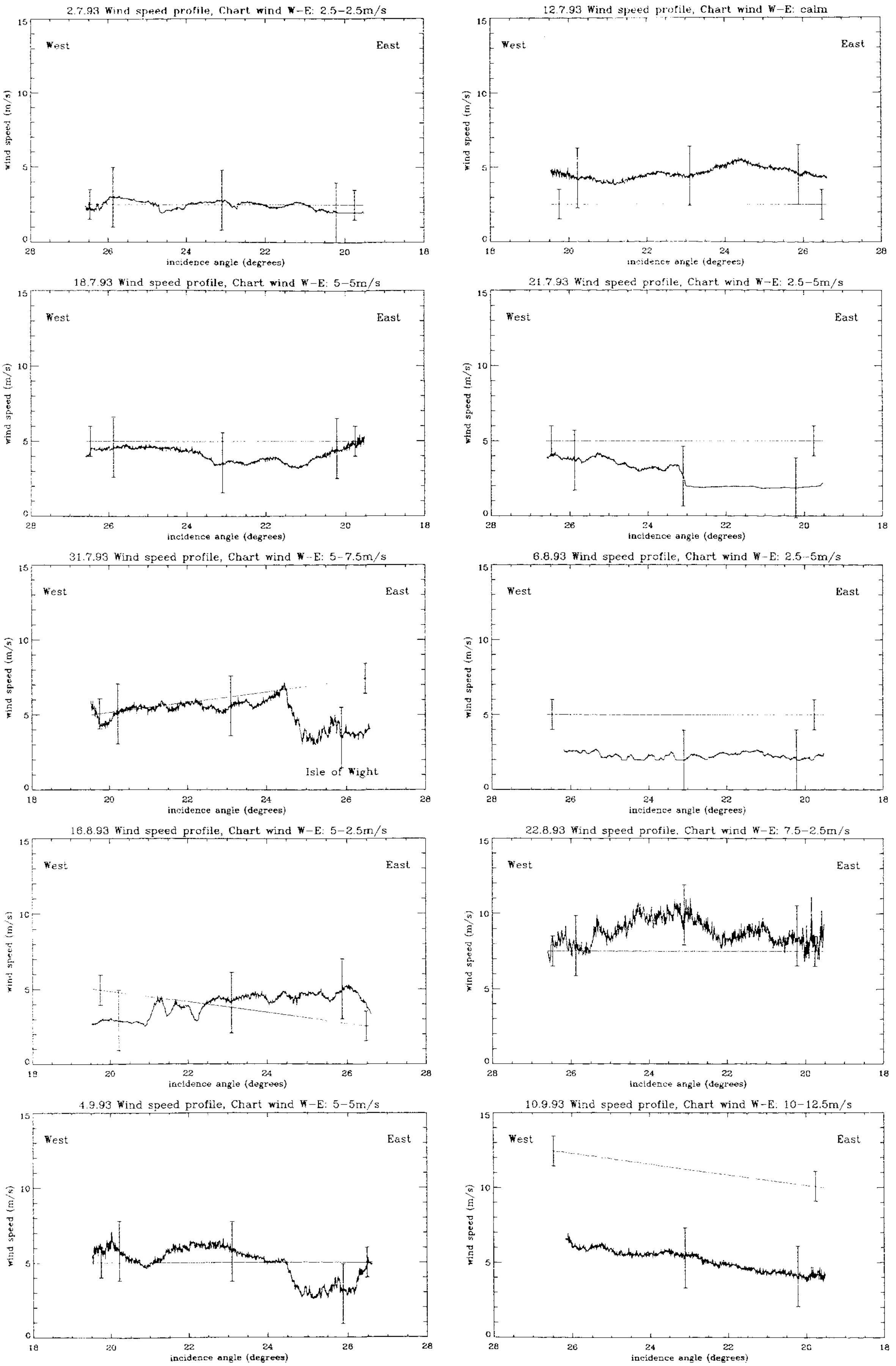

Figure 7.5 (cont)

Figure 7.6 Comparison of SAR-derived wind speed estimates with meteorological synoptic chart values

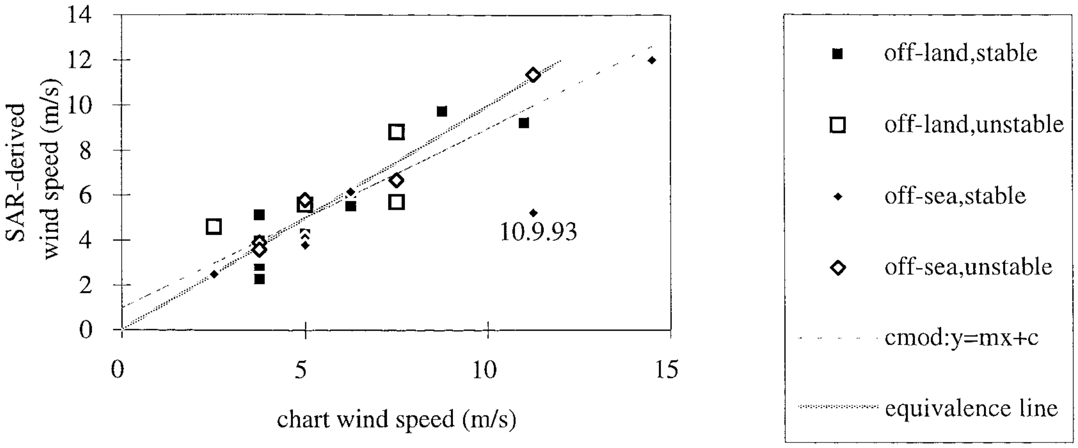

Figure 7.7 Relationship between high frequency variability of SAR-derived wind speed and the mean (anomalous data labelled A-G)

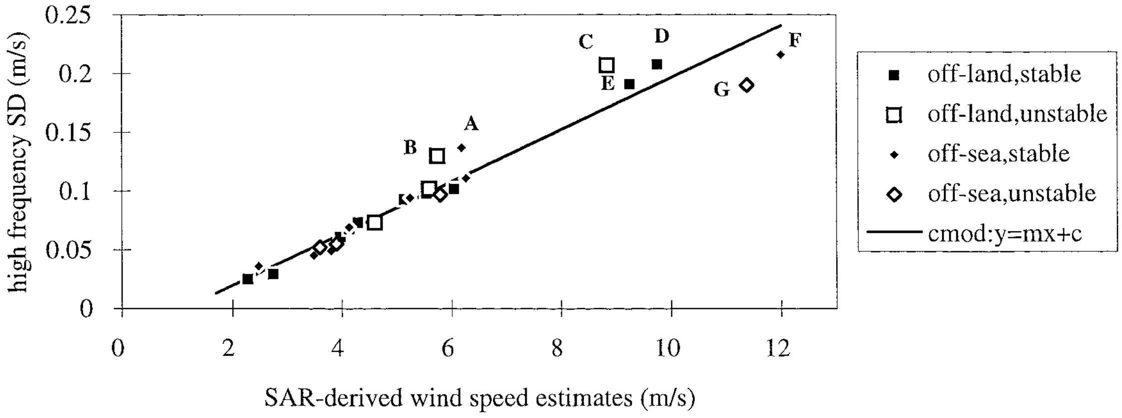

Figure 7.8 Relationship between high frequency variation (SD) of backscatter and mean wind speed

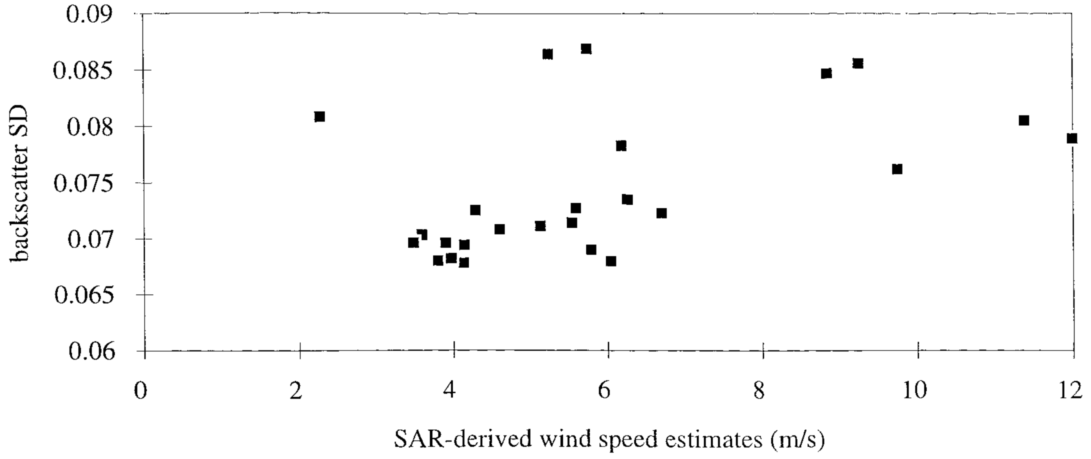

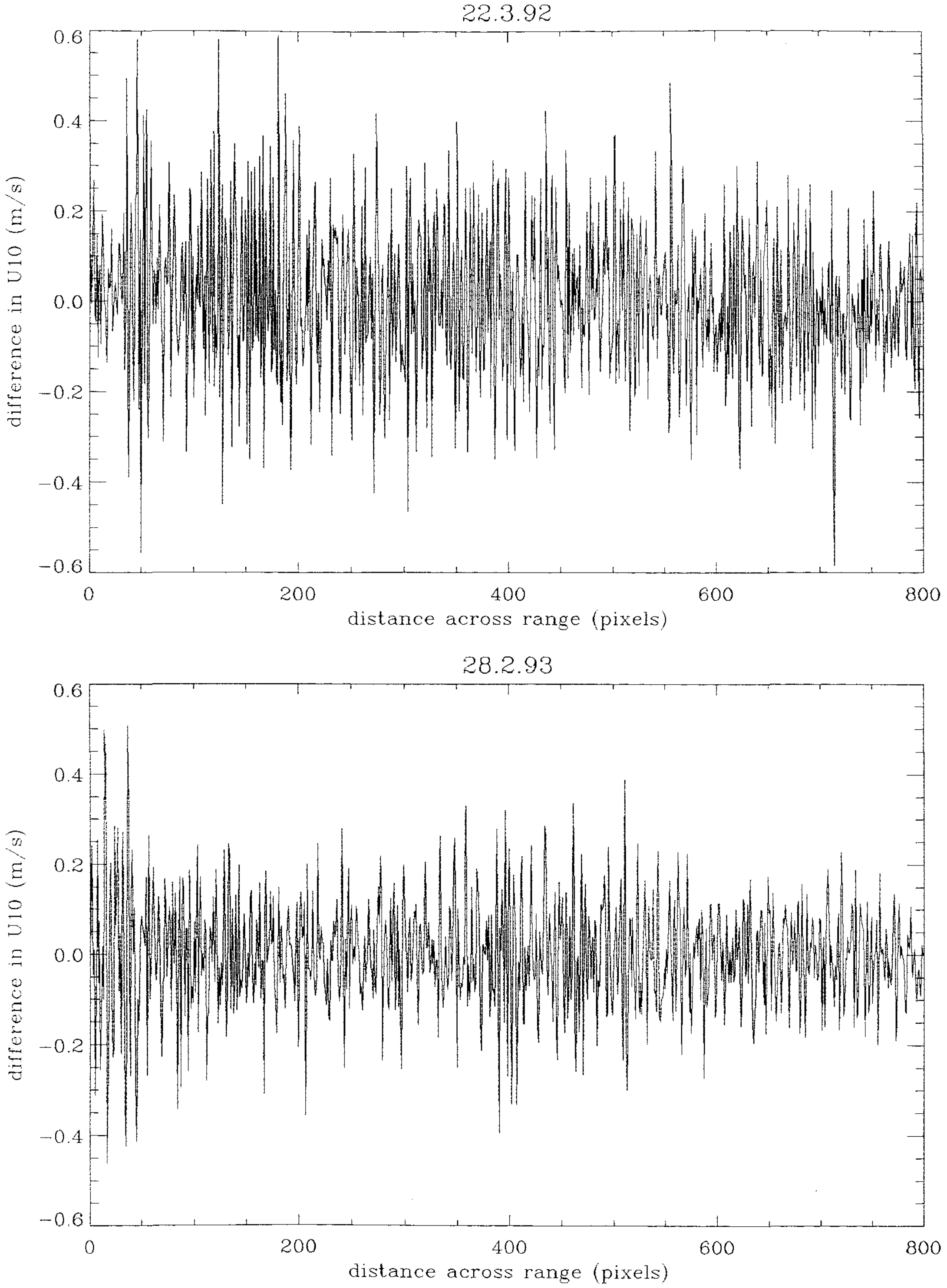

Figure 7.9 Changes in SAR-derived wind speed estimates (u_{10}) across the image. Examples show the range profiles taken from 22.3.92 and 28.2.93 - there is a decrease in variability as the transects enter an area of deeper water (around 600 to 700 pixels across range).

Figure 7.10 (a) Category I: dependence of surface roughness on wind speed

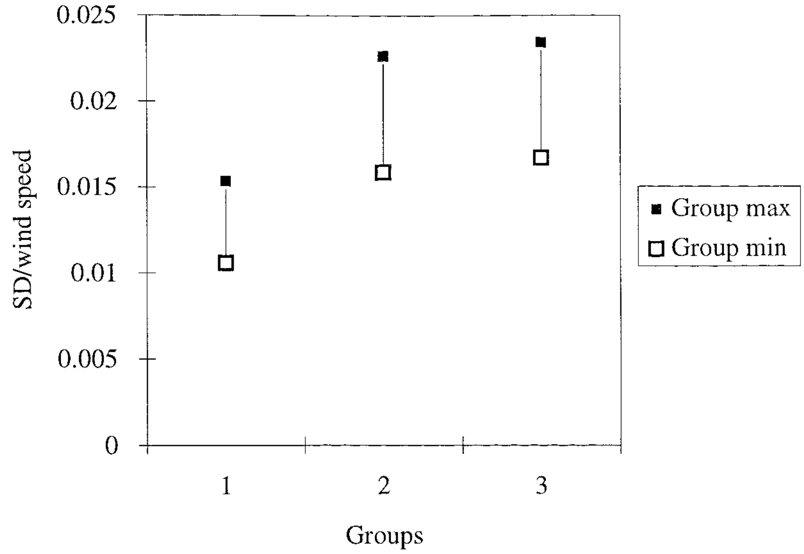

Figure 7.10 (b) Category II: dependence of sea surface roughness on wind speed and bathymetric effects.

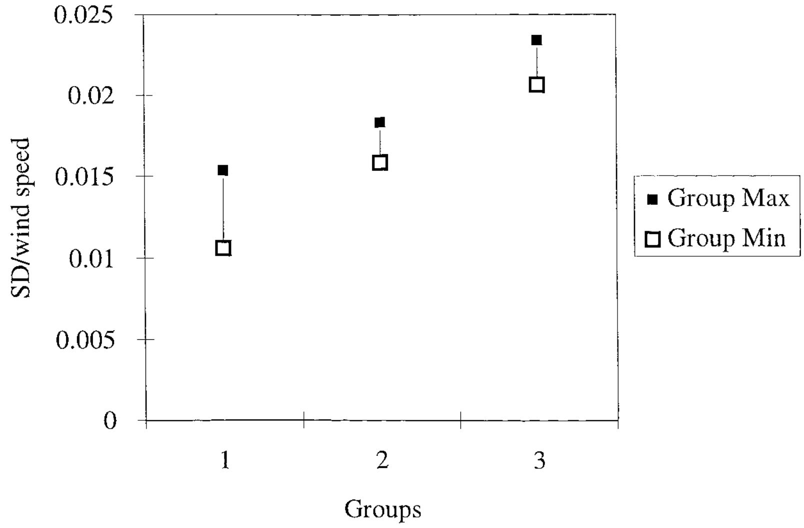

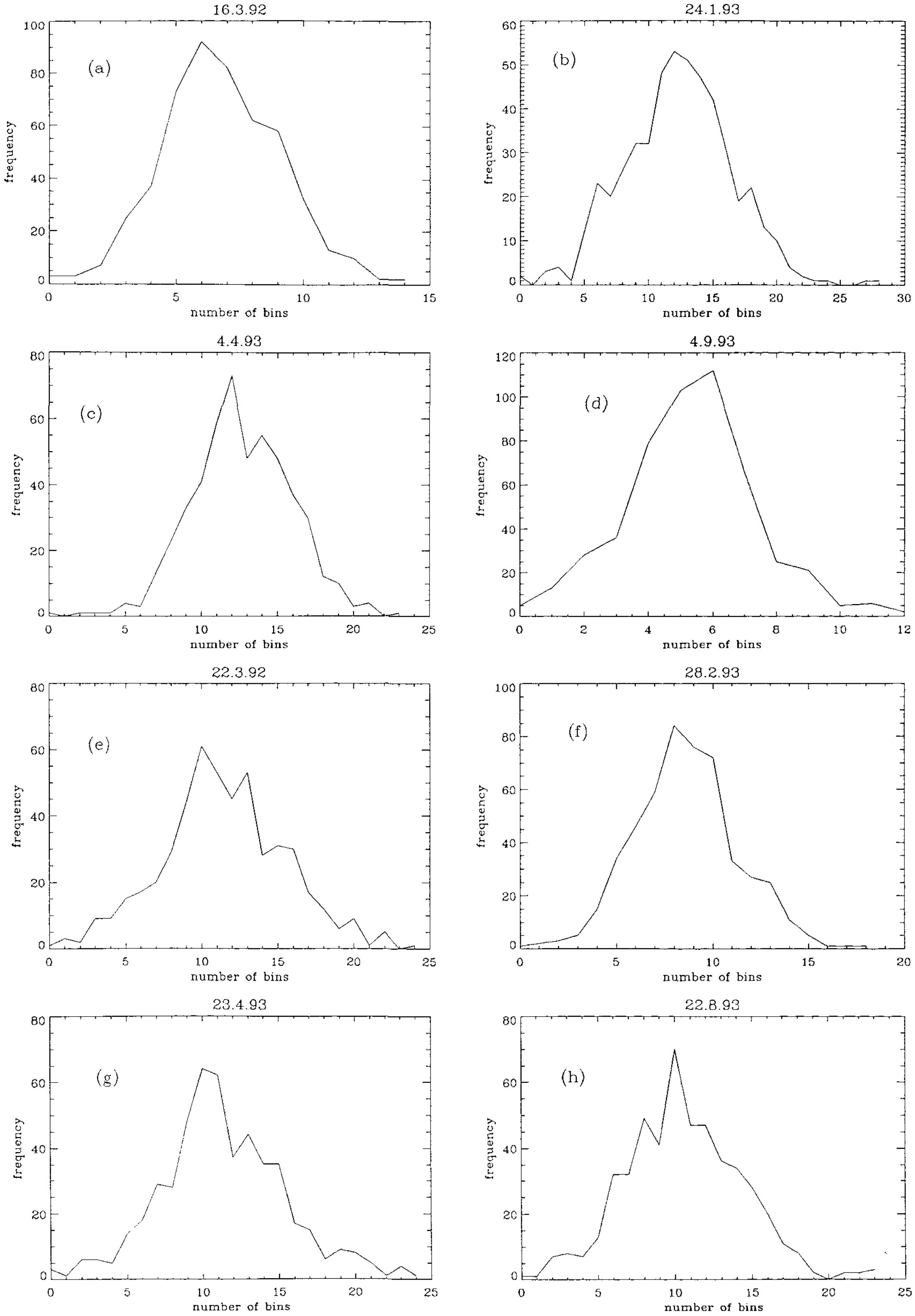

Figure 7.11 (a-h) Histograms of high frequency variations in SAR-derived wind speeds. Taken from range profiles for varied local imaging conditions (16.3.92 represents light winds (< 5 ms^{-1}) and 22.3.92 strong winds, > 10 ms^{-1}).

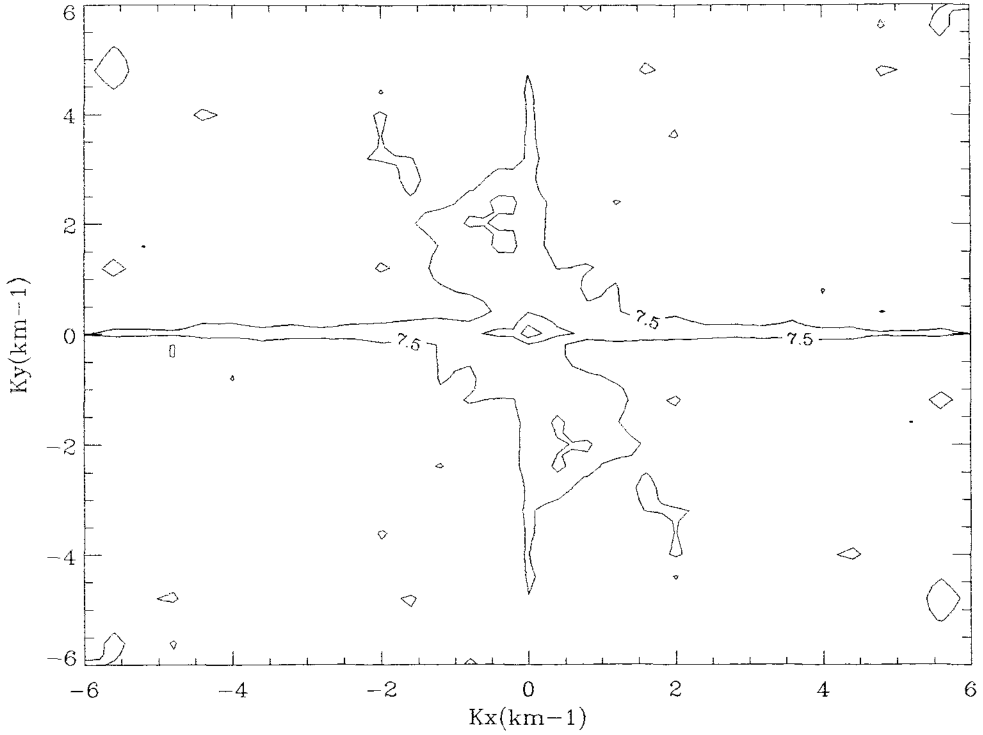

(a) 24jan93 fft plot

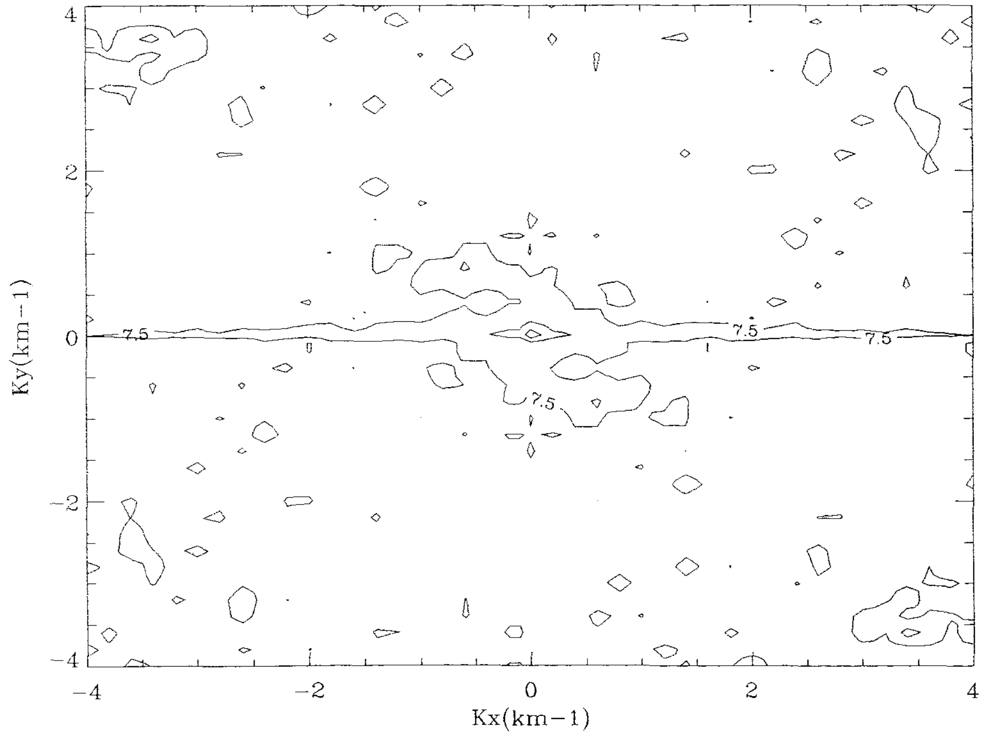

(b) 12feb93 fft plot

Figure 7.12 Examples of power spectra taken to investigate long wavelength trends. Areas taken from SAR images (a) 24.1.93 and (b) 12.2.93.

Figure 7.13 (a) Alignment of long wavelength backscatter trends with wind direction

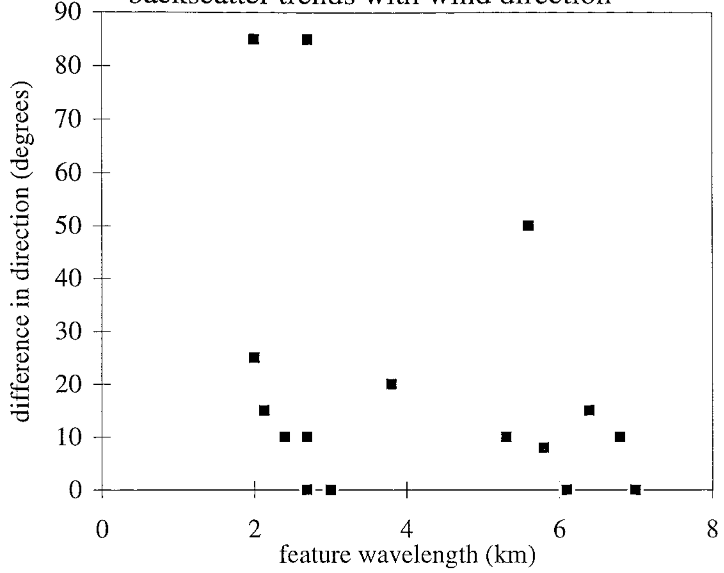

Figure 7.13 (b) Relationship of long wavelength features with wind speed

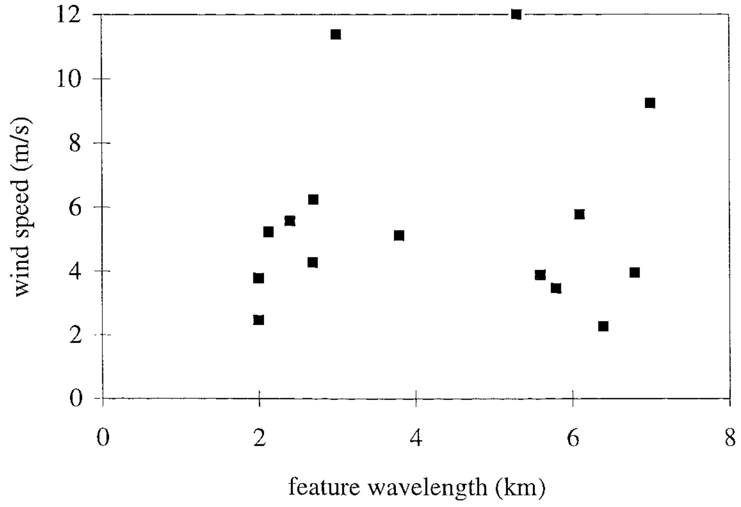

CHAPTER EIGHT

USING SAR-DERIVED APPARENT WIND SPEED ESTIMATES TO EVALUATE SURFACE ROUGHNESS PATTERNS

8.1 INTRODUCTION

The success of using CMOD4 to estimate wind speeds from SAR lead to the recognition of the potential information contained within these data on factors affecting surface roughness. This chapter concentrates on determining how to identify and then quantify the backscatter contribution attributed to wind inputs; a necessary step before investigations of the hydrodynamic contribution to the surface roughness signal can begin. The results from Chapter 7 indicate that fluctuations in the wind speed are closely related to the mean. The relationship may provide a method of determining whether effects additional to local wind conditions are modulating the backscatter signal. In this chapter, fluctuations in SAR-derived wind speeds will be examined more closely and estimates compared to known values. If SAR-derived apparent wind speeds can provide an indication of small scale surface roughness conditions, then the use of apparent wind speed fluctuations to investigate bathymetric effects on small scale surface roughness will be considered. The applicability of the method to determine surface roughness conditions in other regions is also investigated.

Once it is established that the wind speed contribution to surface roughness can be identified, a method of deriving quantitative estimates of the additional hydrodynamic contribution to the modulation of the small scale waves will be investigated. For values of surface roughness to be assessed from a multi-temporal data set or for comparison with physical factors, such as the current speeds, the data must be independent of both the viewing geometric of the satellite and the background imaging conditions. To achieve this measurements of the residual backscatter signal observed across a tidally active, shallow water bathymetric features are investigated in terms of direct measurements of the calibrated backscatter (σ_0') and two other parameters (γ and $S\sigma_0$) to be defined. γ is determined from the SAR-derived wind speed and $S\sigma_0$ is a standardised measure of backscatter. Comparisons between the terms are used to investigate the importance of removing the effects of incidence angle (θ_n) and radar view angle relative to wind direction (f) from σ_0 detected by SAR, factors which are accounted for by CMOD4. The influence of these factors where comparisons are to be made between images acquired in different local imaging conditions and with model predictions, is then investigated.

8.2 AIMS AND OBJECTIVES

The first aim was to distinguish between wind driven radar backscatter and the additional contributions from dynamically driven oceanographic modulations of the surface roughness. To achieve this it is hypothesised, first, that the small scale variability of the wind speed is directly proportional to the mean wind speed and second, that any contribution to the modulation of the surface by hydrodynamic effects will in general cause the variability to deviate from the linear relationship.

The second objective was to derive quantitative estimates of surface roughness variations, in a form that is independent of local imaging conditions. To achieve this additional contribution to scattering attributed to hydrodynamic modulation of the surface waves across a bathymetric feature was investigated. The following hypotheses were tested; first, that the proportion of the residual backscatter attributed to hydrodynamic modulation will be biased by the effects of f and θ_n; and second, that apparent SAR-derived wind speeds are linearly related to the small scale surface roughness.

8.3 DISTINGUISHING BETWEEN WIND DRIVEN AND HYDRODYNAMIC VARIATIONS IN σ_0

The relationship between the magnitude of small scale variability of the wind field and the mean wind speed was investigated by taking extracts over (i) areas of uniform backscatter and (ii) areas where tidal interaction with bathymetry occurs.

8.3.1 Sample areas

Ten images were selected for analysis and from each three extracts were taken, sampling (a) an area assumed to be influenced by wind driven effects only (refered to as uniform), (b) an area of tidal interaction with bottom topography and (c), when covered by the SAR swath, an area of shallow water bathymetry. A region of 12.5 x 12.5 km (1000 x 1000 pixels) was taken from roughly the same locations for each image, figure 8.1 shows the positions. The images and areas selected for the study were chosen according to the results from the analysis of variability of the wind field carried out in Chapter 7. Five samples were taken from range profiles exhibiting an overall high STD of wind speed, lying above the regression line in figure 7.7 and five from images conforming to the linear relationship. Area (a) covers a region of relatively deep water (30 m and more) with uniform bathymetry, whereas, (b) covers a region of varied bathymetry (15 to 46 m). The choice of these two areas was based on the distinct change in the variability of the SAR-derived wind estimates observed between area (a) and area (b), which is noticeably rougher (figure 7.9). This was attributed in Chapter 7 to tidal current interaction with bathymetry and is further investigated here. Area (c) was chosen as a distinctive and unambiguous example of bathymetric effects, covering a shallow water bank (<10 m) off Selsey Bill, which produces a strong backscatter signature in virtually all wind and tide conditions.

8.3.2 Analysis of SAR-derived wind speed values

The procedure for wind speed estimates described in Chapter 7 was followed. The data were calibrated and averaged to a pixel size of 10 x 10 (125 x 125 m) to remove the effects of speckle. Wind speed was then estimated for the array using CMOD4. The advantage of assessing data in terms of wind speed rather than σ_0' is that direct comparisons can be made between images, the effects of range and wind direction relative to radar look direction being removed by the model. Figure 8.2 shows the distribution of the different extracts, a, b and c (plotted as diamonds, squares and triangles respectively) on a plot of wind speed variability against mean wind speed. The magnitude of the variability of the wind field increases monotonically with the mean wind speed. As hypothesised, the data from the uniform areas exhibit a strong linear relationship between SD of the wind speed and the mean. As expected, the variability of the uniform areas is less than for extracts taken over areas influenced by bathymetry. Extracts (b) and (c) also show a positive linear relationship between SD and the mean wind speed, the steepness of the slope appearing to increase with bathymetric effects. The consistency of the results, over a range of wind and tide conditions, imply that SAR-derived wind speed values represent a measure of the real surface roughness and the magnitude of the variability can therefore be related to wind and hydrodynamic driven modulations.

Confidence that the SAR is detecting real fluctuations in wind speed in the uniform area (a) and that the chosen averaging period is sufficient to remove speckle effects, without losing variability information in the data, is improved by comparison of the results with experimental measures of turbulence. Wind speed variability estimates from SAR are based on data averaged over 125 m areas. In terms of time series measurements this is similar to averaging over 10 to 20 seconds for wind speeds in the range 5 to 10 $\mathrm{ms^{-1}}$. This is considered an acceptable averaging period for determining small scale variability of the wind field (Charnock, pers. comm.).

Turbulent flow in the surface layer is composed of the mean value and the fluctuation from the mean. The total wind speed (U) is therefore represented as:

$$U = u + u'$$

where u is the mean wind speed and u′ is the turbulent departure from the mean. Measurements of the scales of turbulence in the surface layer relate the variability of the wind flow to the friction velocity (u_*) using the ratio u'^2/u_*^2. Based on experimental results derived by several authors a mean value of 6 is used for this ratio (Soulsby, 1977). This enables a first order comparison between SAR-derived estimates of wind speed variability and experimental measures of turbulence. An approximation of the SD of a 10 ms^{-1} wind speed using this value is calculated as follows:

$$SD(u) = \sqrt{u'^2}$$

Assume that: $u'^2 = 6u_*^2$

then: $SD(u) = 2.44\ u_*$

To determine u_* for a given mean wind speed (u), the relationship with the drag coefficient is used:

$$u_* / u = \sqrt{C_D}$$

Below 10 ms^{-1}, the C_D does not vary appreciably with wind speed (Large and Pond, 1981) and has been found to be only weakly dependent on wave height and stability (Smith, 1980). The wind speeds estimated from the SAR data in this study all lie between 3 and 10 ms^{-1} and for this calculation C_D is taken as 1.3×10^{-3}.

then: $u_* = 0.036\ u$

$$SD(u) \cong 2.44 \times 0.036\ u$$

$$\cong 0.087\ u$$

Hence, for a wind speed of 10 ms^{-1}, $SD(u) \cong 0.9$ ms^{-1} and at 3 ms^{-1} $SD(u) \cong 0.26$ ms^{-1}. These values closely conform to the estimates of SD from SAR-derived wind speeds of 1.1 ms^{-1} and 0.2 ms^{-1} respectively (figure 8.2).

8.3.3 Determining a threshold for wind driven variability

The variability (SD) of the estimated apparent wind speed is normalised by dividing by the mean. The aim is to define a theshold of this ratio above which variability can be attributed to factors other than wind speed, based on the SD for the uniform region. Figure 8.2 shows that the variability of the data from all the regions increases linearly with wind speed, but the x-axis intercept occurs at 1.5 ms^{-1}, not zero, suggesting that wind speed variability is zero at this level. The explanation for this is unclear, but may be linked to the sensitivity of the SAR to wind speed, since the threshold for detection is around 3 ms^{-1}. Adjusting for the offset and then normalising the data enables a virtually horizontal regression line to be drawn through the points from the uniform area, figure 8.3. A level of 1 SD is used to define the confidence limits (dashed lines) for variability associated with wind driven backscatter, setting the top value value at 0.155. The only "group a" outlier from the line was an extract acquired during the passage of an atmospheric front through the study region. That it does not conform to the 'normal' levels of variability is indicative of other processes, such as increased turbulence ahead of the front roughening the sea surface, and it thus provides a good test of the sensitivity of the method. As hypothesised, the majority of values from extracts (b) and (c) lie more than 1 SD above the theshold, the high variability of the wind speed estimates representing the rougher sea surface signature associated with bathymetric effects. That the sea surface roughness is sensitive to the slight changes in bottom topography occurring at depths of 15 to 25 m in area (b), proved a surprising result. Initial studies of the region had suggested that these effects were only detectable by SAR in strong flood tide conditions (>1 ms^{-1}). Results from this more detailed look at the area suggest that current speeds as small as 0.5 ms^{-1} are capable of modulating the sea surface small scale roughness.

The variability (SD) of the wind speed is effectively a measure of the variability of the small scale roughness and therefore might be expected to contain information about other factors affecting the small scale surface roughness, such as surface currents. Surface current speeds across (b) and (c) ranged from 0.25 ms^{-1} to 1.1 ms^{-1} and varied between ebb and flood (Tidal Atlas). Figure 8.4 shows a plot of currents against the SD of wind speed estimates. The surface variability appears to be independent of the tidal current strength for both ebb and flood conditions. Wind against tide effects on the surface roughness were considered but can not be used to account for the data distribution. The data represent averages over 12.5 km areas and slight differences in the variability of the backscatter caused by small differences in tide may be smoothed out. It would have been expected that the SD observed for the shallow bank region (c) would be much higher than for the relatively deep water, weak features in area (b), whereas, both areas exhibit the same range of SD. That the higher SD for these areas, compared to the uniform area (a), is the result of bottom interaction with the surface current is supported by the visual match of features observed on the image with those on the chart.

8.3.4 Using estimates of wind speed variability as an indication of factors modulating the small scale surface roughness

An empirical relationship can be defined using the small scale variability of the wind speed to separate wind driven modulation from backscatter modulated by both wind and surface currents. For uniform areas (a) unaffected by local currents or bathymetric effects, the surface roughness increases proportionally with the wind speed. The magnitudes of SAR-derived wind speed estimates of variability for a uniform area are in close agreement with estimates from experimental measurements relating turbulence to the friction velocity. It is therefore reasonable to conclude that the averaged fluctuations in backscatter are representative of real turbulence in the wind field. That the SAR is sensitive to wind on the scale of 100 m had not previously been considered; work by Shuchman *et al.* (1994) detected wind speed variations on the 1 km scale. The additional variability in areas (b) and (c) is attributed to tidal current interaction with bathymetry. It appears that currents as small as 0.5 ms^{-1} can respond to differences in bottom topography in depths of 15 to 25 m, significantly modulating the small scale roughness. Using measures of variability in the SAR-derived apparent wind speed can provide an initial indication of whether factors in addition to the natural wind variability are contributing to the surface roughness patterns detected by SAR. To verify the method and to quantitatively investigate the relationship between current-modulated surface roughness and bathymetry it would be necessary to obtain *in situ* measurements of the wind field and current speeds throughout the water column. This is considered beyond the scope of the present study.

The validity of using fluctuations relative to mean wind speed to examine factors affecting backscatter in other areas was investigated. Initial tests were of deep water regions, which to the eye appeared uniform and were away from shelf break features and other possible current activity. These control areas would be expected to conform to the linear relationship and when normalised to lie at or below the threshold for normalised variation driven only by wind variability. Two images covering relatively deep water regions (50 to 75 m) within the English Channel, north of Cherbourg, were sampled. Extracts were selected and analysed as for the procedure used for the local study. Figure 8.3 shows the normalised SD in wind speed for these data (circular symbols) to be lower than that observed for natural variations attributed to only wind driven effects from the uniform area (a) sampled in the coastal study region (diamonds). This may be indicative of a lower degree of variability in slightly more open water conditions; Smith (1988) suggests that unlimited fetch results in a well developed wind field and consequently a smoother sea surface. It would be interesting to test the theory against true deep ocean surface roughness levels from a uniform area; unfortunately, suitable images were not available to test the theory at this stage.

8.4 DERIVING A TECHNIQUE FOR OBTAINING A QUANTITATIVE MEASURE OF RELATIVE CHANGES IN BACKSCATTER FROM ERS-1 SAR: A CASE STUDY USING BATHYMETRY

The next stage of the analysis was to obtain quantitative estimates of relative changes in backscatter across features, that are independent of the local imaging conditions and can be compared both between images and with model results. To achieve this a case study was carried out, studying the additional modulation of the surface roughness attributed to bathymetric effects on the surface currents. The objective is to develop a technique which enables the effects of currents on small scale variations in the surface roughness, caused by an underwater obstacle, to be compared for varied tide and wind conditions, thus enabling the hydrodynamic contribution to backscatter to be estimated.

The relationship investigated in § 8.3, between the small scale variability of the wind field and the mean wind speed can provide an indication that oceanographic effects are affecting the σ_0' detected, but cannot provide a quantitative measure of their contribution to the signal. Theoretically, if the wind contribution to σ_0' can be determined, then additional modulation of the signal can be attributed to hydrodynamic modulation of the surface caused by current interaction with the bottom topography. If comparisons of differences in residual σ_0 are to be made between images or with model predictions, then the number of variables influencing the residual backscatter signature must be reduced. Variations in backscatter caused by changes in sea bed slope and horizontal surface current gradient can be compared by studying signals from a profile taken in the same position on each image. To account for differences in the levels of wind speed on different days imaged and therefore the different background scattering conditions, the residual σ_0 values are divided by the the mean σ_0. This would be expected to effectively normalise the data, removing the differences from the wind contribution to the surface roughness signature. However, σ_0' is a measure of surface roughness, set to an arbitary scale, that in absolute terms is dependent on the satellite viewing geometry relative to the wind direction. Whether σ_0' provides a linear representation of the surface roughness, which can therefore be satisfactory normalised by dividing the residual by the mean, needs to be carefully investigated. Models relating backscatter to hydrodynamic modulation, such as those of Alpers and Hennings (1984, referred to in future as A&H in this chapter); Shuchman *et al.* (1985); Holliday *et al.* (1987), assume this to be the case and use the relationship $\delta\sigma/\sigma_0$, relying on normalising the residual change in the backscatter cross section to eliminate the spurious influence of viewing geometry. Whether this is sufficient when comparing data from different images to account for the influence on the measured backscatter of differences in the wind direction relative to the radar view angle (*f*) or range effects (θ_n) is examined in this section.

The potential for using a SAR-derived wind speed value, as an alternative measure of surface roughness to determine the hydrodynamic modulation of the surface waves across a bathymetric feature, is also considered. It is recognised that SAR-derived estimates of wind speed across an area modulated by currents do not depict real winds and the value derived is referred to as the apparent estimated wind speed. Effectively, this is the wind speed which would be required to generate the observed surface roughness in the absence of modulations. SAR-derived apparent wind speed variations across a feature (the residual) are normalised relative to the local mean, similarly to the ratio $\delta\sigma/\sigma_0$, and are referred to as γ. By using γ the effects of f and θ_n are removed. The results are compared with the direct measures of normalised σ_0 variations. The possibility of re-calculating the ratio in terms of standardised backscatter intensity ($S\sigma_0$), for which the effects of f and θ_n are removed, is tested.

The correspondence between σ_0, γ and $S\sigma_0$ and real surface roughness conditions is examined, looking first at the effectiveness of normalising to account for variations between scenes of the mean background conditions and then at the relationship between measured residual changes in surface roughness and simple physical variables, such as the tidal current.

8.4.1 Methods

The Shingles bank, in the western approaches to the Isle of Wight, is a distinctive, shallow water bathymetric feature, which is detected by SAR under virtually all wind and tide conditions, making it an ideal feature to study. Nineteen of the images acquired cover the feature, enabling relative changes in σ_0 to be examined for varied wind and tide conditions. Backscatter profiles were taken approximately orthogonally across the bank from the same location on each image (figure 8.5). To obtain a profile representative of average conditions across the bank an area 10 x 300 pixels was selected. The data were calibrated and then block averaged 10 x 10 to reduce speckle effects (as in Chapter 5). The resultant profile is therefore derived from 125 m pixels and in length covers a distance of 4.22 km. To provide a measure of the mean backscatter and wind conditions for each image an area 200 x 200 pixels was taken from a uniform region in the deeper water to the west of the bank. These data are also averaged 10 x 10 pixels and calibrated before calculating the mean.

Once calibrated, backscatter can also be represented as a wind speed value. Figure 8.6 presents the profiles across the bank in terms of apparent wind speed and calibrated backscatter profiles (dotted line), with the mean conditions from the adjacent areas overlain (solid line). To study the normalised $\delta\sigma$ across a feature it is helpful to present backscatter as a linear (denoted as I on the figures) rather than as the conventional logarthimic dB values. The distinctive peak in both the backscatter and apparent wind speed profiles was used as the measure of hydrodynamic effects on surface roughness conditions; the slight trough observed on some images was neither clear nor consistent enough to use. The difference between the profile peak and area mean (both in terms of σ_0 and apparent wind speed) gives a measure of the change in roughness, which is attributed to the modulation of the surface current field by bottom topogaphy. The residual is then normalised by dividing by the mean to obtain the ratio $\delta\sigma/\sigma_0$ and γ, which is independent of variations between images. Confidence that the adjacent areas are representative of local backscatter and wind conditions is given by the close match between the average values and the backscatter levels on the profiles either side of the bank. The additional modulation of the signal across the bank can then be compared between images, studying both the residual and ratio values.

A standardised backscatter, from which dependence on f and θ_n have been removed, was re-calculated from the apparent wind speed estimates by passing the data back through CMOD4. The value f was set to 0°, optimum viewing conditions and θ_n to the reference incidence angle of 23°. By setting the data to a standard satellite viewing geometry, it would be expected that normalised relative changes in backscatter would be comparable between images; the values being independent of the mean wind conditions.

8.4.2 Results

Figure 8.6 shows the range of surface roughness signatures obtained across the Shingles bank from January to September 1993. The magnitude, shape and position of the peak can be seen to vary substantially for the different wind and tide conditions sampled. Based on the mean background wind speeds, the conditions sampled vary from calm to a maximum of 5.8 ms^{-1}; the bank is close inshore and hence, the area is relatively sheltered. Acquiring data over the same area for a substantial period of time, enabled the surface roughness signature to be examined for the range of tidal states occurring. For example, the profiles for 23.4.93, 22.5.93 and 12.7.93 represent slack water conditions and no distinct peak occurs; the former two profiles were acquired in the maximum wind speeds sampled and it appears that it is the variability of the current speed across the bank that is the major influence on the surface roughness signature. In strong tide conditions, such as on 12.2.93, 28.5.93, 26.6.93 and 22.8.93, where the currents are in the order of 1.5 ms^{-1}, a clear peak is observed on each profile.

The CMOD4 modelled predictions of backscatter values equivalent to the sampled range of wind speeds, for the imaging conditions specific to each image, are overlain on the plots of backscatter (straight lines on figure 8.6, right hand column). That the same σ_0' value could be equivalent to different wind speeds on different days depending on f and θ_n can clearly be seen. For example, a peak backscatter value of -4.5 dB is approximately equivelent to a wind speed of 8 ms^{-1} on 8.1.93 compared to 4 ms^{-1} on 7.6.93; the values of f are 33° and 13° respectively. These factors also influence the relative differences in the size of the residual signature and therefore the ratios for σ_0' and γ. The differences between the residual values for backscatter and apparent wind speed (peak - mean) are best shown by comparing the plots in figure 8.6. The profiles for 16.8.93 are very different, the residual value in terms of apparent wind speed is considerably larger than that for backscatter. However, where light wind conditions prevailed, such as for the 19.3.93 and 2.7.93, the trend is reversed and the difference between the apparent wind speed peak relative to mean is much smaller.

Figure 8.7 (a-c) show the respective ratio (for σ_0, γ and $S\sigma_0$) plotted against mean wind-speed and grouped according to the tidal currents. The plots show the effects of normalising these data, enabling the ratios for similar tidal states to be compared; data in the same current speed groups would be expected to result in a similar ratio. The absolute values of the ratios and spread of the data is similar for all three cases. However, the σ_0' ratios are widely spread for same tide conditions, giving a false impression of a dependence on wind speed. In the case of γ the data within the same tidal groups lie close to a horizontal line. Although the $S\sigma_0$ data are slightly better grouped than σ_0', tides of the same state are poorly aligned. The differences between the data are best shown by the two tidal groups for which 3 to 4 images were acquired during similar tidal conditions. γ values derived from images acquired during a flood tide ranging from 1.4 ms^{-1} to 1.5 ms^{-1} (circle outlines) and an ebb tide of 1.5 ms^{-1} to 1.6 ms^{-1} (diamond outlines) are closely aligned in the horizontal axis (figure 8.7a). However, in terms of σ_0' and $S\sigma_0$ these points are very scattered (figure 8.7 b and c).

The relationship between the normalised ratios for σ_0, γ and $S\sigma_0$ and the surface roughness was tested to determine whether the values provide a linear representation of the variations in surface roughness across the bank. It would be expected that stronger tides would produce a larger residual backscatter signal (rougher surface) than weaker ones, consequently the normalised data would display a positive monotonic relationship with current speed. Figure 8.8 (a-c) demonstrates more clearly the relationship between mean tidal current and the ratios for σ_0, γ and $S\sigma_0$. The tidal currents were taken from the Admiralty tidal atlas and provide an approximation to tidal conditions at the time of the SAR pass. The data were divided into ebb and flood conditions in order to examine any differences in current gradients between the tidal states. The data representing σ_0' are very scattered and, similarly, $S\sigma_0$ shows a poor relationship with the current speed, having a correlation coefficient, r^2, of 0.2. The measurement of the variation in the surface roughness in terms of γ exhibits a strong, positive linear relationship with the surface current ($r^2 = 0.8$). Evidence from the data analysed in this study suggests that the ebb and flood tidal states conform to the same linear regression with γ.

8.4.4 Discussion and Summary

Analysis of the dependence of σ_0', γ and $S\sigma_0$ on mean wind speed conditions demonstrate that only the ratio for γ, determined from apparent SAR-derived wind speed estimates, provides a linear representation of the small scale surface roughness. The data are effectively normalised, removing the effects of scene-to-scene variations in backscatter attributed to the wind speed. Normalising backscatter is clearly insufficient to remove the non-linearities introduced into the data by the effects of f and θ_n; a requirement that is esssential if comparisons are to be made between images, with physical variables, such as tidal currents, or with model predictions.

Only γ displays a positive linear relationship with current speeds, reinforcing these results. The ratio for γ is directly proportional to real surface roughness conditions. Confidence that it is tidal currents and not other factors affecting the surface roughness signature is given by the lack of measurable perturbations at slack water compared to the distinctive signature at most other tidal states. The current speed threshold for significant modulation of the small scale surface waves across the Shingles bank to occur, is estimated from these results to lie between 0.8 and 1 ms^{-1}, figure 8.8(b). For tidal currents equal or greater than this there does not appear to be a minimum wind speed below which the feature cannot be detected. However, the linearity of the relationship between γ and current speed only exists for currents of 0.8 ms^{-1} or greater. It would appear that there is potential for estimating tidal currents across the Shingles bank from peak surface roughness values using the apparent wind speed.

The linear relationship between γ and the tidal currents emphasises the importance of removing the effects of the satellite viewing geometry from the data; using the value γ considerably improves the results achievable compared to the direct measure of σ_0'.

It was hoped that redefining the data in terms of backscatter ($S\sigma_0$) using CMOD4 would produce results comparable to those achieved using γ, the effects of f and θ_n being removed.

However,this was not the case, suggesting that re-calculating the data as σ_0 using the model is not viable. To correct for the effects of f the model defines a series of curves with different gradients and hence, a range of backscatter values can result in the same wind speed. Alternatively, a σ_0 value for f=13° can be equivelent to a lower wind speed than a smaller value of σ_0, but at f=80° (figure 8.9). In addition, although the wind speed to σ_0 relationship described by the model is near-linear for the winds in the range 5 to 15 ms^{-1}, outside this range the curve is non-linear. Given that the majority of data sampled for this study lie below 6 ms^{-1} and the values of f vary greatly, it is not surprising that the linear relationship found for γ is not maintained when the data are passed back through the model to determine a $S\sigma_0$. Hence, the apparent wind speed ratio, γ, derived using CMOD4 provides a better representation of surface roughness conditions than σ_0. At wind speeds less than 2 ms^{-1}, such as for the 3.5.93 (figure 8.6), the CMOD4 estimates are set to a fixed minimum level (1.9 ms^{-1}), whereas, the backscatter value disappears into noise and thus, gives an artificially large residual value between peak and mean. The much improved ratios achieved from the images sampled in the low wind speed range (<5 ms^{-1}) using γ, compared to using a backscatter ratio, increases confidence that the empirically determined model is a good representation of the relationship between backscatter and wind speed.

Re-calculating a $S\sigma_0$ from the CMOD4-derived apparent wind speed estimates using a simple Bragg model did improve the σ_0 relationship with current speed, giving a correlation coefficient of $r^2 = 0.62$ (figure 8.10). Given a sufficiently accurate model to generate σ_0 from wind speed it would be expected that the values would provide a representation of surface roughness comparable to that achieved using γ.

8.5 COMPARISON OF MEASURED RELATIVE CHANGE IN SURFACE ROUGHNESS ACROSS THE SHINGLES BANK WITH THEORETICAL PREDICTIONS

Models of backscatter modulation across a bathymetric feature assume a linear relationship between surface roughness and current velocity, given that the other parameters such as depth remain constant; where investigating a single feature this can be considered to be the case. However, the results from § 8.4 clearly establish that neither σ_0, nor $S\sigma_0$ provide a linear representation of surface roughness. Hence, having established that only γ gives an effective measure of the hydrodynamic contribution to the additional modulation of backscatter across a bathymetric feature, it is now examined in relation to experimental and model predictions from other work in this field. The aim is to determine whether changes in surface roughness in terms of γ are of similar orders of magnitude to theoretical predictions of backscatter from a model. The shape and presence of peak and trough features in the profile across the Shingles bank are also compared with the model predictions.

8.5.1 Theory

A thorough analysis of several bathymetric imaging models was carried out by Vogelzang *et al.* (1989), in an extensive study of the sandbanks off the Dutch coast, combining *in situ* and radar data (SAR and SLAR). Comparisons were made between the following models: A&H; Shuchman *et al.* (1985); Holliday *et al.* (1987). It is accepted that models of the imaging mechanism should be based on three steps. Interaction between tidal flow and bottom topography produces variations in the current velocity at the sea surface, which is described using the continuity equations. Varying the surface current velocity modulates the wind generated wave spectrum, altering the distribution of the small scale waves and this is calculated using the action balance equation. Modulations in the wave spectrum are detected as spatial variations in the radar backscatter and are related to the sea surface roughness using first order Bragg scattering theory.

For this study, the simple first order model proposed by A&H is considered adequate for comparison between theory and ERS SAR-derived measures of variations in the magnitude of the surface roughness modulation using γ. Although they assume a fixed relaxation rate and do not include advection terms, results from Vogelzang *et al.* (1989) suggest the models all predict similar modulation depths of the radar, providing the model is not applied to X-band radar (where simple relaxtion models break down). The advection term is important in determining the position of the peak modulation relative to the bottom topography, an important factor if the data are to be used for mapping purposes.

The A&H theory predicts a 'double' backscatter signature across a bathymetric feature, differing flow rates across a bank resulting in divergent and convergent zones as the water is forced to travel faster and then slower as it passes over the shallow region. The faster currents occur as the bank shallows and the diverging currents produce a decrease in the surface wave amplitude and an increase in wavelength. This results in a decrease in the spectral intensity and therefore the radar backscatter also decreases and a dark bank is observed uptide of the bank. Conversely, as the waves pass over the bank into the deeper water the converging surface currents produce an increase in the surface wave amplitude and a decrease in wavelength, effectively compressing the small scale waves, and radar backscatter increases with the spectral density of the short waves. This appears as a band of bright backscatter along the downtide boundary of the bank. If the current is reversed then the backscatter signature also reverses position. Vogelzang *et al.* (1989) observed these features and found a strong relationship between backscatter signal and bottom depth, the radar extremes occurring over maximum variations in the bottom slope, in agreement with the models.

8.5.2 Applying the Alpers and Hennings model

A&H represent bathymetric effects on the radar backscatter in terms of the current gradient modulation of the small scale surface waves. The model predicts that the modulation should be represented as follows:

$$\delta\sigma/\sigma_0 = |4+ y/\mu|.\ U_0\, d_0 \cos^2\phi\ \ d'/d^2$$

where: $\delta\sigma$ is the difference between peak and mean backscatter (σ_0), which in this study is investigated in terms of γ; y is the ratio of the group velocity to the phase velocity, which is 0.5 for gravity waves; μ is the relaxation rate; U_0 is the tidal current across the bank; d_0 the reference depth adjacent to the bank; ϕ is the angle between the radar look direction and a profile orthogonal to the sandbank; d' is the gradient of the depth profile; and d is the new depth.

The model was applied to the profile taken across the Shingles bank for currents ranging from 0.5 to 1.5 ms^{-1}. The angle ϕ was set to 20° for a descending SAR pass and the depth adjacent to the bank was taken as 20 m (d_0). The gradient across the bank was caculated over intervals of approximately 300 m to account for the very rapid change in slope. The value of μ was set at 0.1 s^{-1}, based on the definition that the relaxation rate (or wave growth rate) is 10 to 100 times the wave period, as used by A&H. For the 7.16 cm waves visible to C-band radar this gives a range of 2 to 21 seconds and a relaxtion time of 10 was chosen.

Figure 8.11 shows the modelled results for both ebb and flood tide conditions for currents ranging from 0.5 to 1.5 ms^{-1}. Clearly an increase in the current velocity results in an increase in the surface roughness. For flood tide conditions the model predicts very high $\delta\sigma/\sigma$ values, ranging from 4 to 8, whereas in comparison, for ebb tide conditions $\delta\sigma/\sigma$ lies between 1 to 4.

8.5.3 Comparing the SAR-derived measures of surface roughness in terms of γ with modelled predictions

A comparison was made between SAR-derived ratios of γ as a measure of surface roughness across the Shingles bank with predicted backscatter modulations ($\delta\sigma/\sigma$) using A&H model. The aim was to compare orders of magnitude and variations in the surface roughness profiles beteween the data.

In figure 8.12 (a-c) the SAR-derived data are displayed as profiles of the ratios across the Shingles bank. Comparing these profiles further emphasises the disparity between the use of γ, σ_0 and $S\sigma_0$ (as given by figure 8.12 b and c), as a representation of surface roughness. Table 8.1 shows the tidal current and wind speeds ranked in decending order for the examples used in this figure. In terms of γ the surface roughness increases proportionally with current speed, stronger tides producing a larger peak irrespective of the wind speed; in good agreement with the model predictions. This is not the case for the profiles of σ_0 or $S\sigma_0$. For example, peak values representing the same current speed (2.7.93 and 16.8.93) are quite widely separated and the smaller current on 19.3.93 is disproportionaly large.

The magnitude of the SAR-derived values of γ are similar to the model predictions of $\delta\sigma/\sigma$ for the ebb tide. The differences could be attributable to smaller tidal currents in the real case than those used in the calculation (the values are for the region, and are taken from the Admiratly Tidal Atlas). However, model estimates for the flood tide are considerably higher than those measured (γ) and the disparity in size between the ebb and flood tidal states is not observed from the SAR data. The secondary peak predicted for flood conditions, marking the eastern edge of the channel, is in close agreement with the measured values.

Not surprisingly, the comparison between the positions of the measured and modelled peaks in surface roughness suggests the mechanisms across such a shallow water feature are considerably more complex than the simple flow of tide across the bank used in this model. Although a dip in the γ profile does occur uptide of the bank, it is only a weak feature compared to the double signature predicted by the A&H model. In addition, the maximum γ does not occur above the peak as suggested by the model for both the ebb and flood tide directions. In fact, the predicted profile for the ebb tide indicates a trough downtide of the bank, this does not conform with theory; it would appear that the model cannot perform properly across such a steep feature.

Using γ alters the magnitude of the profiles, but the position of the peaks relative to the bottom topography remains the same. The peaks in backscatter occur above the areas of maximum bathymetric gradient downtide of the bank, as suggested by theory (but not predicted by the model) and observed by Vogelzang *et al.* (1989). The possibility that waves breaking across the bank are contributing to the peak in backscatter can therefore be disputed, since the maximum surface roughness signature would be expected to occur directly above the shallows if this were the case.

Table 8.1 Summary of the tidal current and wind speeds for the examples used in figure 8.13, ranked in descending order.

Date & symbol in figure 8.12	Tidal current (ms^{-1})†	Wind speed (ms^{-1})	Tide Rank (decending)	Wind speed Rank (descending)
12.2.93 (__)	+1.4	4	a	2
28.2.93 (-...-)	+1.1	4.4	b	1
28.5.93 (.....)	+1.4	4.3	a	3
26.6.93 (-.-.-)	+1.4	3.1	a	3
4.9.93 (----)	+1	3.9	c	4
8.1.93 (-...-)	-1.1	3.5	d	3
19.3.93 (__)	-1.3	2	b	5
17.4.93 (----)	-1.2	4.6	c	1
2.7.93 (......)	-1.5	2.2	a	4
16.8.93 (-.-.-)	-1.5	4	a	2

† + = flood tide, - = ebb tide

The position of the peak is observed to change in shape and position relative to the wind speed. Although only winds ranging from 2.5 to 6 ms^{-1} are sampled here, it is noticeable that in lighter wind speeds (<3 ms^{-1}) the peak backscatter occurs further away from the top of the bank and has a broader signature, on both ebb and flood tides. The relaxation rate is postulated to decrease with the wind speed (Hughes, 1978), the effects of this factor on the hydrodynamic modulation may account for the change in peak position relative to the wind speed. An increase in the wave growth time relative to the advection time would mean the surface roughness takes longer to recover from the modulation of the waves and the effects of surface straining by currents are seen further from the source. Although the light wind speed examples are in the range 2 to 3 ms^{-1} and, the presence of dark regions on the image of 19.3.93 indicates the conditions to be close to the threshold wind speed below which the

7 cm Bragg waves are not generated, patches of wind are observed in the Shingles bank region, which are sufficient to be modulated.

The model which predicted troughs over the very shallow region did not correspond to the variations in backscatter measured by SAR across the Shingles bank. The main criticism of the model is the assumption that currents flow directly across a mobile bank, clearly this is not the case, currents often forming an eddy system around a linear sandbank (Pattiaratchi and Collins,1987). The flow of currents around and over the bank creates a complex current system, shear zones and eddies are likely to occur between water flowing adjacent to the bank and that in the deeper channel, which could generate the surface roughness patterns observed on the SAR images.

8.6 CONCLUSIONS

An empirical relationship can be defined using the small scale variability of the wind speed to separate wind driven effects on the surface roughness from those modulated by both wind and surface currents. It has been demonstrated that the small scale variability of the wind speed is directly proportional to the wind speed and that any contribution to the modulation of the surface by hydrodynamic effects will cause the variability to deviate from the linear relationship. Confidence in this result is increased by the close correspondence between the magnitude of SAR-derived wind speed variability and estimates from experimental measurements relating turbulence to the friction velocity. That the SAR could be used to investigate wind speed variability on scales of 100 m had not previously been contemplated. An investigation of two images further offshore in the English Channel suggested that, in accordance with theory, where a well developed wind field can occur the sea surface is smoother.

A more detailed investigation of ERS-1 SAR surface roughness signatures has shown that using a normalised SAR-derived apparent wind speed residual (γ) provides a better representation of perturbation of the small scale waves than direct measures of backscatter.

It has been established that the effects of different wind directions relative to radar view angle (*f*) and incidence angle (θ_n) produce non-linearities in the backscatter values which cannot be accounted for by normalising the data. Comparisons between measured variations in surface roughness across a bathymetric feature in terms of γ, σ_0, and $S\sigma_0$ for varied tide conditions and with theoretical predictions, further demonstrated that only γ is linearly related to current speed; an increase in the current speed produces a proportional increase in the surface roughness, as assumed by theoretical models describing surface roughness variations across a bathymetric feature, such as that by A&H. Clearly it is essential that the spurious effects of the viewing geometry are removed if comparisons of surface roughness variations are to be made with physical variables, such as currents, between images or with model predictions. To achieve these corrections an estimate of wind direction is required, often not available from the SAR image; the analysis of SAR data thus requires additional data, either from models or *in situ* measurements.

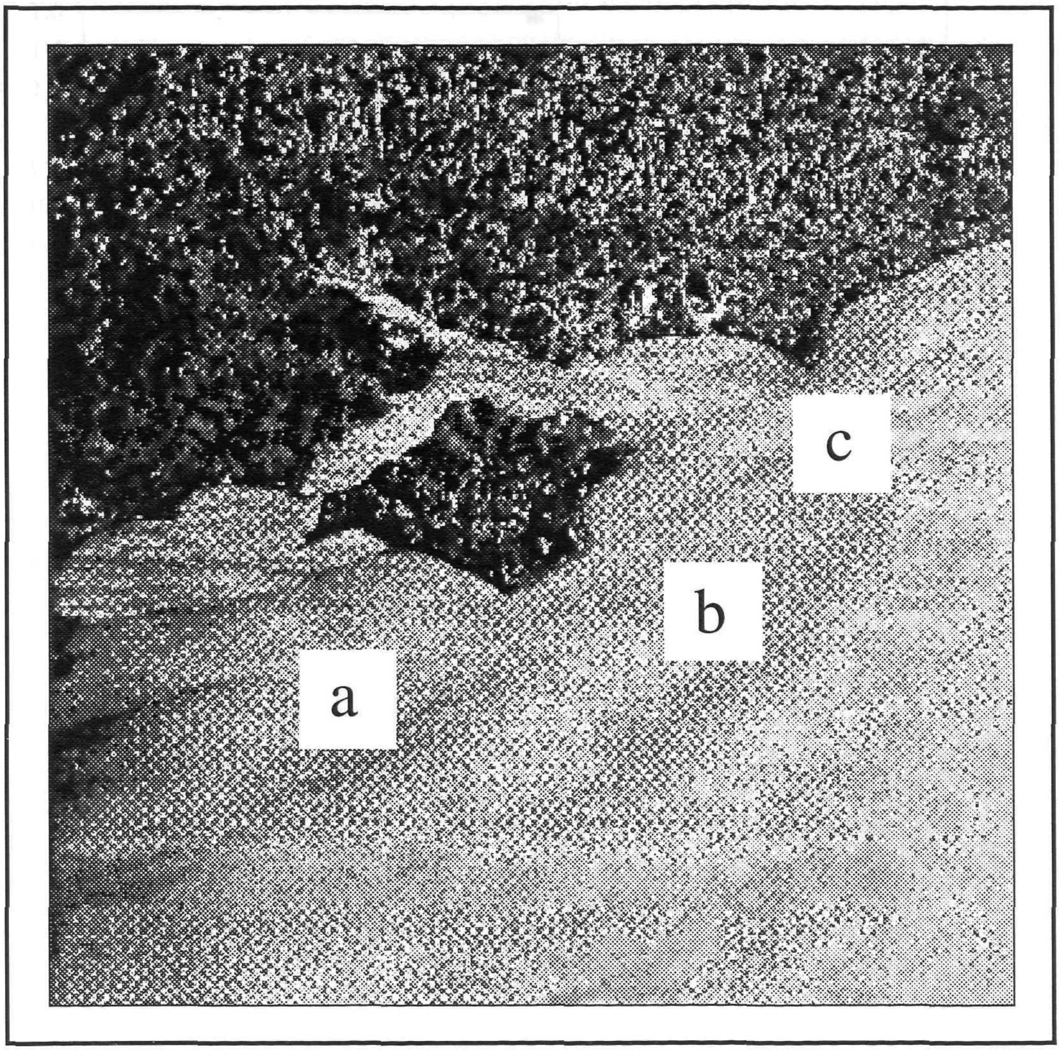

Figure 8.1 Locations of the extract boxes (a), (b) and (c), overlain on SAR image 13.3.92.

Figure 8.2 SD wind speed v mean wind speed

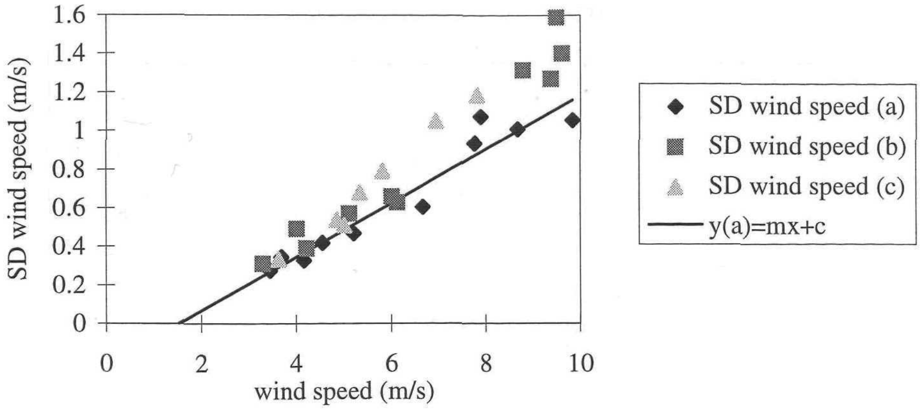

Figure 8.3 Separating wind speed variability from other effects on surface roughness

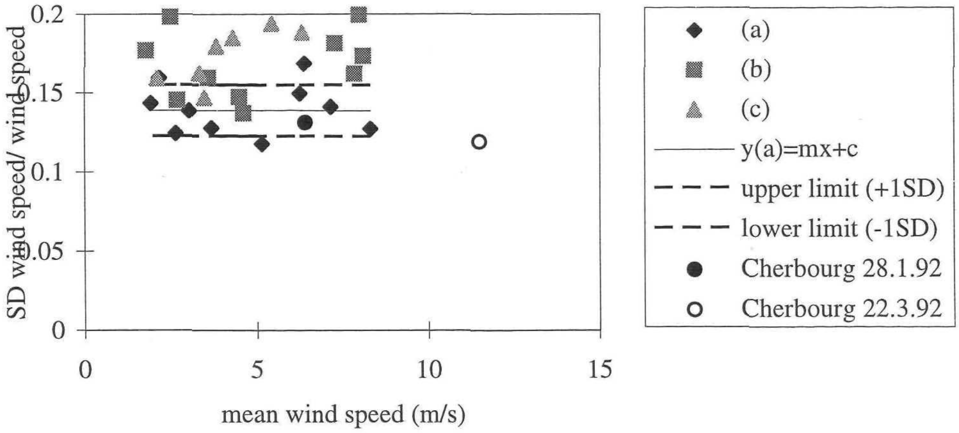

Figure 8.4 Wind speed variability relationship with currents for areas (b) and (c) for flood and ebb tides

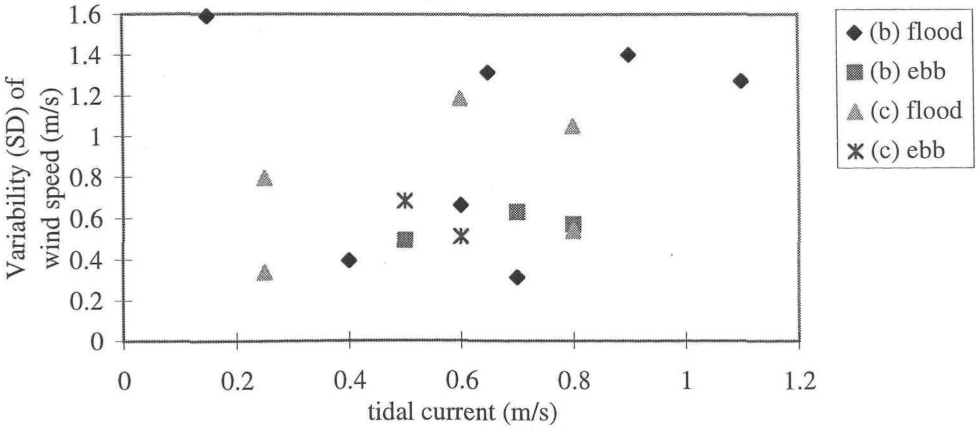

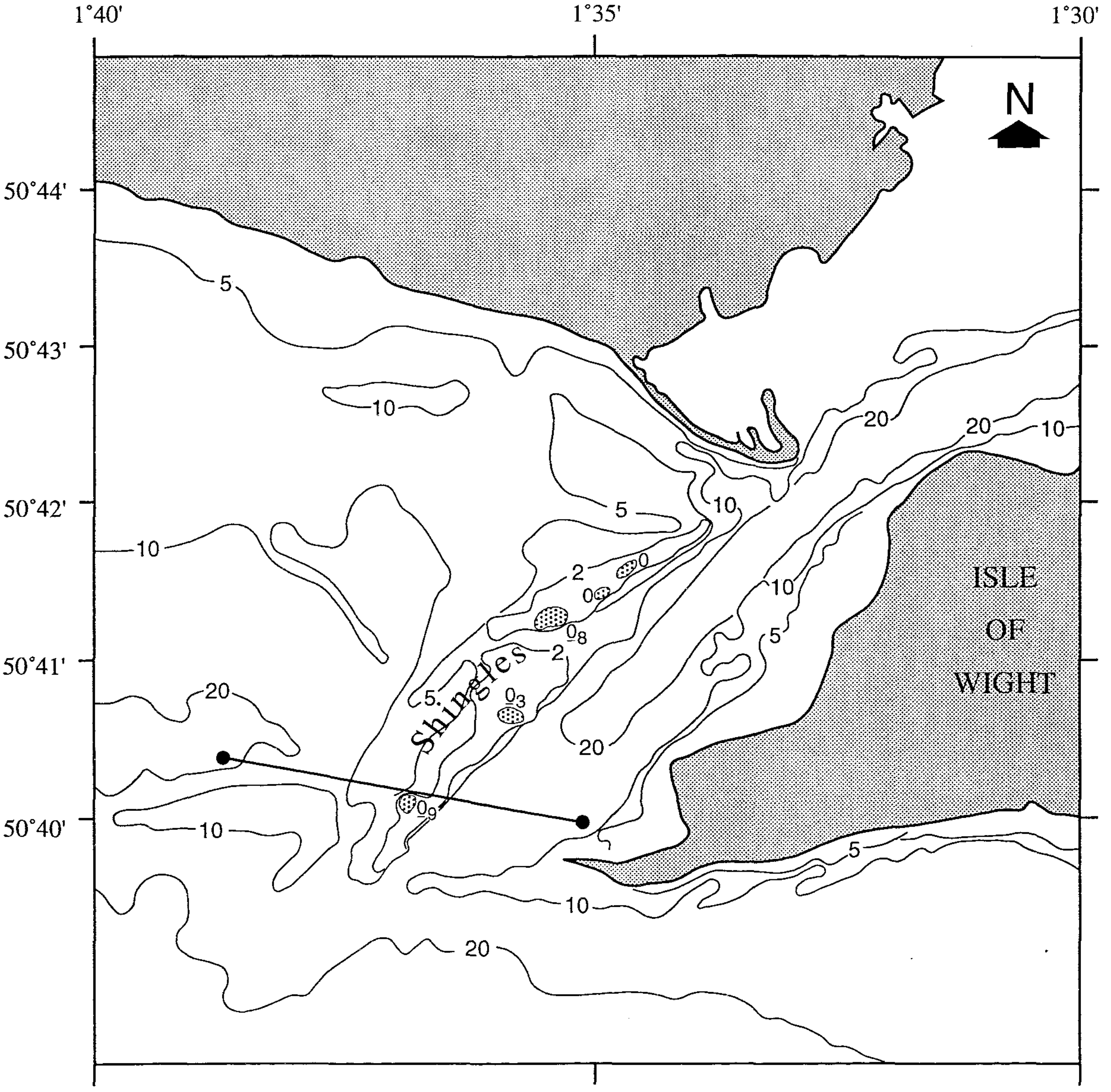

Figure 8.5 Location of the backscatter profile taken across the Shingles bank.

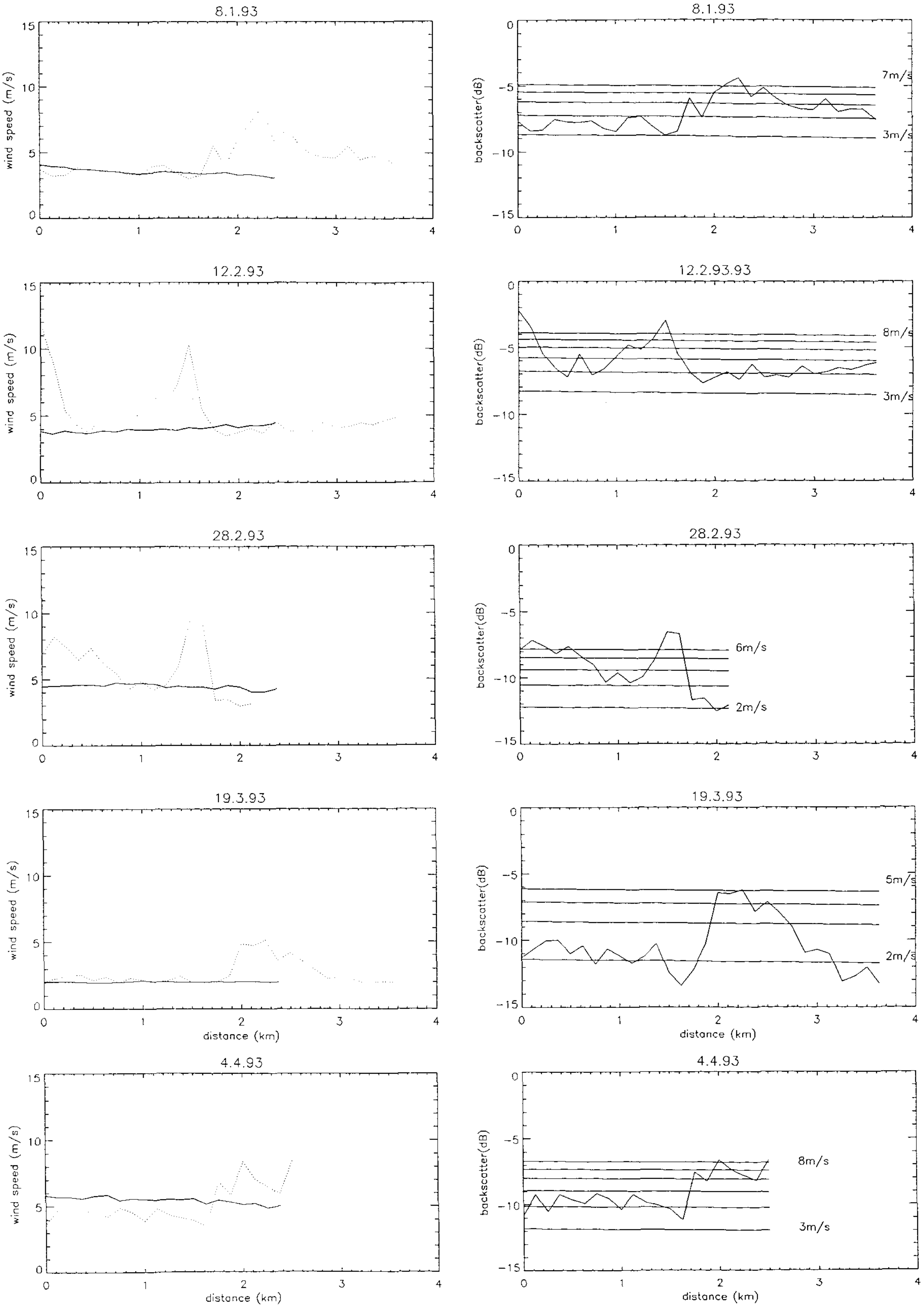

Figure 8.6 Profiles showing changes in surface roughness across the Shingles bank. Left column: SAR-derived apparent wind speed (dotted line) across the bank and the mean wind speed estimate from adjancent area (solid line). Right column: Backscatter (dB) across the bank overlying the CMOD4 predicted backscatter values for the given imaging conditions.

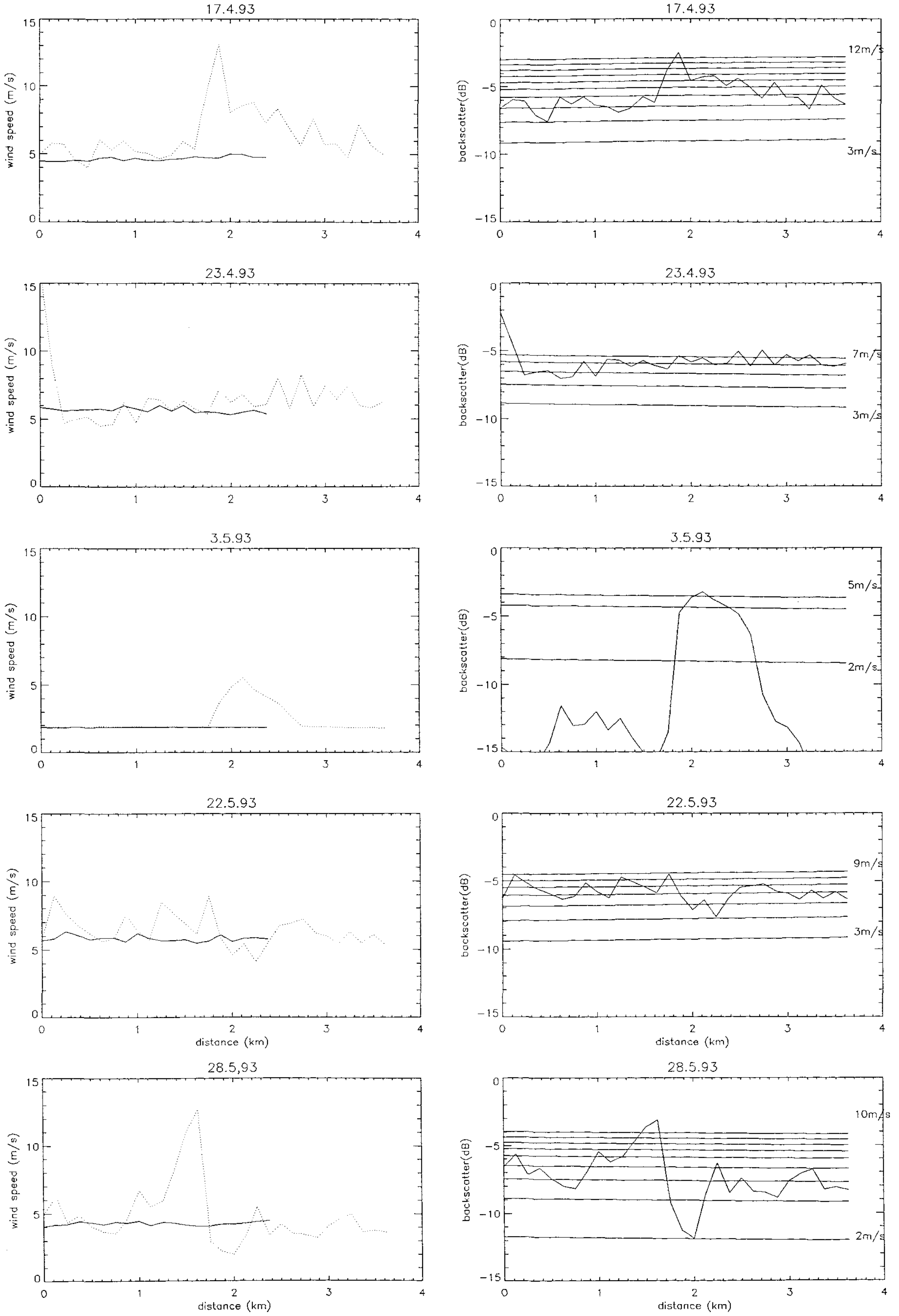

Figure 8.6 (cont.)

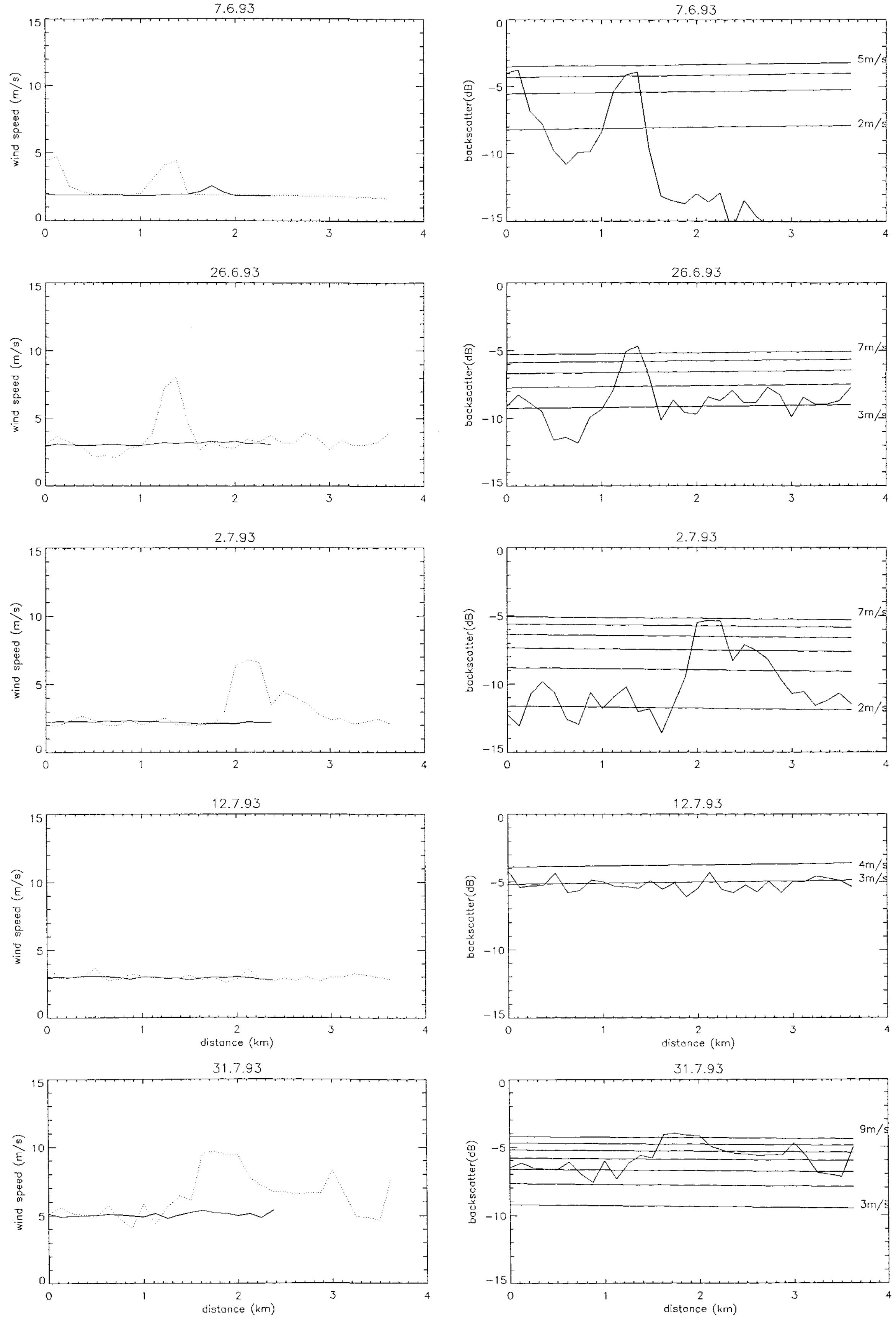

Figure 8.6 (cont.)

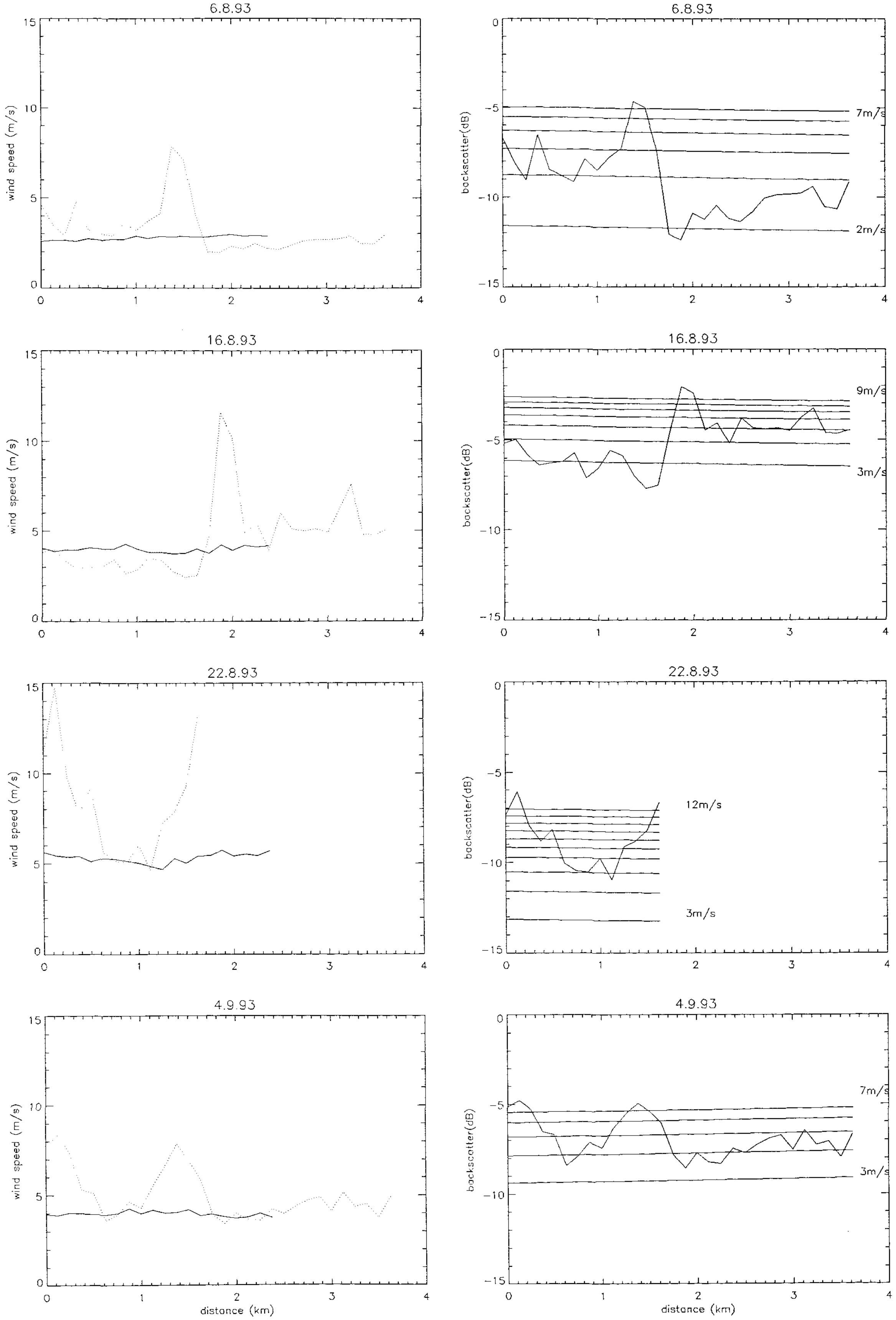

Figure 8.6 (cont.)

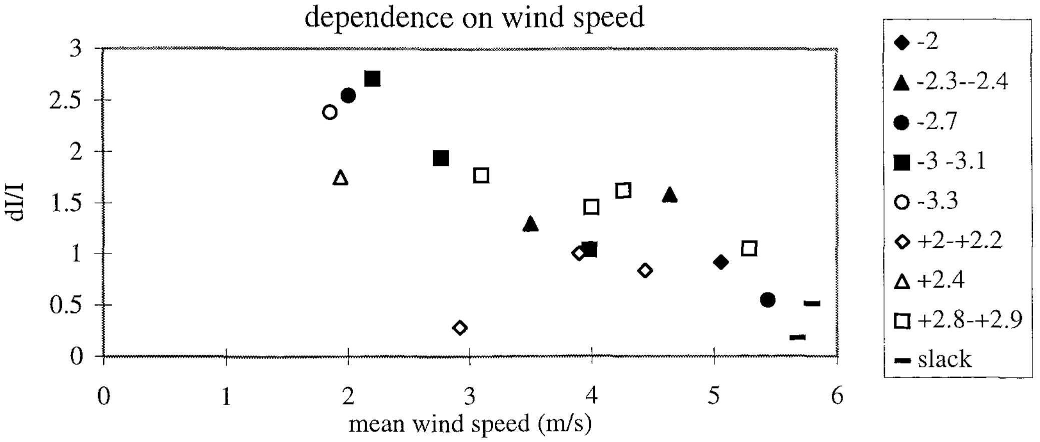

Figure 8.7 (a): Normalised calibrated backscatter (dI/I) dependence on wind speed

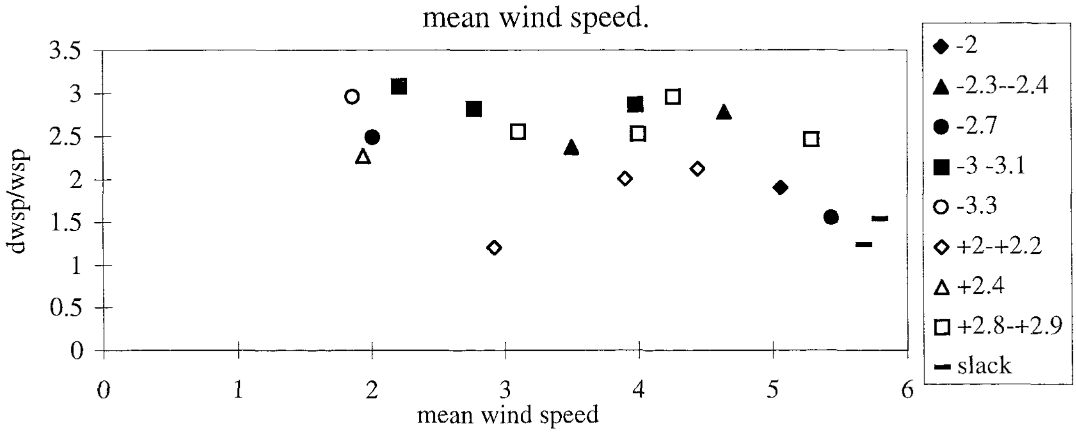

Figure 8.7(b): Normalised wind speed (dwsp/wsp) dependence on mean wind speed.

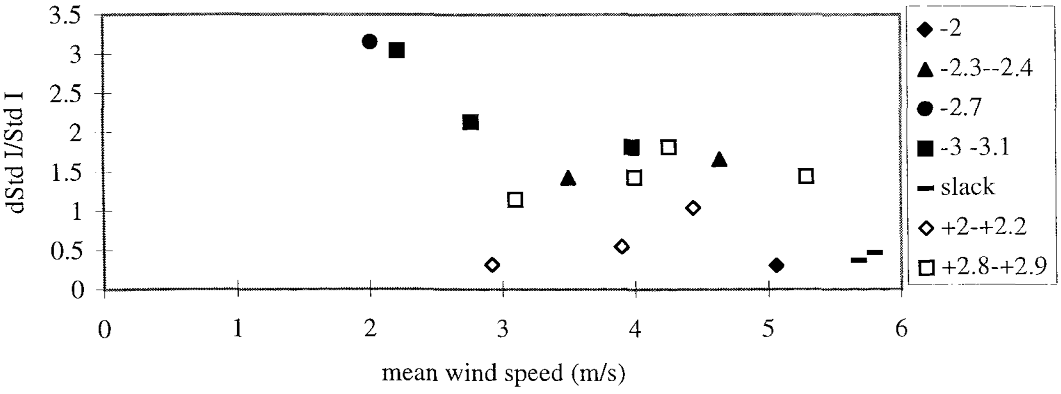

Figure 8.7(c): Normalised standardised backscatter (dStd I/Std I) dependence on mean wind speed.

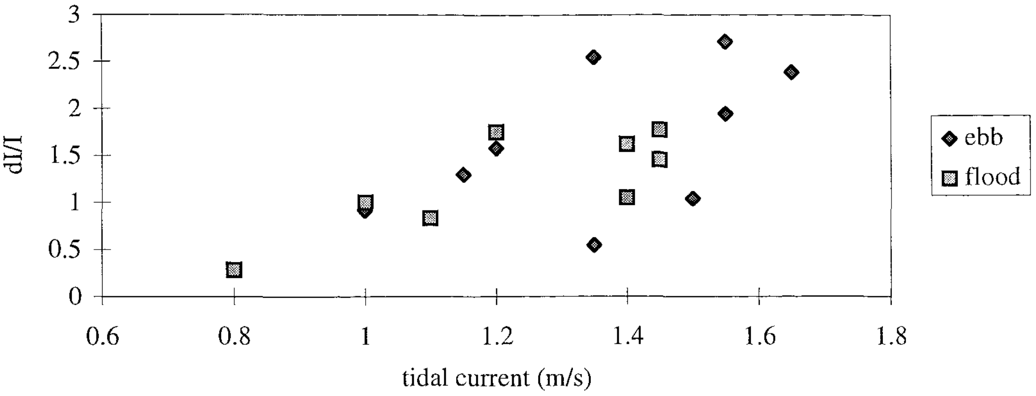

Figure 8.8(a): Normalised calibrated backscatter (dI/I) relationship with tidal current

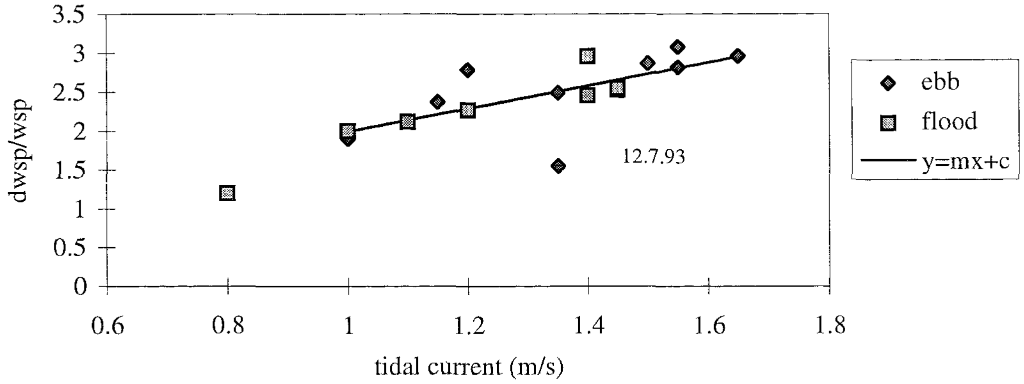

Figure 8.8(b): Normalised wind speed ratio (dwsp/ wsp) relationship with tidal current

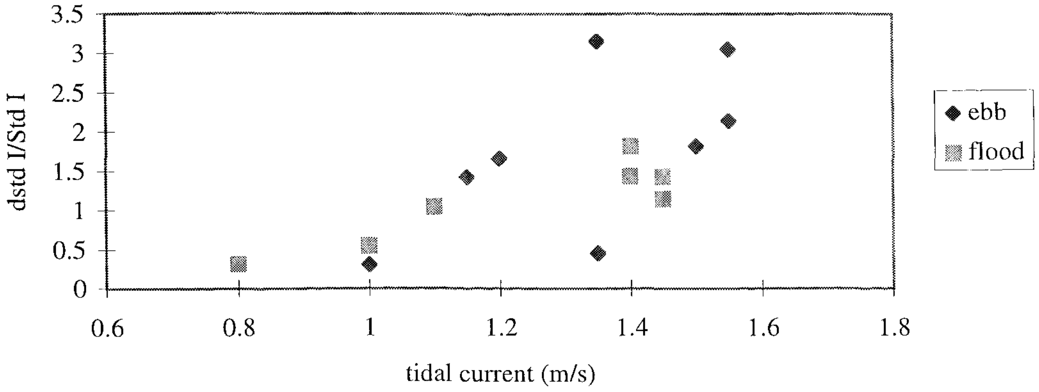

Figure 8.8(c): Normalised standardised backscatter (dStd I/StdI) relationship with tidal current

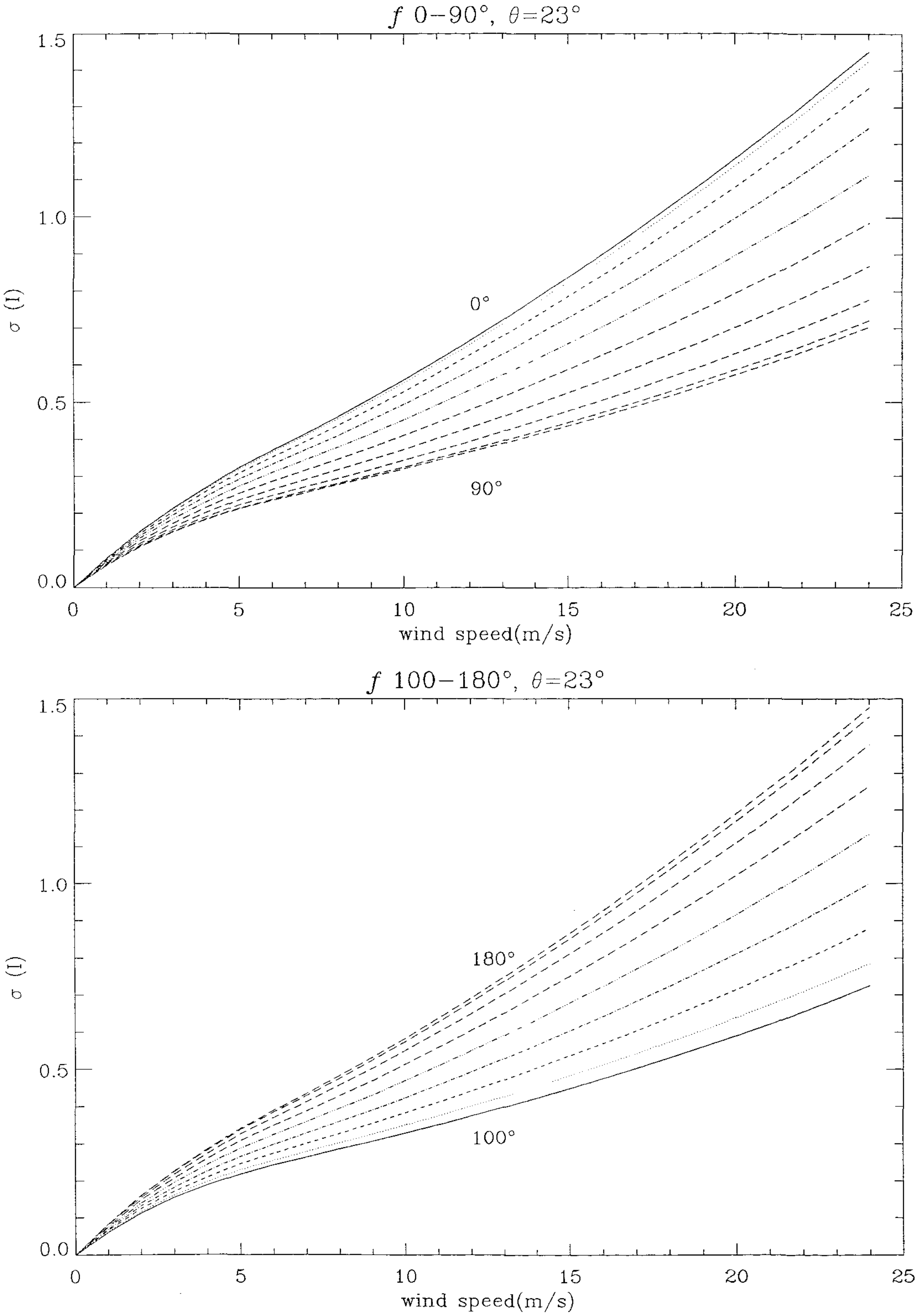

Figure 8.9 Backscatter (σ_0) to wind speed relationship given by CMOD4. Derived for upwind (0°) to downwind (180°) wind directions relative to radar view angle (*f*), for the SAR reference incidence angle, $\theta = 23°$. Backscatter (σ_0) is presented as a linear scale of intensity (I).

Figure 8.10: Normalised re-calculated backscatter using a Bragg model.

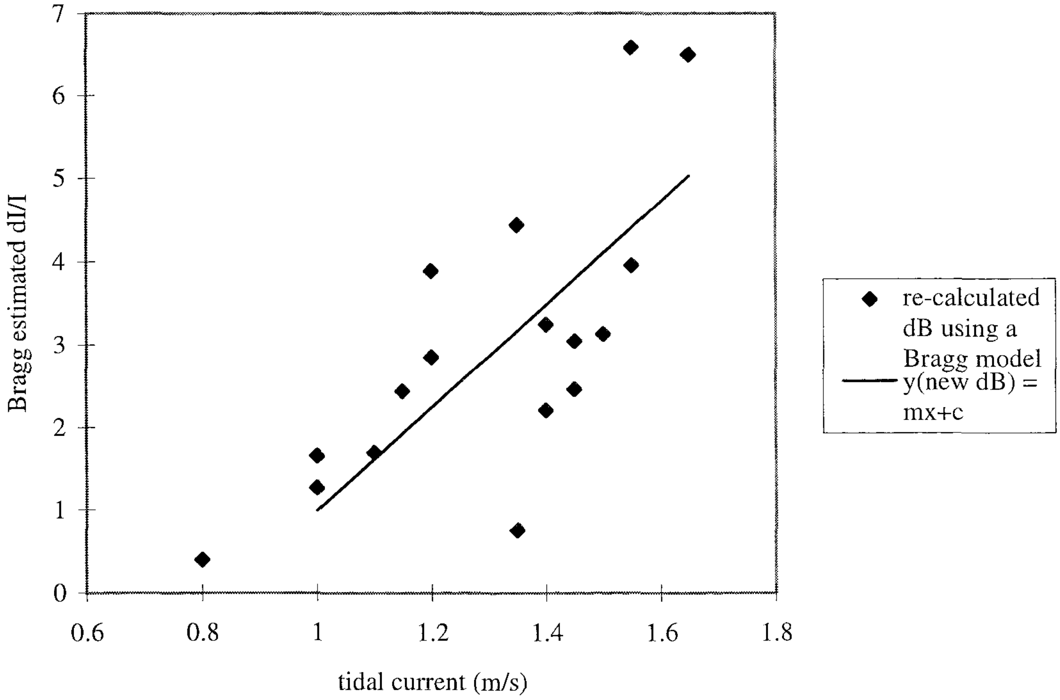

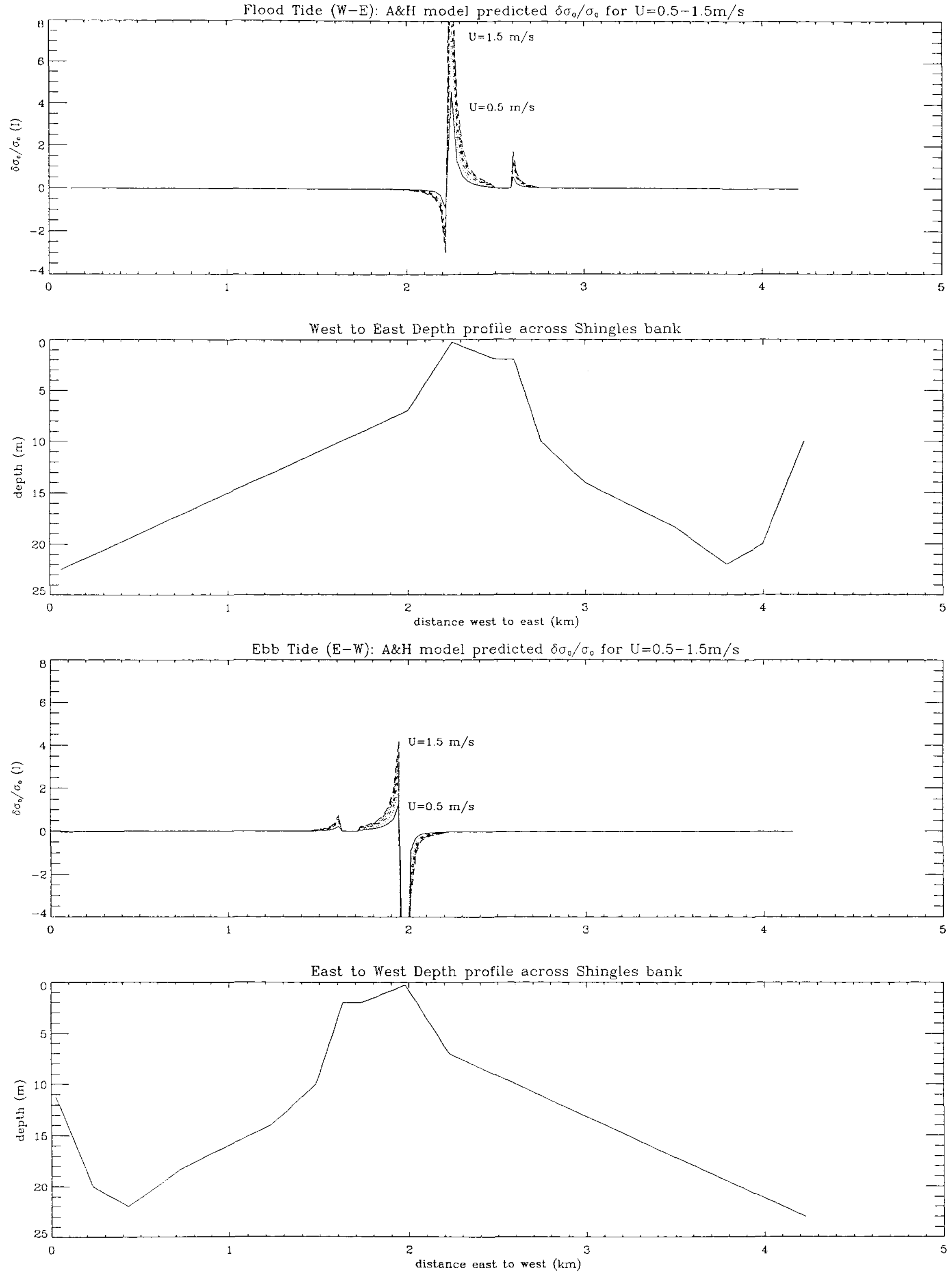

Figure 8.11 A&H modelled backscatter signal for the Shingles bank.
Calculated backscatter ratio for flood and ebb tide conditions for current speeds of 0.5 to 1.5 ms^{-1}. The depth profile is plotted west to east and vice versa, showing the different flow characteristics of the bank, such that the currents are from left to right across the page for both tidal states.

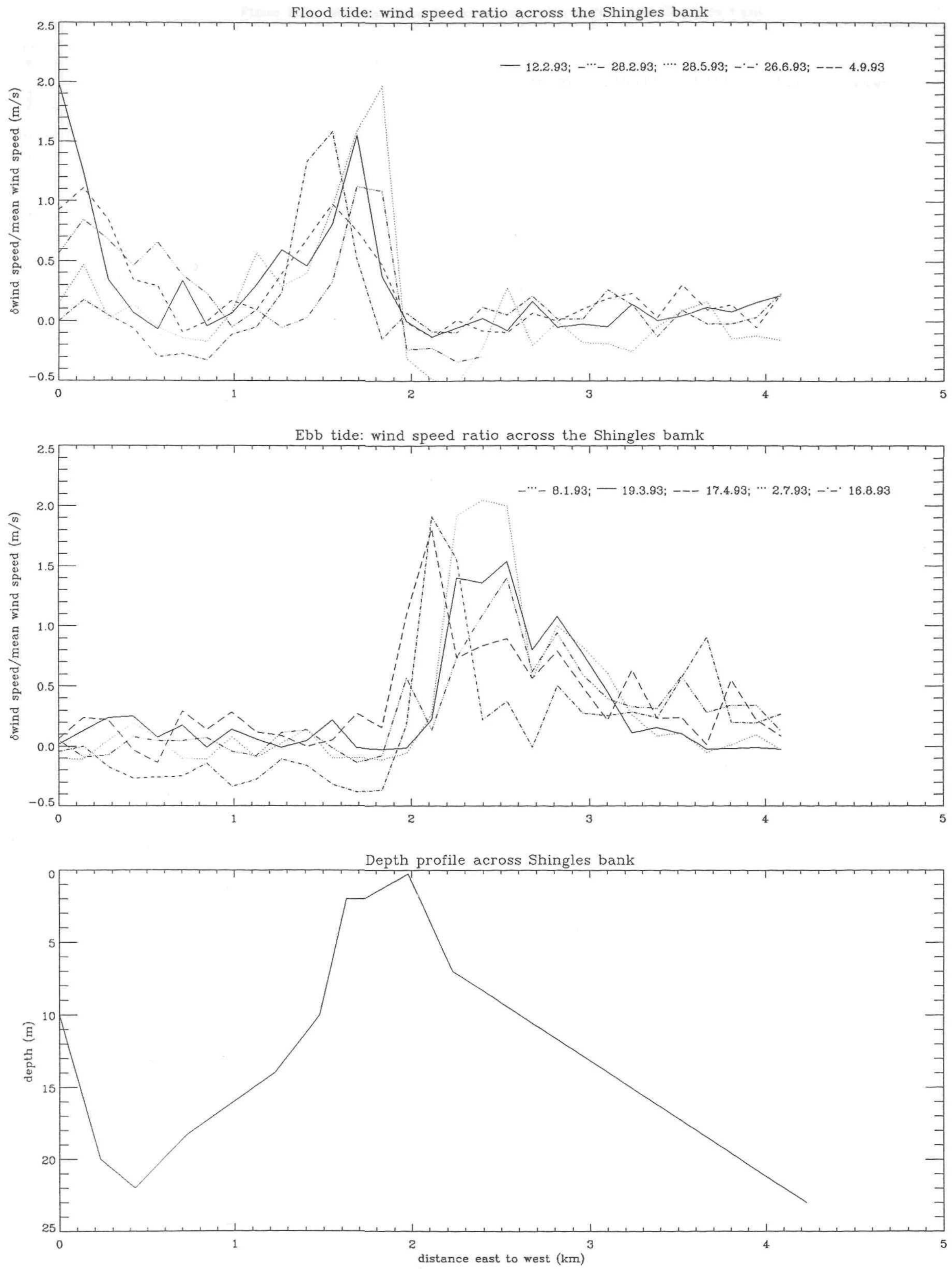

Figure 8.12 SAR derived estimates of surface roughness variations across the Shingles. (a-c) Profiles from several images of apparent wind speed (γ), standardised backscatter ($S\sigma_0$) and calibrated backscatter (σ_0) ratios for ebb and flood tide conditions, plotted east to west across the bank, according to the depth profile.

(a) Profiles of SAR-derived apparent wind speed ratios determined using CMOD4.

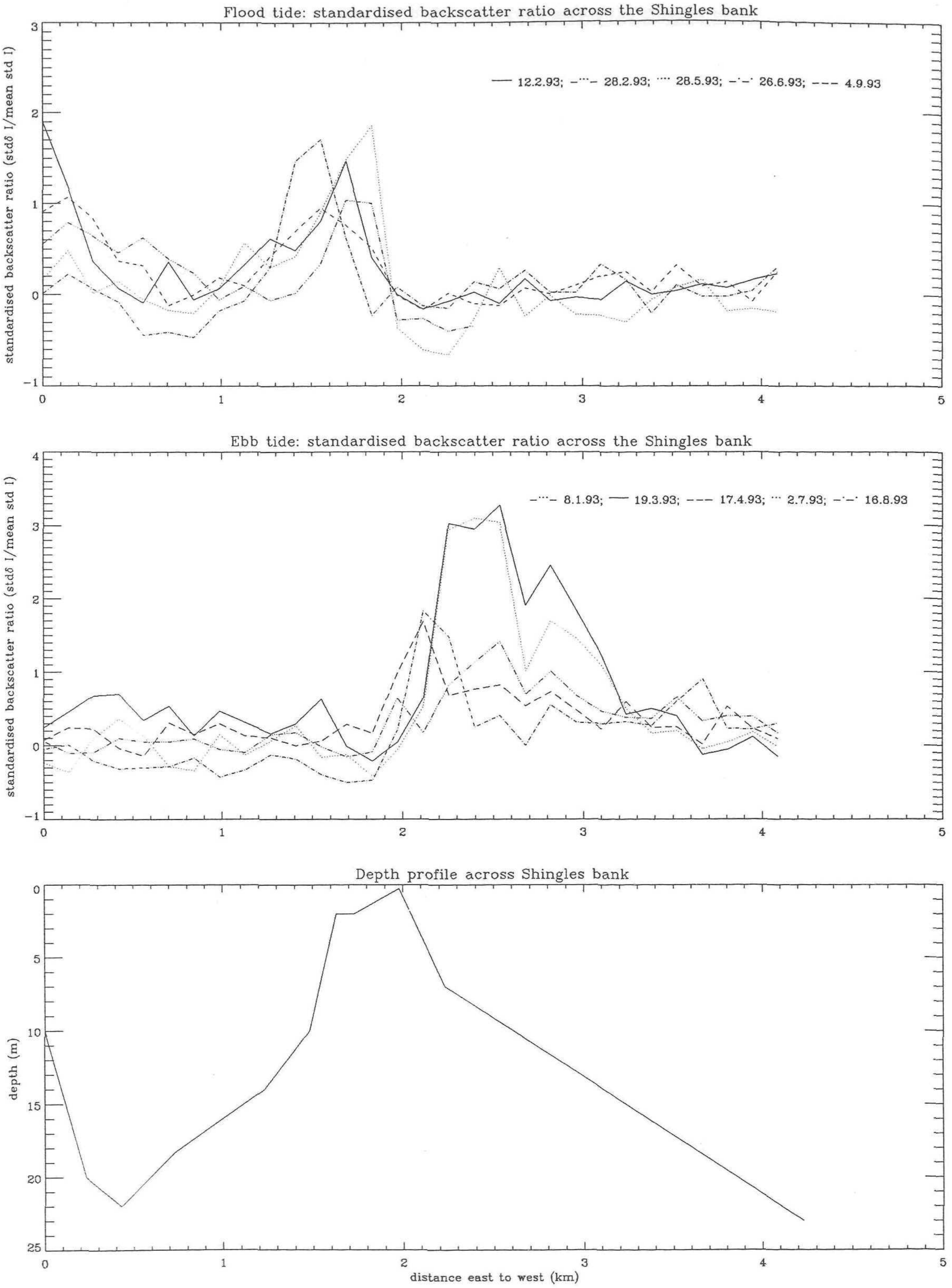

Figure 8.12 (b) Profiles of standardised backscatter ratios, determined using CMOD4.

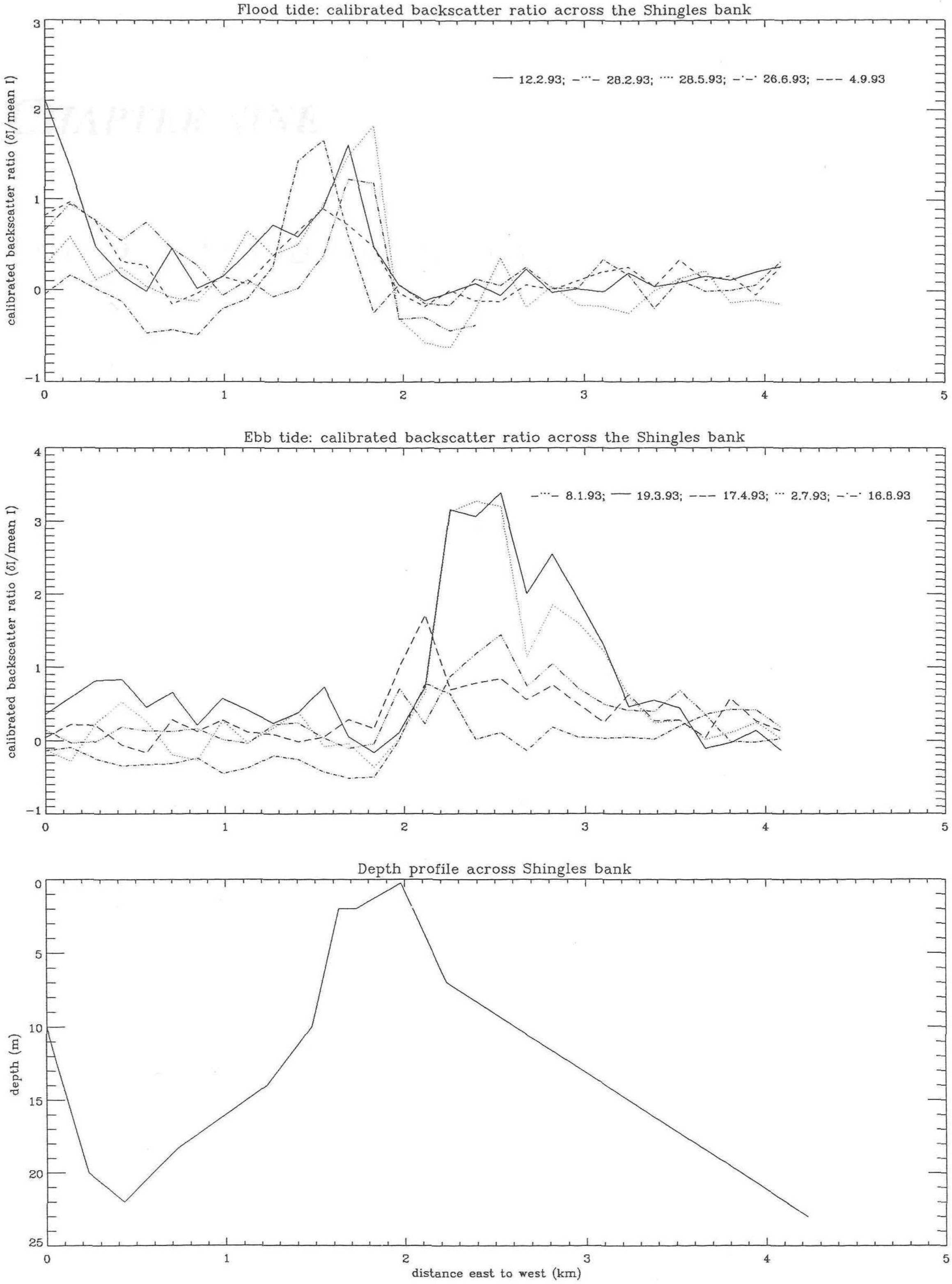

Figure 8.12 (c) Profiles of calibrated backscatter ratios.

CHAPTER NINE

CONCLUSIONS AND FUTURE WORK

9.1 CONCLUSIONS

The initial phase of this study was an investigation of the Seasat SAR images. This provided a basis for the major part of the work, which was the rigorous quantitative examination of the ERS-1 SAR data. The results emphasise the advantages of being able to examine a multi-temporal sequence of data, acquired by a very stable sensor. The main conclusions drawn are as follows:

- Full calibration of the SAR data is essential if quantitative analysis of backscatter signatures is to be undertaken (even of relative changes). This includes accounting for power loss due to saturation of the ADC; a correction not previously recognised or implemented by other users.

- The CMOD4 scatterometer wind retrieval model can be used to estimate wind speeds from the UK-PAF SAR data to accuracies within the error bands of the model, where a wind direction can be obtained. This was achieved at 100 m scales, a level of detail not previously contemplated.

- The high frequency variability (over a scale of 125 m) of the wind field detected by SAR is directly proportional to the mean wind speed. Any contribution to the modulation of the surface by hydrodynamic effects will cause the variability to deviate from the linear relationship.

- It is essential that the spurious effects of the SAR viewing geometry are removed if comparisons of the backscatter signature of surface roughness variations are to be made with physical variables, such as currents, between images or with model predictions. The analysis of SAR therefore requires additional information about the local wind direction.

- The normalised SAR-derived apparent wind speed residual (γ) provides a better representation of the surface roughness than can be achieved using a direct measure of backscatter. The effects of the radar viewing geometry produce non-linearities in the backscatter values which cannot be accounted for by normalising the data.

- To achieve any quantitative comparisons of SAR images with physical variables a high priority should be given to acquiring contemporaneous *in situ* measurements.

9.2 FUTURE WORK

The results achieved in this study provide the basis for future quantitative analysis of SAR data. However, before the investigations of specific factors affecting the surface roughness can be further developed these results should be rigorously tested using detailed *in situ* measurements:

- A detailed verification of the SAR-derived estimates of wind speed using CMOD4 is needed. This would involve comparing contemporaneous SAR and *in situ* measurements from a number of buoys or ships across a study region, over the complete range of wind and tide conditions. The accuracy of the model, as well as the sensitivity of the SAR to variations in the wind speed, could then be tested. The possibility of improving the accuracy by using more than one wind direction for the entire image should also be investigated.

- To verify that SAR can provide a proportional representation of surface roughness that can be related to the energy of the short wave spectrum. This could be achieved by confirming the linear dependence of the normalised wind speed ratio on surface roughness, comparing SAR-derived estimates with *in situ* measurements of the surface currents.

Once established the method developed here will provide a robust means to analyse SAR data, which will enable comparisons of backscatter signatures to be made between images or with physiscal variables. Some suggestions for future work which have arisen from this study are:

- A comparison between wind speed estimates for coastal and deeper water regions, investigating relative differences in surface roughness between these areas.

- Use of detailed maps of wind speed to investigate gradients and variability in the wind field associated with local weather fronts and transient wind patterns, such as a sea breeze, in the coastal zone.

- Test the effectiveness of model descriptions of backscatter variations across bathymetry. An interesting case study would be to compare the performance of models for two different types of underwater obstacle: a rocky ledge where the currents might be expected to flow straight across the feature; and a mobile bank where the current paths are more complex, producing a single peak in the backscatter signature.

REFERENCES

Allan T.D. 1983 A review of Seasat. In: *Satellite microwave remote sensing.* Allan T.D. (editor), Chichester, Ellis Horwood, 15-44.

Allan T.D. and T.H. Guymer 1984 Seasat measurement of wind and waves of selected passes over JASIN. *International Journal of Remote Sensing*, **5**, 379-408.

Alpers W. 1983 Imaging ocean surface waves by synthetic aperture radar - a review. In: *Satellite microwave remote sensing.* Allan T.D. (ed), Chichester, Ellis Horwood, 107-119.

Alpers W. and I. Hennings 1984 A theory of the imaging mechanism of underwater bottom topography by read and synthetic aperture radar. *Journal of Geophysical Research,* **89**, C6, 10,529-10,546.

Alpers W. and E. Salusti 1983 Scylla and Charybdis observed from space. *Journal of Geophysical Research,* **88**, C3, 1800-1808.

Alpers W. and B. Brummer 1994 Atmospheric boundary layer rolls observed by the synthetic aperture radar aboard the ERS-1 satellite. *Journal of Geophysical Research*, **99**, C6, 12,613-12,621.

Askari F., Geernaeft G.L. and W.C. Keller 1993 Radar imaging of thermal fronts. *International Journal of Remote Sensing*, **14**, 2, 275-294.

Boxall S.R. and I.R. Robinson 1987 Shallow sea dynamics from CZCS imagery. *Advances in Space Research,* **7**, no.2, 37-46.

Brown R. A. 1990 Surface fluxes and remote sensing of air-sea interactions. In: Surface waves and fluxes, **1**, 7-27, editors G.L. Geernaert and W.J. Plant.

Businger J.A. and W.J. Shaw 1984 The response of the marine boundary layer to mesoscale variations in the sea-surface temperature. Dyn. Oceans Atmosphere, **8**, 267-281.

Carruthers J.N. 1928 The flow of water through the Straits of Dover as gauged by continuous current meter observations at the Varne Light vessel. Fisheries Investigations, Ministry of Agriculture, Fisheries and Food, G.B., Series II, *Salmom Freshwater Fisheries,* **11(1)**, 1-109.

Castaneda J. 1994 Modelling and measuring (by HF radar) dispersion in the coastal zone. Ph.D. thesis submitted to University of Southampton, department of Oceanography.

Cheney R.W. 1976 A census of rings in the Gulf Stream system, U.S. Naval Oceanography Office, Washington, D.C.

De Loor G.P. 1981 The observation of tidal patterns, currents, and bathymetry with SLAR imagery of the sea. *IEEE Journal of Oceanic Engineering,* **OE-6**, 124-129.

Dewez S., P. Clabaut, O. Vicaire, C. Beck, H. Chamley and C. Augris 1989 Transits sedimentaires resultants aux confins Manche-mer du Nord. *Bulletin Society geological France,* **8**, 5, 1043-1053.

Donelan M. A. and W.J. Pierson 1987 Radar scattering and equilibrium ranges in wind generated waves with application to scatterometry. *Journal of Geophysical Research,* **92**, C5, 4971-5029.

European Space Agency (ESA) ESA ERS-1 Product Specification. SP-1149, issue 3.0, June, 1992.

Ewing G. 1950 Slicks, surface films and internal waves. *Journal of marine research,* **9**, 161-187.

Feindt F., V. Wismann, W. Alpers and W.C. Keller 1986 Airborne measurements of the ocean radar cross section at 5.3 Ghz as a function of wind speed. *Radio Science,* **21**, No.5, 845-856.

Fluxmanche 1993 Hydrodynamics and Biogeochemical fluxes in the eastern Channel; fluxes into the North Sea. June 1990 to August 1993, Mast 0053-C (EDB).

Friehe C.A., W.J. Shaw, D.P. Rogers, K.L. Davidson, W.G. Large, S.A. Stage, G.H. Crescenti, J.S. Khalsa, G.K. Grennhut and F. Li 1991 Air-sea fluxes and surface layer turbulence around a sea surface temperature front. *Journal of Geophysical Research,* **96**, C5, 8593-8609.

Gasparovic R.F., J.R. Apel, D.R. Thompson and J.S. Tochko 1986 A comparison of SIR-B synthetic aperture radar data with ocean internal wave measurements. *American Association for the Advancement of Science,* **232**, 1529-1531.

Gastel K. 1987 Imaging by x band radar of subsurface features: A nonlinear phenomenon. *Journal of Geophysical Reasearch,* **92**, C11, 11,857-11,865.

Gerling T.W. 1986 Structure of the Surface Wind Field from the Seasat SAR. *Journal of Geophysical Research,* **91**, C2, 2308-2320.

Gossard E.E. and W.H. Munk 1954 On gravity waves in the atmosphere. *Journal of Meteorology,* **2**, 259-269.

Greenhut G.K. 1982 Stability dependence of fluxes an bulk transfer coefficients in a tropical boundary layer. *Boundary Layer Meteorology,* **24**, 253-264.

Harris P.T., G.M. Ashley, M.B. Collins and A.E. James 1986 Topographic features of the Bristol Channel sea-bed: a comparison of SEASAT (synthetic aperture radar) and side-scan sonar images. *International Journal of Remote Sensing,* **7**, 1, 119-136.

Hartwig E.O. and F.L. Herr 1984 Chemistry and biology of the sea-surface interface. Relationships to remote sensing. Office of Naval Research, American Institute of Biological Sciences.

Hasslemann K. 1962 On the non-linear energy transfer in a gravity wave spectrum. *Journal of Fluid Mechanics*, **12**, part 1, 481-500.

Hayes R.M. 1981 Detection of the Gulf Stream. In: *Spaceborne synthetic aperture radar for oceanography,* The John Hopkins oceanographic studies, 7, 146-160.

Holliday D., G. St-Cyr and N.Woods 1986 A radar ocean imaging model for small to moderate incidence angles. *International journal of remote sensing,* **7**, 12, 1809-1834.

Hsu S.A., R. Fett and P.E. La Violette 1985 Variations in atmospheric mixing height across oceanic thermal fronts. *Journal of Geophysical Research,* **90**, C2, 3211-3224.

Huang N.E., T. Davidson, Chen and C. Tung 1972 Interactions between steady non-uniform currents and gravity waves with applications for current measurements. *Journal of Physical Oceanography,* **2**, 420-431.

Huges B.A. 1978 The effects of internal waves on surface wind waves. Part 2: Theoretical analysis. *Journal of Geophysical Research,* **83**, C, 455-465.

Hutchins M. 1994 ERS-1 off-line Cal/Val status report. DRA/CIS(CSC2)/5/14-CR-001.

Ivanov A. Yu., V.P. Nefed'yev, A.V. Smirnov and V.S. Etkin 1986 Investigation of the dynamics of mesoscale fronts from the data of remote sensing of the ocean at microwave frequencies. *Izvestiya, Atmosphere and oceanic physics*, **22**, 4, 337-341.

Johannessen J.A., R.A. Shuchman, O.M. Johannessen, K.L. Davidson and D.R. Lyzenga 1991 Synthetic aperture radar imaging of upper ocean circulation and wind fronts. *Journal of Geophysical Research,* **96**, C6, 10,411-10,422.

Johannessen J.A., L.P. Roed, O.M. Johannessen, G. Evensen, B. Hackett, L.H. Pettersson, P.M. Haugan and S. Sandven 1992 Monitoring and modelling of the marine coastal environment. Presented at the First Thematic Conference on Remote Sensing for Marine and Coastal Environments, New Orleans, USA.

Johannessen J.A., R.A. Shuchman, K. Davidson, O. Frette, G. Digranes and O.M. Johannessen 1993 Coastal ocean studies with ERS-1 SAR during NORCSEX'91. *Proceedings First ERS-1 Symposium - Space at the Service of our Environment,* Cannes, France, November 1992, ESA SP-359.

Jones W.L., Schroeder L.C. and J.L.Mitchell 1977 Aircraft Measurements of the Microwave Scattering Signature of the Ocean. *IEEE Journal of Oceanic Engineering,* **OE-2**, No.1, 52-61.

Jones W.L., Schroeder L.C., Boggs D.H., Bracalente E.M., Brown R.A., Dome G.J., Pierson W.J. and F.J. Wentz 1982 The SEASAT -A Satellite Scatterometer: The Geophysical Evaluation of Remotely Sensed Wind Vectors over the Ocean. *Journal of Geophysical Research,* **87**, C5, 3297-3317.

Kasischke E.S., Y.C. Tseng, G.A. Meadows and A.K. Liu 1983 Observations of internal waves and frontal boundaries on Seasat SAR imagery collected over the eastern North Atlantic Ocean. Presented at the seventeenth International Symoposium on Remote Sensing of the Environment, Ann Arbor, MI., 1193-1212.

Keller W.C., W.J. Plant and D.E. Weissman 1985 The dependence of x-band microwave sea return on atmospheric stability and sea state. *Journal of Geophysical Research,* **90**, C1, 1019-1029.

Keller W.C., V. Wismann and W. Alpers 1989 Tower based measurements of the ocean C-band radar backscattering cross section. *Journal of Geophysical Research,* **94**, C1, 924-930

Kenyon N.H. 1983 Tidal Current bedforms investigated by Seasat. In: *Satellite microwave remote sensing.* Allan T.D. (ed), Chichester, Ellis Horwood, 261-270.

Khalsa S.J.S and G.K. Greenhut 1989 Atmospheric turbulence structure in the vicinity of an oceanic front. *Journal of Geophysical Research,* **94**, C4, 4913-4922.

Lake B.M. and H.C. Yeun 1978 A new model for non-linear gravity waves. *Journal of Fluid Mechanics,* **88**, part 1, 33-62.

Lancashire D.C. 1987 ERS-1 AMI Calibration and Characterisation Plan. ER-PL-MSS-AM-0008, issue 13, March 1987.

Large W.G. and P.Pond 1981 Open ocean momnentum flux measurements in moderate to strong winds. *Journal of Physical Oceanography,* **11**, 324-336.

Laur H. 1992 ERS-1 SAR calibration: Derivation of backscattering coefficient σ_0 in ERS-1 SAR PRI products. European Space Agency, issue 1, rev.0.

Laur H., Meadows P., Sanchez J.I. and E. Dwyer 1993 ERS-1 SAR radiometric calibration. Proceedings of the CEOS SAR calibration workshop (ESA-WPP-048).

La Violette P.E. 1983 The Grand Banks Experiment: A satellite/ aircraft/ ship experiment to explore the ability of specilised radars to define ocean fronts. Naval Ocean Research and Development Activity report 49.

Lecomte P. 1993 CMOD4 Model Description. ESA/ESRIN document no. ER-TN-ESA-GP-1120, issue 1.2.

Lichey D.E., M.G. Mattie and L.J. Mancini 1981 Tracking of a warm water ring. In: *Spaceborne synthetic aperture radar for oceanograph.* The John Hopkins oceanographic studies, 7, 171-184.

Liu W.T. 1984 The effects of the variations in sea surface temperature and atmospheric stability in the estimation of average wind speed by Seasat-SASS, *Journal of Physical Oceanography*, **14**, 392-401.

Long A.E. 1985 Towards a C-band radar sea echo model for the ERS-1 scatterometer. Proceedings of a conference on spectral signatures, Les Arc, France, ESA SP-247.

Lyzenga, D.R. 1991 Interaction of short surface and electromagnetic waves with ocean fronts. *Journal of Geophysical Reasearch*, **96**, C6, 10,765-10,772.

Matthews A. 1994 High spectral resolution remote sensing of phytoplankon in the coastal zone. Ph.D. thesis submitted to University of Southampton, department of Oceanography.

Matthews A. and S.R. Boxall 1994 Application of airborne remote sensing in coastal frontal dynamics. Proceedings of the first international airborne remote sensing conferene and exhibition, **vol. 2**.

Matthews J.P., V.R. Wismann, K. Lwiza, R. Romeiser, I. Hennings and G.P. de Loor A study of frontal boundaries near the Rhine plume by radar scatterometer, airborne thematic mapper and *in situ* techniques. In preparation.

McClain C.R., N.E. Huang and P.E. La Violette 1982 Measurements of sea-state variations across oceanic fronts using laser profilometry. *Journal of Physical Oceanography,* **12**, 1228-1244.

McLeish W. and D.B. Ross 1985 Wave refraction in an ocean front. *Journal of Geophysical Research,* **90**, C6, 11,929-11,938.

Meadows G.A., R.A. Shuchman, Y.C. Tseng and E.S. Kasischke 1983 SEASAT synthetic aperture radar observations of wave-current and wave-topographic interactions. *Journal of Geophysical Reasearch*, **88**, C7, 4393-4406.

Meadows P.J. 1993 ERS-1 SAR PRI Status Report. GEC-Marconi Technical Report Y/218/9898, issue 1, January 1993.

Meadows P.J. and C.M. Stapleton 1994 ERS-1 SAR Analogue to Digital Converter Saturation. MRC Science Group Phase E3, document number PF-TN-MRC-0012, 15.3.94.

Meadows P.J. and P.A. Wright 1994 ERS-1 SAR analogue to digital converter saturation. *Proceedings of the CEOS SAR calibration workshop,* Ann Arbor, Michigan, USA, 28-30 September 1994.

Moore R.K. and W.J. Pierson 1966 Measuring sea state and estimating surface winds from a polar orbiting satellite. Paper presented at Proceedings International Symposium Electromagnetic Sensing of Earth from Satellites, Miami Beach, Fla., Nov. 22-24, 1966.

Nash L.A. and S.R. Boxall 1993 Water fluxes through the Strait of Dover. Sub-task W2 in Fluxmanche final report: Hydrodynamics and Biogeochemical fluxes in the eastern Channel; fluxes into the North Sea. June 1990 to August 1993, Mast 0053-C (EDB).

Pattiaratchi C. and M. Collins 1987 Mechanisms for linear sandbank formation and maintenance in relation to dynamical oceanographic observations. *Progress in Oceanography,* **19**, 117-176.

Phillips O.M. 1977 The dynamics of the upper ocean. (2nd edn), Cambridge University Press.

Phillips O.M. 1981 The structure of short gravity waves on the ocean surface. In: *Spaceborne synthetic aperture radar for oceanography,* The John Hopkins oceanographic studies, No.7, 24-31.

Phillips O.M. 1988 Radar returns from the sea surface - Bragg scattering and breaking waves. *Journal of Physical Oceanography,* **18**, 1065-1075.

Pingree R.D., G.R. Forster and G.K. Morrison 1974 Turbulent convergent tidal fronts. *Journal Marine Biological Association,* **54**, 469-479.

Pingree R.D. and G.T. Mardell 1981 Slope turbulence, internal waves and phytoplankton growth at the Celtic Sea shelf-break. *Phil. Trans. Royal Society London*, **A302**, 633-682.

Pingree R.D., G.T. Mardell and L. Maddock 1985 Tidal mixing in the Channel Isles Region derived from the results of remote sensing and measurements at sea. *Estuarine, Coastal and Shelf Science,* **20**, 1-18.

Pingree R.D. and G.T. Mardell 1987 Tidal flows around the Channel Islands. *Journal of marine biology association U.K.*, **67**, 691-707.

Robinson I.S. 1985 Satellite Oceanography - an introduction for oceanographers and remote-sensing scientists. Ellis Horwood series in Marine Science.

Ross D.B. 1981 The wind speed dependency of ocean microwave backscatter. In: *Spacebourne synthetic aperture radar for oceanography*, edited by: R.C. Beal; P.S. DeLeonibus and I. Katz, John-Hopkins Press, Baltimore, Md., 24-31.

Ruddick K.G. and J.B. Moens 1993 ERS-1 synthetic aperture radar imagery of the Rhine-Meuse plume discharge front - preliminary results and plans. In: a synthesis of space related research in Belgium - 'Observation de la Terre'.

Sager G. and R. Sammler 1964 Atlas der tidewasserstande fur die Nordsee, den Kanal und die Irischen See. Berlin Institut fur Meereskunde, Rostock.

Sager G. and R. Sammler 1968 Atlas der Gezeitenstrome fur die Nordsee, den Kanal und die Irischen See. Sehydrograhischer Dienst der DDR, Rostock, 58.

Scott J.C. 1986a The effect of organic films on water surface motions. In: *Oceanic whitecaps and their role in air-sea exchange processes,* (eds. E.C. Monahan and G. MacNiocaill), Galway University Press, 159-165.

Scot J.C. and C. Brownsword 1994 Flowing hot and cold. *Physics world*, 28.

Scully-Power P. 1986 Navy oceanographer Shuttle observations, STS 41-G: Mission Report, NUSC Technical Document 7611.

Shuchman R.A., D.R. Lyzenga and G.A. Meadows 1985 Synthetic aperture radar imaging of ocean-bottom topography via tidal-current interactions: theory and observations. *International Journal of Remote Sensing,* **6**, 1179-1200.

Shuchman R.A., J. Johannessen, C. Rufenach, K. Davidson and C. Wackerman 1993 Determination of Wind Speed, Wind Direction and Atmospheric Structure using ERS-1 SAR data during NORCSEX'91. *Proceedings International Geoscience and Remote Sensing Symposium (IGARSS): Better Understanding of Earth Environment*, 18-21 August 1993, Tokyo, Japan, 537-539.

Shuchman R., Johannessen J., Rufenach C., Davidson K., and C.Wackerman 1994 Determination of wind speed and direction using ERS-1 SAR data during NORCSEX'91. Proceedings second ERS-1 symposium - Space at the service of our environment, Hamburg, Germany, 11-14 October, 1993. ESA SP-361 (January 1994).

Simpson J.H. and J.R. Hunter 1974 Fronts in the Irish Sea. *Nature*, **vol. 250**, 404-406.

Simpson J.H., D.G. Hughes and N.C.G. Morris 1977 The relation of seasonal stratification to tidal mixing on the continental shelf. *Deep Sea Research,* **24(supplement)**, 327-340.

Simpson J.H., C.M. Allen and N.C.G. Morris 1978 Fronts on the continental shelf. *Journal of Geophysical Research,* **83**, C9, 4607-4614.

Smith A.M., C. Wilson and P.J. Meadows 1994 The EODC SAR processor. *International journal of remote sensing,* **15**, 4, 785-801.

Smith S.D. and E.G. Banke 1975 Variation of the sea surface drag coefficient with wind speed. *Quaterly Journal Royal Meteorological Society*, **101**, 655-667.

Smith S.D. 1988 Coefficients for Sea Surface Wind Stress, Heat Flux and Wind Profiles as a function of Wind Speed and Temperature. *Journal of Geophysical Research,* **93**, C12, 15,467-15,472.

Soulsby R.L. 1977 Similarity scaling of turbulence spectra in marine and atmospheric boundary layers. *Jouranl of Physical Oceanography,* **7**, 934-937.

Stewart R.H. 1985 Methods of satellite oceanography. University of California press.

Stoffelen A. and D.L.T. Anderson 1993 Wind retrieval and ERS1- Scatterometer Radar Backscatter Measurements. *Adv. Space Research*, **13**, No.5, (5)53-(5)60.

Thomson R.E., P.W. Vachon and G.A. Borstad 1992 Airborne synthetic aperture radar imagery of atmospheric gravity waves. *Journal of Geophysical Reasearch*, **97**, C9, 14,249-14,257.

Thorpe S.A. 1985 Small-scale processes in the upper ocean boundary layer. *Nature*, **318**, 519-522.

Tilley D.G. and R.C. Beal 1993 ERS-1 and ALMAZ SAR ocean wave imaging over the Gulf Stream and the Grand Banks. *Proceedings First ERS-1 Symposium - Space at the Service of our Environment,* Cannes, France, November 1992, ESA SP-359.

Topliss B.J., Guymer T.H. and A. Viola 1994 Radar and infrared measurements of a cold eddy in the Tyrrhenian Sea.

UK-PAF 1993 ERS-1.SAR.PRI Health Report, ESA, compiled by UK-PAF.

Vachon P.W., Liu A.K. and E Mollo-Christensen 1992 Observations of the Gulf Stream by the CCRS SAR during SWADE. *EOS Transactions,* American Geophysical Union, **73**, 2, 14-15.

Vachon P.W. 1994 An ERS-1 SAR image of atmospheric lee waves. *Journal of Geophysical Reasearch*, **99**, C11, 22483-22490.

Valenzuela G.R. 1978 Theories for the interaction of electromagnetic and ocean waves. A review, *Boundary Layer Meteorology,* **13**, 61-85.

Vesecky T.V. and R.H. Stewart 1982 The observation of ocean surface phenomena using imagery from the SEASAT synthetic aperture radar: An assessment. *Journal of Geophysical Reasearch*, **87**, C5, 3397-3430.

Vogelzang J., G.J. Wensink, G.P. De Loor, H.C. Peters, H. Pouwels and W.A. van Gein 1989 Sea bottom topography with X-band SLAR. Report for the Netherlands remote sensing board, bcrs 89-25.

Vogelzang J., H.C. Peters, G.P. DeLoor, H. Pouwels and G.J. Wensink 1992 Sea bottom topographywith X-band SLAR: the relation between radar imagery and bathymetry. *International Journal of Remote Sensing,* **13(10)**, 1943-1958.

Watson G. and I.S. Robinson 1990 A study of internal wave propagation in the Strait of Gibraltar using shore-based marine radar images. *Journal of Physical Oceanography,* **20**, 374-395.

Weissman D.E. and T.W. Thompson 1977 Detection and interpretation of ocean roughness variations across the Gulf Stream inferred from radar cross section observations. Oceans '77, MTS-IEEE, 14B1-10.

Weissman D.E., T.W. Thompson and R. Legekis 1980 Modulation of sea surface radar cross section by surface stress: wind speed and temperature effects across the Gulf Stream. *Journal of Geophysical Reasearch*, **85**, C9, 5032-5042.

Wismann V. 1992 A C-band wind scatterometer model derived from the data obtained during the ERS-1 calibration/ validation campaign. *Proceedings First ERS-1 Symposium - Space at the Service of our Environment*, Cannes, France, 4-6 November, 1992. ESA SP-359.

Wu J. 1991 Effects of atmospheric stability on ocean ripples: A comparison between optical and microwave measurements. *Journal of Geophysical Reasearch*, **96**, C4, 7265-7269.